Non-parametric and Non-filtering Methods for Rolling Element Bearing Condition Monitoring

Hamid Faghidi

Thesis submitted to the Faculty of Graduate and Postdoctoral studies in partial fulfillment of the requirements for the

Doctorate in Philosophy degree

in Mechanical Engineering

Ottawa-Carleton Institute for Mechanical and Aerospace Engineering

University of Ottawa

Abstract

Rolling element bearings are one of the most significant elements and frequently-used components in mechanical systems. Bearing fault detection and diagnosis is important for preventing productivity loss and averting catastrophic failures of mechanical systems. In industrial applications, bearing life is often difficult to predict due to different application conditions, load and speed variations, as well as maintenance practices. Therefore, reliable fault detection is necessary to ensure productive and safe operations.

Vibration analysis is the most widely used method for detection and diagnosis of bearing malfunctions. A measured vibration signal from a sensor is often contaminated by noise and vibration interference components. Over the years, many methods have been developed to reveal fault signatures, and remove noise and vibration interference components.

Though many vibration based methods have been proposed in the literature, the high frequency resonance (HFR) technique is one of a very few methods have received certain industrial acceptance. However, the effectiveness of the HFR methods depends, to a great extent, on some parameters such as bandwidth and centre frequency of the fault excited resonance, and window length. Proper selection these parameters is often a knowledge-demanding and time-consuming process. In particular, the filter designed based on the improperly selected bandwidth and center frequency of the fault excited resonance can filter out the true fault information and mislead the detection/diagnosis decisions. In addition, even if these parameters can be selected properly at beginning of each process, they may become invalid in a time-varying environment after a certain period of time. Hence, they may have to be re-calculated and updated, which is again a time-consuming and error-prone process. This undermines the practical significance of the above methods for online monitoring of bearing conditions.

To overcome the shortcomings of existing methods, the following four non-parametric and non-filtering methods are proposed:

1. An amplitude demodulation differentiation (ADD) method,
2. A calculus enhanced energy operator (CEEO) method,
3. A higher order analytic energy operator (HO_AEO) approach, and
4. A higher order energy operator fusion (HOEO_F) technique.

The proposed methods have been evaluated using both simulated and experimental data.

Acknowledgements

First of all, I would like to express my sincere thanks to my supervisor Professor Ming Liang for his invaluable guidance, and knowledge. His friendship, help, and financial support have made it possible for me to complete this PhD thesis. I have learned a lot from his discussions, step-by-step guidance and the painstaking effort in helping with the writing of this thesis.

I wish to thank those who encouraged me to accomplish the study from Master to PhD over the past four years.

I would like to thank a friendly and cheerful group of fellow students, postdoctoral fellows and visiting scholars in Professor Liang's research group.

I am also grateful to the PhD Committee members for their time and help.

Contents

List of Figures

List of Tables

Nomenclature

A	amplitude of fault impulse (Used in Eq. (3.2))
AD ( )	amplitude-demodulated version of a signal (Used in Eq. (3.4))
ADD	amplitude demodulation differentiation method
ADD_1 ( )	first order derivative of amplitude demodulation (Used in Eq. (3.6))
ADD_2 ( )	second order derivative of amplitude demodulation (Used in Eq. (3.8))
Analytic ( )	analytic version of a signal (Used in Eq. (3.3))
AR	autoregressive model (Used in Eq. (2.9))
Bic	bicoherence (Used in Eq. (2.16))
Bis	two-dimensional Fourier transform (Used in Eq. (2.15))
CEEO ( )	calculus enhanced energy operator (Used in Eq. (4.17))
D ( )	differentiation operator (Used in Eq. (4.3))
d_b	diameter of a rolling element (Used in Eq. (2.10))
d_m	pitch diameter (Used in Eq. (2.11))
E { }	statistical expectation operator (Used in Eq. (2.5))
EO_2	second order energy operator (traditional energy operator) (Used in Appendices A)
EO_3	third order energy operator (Used in Appendices A)
EO_4	fourth order energy operator (Used in Eq. (6.4))
EO_j	order j energy operator (Used in Eq. (6.12))
F_j	the weight of the jth order AEO (Used in Eq. (5.30))
f_s	shaft rotational frequency (Used in Eq. (2.11))
H( )	Hilbert transform (Used in Eq. (5.4))
HO_AEO ( )	higher order analytic energy operator (Used in Eq. (5.30))
HOEO_F ( )	high order energy operator fusion (Used in Eq. (6.11))
I( )	integral operator (Used in Eq. (4.13))
Im	imaginary part of a signal (Used in Eq. (5.8))
J	total number of orders (Used in Eq. (5.30))
k	index of vibration interferences (Used in Eq. (3.2))
K	total number of vibration interferences (Used in Eq. (3.2))

Kurt	kurtosis of time series (Used in Eq. (6.13))
$K_Y(f)$	spectral kurtosis of the Fourier transform of $y(t)$, $(Y(f))$
L	amplitude of the vibration interference (Used in Eq. (3.1))
LO_1 ( )	first order layer operator (Used in Eq. (4.14))
LO_2 ( )	second order layer operator (Used in Eq. (4.16))
NB	number of rolling elements (Used in Eq. (2.10))
$p\ (t)$	arbitrary signal (Used in Eq. (2.22))
P_a	power of fault impulses (Used in Eq. (3.11))
$PO\ (f)$	the spectral density function of a signal (Used in Eq. (2.14))
P_v	power of the vibration interference (Used in Eq. (3.11))
$P_{x(t)}$	probability distribution function of $x(t)$ (Used in Eq. (2.4))
$r\ (t)$	a mixture of fault-generated impulse and vibration interferences (Used in Eq. (3.2))
$R\ (t)$	analytic version of $r(t)$ (Used in Eq. (3.3))
Re	real part of a signal (Used in Eq. (5.8))
Rms	root mean square (Used in Eq. (2.2))
$R_x\,(t,\tau)$	autocorrelation function of $x(t)$ with time lag τ (Used in Eq. (2.6))
S ( )	analytic energy operator (AEO) (Used in Eq. (5.13))
S_1 ( )	first order analytic energy operator (Used in Eq. (5.21))
S_2 ( )	second order analytic energy operator (Used in Eq. (5.22))
S_3 ( )	third order analytic energy operator (Used in Eq. (5.24))
S_4 ( )	fourth order analytic energy operator (Used in Eq. (5.26))
Sa	time synchronous average (Used in Eq. (2.8))
S_Q	the Qth order continuous analytic energy operator (Used in Eq. (5.29))
$\mathrm{s_p}$	collective identical impact (Used in Eq. (2.3))
T_p	time period corresponding to fault characteristic frequency (Used in Eq. (3.1))
u ()	unit step function (Used in Eq. (3.1))
$U\ (t)$	amplitude-modulation of a mono-component signal (Used in Eq. (5.6))
$v\ (t)$	vibration interference (Used in Eq. (3.2))
W_f ( )	the Wigner-Ville distribution of a signal (Used in Eq. (2.18))
wi	window function (Used in Eq. (2.17))
W_s ( )	the smoothed pseudo-Wigner-Ville distribution (Used in Eq. (2.19))
$X\ (f)$	the Fourier transform of $x(t)$ (Used in Eq. (2.13))
$x\ (t)$	faulty bearing signal in the absence of interferences and noise (Used in Eq. (3.2))
y_i	random variable (Used in Eq. (2.1))

Z	analytical form of the signal (Used in Eq. (5.2))
z(t)	mono-component signal (Used in Eq. (5.1))
$\hat{z}(t)$	Hilbert transform of signal $z(t)$ (Used in Eq. (5.3))
α_j	coefficients of HOEO_F related to order j (Used in Eq. (6.15))
β	structural damping characteristic frequency (Used in Eq. (3.1))
γ_3	normalized third central moment (Used in Eq. (2.2))
γ_4	normalized fourth central moment (Used in Eq. (2.2))
γ_6	normalized sixth central moment (Used in Eq. (2.2))
δ_Γ	hard thresholding (Used in Eq. (7.2))
$\eta'(t)$	frequency modulation of a mono-component signal (Used in Eq. (5.6))
μ	mean value of a random variable (Used in Eq. (2.1))
σ^2	variance of a random variable (Used in Eq. (2.1))
τ	roller slippage, the realization of a zero mean, uniformly distributed random variable, with standard deviation of $0.01T_p$ to $0.02T_p$ (Used in Eq. (3.1))
ψ ( )	energy operator (Used in Eq. (2.23))
ψ_d ( )	energy operator in discrete format (Used in Eq. (2.23))
ω_{IF}	instantaneous frequency (Used in Eq. (2.22))
ω_{Ik}	frequency of the kth interference (Used in Eq. (3.2))
ω_m	frequency of the single vibration interference (Used in Eq. (2.25))
ω_r	excited resonance frequency (Used in Eq. (3.2))
Γ	universal threshold (Used in Eq. (7.1))

Acronyms

AEO	analytic energy operator
CWD	Choi-William distribution
DWT	discrete wavelet transform
FFT	fast Fourier transform
MAD	median absolute deviation
SIR	signal-to-interference ratio of a signal
SNR	signal-to-noise ratio of a signal
STFT	short time Fourier transform
TAWS	time averaged wavelet spectrum
WT	wavelet transform
WVD	Wigner-Ville distribution
ZAM	Zhao-Atlas-Mark
FCF	fault characteristic frequency

Chapter 1

Introduction

1.1 Basic concept and motivation

Modern industry requires efficient and reliable condition monitoring and predictive maintenance to reduce cost, shorten the time of repair, and prevent catastrophic failures. Considerable attention has been given to industrial applications of vibration analysis techniques for the early detection of failure in rotating machinery. The use of fast and reliable algorithms is the key to detecting faults at early stage and preventing further damage. In addition, the efficient online monitoring of mechanical systems can help to prevent accidents. For instance, there were 1396 civil helicopter accidents in the US from 1990 to 1996 according to the National Transportation Safety Board (NTSB) (Iseler and De Maio, 2002). In 1999, a total of 192 turbine helicopter incidents occurred in the world. Some failures related to engine problems, and other were caused by mechanical failures of the helicopters (Zakrajsek et al., 2006). Some of these accidents could have been avoided if effective on-line monitoring systems were made available.

Fault identification methods should remain effective in the presence of noise and vibration interferences generated from various sources such as shaft imbalance, gear meshing, electrical and mechanical components. Several signal-processing techniques for improving the efficiency of bearing fault detection have been proposed (e.g., McFadden and Smith, 1985; Tandon and Choudhury, 1999; Dron et al., 2010). The most widely used methods are time domain, frequency domain, and time-frequency vibration signal analyses. The well-known time domain methods are statistical approaches using the root mean square, skewness, and kurtosis. Unfortunately, these statistical techniques require prior system information including these values of these parameters obtained when the system is healthy to perform comparison between healthy and current conditions (Williams et al., 2001).

Time-frequency techniques are common methods used for non-stationary condition (e.g., Auger and Flandrin, 1995; Satish, 1998; Baydar and Ball, 2001). One of the tools of time-frequency approach is wavelet transform, employed in many fields due to its capability for multi-resolution signal decomposition. However, the time-frequency techniques are sensitive to changes in environmental and operational conditions because of their dependency on some parameters such as window length, centre frequency, and bandwidth during machine operation. In addition, these techniques may not be fast enough for online monitoring (Jones, 2001; Zheng et al., 2002).

It has been shown that in a high-frequency band, the fault signature can be more clearly observed than in the low frequency regions because the periodical fault impulse generated by a bearing defect will resonate at a much higher frequency band with lower noise level. For this reason, the high-frequency resonance (HFR) technique based on amplitude demodulation of band-pass filtered signal is widely used for machine fault detection (McFadden and Smith, 1984; Rai and Mohanty, 2007). However, for a complex mechanical system, it is often difficult to determine the high-frequency resonance band without significant cost and time due to the use of complex signal-processing techniques and possibly, impact tests.

As such, a non-parametric method was suggested by Bozchalooi and Liang (2009). This parameter-free fault detection algorithm is based on the differentiation of a signal with maximum likelihood estimation. Furthermore, Liang and Soltani Bozchalooi (2010) presented another parameter-free method based on the energy operator approach for bearing fault detection. They have demonstrated that the non-parametric methods such as the differentiation of signals and the energy operator have a great potential to replace the HFR techniques.

1.2 Objectives and methodology

The principal purpose of this research is to investigate rotating machinery fault detection in a practical way for industrial applications. The proposed algorithms are non-parametric, non-filtering, fast, and simple to implement.

Most commercial fault detection packages for mechanical systems use conventional methods such as fast Fourier transform, envelope method, and HFR techniques. The main difficulty in the use of these techniques is their parameter dependence. The parameters as mentioned above are often difficult to obtain. In addition, Fourier transform does not provide time information and the envelope method is sensitive to noise, and vibration interference components. Therefore, the new non-parametric algorithms will help to overcome these problems. However, the implementation of an overly simplified non-parametric approach may not adequately handle the effects of noise and vibration interferences.

Currently, well-known non-parametric methods are the energy operator and the differentiation operator. These available non-parametric methods have their own disadvantages such as their sensitivity to noise and vibration interference. Therefore, new methods should be proposed to solve the aforementioned issues in bearing fault detection and online monitoring with acceptable performance in the presence of intensive background noise and interference components.

Therefore, the main objectives of this thesis are to develop non-parametric and non-filtering methods, i.e., an amplitude demodulation differentiation (ADD) method, a calculus enhanced energy operator (CEEO) method based on combination of a first and second order of the layer operator method with complementary capabilities in handling noise and interferences, a higher order analytic energy operator (HO_AEO) technique by introducing new operator called analytic energy operator, and finally a higher order energy operator fusion (HOEO_F) method. The proposed approaches can perform reasonably well under different levels of noise and vibration interfering components generated from a gearbox, misalignment shaft, motor, and electrical components.

Chapter 2

Literature review and fundamental concepts

According to sensor data available and types of measurements taken, most methods to monitor the condition of bearing can be categorized into the following groups: vibration monitoring, chemical analysis and temperature monitoring. Their advantages and disadvantages are summarized in Table 2.1. Despite the diversity of bearing monitoring strategies, vibration monitoring is widely used method in reality and research (Zhou et al., 2007). The main reasons include the inexpensive sensors, information-rich signal and multi-functionality (can be used to detect both component fault such as bearing faults, and structure malfunctions, e.g., shaft misalignment and mass imbalance).

Table 2.1 Summary table of different bearing condition monitoring methods.

Monitoring Schemes	**Major Advantages**	**Major disadvantages**
Vibration Monitoring	Reliable, Standardized (Related standard ISO10816), inexpensive, easy to implement	Require sophisticated signal analysis methods
Chemical Analysis	Directly monitoring the bearing and its oil	Limited to bearing with closed-loop oil supply system, specialist knowledge is required, cannot detect operational malfunctions (e.g., misalignment and imbalance), costly
Temperature measurement	Standard available in some industries	Embedded temperature detector required, other factors may cause same temperature raise, costly

The signature of a defective bearing is spread across a wide frequency band because of the impulsive nature of fault vibration signal, and hence can easily be masked by noise and vibration interferences. The weak signature of a bearing fault, at the early stage of defect development, is even more difficult to detect. As such, this review will focus on vibration signal analysis methods for bearing fault detection. These methods can be classified into,

- Time-domain method,
- Frequency-domain method, and
- Time-frequency method

Each of these methods employs particular strategies to suppress the effect of noise and vibration interferences to reveal fault signature. These methods are reviewed in the following sections.

2.1 Time-domain methods

2.1.1 Statistical approach

Online monitoring of rotating machinery can be categorized into several types. The first one includes statistical time-domain methods such as root mean square, peak value, skewness, and kurtosis (Dron et al., 2010; Tandon and Choudhury, 1999). These methods exploit statistically the characteristic differences between healthy and faulty bearings in the time domain. The primary issue of the application of these time-domain methods is their requirement of healthy signal information and prior knowledge (Hu et al., 2007; Samanta et al., 2003; Wang et al., 2004).

The RMS of a raw signal is one of the most basic methods to detect a fault in the time domain. The crest factor and kurtosis are two indicators that are sensitive to the signal form. They may allow the detection of the defects in evolution generating periodical shocks such as bearing or spline clearance, friction, spalling in gear teeth or bearings. However, they are not sensitive enough to measure incipient faults in particular cases (Pachaud et al., 1997).

Some statistical parameters such as probability density and kurtosis have been proposed for rotating machinery fault detection (Heng and Nor, 1998; Martin and Honarvar, 1995).

Mean and variance are the first and second moments of probability distribution respectively. Kurtosis is defined as fourth moment of the distribution. This indicator enables us to measure the relative peak or flatness of a distribution when compared to a normal distribution (McInerny and Dai, 2003).

The Root mean square (RMS), peak value, kurtosis and crest factor have been combined with high-frequency resonance techniques and an adaptive line enhancer to detect faults and localize damages in rolling bearings (Williams et al., 2001). Mean (μ), and variance (σ^2) can be defined as

$$\mu = E\left\{y_i\right\}, \bar{y}_i = y_i - \mu, \ \sigma^2 = E\left\{\bar{y}_i^{\,2}\right\} \tag{2.1}$$

Root mean square (Rms), skewness (normalized third central moment, γ_3), kurtosis (normalized fourth central moment, γ_4), and normalized sixth central moment (γ_6) can be represented as follow (Samanta et al., 2003)

$$\text{Rms} = \left[\frac{\sum \bar{y}_i^{\,2}}{n}\right]^{1/2}, \gamma_3 = \frac{E\left\{\bar{y}_i^{\,3}\right\}}{\sigma^3}, \gamma_4 = \frac{E\left\{\bar{y}_i^{\,4}\right\}}{\sigma^4}, \gamma_6 = \frac{E\left\{\bar{y}_i^{\,6}\right\}}{\sigma^6} \tag{2.2}$$

The different characteristic features of the time-domain vibration signal in various bearing conditions have been employed as inputs to artificial neural network (Samanta et al., 2003). The use of these four signal features resulted in a certain success in both training and test of the neural network. In some cases, the result was unaffected by Rms.

In the following, a simple model for the vibration signal of a bearing under defective condition by a single defect is derived. The signal is shown in Fig. 2.1. This model clarifies concepts of statistical properties of a faulty bearing vibration signal. Vibration signal generated from a defect in a rolling bearing can be written as (Randall et al., 2001)

$$x(t) = \sum_i A_i s_p(t - iT - \tau_i) \tag{2.3}$$

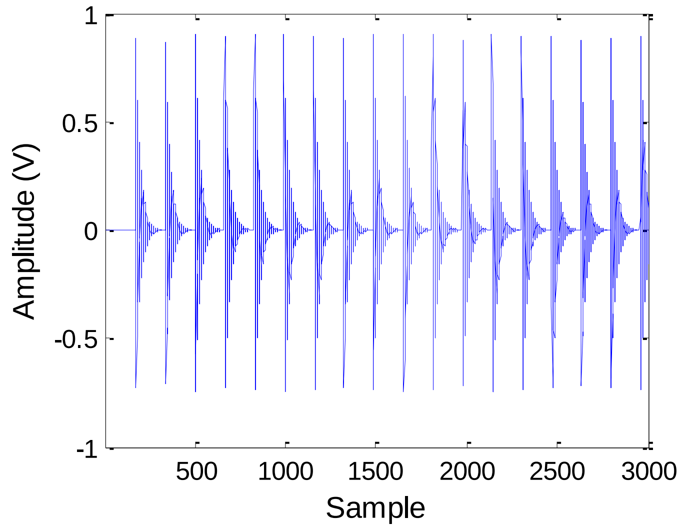

Fig. 2.1. Typical signal of a faulty bearing generated by the statistical model.

where T is the average time duration between two impacts, $s_p(t)$ represents oscillating behaviour due to the fault, A_i denotes the amplitude of the ith impact force and τ_{i} is a time lag from its mean period due to the slippage factor. It is assumed that the time of impact is short enough compared to the reciprocal of the dominant resonance frequency. Therefore, s_p (t) can be considered as collective identical impacts. One of these identical impacts is shown in Fig. 2.2.

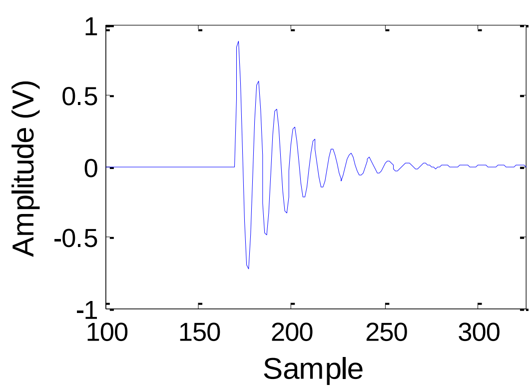

Fig. 2.2. A single simulated fault impulse.

Vibration signal from a faulty bearing is a combination of several periodically impulsive signals with random noise and other unknown disturbances. For a stationary condition, signal does not change statistically with time and the moments of the signal remain steady. If the statistics of the signal have a periodically time varying characteristics, it can be stated as a cyclostationary signal. The weak or wide sense cyclostationarity of a signal relies on the deviations of the mean and autocorrelation of the signal (Halim et al., 2008).

A random process $x(t)$ is cyclostationary of order N with a period T. For each set of measurement sample n=1,2,...,N and given time $t_1, t_2, ..., t_n,$ the probability distribution function $P_{x(t)}$ is periodic with period T (Antoniadis and Glossiotis, 2001).

$$P_{x(t)} = P_{x(t+T)} \tag{2.4}$$

A first order cyclostationary process, N=1, can be identified by the mean of the signal

$$mean\left(x(t)\right) = E\left(x(t)\right) \tag{2.5}$$

An example of this process could be a sinusoidal signal with added white noise.

The second-order theory of cyclostationary signals deals with the autocorrelation function

$$R_x(t, t-\tau) = R_x(t,\tau) = E\left\{x(t)x(t-\tau)\right\} \tag{2.6}$$

Based on the definition of cyclostationary signals, this function of the signal $x(t)$ is periodic in t for each time shift τ, and it can be written as

$$R_x(t,\tau) = R_x(t+kT,\tau),\ k = 0,1,2,\ldots \tag{2.7}$$

The time synchronous averaging (TSA) of a signal can extract a periodic waveform in the presence of additive noise. The repetitive signals through the TSA can indicate the information related to the faults to be diagnosed (McFadden, 1991). In most cases, the TSA application was modeled by the convolution of noisy signal with a finite train of impulses in which the period of impulses is equal to the period of desired faulty signal. It performs similarly to comb filter. The time synchronous averaging of signal needs either accurate information of the periodic frequency of the target signal, if it is periodic, or else a reference signal which is synchronous with the first one. Therefore, due to time synchronous averaging characteristic which is similar to comb filter behaviour cannot correctly describe the extraction of repetitive features from noisy signal and it also requires processing over an infinite time. Thus, the obtained result is not exactly periodic (McFadden, 1987a). The modified model solves some issues of current TSA with the existing model in that it depends on knowledge of only a finite block of the noisy signal and it produces a periodic result. The revised model works based on a rectangular window in the time domain of the noisy signal and by removal of known periodic noise from the frequency domain (McFadden, 1987a).

According to the time synchronous average, a vibration signal $x(t)$ is averaged for one particular time period T by measuring the mean of signal sequences that is calculated for a number of period N by a time interval T (Halim et al., 2008)

$$Sa(t) = \frac{1}{N}\sum_{l=0}^{N-1} x(t + lT) \tag{2.8}$$

This methodology can be applied on a raw vibration signal which is produced by tooth gear over one complete revolution of the gear or one complete revolution of a shaft in the time domain. Increasing the number of average should enhance periodic identification or remove more non-synchronous components. On the other hand, the large number of averages causes an increase in computation cost.

McFadden and Toozhy (2000) combined time synchronous technique with high resonance frequency method to analysis vibration of gear for the early failure detection. This technique is mostly useful for complex systems such as gearboxes as it eliminates the vibration from other system elements. Therefore, fewer problems result during the study of a simpler system (McFadden, 1987b).

Residual signal was used for diagnosing bearing and gear defects in which this method consisted of the time synchronous averaged signal with the primary meshing and shaft components along with their harmonics. Difference signals were obtained by removing the regular meshing components and shaft rotating frequency as well as its harmonics from the time synchronous averaged signal. In addition, difference signal can be measured by eliminating first-order sidebands from the residual signal. The difference signal was used to diagnose gearbox faults (Lebold, M. et al., 2000a, 2000b).

2.1.2 Time-domain filter based method

Generally, filters have been used to suppress noise when a signal corrupted by additive noise. For this purpose, filters can be designed in fix or adaptive shape. Fixed filters require prior knowledge of both the signal and noise. However, adaptive filters have the ability to adjust their own parameters automatically, and their design needs little or no prior knowledge of signal or noise characteristics. In the time-domain methods, there are several filter-based approaches such as adaptive noise cancelling (ANC) and demodulation based on a high-frequency resonance region. Demodulations in particular amplitude demodulation are important signal-processing techniques for machinery fault detection. Characteristics of nonlinear systems and intermittent transient response were recognized with amplitude and frequency modulation methods so as to process stationary/transient responses (Pai and Palazotto, 2008).

Fan and Zuo (2006) presented a fault detection approach that combines envelope and wavelet packet transform. Their results show that this combination is effective to extract modulating signal. For amplitude demodulation, a proper band-pass filter should be designed according to the excited resonance by the fault. Based on the envelope signal, the algorithm could be reversed to recreate the vibration signal with noise eliminated (Sheen, 2007). Feldman (1994) identified instantaneous parameters such as natural frequency, damping characteristics and their dependencies on vibration amplitude and frequency. Adaptive modulation methods for gear crack detection were proposed by Brie et al. (1997).

The adaptive algorithm is intended to account for the slow variations of the signal, and two methods are suggested. One is the recursive least square (RLS) approach based on the linear version of the signal, and the second one is the least mean square (LMS) approach to estimate the amplitude and phase of the signal. Another technique which is accepted for gear in the vibration analysis of gear systems is signal averaging (McFadden and Smith, 1985). When sufficient averages are taken, all the vibrations from the gearbox which are asynchronous with the rotation of the gear tend to cancel out. Thus, local variations should become visible in the meshing pattern, including modulation.

Noise cancellation is an alternative to optimal filtering which has advantages in many applications. However, noise cancellation can be unreliable if carried out improperly, e.g., it could amplify noise strength. Self-adaptive noise cancellation (SANC) is one of the most widely applied noise cancellation algorithms. Fig. 2.3 illustrates adaptive noise cancelling procedure (Chaturved and Thomas, 1981). A signal *s* is transmitted over a channel to a sensor which receives uncorrelated noise n_0 at the same time. A second sensor collects a noise n_1 which is uncorrelated with signal *s* but in some unknown way correlated with noise n_0. This sensor is considered as a receiver for reference signal to input to the canceller. The noise n_1 is filtered to achieve *y* that is similar to n_0. This output subtracted from the primary input $s+n_0$ to produce the system output $z= s+n_0-y$. The reference input is processed by an adaptive filter which differs from a fixed filter where it automatically adjusts its own impulse feedback. Adjustment is accomplished through a process that responds to an error signal dependent on the filter's output.

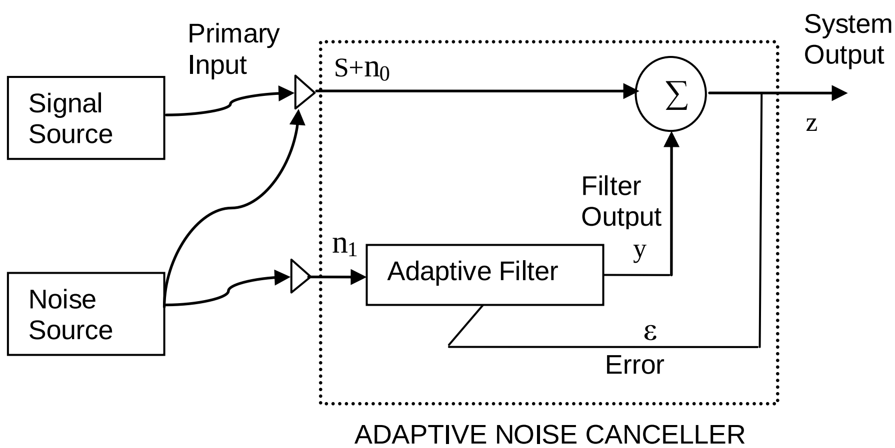

Fig. 2.3. The adaptive noise cancelling scheme.

In a study by Ho and Randall, (2000), SANC with envelope analysis was used to remove noise. This de-noising method was designed based on an adaptive noise cancelling filter and a wavelet-based de-noise estimator (Shao and Nezu, 2005). Adaptive noise cancellation can be accomplished with little risk of distorting the signal or increasing noise level if filtering is controlled by an appropriate adaptive process. Shao and Nezu (2005) have shown that mixture de-noising is a powerful method for identifying faults in bearings, depending on the speed of the bearing and the size and location of the defect. This applies especially when extracting early fault features of bearings under heavy noise. Coherent filtering technique can help to enhance signal-to-noise ratio (SNR) (Chaturved and Thomas, 1981). Adaptive noise cancelling can be applied to improve SNR even in those situations where a reference signal is unavailable. In general, the demodulation step starts with using conventional Infinite Impulse Response (IIR) filters such as Butterworth, Chebyshev, Bessel, and Elliptic in pass band or stop band. Prony's model was an algorithm for finding an IIR filter with an imposed time-domain impulse response (Chen and Mechefske, 2002). A Prony model based method has the potential to be efficient for analyzing transient vibration signals and machine condition monitoring (Chen and Mechefske, 2002).

2.1.3 Stochastic approach in the time domain

Stochastic methods have also been used for machinery fault detection in the time domain. Some of the basic concept of chaos theory was introduced in Logan and Mathew (1996) and further details of a method for quantifying a fractal dimension from a time series, and the correlation dimension was explained. Basseville et al. (2000) described machinery faults as a shifting model of eigenstructure of a linear dynamical system and also analyzed fault based on stochastic subspace identification methods. Furthermore, Mevel et al. (1999) suggested a statistical local approach corresponding to covariance-driven stochastic identification for monitoring machinery devices. Wang and Lin (2003) proposed a phase space reconstruction method based on the singular value decomposition technique for large rotating machine and gear system condition monitoring. Non-linear adaptive algorithms for independent component analysis (ICA) have been applied to separate unknown, statistically independent sources that are mixed in dynamic systems. Information maximization is based on the blind source separation algorithms in order to measure gear vibration (Roan et al., 2002).

Autoregressive (AR) model is an effective tool to identify fault features without studying fault mechanisms of a system. By using an autoregressive model, significant hidden information can be extracted. AR modelling is an alternative approach in comparison to the discrete Fourier transform in calculation of a power spectrum. In AR modeling, each value of acquired time sequence is regressed on past sample values. The number of past used values is called model order. The AR model predicts the current values of time series from the past values of the same series. The autocorrelation function can be considered as future dependency on past values. Corresponding to Eq. (2.6) we can say that autocorrelation is the average of product over a data sample with an advanced one by a lag of same data sample. Basically, the AR model may be stated as a set of autocorrelation functions. AR modelling in the time domain is based on a simple theory that the most current data points include more information than the other data points. Each recent value series can be predicted as a weighted sum of the previous values of the same series plus an error term. The AR model is defined by (Franaszczuk and Bergey, 1999; Takalo, 2005) as:

$$AR[n] = \sum_{i=0}^{M} a_i x[n-i] + \varepsilon(n) \tag{2.9}$$

where $x[n]$ is the current value of time series, a_i*'s* are weighting coefficients or predictor parameters, M is the model order which indicate number of past values, and $\varepsilon(n)$ represents a one-step prediction error that is a difference between predicted value and the current value at the same point. The autoregressive model is illustrated in Fig. 2.4.

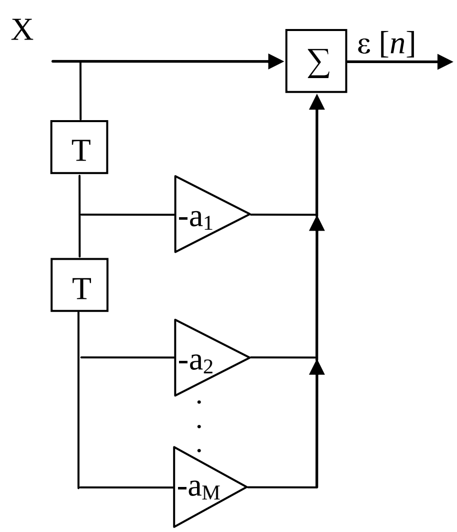

Fig. 2.4. The AR model.

The AR model has been jointly applied with the empirical mode decomposition (EMD) method to extract fault signature (Junsheng et al., 2006). AR model can reflect the characteristics of a dynamic system, but the autoregression parameters of AR model are sensitive to the variation of conditions. The AR model is an effective approach for the stationary signal. To solve the issue of non-stationary, EMD method can be applied to decompose the non-stationary vibration signal into several intrinsic mode functions (IMFs) which are stationary. Furthermore, the AR model is applied for the detection and diagnosis of gear fault (Wang and Wong, 2002). The AR model of the vibration signal is established in a healthy state of gear to predict error of the filter for processing the future-state signal from the same gear.

The most of the threshold methods applied in the time domain. The commonly applied threshold methods are soft- and hard-threshold approaches. Donoho (1995) introduced a soft-threshold with the universal threshold to construct unknown function from noisy data over specified samples. Wavelet thresholding provides a new de-noising approach to reduce speckle noise in synthetic aperture radar images (Kaufmann and Galizzi, 1996). This method is based on the thresholding of the wavelet coefficient of the distinction image. In another similar method, Lang et al. (1996) employed thresholding in the wavelet transform domain by using undecimated, shift-invariant, and non-orthogonal wavelet transform. Lin et al. (2004) utilized non-orthogonal wavelet transform and applied maximum likelihood estimation-based (MLE) threshold to de-noise signal vibration from mechanical systems (Hyvärinen, 1999).

2.2 Frequency based method

Another approach for fault detection is based on frequency-domain analysis. Discrete fast Fourier transform is a useful tool in many applications. One of the most widely accepted methods in industry for vibration monitoring is the high-frequency resonance technique to obtain envelope spectrum (McFadden and Smith, 1984). The fundamental concept of high resonance frequency is originated from the fact that the faulty part of a rolling element bearing contacts with another surface in the bearing under load and such a contact in every revolution results in generation of impulse vibration. The main characteristic of this impulse is its short time duration when compared with the time interval between impulses. Therefore, it is a wide band signal with its energy spreading over a wide range of frequencies with low energy level. Because of this wide energy distribution, detection of bearing defect is difficult with conventional spectrum approaches. This is especially true in the presence of vibration interferences from gears and other mechanical and electrical components.

Defects may occur on different bearing elements such as inner race, outer race, and balls depending on the working conditions. Each of these bearing elements has an associated fault characteristic frequency as well as its harmonics. A defect on a bearing element leads to the increased energy at its fault frequency. The fault characteristic frequencies of bearing elements can be calculated from distinct kinematic such as geometry of the bearing and shaft rotational speed (Kıral and Karagülle, 2006). Fault characteristic frequencies for a bearing with stationary outer race can be defined as follows

$$\text{Outer race fault frequency: } F_{outer} = \frac{NBf_s}{2d_b}\left(1 - \frac{d_b}{d_m}\cos\alpha_c\right) \tag{2.10}$$

$$\text{Inner race fault frequency: } F_{inner} = \frac{NBf_s}{2}\left(1 + \frac{d_b}{d_m}\cos\alpha_c\right) \tag{2.11}$$

$$\text{Rolling element fault frequency: } F_{re} = f_s\frac{d_m}{d_b}\left(1 - \frac{d_b^2}{d_m^2}\cos^2\alpha_c\right) \tag{2.12}$$

where f_s is the shaft rotational frequency, d_m represents the pitch diameter, d_b is the diameter of the rolling element, NB is the number of rolling elements, and α_c represents the contact angle. A typical rolling element bearing as well as the parameters in the above equation is shown in Fig. 2.5. However, the fault characteristic frequencies may vary slightly due to a consequence of slipping and skidding in the rolling element bearings during an operation (Prashad, 1987).

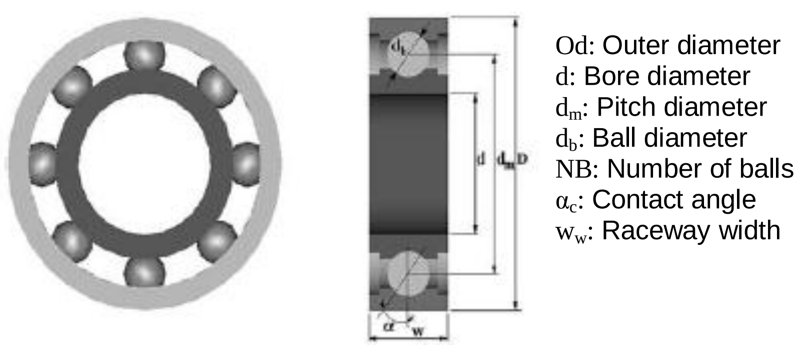

Fig. 2.5. Dimensions of a rolling element bearing.

The impact of a bearing fault excites the resonance in the system at a frequency that is higher than many other frequencies from several sources. This phenomenon also causes some of energy to concentrate to a narrow band. The narrow band of the concentrated energy provides better chance to detect fault than a wide distributed band of energy because of the relatively high signal to noise ratio and less interference. However, the identification of the high-frequency resonance band is not always straightforward. The typical example of a faulty bearing spectrum with a resonance frequency band around 2000 Hz is shown in Fig. 2.6.

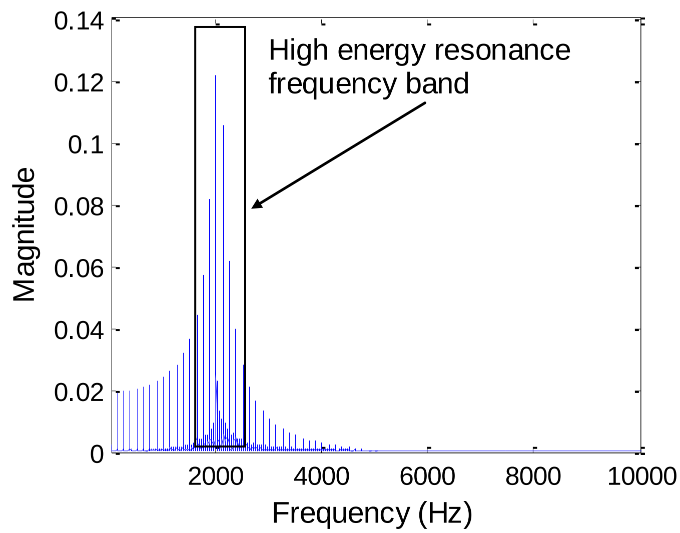

Fig. 2.6. Spectrum of the faulty bearing with a resonance frequency band around 2000 Hz.

Many studies have been conducted to identify the resonance band. This information is then used to define the center frequency and bandwidth of a bandpass filter for amplitude demodulation. Antoni and Randall (2006) introduced spectral kurtosis (SK) approach. The main problem with the kurtosis approach is that it is ineffective in handling signals with high level noise. In addition, the SK method could not capture the impulsiveness of the bearing fault if the signal contains strong vibration components from multiple sources. The SK is the local application of kurtosis in different frequency band. As a result, this technique avoids using the full-band kurtosis assessment and finds the frequency bands with highest SK values to locate the resonance band (Antoni and Randall, 2006). However, the SK method does not work appropriately in the presence of a strong non-Gaussian noise and high amplitude interfering vibrations (Barszcz and JabŁoński, 2011).

Another frequency domain approach involves the use of bispectral analysis and the application of pattern recognition technique on biocoherence (Li et al. 1996). The Fourier transform of a measured signal, $x(t)$, is denoted as

$$X(f) = |X(f)| \exp(j\varphi) \tag{2.13}$$

where $|X(f)|$ and φ are magnitude and phase angle respectively. Then the spectral density function of $x(t)$) can be defined as

$$PO(f) = E\left[X(f) X^*(f)\right] \tag{2.14}$$

where the asterisk represents complex conjugate. By using the same notation, the bispectrum can be regarded as two-dimensional Fourier transform of third moment of $x(t)$, i.e.,

$$Bis(f_1, f_2) = E\left[X(f_1) X(f_2) X^*(f_1 + f_2)\right] \tag{2.15}$$

As shown in Eq. (2.15), the bispectrum is symmetric about the axis $f_1 + f_2$. Intuitively, when the signal at frequencies of f_1, f_2, and $f_1 + f_2$ is independent of one another, the bispectrum will be small. The bispectrum will be large when the signal at these frequencies is correlated.

In practice, bispectrum may be achieved by taking N separate datasets, or dividing a single dataset into N segments. A windowing function is applied to each segment, and the Fourier transforms of all segments are averaged (Hillis et al., 2006). The statistical significance of any correlation can be determined by the quantitative statistical tool which is called bicoherence. The bicoherence can be defined as

$$Bic(f_1, f_2) = \frac{|Bis(f_1, f_2)|}{\left[|X(f_1) X(f_2)|^2 |X(f_1 + f_2)|^2\right]^{0.5}} \tag{2.16}$$

A combination approach is presented by Stack et al. (2004) to identify single-point defect in rolling element bearing. It includes amplitude modulation and bispectrum to detect instantaneous amplitude magnitude and quadratic phase coupling. Bispectrum is defined as the Fourier transform of the third-order cumulant (Hillis et al., 2006). Ning and Gao (1992) modified the bispectrum from the view of amplitude modulation with regard to quadratic phase coupling to detect amplitude modulation.

Fast Fourier transform of intrinsic mode decomposition with the Hilbert-Huang transform (HHT) process has been incorporated to exploit the efficiency of the Hilbert transform in the frequency domain (Rai and Mohanty, 2007). Non-parametric cyclic estimator is derived from general quadratic form which is suitable for cyclostationary signals. This version of cyclic spectral analysis yields as particular cases of ‘‘cyclic’’ versions of the smoothed and averaged periodograms (Antoni, 2007a, 2009). Bearings in operations have a prominent property, i.e., random cyclostationary. Antoni, (2007b) demonstrated that an optimal cyclic coherence approach can detect bearing faults at high level of background noise. Indicator of cyclostationary from orders 1 to 4 has been introduced corresponding to gear fault diagnosis (Raad et al., 2008). Furthermore, Feng et al. (2009, 2011) assessed gear tooth crack damages based on the cyclic correlation function of amplitude and frequency modulation signals. After comparing the cyclostationary and bispectrum methods, a new method was developed that can better deal with cyclostationary signals (Bouillaut and Sidahmed, 2000).

2.3 Time-frequency methods

One of the initial time-frequency techniques for machinery fault diagnosis is short time Fourier transform (STFT) (Satish, 1998). STFT can be applied for non-stationary conditions as it has the capability to represent signals in both the time and frequency domains. The STFT is a popular tool because of its simplicity. The basic idea of STFT is to divide a signal into ideal overlapping time segments by a windowing method, and then to apply fast Fourier transform for each segment. This kind of windowing approach is called spectrogram. The STFT can be defined in continuous space as

$$\mathrm{STFT}\left(f,\tau\right)=\int_{-\infty}^{\infty}x\left(t\right)wi(t-\tau)\exp(-j2\pi ft)dt \tag{2.17}$$

where $wi(t)$ is window function whose position is determined in time by τ.

The main difficulty in the application of the STFT is its constant resolution for all frequencies because it provides the same window length for scanning the entire signal. Therefore, the wide window provides a good resolution in the frequency domain but poor resolution in the time domain. The Wigner-Ville distribution (WVD) can also be represented in both time and frequency domains. From the Cohen class, the Wigner-Ville distribution (WVD) is extensively used to detect local faults in gearboxes, and plays a central role in the analysis of second-order characteristics of random signals (Baydar and Ball, 2001). WVD has a good time and frequency resolution and computational efficiency. The Wigner-Ville distribution is expressed as:

$$W_f(t,\omega) = \int_{-\infty}^{\infty} x(t-\tau/2)\,x^*(t+\tau/2)\exp(-j\omega\tau)\,d\tau \tag{2.18}$$

where $x(t)$ is the time signal, and $x^*(t)$ is its complex conjugate. The problem with the WVD is the interference terms known as cross terms in the frequency component. For this reason, the modified version of the WVD, i.e., the smoothed pseudo-WVD, is employed to suppress the interference terms. However, this modification is at the expense of the reduced frequency resolution (Rajagopalan et al., 2005). The smoothed pseudo-WVD is given by:

$$W_s(t,\omega) = \frac{1}{2\pi}\iint_{-\infty}^{\infty} W_f(t,\tau)\,wi(\omega-\gamma)\,g(t-\tau)\,d\gamma\,d\tau \tag{2.19}$$

In this equation, two independent windows co-exist. $W_s(t,\omega)$ is a function of truncating window application to the time domain, and can be considered as frequency resolution of WVD. $g(t)$ is a smoothing window which can be represented as the time resolution.

The Choi-William distribution (CWD) and Zhao-Atlas-Mark (ZAM) distribution are another two time-frequency methods, which can improve the readability and provide strong cross-term suppression capability while offering finer frequency resolution (Lee et al., 2001). The CWD can be obtained as

$$CW_f\left(t,f\right)=\left[\frac{2}{\pi}\right]^{0.5}\iint\left[\begin{array}{l}\frac{\zeta}{|\tau|}\exp\left(-\frac{2\zeta^2\left(s-t\right)^2}{\tau^2}\right).\\ x\left(s-\tau/2\right)x^*(s+\tau/2)\exp(-j\pi f\tau)dsd\tau\end{array}\right] \tag{2.20}$$

where ζ is a constant scaling factor to suppress the cross-term, and $x(t)$ is the time signal.

However, the CWD and ZAM are slow methods and not suited to large dataset analysis and online monitoring (Zhao et al., 1990). The reduction or elimination of interference terms will also lead to loss of time-frequency resolution. For this reason, the reassigned method, a modified version of time-frequency distributions and time-scale representation by moving value away from computed sources, was developed (Auger and Flandrin, 1995). The value of each point of time-frequency representation is shifted by reassigned operators which are signal -dependent. In addition, the CWD has some significant characteristic such as energy conservation and localized chirp and impulses (Auger and Flandrin, 1995; Peng et al., 2002). Concentration of frequency domain and readability can be improved by using reassigned method; also it can reduce interference terms in the time-frequency representation (Peng et al., 2002). However, the reassigned time-frequency representation greatly compromises speed.

2.3.1 Wavelet transform

Wavelet transform (WT) is another time-frequency approach. In comparison to other time-frequency methods, WT has many distinct merits including multi-resolution analysis. The discrete wavelet transform (DWT) can also analyze a signal with fewer interference terms and fine time and frequency resolution (Jones, 2001; Quek et al., 2001).

Cole et al., (2006) presented dyadic wavelets for the control of multi-frequency rotor vibration, and wavelet basis for various operations. Matching wavelets can be used to detect transients in mechanical systems. Wang (2001) introduced a three-dimensional time-frequency-scale wavelet representation. Time and scale parameters of wavelet transform and frequency have been maximized to find similar signal segments.

Nikolaou and Antoniadis (2002) described a demodulation method corresponding to the complex shifted Morlet wavelet family. A primary work of their work is the systematic approach to select crucial parameters such as time and scale parameters. Scale-wavelet power spectrum and auto-correlation analysis of time-wavelet power spectrum are two methods which are useful to extract a feature of rolling bearing fault signal (Junsheng et al., 2007). Scale-wavelet power spectrum gives the power density function with a different scale. In addition, the time-wavelet power spectrum descrices the distribution of all energy of signal in the time axis. Zheng et al. (2002) employed the time averaged wavelet spectrum (TAWS) based on continuous Morlet wavelet to extract gear fault information. Corresponding to the TAWS, two new methods including the spectrum comparison method and the feature energy method have been proposed for gear fault diagnosis. Nevertheless, the wavelet transform has some deficiencies such as energy leakage, border distortion and the inevitable occurrence of overlapping.

A comparison of the above primary methods in various aspects such as parameter dependence, filtering process, and computation efficiency is summarized in Table 2.2.

Table 2.2 Comparison of primary methods for machine fault detection.

Fault detection Methods	**Requirement of prior knowledge (i.e., healthy bearing data)**	**Dependence on selecting Parameter**	**Require ment of filtering process**	**Speed of algorithm (simplicity of algorithm)**
Time-domain methods (Root mean square, Skewness, Kurtosis)	Yes	No	No	High
Frequency-domain methods (High-frequency resonance based methods)	No	Yes	Yes	Low/medium
Time-frequency methods (Wavelet methods)	No	Yes	Method dependent	Low

2.4 Advantages and disadvantages of primary methods for bearing fault detection of mechanical system

The primary disadvantage of statistical time-domain methods such as root mean square, skewness, and kurtosis is their requirement for prior information, mainly the reference healthy bearing signal. Furthermore, they do not perform properly if the noise or interference levels change during online monitoring. For example, the operational and environmental conditions as well as unpredicted factors can generate errors in the fault detection indicators. On the other hand, statistical analysis does not require any parameter selection and re-calibration if each set of measured signals is obtained directly from sensors without applying such pre-processing steps. In addition, because of the simplistic nature of the statistical algorithms, they work efficiently and seem suitable for online monitoring.

The high-frequency resonance based methods, though widely used in industry, suffers from its parameter-dependence. Improperly selected parameters such as the center frequency and bandwidth could mislead the detection process. In addition, even if idle parameters can be selected initially, they may no longer be valid when operation conditions change.

Among the time-frequency methods, the STFT method suffers from resolution problem, the WVD has the cross-term problem, and the SPWVD leads to poor frequency resolution. Furthermore, all these time-frequency are computation-demanding and hence it is challenging to apply them for online condition monitoring.

The principal advantage of the wavelet method is its ability to handle a noisy signal effectively with good time and frequency resolutions. However, two parameters need to be well defined, namely, scale and translation. Therefore, similar to the high-frequency resonance technique, a problem arises with parameter selection and re-calibration. In addition, because WT is based on re-calculation of parameters and representation in time and frequency, the speed of WT performance may not be fast enough.

Practical online monitoring for mechanical system fault detection obviously needs some methodologies with desired characteristics as follows:

- Independent of prior knowledge,

- Non-parameter,
- Non-Filtering,
- Versatile,
- Easy to implement, and
- Computationally efficient.

2.5 Preliminary work in non-parametric fault detection approaches

A non-parametric method is proposed by Bozchalooi and Liang, (2009) for detecting bearing faults. This technique is based on differentiation and maximum likelihood estimation. The high-amplitude and low frequency of the vibration interference can make the traditional amplitude demodulation approach ineffective. Their differentiation approach can enhance a faulty signal in the presence of vibration interferences. Furthermore, maximum likelihood estimation is applied to reduce the effect of noise in the signal by using optimization techniques.

One of the most notable operators with many advantages and applications is the Teager energy operator. Liang and Soltani Bozchalooi (2010) presented another parameter-independent method based on the Teager energy operator. The Teager energy operator can employ both amplitude and frequency modulations simultaneously. This enhances the signal quality for bearing fault detection without the need for an interference removal step.

2.5.1 Teager energy operator

The energy operator $\psi()$ applied on continuous signal $p(t)$ is defined as (Maragos et al., 1993)

$$\psi\left(p(t)\right)=\left(\frac{\mathrm{d}\,p(t)}{\mathrm{d}t}\right)^2-p(t)\frac{\mathrm{d}^2\,p(t)}{\mathrm{d}t^2} \tag{2.21}$$

The extraction of particular patterns such as transient impulsive fault signatures relies on the combined amplitude and frequency demodulation. Now consider an arbitrary signal $p(t)$

$$p(t)=\Lambda(t)\cos\varphi(t) \tag{2.22}$$

where $\Lambda(t)$ is time varying amplitude, $\varphi(t)$ is a phase of the signal, and $\omega_{IF} = \left(\frac{\mathrm{d}\varphi(t)}{\mathrm{d}(t)}\right)$ is the instantaneous frequency of the signal $p(t)$. It can be shown that for the continuous signal $p(t)$ form Eq.(2.21) (Hanson et al., 1993)

$$\psi\left(p(t)\right) = \Lambda^2(t)\,\omega_{IF}^2(t)$$

The discrete form of the energy operator is given as (Evangelopoulos and Maragos, 2006; Maragos et al., 1993)

$$\psi_d\left(p(n)\right) = p^2(n) - p(n-1)\,p(n+1) \tag{2.23}$$

Similarly, it is shown (Bovik et al., 1992) that

$$\psi_d\left(p(n)\right) = a^2(n)\sin^2\left(\varphi(n) - \varphi(n-1)\right) \tag{2.24}$$

According to Eqs. (2.21) and (2.24), the amplitude modulation (AM) and frequency modulation (FM) of signal have been extracted by the energy operator. Although the energy operator has mainly been applied to separate AM and FM of a target signal, the separation of such data is not necessary in the context of machinery fault detection (Liang and Soltani Bozchalooi, 2010).

2.5.2 Amplitude demodulation and frequency demodulation using the energy operator for the bearing fault model

The effect of energy transformation is applied on a faulty bearing with a vibration interference (Bozchalooi and Liang, 2009; Liang and Soltani Bozchalooi, 2010) expressed as

$$r(t) = Ae^{-\beta t}\cos\left(\omega_r t + \theta\right) + L\cos\omega_m t \tag{2.25}$$

where A is the amplitude, β is the structural damping characteristic frequency, ω_r is excited resonance frequency, L represents amplitude of interfering vibration, and ω_m is the frequency of the interference.

The energy transformed version of this mixed signal can be written as

$$\psi\left(r(t)\right)=\left(\frac{\mathrm{d}r(t)}{\mathrm{d}t}\right)^2-r(t)\frac{\mathrm{d}^2r(t)}{\mathrm{d}t^2}=A^2\omega_r^2e^{-2\beta t}+ALh(t)e^{-\beta t}+L^2\omega_m^2 \tag{2.26}$$

where

$$\begin{aligned}h(t)=2\beta\omega_m\cos\left(\omega_rt+\theta\right)\sin\omega_mt+2\omega_r\omega_m\sin\left(\omega_rt+\theta\right)\sin\omega_mt\\+\omega_m^2\cos\left(\omega_rt+\theta\right)\cos\omega_mt-\beta^2\cos\left(\omega_rt+\theta\right)\cos\omega_mt\\-2\beta\omega_r\sin\left(\omega_rt+\theta\right)\cos\omega_mt+\omega_r^2\cos\left(\omega_rt+\theta\right)\cos\omega_mt\end{aligned}$$

The energy transformed signal mixture includes three terms. The first two terms are amplitude-demodulated term and high frequency component, and the third term $L^2\omega_m^2$ represents the interfering signal component. The first term $A^2\omega_r^2e^{-2\beta t}$ is the squared envelope of fault signature, scaled by factor ω_r^2 which is usually of large value. This factor obviously shows the influence of energy operator on amplitude-demodulation. The significant characteristic of the energy operator is its ability to suppress the effect of vibration interferences.

2.5.3 The signal-to-interference ratio

To quantify the level of vibration interferences for a signal mixture $r(t)= a(t)+ v(t)$ (where $a(t)$ is the faulty bearing vibration and $v(t)$ is the vibration interference), the SIR was proposed as follows (Bozchalooi and Liang, 2009; Liang and Soltani Bozchalooi, 2010)

$$\mathrm{SIR}\left(r(t)\right)=\frac{(1/T)\int_0^T a^2(t)\mathrm{d}t}{(1/T)\int_0^T v^2(t)\mathrm{d}t}=\frac{P_a}{P_v} \tag{2.27}$$

where T is the signal length, P_a the power of fault impulses and P_v the power of the vibration interference. Fig. 2.7 illustrates the process of the non-parametric method. Acquired signal from a faulty machine consists of fault impulse signature of the bearing, noise and vibration interference components. By applying a simple, non-parametric and non-filtering method, faulty features will be enhanced.

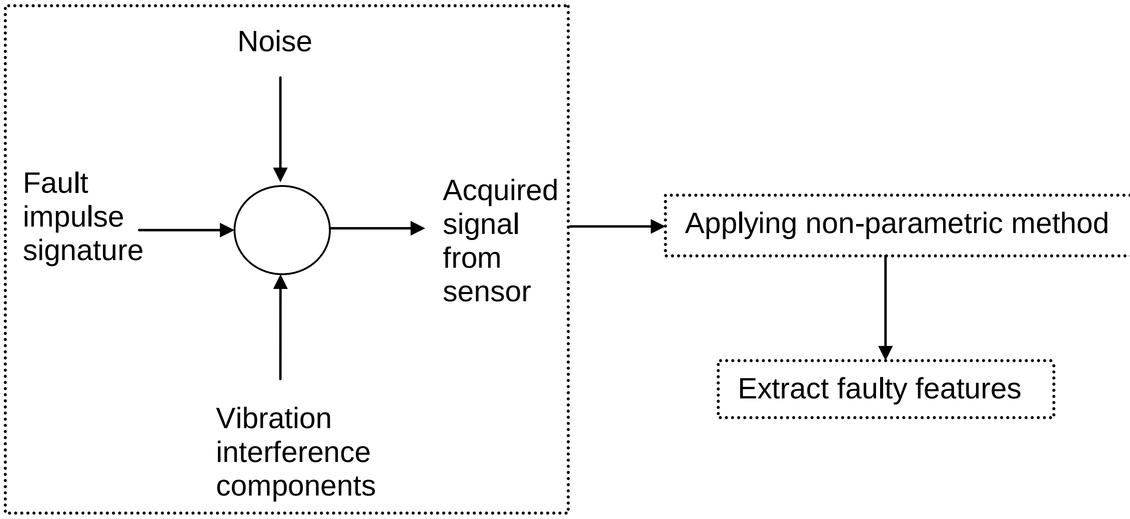

Fig. 2.7. Non-parametric method process.

2.6 Motivation

The above review of the existing methods for bearing fault detection has indicated that each method has its own advantages and disadvantages. The common problem with most of the existing methods, in particular the widely used HFR methods, is the requirement of the filtering process and hence the prior knowledge of the fault-excited resonance band. Such information is not always easily available and is often difficult to obtain. As such, the main purpose of this study is the development of non-filtering and non-parametric bearing fault detection methods.

Chapter 3

An amplitude demodulation differentiation method for bearing fault detection in the presence of multiple interferences[1]

In this chapter, a new non-parametric method is proposed based on the differentiation of amplitude demodulated signal. This method is motivated by the following observations:

(a) The relative strength of the faulty bearing signature can be boosted by differentiating the signal (Bozchalooi and Liang, 2009) but when the signal is severely contaminated by noise, this method may not be effective.

(b) The amplitude demodulation approach (namely envelope method) can enhance the detectability of the fault signal in the presence of noise as shown in Fig. 3.3.

(c) The amplitude modulation and phase modulation are basic concepts in signal-processing and are widely used for many applications. The derivative of phase modulation yields frequency modulation and its translation property can be used for signal transformation. However, the potential application of the derivative of amplitude modulation has not yet been explored (Benitez et al., 2001; Moorer, 1977).

Therefore, the joint application of both differentiation and amplitude demodulation can lead to a new version of non-parametric method. As such, this chapter proposes to use the derivative of the amplitude-demodulated signal for bearing fault detection. To facilitate

[1] Appeared in *Measurment and science technology*, vol.24, no.10, 2013, pp 105013.
See Appendix B.1 for MATLAB script.

discussions, the proposed method is called amplitude demodulation differentiation (ADD) method hereafter. A comparison between the new approach and two other non-parametric methods will be carried out in this chapter and later in Chapter 7. The performance of the new approach in the presence of noise and vibration interferences is much better than that of the differentiation of the raw signal as shown in Fig. 7.5 and Fig. 7.7. However, though the new method can better enhance a signal than the energy method when the signal contains high level vibration interferences, its capability in handling higher level noise is not as effective as the energy operator as illustrated in Fig. 7.6.

It is shown that the proposed algorithm can effectively improve signal to interference ratio (SIR) and thus can reveal the bearing fault characteristic frequency without using the filtering process. This new approach is based on the derivation of the amplitude-demodulated signal. Its performance is evaluated using both simulation and experimental data. The proposed method is parameter-free and does not involve prior knowledge and historical data about the mechanical system. In addition, the computational simplicity of the new approach makes it suited for industrial application, particularly online monitoring.

3.1 Performance evaluation of the envelope method for bearing fault detection on a simulated signal with noise

In this subsection, the performance of the commonly used envelope method under different noise levels is examined by comparison with the differentiation method using simulated signals. The vibration signal of a faulty bearing can be expressed as (Liang and Soltani Bozchalooi, 2010):

$$x(t)=\sum_{m=-M}^{M} A_m e^{-\beta\left(t-mT_p-\tau\right)} \cos\left(\omega_r\left(t-mT_p-\tau+\theta_m\right)\right)u\left(t-mT_p-\tau\right) \tag{3.1}$$

where A_m is the amplitude of the mth fault impulse, T_p is the time period corresponding to the fault characteristic frequency (FCF), β the structural damping characteristic frequency, ω_r the excited resonance frequency, τ represents the effect of random slippage of the rolling elements and $x(t)$ is the vibration signal containing $2M+1$ fault generated impulse. $u()$ is a step function. The parameters used for the simulation are listed in the following table:

Parameter	A_m	β	T_p	τ	ω_r	θ_m
Value	1	1500	0.02	Random number	5000	$\pi/8$

For comparison, the simulated faulty bearing signal is mixed with different levels of white Gaussian noise shown in Fig. 3.1-3.3(a) with SNR = 0 dB, SNR = -5 dB , and SNR = -12 dB respectively. The white Gaussian noise is added using the MATLAB command ‘awgn’.

Figs. 3.1-3.3(b) show the spectrum of the faulty bearing signal mixed with a certain level of noise specified by the SNR. These figures indicate that the Fourier transformed signals can reveal the fault when SNR = 0 dB but fail to do so when SNR = -5 and -12 dB. Then the envelope and differentiation methods are compared using the same set of signal mixtures. The results of the two methods are plotted respectively in parts (c) and (d) of Figs. 3.1 to 3.3, which indicate that for higher SNRs, i.e., 0 and -5 dB, both methods work well. However, when SNR is reduced to -12 dB, the envelope method outperforms the differentiation method. In this case, the envelope method can still detect at least 10 harmonics of the FCF but the differentiation method can only vaguely reveal a few. These results indicate that the envelope method has a stronger noise handling capability than the differentiation method.

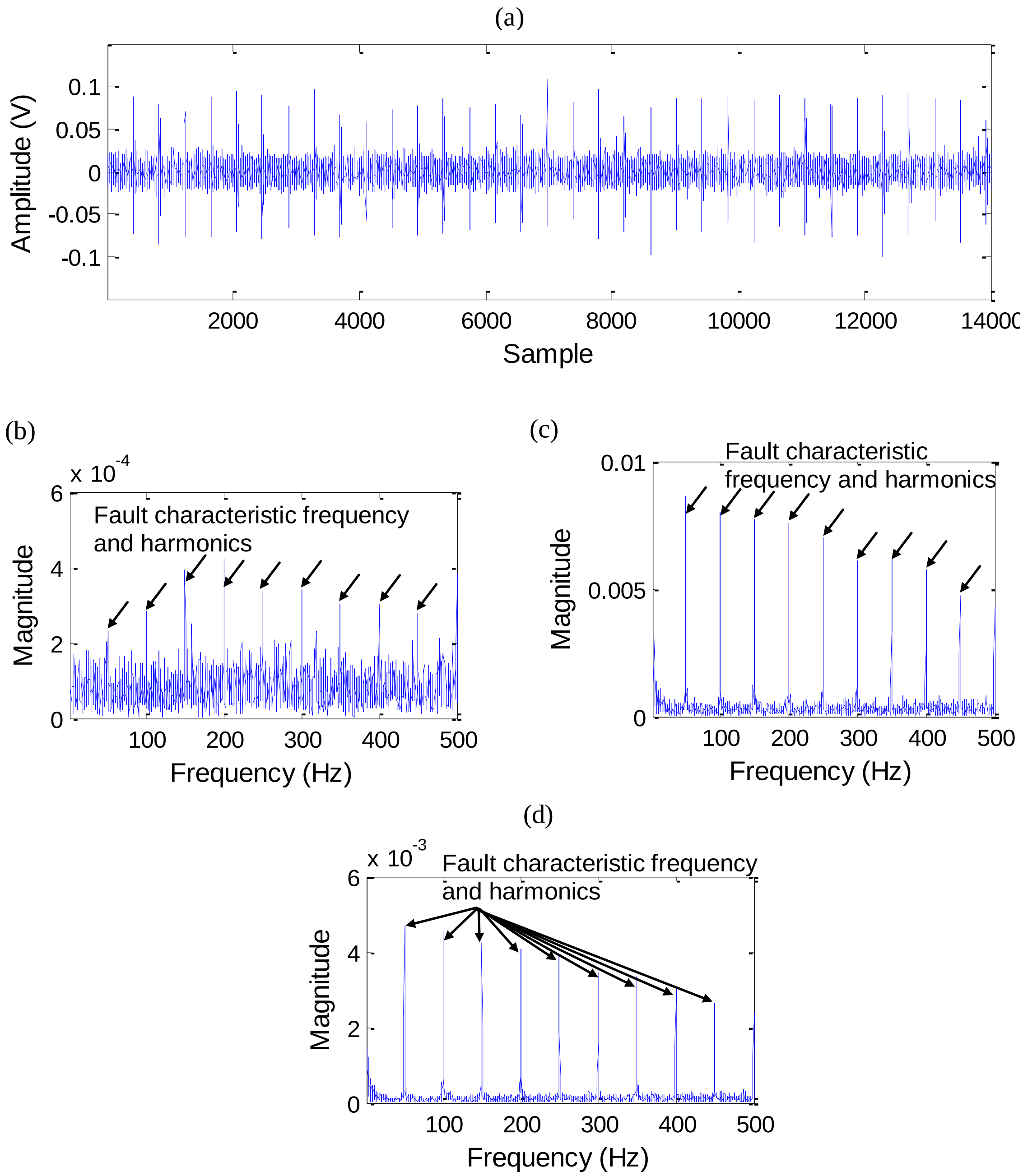

Fig. 3.1. Simulated faulty bearing signal: (a) mixture of the signal and noise (SNR= 0 dB) (b) spectrum of the signal-noise mixture, (c) envelope spectrum of the derivative (difference) of the signal-noise mixture, and (d) envelope spectrum of the signal-noise mixture.

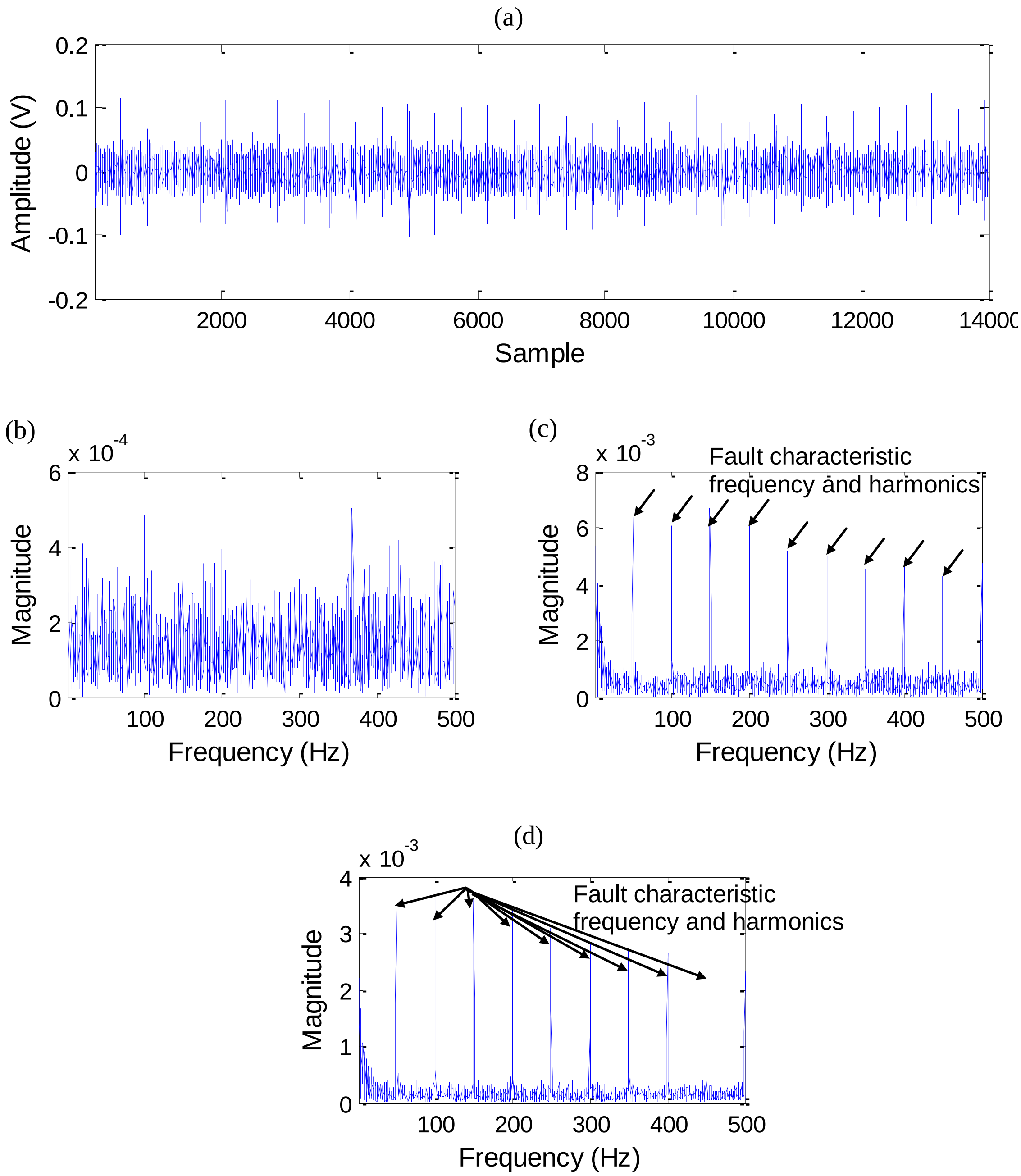

Fig. 3.2. Simulated faulty bearing signal: (a) mixture of the signal and noise (SNR= -5 dB) (b) spectrum of the signal-noise mixture, (c) envelope spectrum of the derivative (difference) of the signal-noise mixture, and (d) envelope spectrum of the signal-noise mixture.

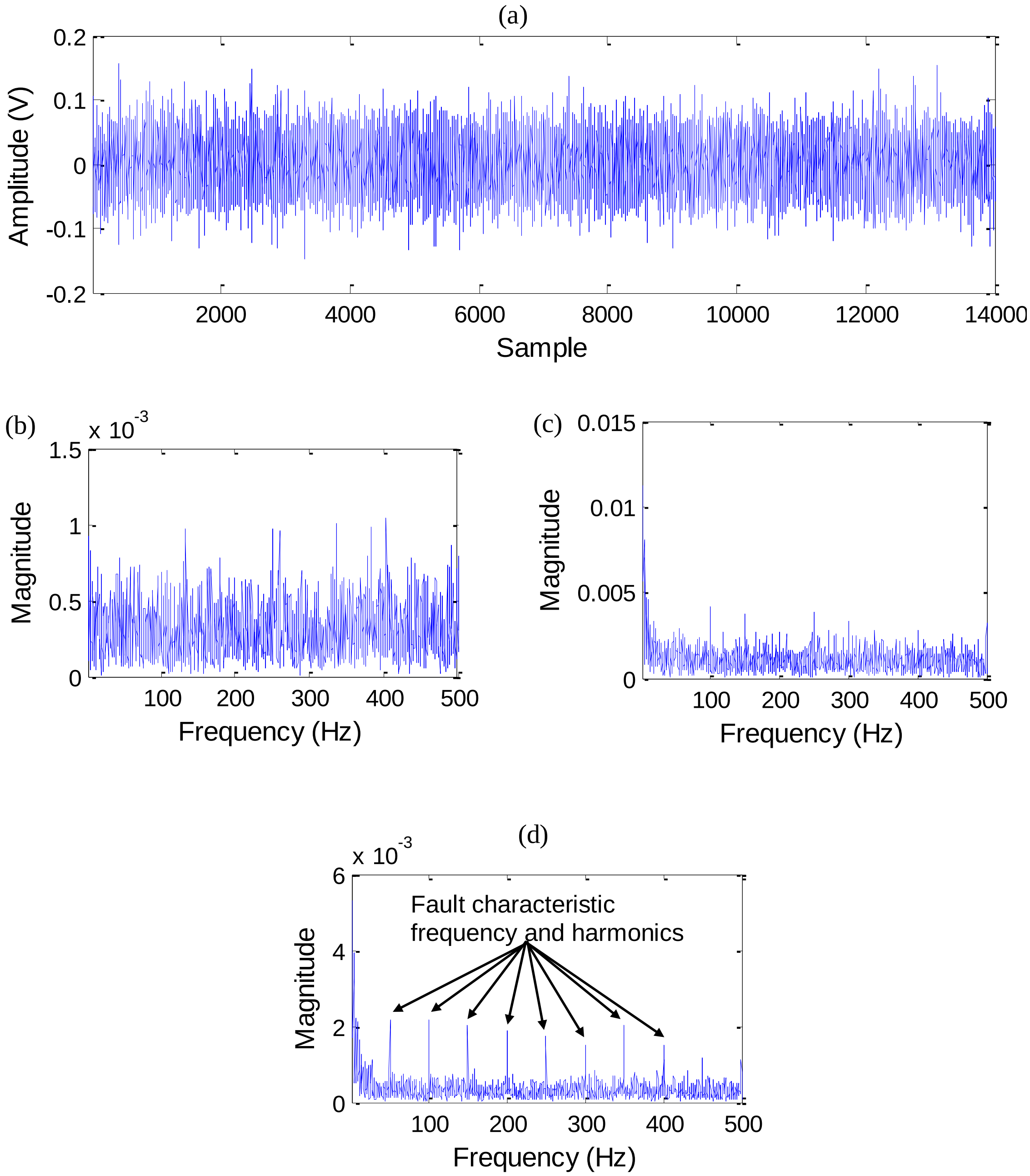

Fig. 3.3. Simulated faulty bearing signal: (a) mixture of the signal and noise (SNR= -12 dB) (b) spectrum of the signal-noise mixture, (c) envelope spectrum of the derivative (difference) of the signal-noise mixture, and (d) envelope spectrum of the signal-noise mixture.

3.2 Effect of multiple interferences on amplitude demodulation performance

In reality, the signal is not only contaminated by the background noise, but also complicated by the vibration interferences caused by shaft misalignment, gear meshing, and shaft imbalance. In this section, we show that the AD performance deteriorates in the presence of multiple interferences. Consequently the ADD method will be developed in the next section to alleviate this difficulty. For this purpose, we consider the following signal mixture

$$r(t) = x(t) + v(t) = Ae^{-\beta(t)} \cos(\omega_r t + \varphi) + \sum_{k=1}^{K} L_k \cos \omega_{Ik} t \tag{3.2}$$

where $x(t)$ is the faulty bearing signal component, $v(t)$ represents multiple interferences, A is the amplitude of the fault signal, β is the structural damping characteristic frequency, ω_r is the frequency of the excited resonance, ω_{Ik} represents the frequency of kth interference component, and L_k denotes the amplitude of the kth interference component.

The analytic version of $r(t)$ can be written as

$$\text{Analytic}(r(t)) = R(t) \approx Ae^{-\beta t + j(\omega_r t + \varphi)} + \sum_{k=1}^{K} L_k e^{j(\omega_{Ik} t)} \tag{3.3}$$

Therefore, the amplitude-demodulated signal can be written as

$$\text{AD}(R(t)) \approx \left[\begin{array}{l} \left(Ae^{-\beta t} \cos(\omega_r t + \varphi) + \sum_{k=1}^{K} L_k \cos \omega_{Ik} t \right)^2 + \\ \left(Ae^{-\beta t} \sin(\omega_r t + \varphi) + \sum_{k=1}^{K} L_k \sin \omega_{Ik} t \right)^2 \end{array} \right]^{1/2} \tag{3.4}$$

The above equation reduces to

$$\text{AD}(R(t)) \approx Ae^{-\beta t} \cos(\omega_z t + \varphi) + \sum_{k=1}^{K} L_k + \sum_{p=1}^{K} \sum_{k=p+1}^{K} L_k \cos((\omega_{Ip} - \omega_{Ik}) t) \tag{3.5}$$

where $\omega_z \approx \omega_{zk} = \omega_r - \omega_{Ik}$ because $\omega_r \gg \omega_{Ik}$ for most the applications. According to equation Eq. (3.5), the amplitude demodulation is strongly affected by interference components, particularly when the amplitudes of interferences are larger than that of the bearing fault signal. Therefore, the demodulation (envelope) of a bearing fault impulse is not visible in the presence of multiple periodic components and hence the fault cannot be detected.

In summary of sections 3.1 and 3.2, the AD is effective in noise handling but falls short in dealing with interferences. To process signals contaminated by both noise and interferences, a new method is needed.

3.3 Development of the amplitude demodulation differentiation method

In this section, the ADD method will be developed to suppress interference components or boost the relative strength of fault impulses. In other words, this step can improve the SIR of the measured signal and therefore, can enhance the fault detectability. A closer look at Eq. (3.5) indicates that it is possible to mitigate the effect of interfering signal components by differentiation. The first derivative of Eq. (3.5) with respective to time is given by

$$\begin{aligned}
\mathrm{ADD}_1(t) &= \mathrm{Diff}\left(\mathrm{AD}\left(R(t)\right)\right) = \\
&-A\omega_z e^{-\beta t}\sin\left(\omega_z t+\varphi\right) - A\beta e^{-\beta t}\cos\left(\omega_z t+\varphi\right) \\
&-\sum_{p=1}^{K}\sum_{k=p+1}^{K}\left(\omega_{Ip}-\omega_{Ik}\right)L_k\sin\left(\left(\omega_{Ip}-\omega_{Ik}\right)t\right)
\end{aligned} \tag{3.6}$$

Eq. (3.6) shows that the direct influence of interference signals as expressed by $\sum_{k=1}^{K} L_k$ has been eliminated. At the same time, the fault signature is enhanced significantly because of the multiplication of the resonance frequency (it is much higher than the interference frequencies in most applications) in the fault impulse term.

Eq. (3.6) can be simplified as

$$\mathrm{ADD}_1(t) \approx -V e^{-\beta t}\cos\left(\omega_z t+\varphi-\rho\right) - \sum_{p=1}^{K}\sum_{k=p+1}^{K}\left(\omega_{Ip}-\omega_{Ik}\right)L_k\sin\left(\left(\omega_{Ip}-\omega_{Ik}\right)t\right) \tag{3.7}$$

$$V = A\sqrt{\omega_z^2+\beta^2}\ ,\ \sin\rho = \frac{A\omega_z}{V},\ \cos\rho = A\frac{\beta}{V}$$

Similarly, the impulsive fault signature could be further enhanced by differentiating the above equation as follows

$$\begin{aligned}\mathrm{ADD}_2(t) = \mathrm{Diff}\left(\mathrm{ADD}_1(t)\right) = \\ V\omega_z e^{-\beta t}\ \sin\left(\omega_z t+\varphi-\rho\right)+V\beta e^{-\beta t}\ \cos\left(\omega_z t+\varphi-\rho\right) \\ -\sum_{p=1}^{K}\sum_{k=p+1}^{K}\left(\omega_{Ip}-\omega_{Ik}\right)^2 L_k \cos\left(\left(\omega_{Ip}-\omega_{Ik}\right)t\right)\end{aligned} \tag{3.8}$$

The above equation can be re-cast as

$$\begin{aligned}\mathrm{ADD}_2(t) \approx A\left(\omega_z^2+\beta^2\right)e^{-\beta t}\cos\left(\omega_z t+\phi\right) \\ -\sum_{p=1}^{K}\sum_{k=p+1}^{K}\left(\omega_{Ip}-\omega_{Ik}\right)^2 L_k \cos\left(\left(\omega_{Ip}-\omega_{Ik}\right)t\right)\end{aligned} \tag{3.9}$$

$$\varphi-\rho-\gamma=\phi\ ,\sin\gamma=\frac{V\omega_z}{A\left(\omega_z{}^2+\beta^2\right)},\ \cos\gamma=\frac{V\beta}{A\left(\omega_z{}^2+\beta^2\right)}$$

Although the differentiation process can be further repeated, additional differentiations may not further improve the result because the real signal also contains background noise with frequencies spreading over the entire frequency range of interest. Additional differentiation steps will also amplify the high frequency noises. As such, the differentiation order is limited to 2. The procedure of the proposed method is summarized in the flowchart in Fig. 3.4 with number of differentiations, *N*, being set to 2 for the above reason.

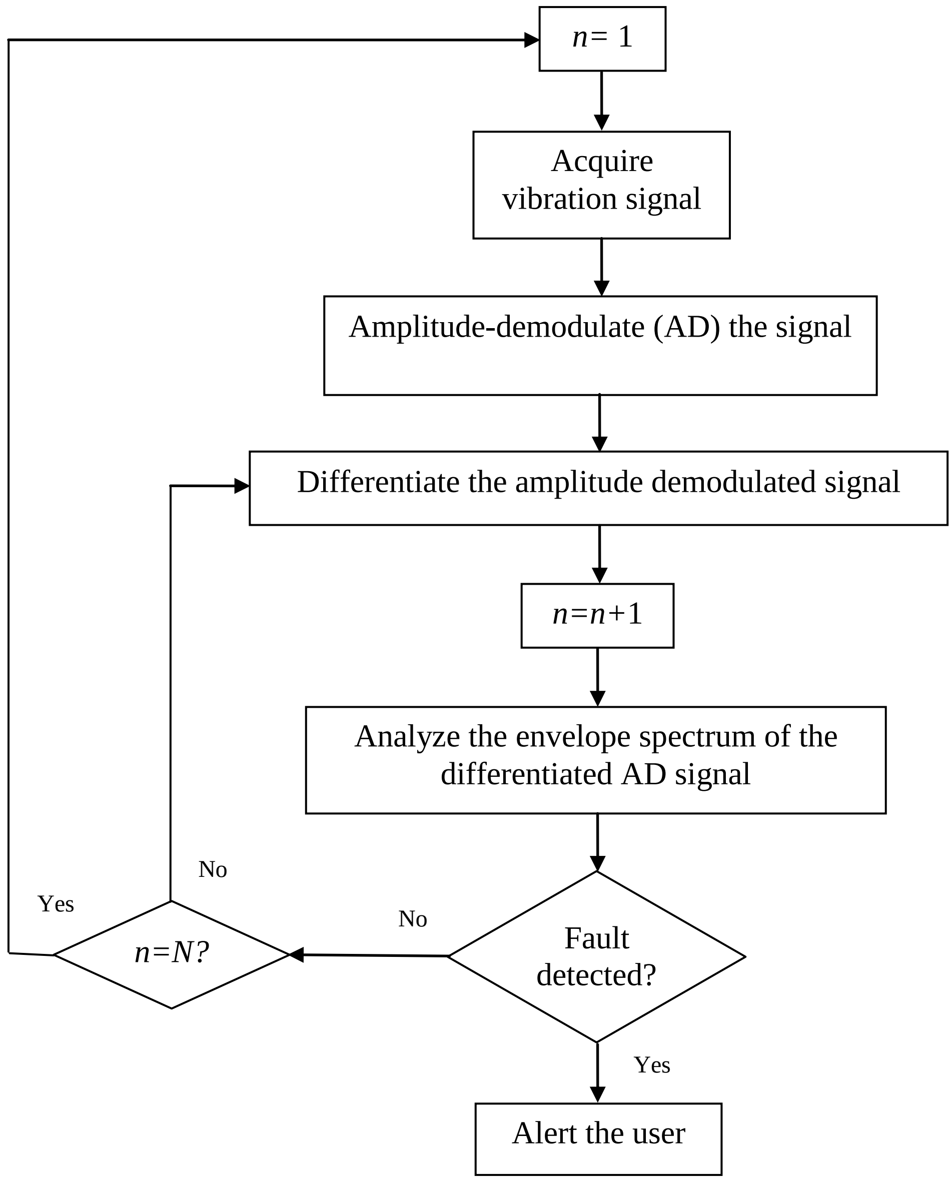

Fig. 3.4. Flowchart of the ADD method.

3.4 Comparison of the ADD method and energy operator in terms of the signal-to-interference ratio

To evaluate the ADD method, it is compared with another non-parametric method, i.e., the energy operator method based on the SIR criterion. For fair comparison, the energy operator is expanded mathematically for multiple vibration interferences (by applying Eq. (2.21) to $r(t)$) as follows

$$\psi\left(r\left(t\right)\right)=A^2\omega_r^2 e^{-2\beta t}+Ab_\psi\left(t\right)e^{-\beta t}+\sum_{k=1}^{K}L_k^2\omega_{Ik}^2 \tag{3.10}$$

where $b_\psi(t)$ is given below

$$\begin{aligned}b_\psi\left(t\right)=&\,2\beta\cos\left(\omega_r t+\theta\right)\sum_{k=1}^{K}L_k\omega_{Ik}\sin\omega_{Ik}t+2\omega_r\sin\left(\omega_r t+\theta\right)\sum_{k=1}^{K}L_k\omega_{Ik}\sin\omega_{Ik}t\\&+\cos\left(\omega_r t+\theta\right)\sum_{k=1}^{K}L_k\omega_{Ik}^2\cos\omega_{Ik}t-\beta^2\cos\left(\omega_r t+\theta\right)\sum_{k=1}^{K}L_k\cos\omega_{Ik}t\\&-2\beta\omega_r\sin\left(\omega_r t+\theta\right)\sum_{k=1}^{K}L_k\cos\omega_{Ik}t+\omega_r^{\ 2}\cos\left(\omega_r t+\theta\right)\sum_{k=1}^{K}L_k\cos\omega_{Ik}t\end{aligned}$$

According to Eq. (3.10), the energy operator result consists of three terms: the AD term $A^2\omega_z^{\ 2}e^{-2\beta t}$, the high frequency component $Ab_\psi(t)e^{-\beta t}$, and the interference signal contents $\sum_{k=1}^{K}L_k^2\omega_{Ik}^2$. The AD term is the squared envelope of the fault signal multiplied by an exponentially decaying factor. The second term represents high-frequency components with a combination of an exponential decaying factor of the fault signature and the interfering signal contents. The second term will not contribute to fault detection because of its high-frequency components (Liang and Soltani Bozchalooi, 2010). In the following, in order to calculate the signal-to-interference ratio, the first term is considered as a faulty bearing vibration and the third as vibration interferences.

The SIR of a fault bearing signal with multiple interferences can be defined as (Liang and Soltani Bozchalooi, 2010)

$$\mathrm{SIR}\left(r\right)=\frac{\left(1/T\right)\int_0^T x^2\left(t\right)\mathrm{d}t}{\left(1/T\right)\int_0^T\sum_{k=1}^{K}v_k^{\ 2}\left(t\right)\mathrm{d}t}=\frac{P_x}{P_v} \tag{3.11}$$

where $x(t)$ is the faulty bearing vibration, and $\sum_{k=1}^{K}v_k\left(t\right)$ represents multiple vibration interferences.

In the following, the SIR of the twice ADD processed signal will be derived. However, only the AD term (i.e., the first term of Eq. (3.10)) and the interference signal contents (i.e., the third term of Eq. (3.10)) will be taken into account in calculating the powers associated with the fault impulsive signal component and the interference component respectively for obtaining the SIR of the transformed signal because the first and the third terms are the dominant terms in Eq. (3.10). Hence the SIR of $\mathrm{ADD}_2(t)$ can be obtained from Eqs. (3.9) and (3.11) as follows

$$\begin{aligned}\mathrm{SIR}\left(\mathrm{ADD}_2\left(r(t)\right)\right) &= \frac{\left(\frac{1}{T_P}\right)\int_0^{T_P} A^2\left(\omega_z^2+\beta^2\right)^2 e^{-2\beta t}\cos^2\left(\omega_z t+\phi\right)\mathrm{d}t}{\left(\frac{1}{T}\right)\int_0^{T}\sum_{p=1}^{K}\sum_{k=p+1}^{K} L_k^2\left(\omega_{Ip}-\omega_{Ik}\right)^4\cos^2\left(\left(\omega_{Ip}-\omega_{Ik}\right)t\right)\mathrm{d}t} \\ &\approx \frac{\left(\frac{1}{T_P}\right)\int_0^{\infty} A^2\left(\omega_z^2+\beta^2\right)^2 e^{-2\beta t}\cos^2\left(\omega_z t+\phi\right)\mathrm{d}t}{\left(\frac{1}{T}\right)\int_0^{T}\sum_{p=1}^{K}\sum_{k=p+1}^{K} L_k^2\left(\omega_{Ip}-\omega_{Ik}\right)^4\cos^2\left(\left(\omega_{Ip}-\omega_{Ik}\right)t\right)\mathrm{d}t}\end{aligned} \tag{3.12}$$

where T is the period of vibration interference, and T_p is the time period corresponding to the fault characteristic frequency.

After integrations, the signal-to-interference ratio of the ADD processed signal can be written as

$$\begin{aligned}\mathrm{SIR}\left(\mathrm{ADD}_2\left(r(t)\right)\right) \approx &\frac{A^2\left(\omega_z^2+\beta^2\right)^2}{2T_p\beta\left[\sum_{p=1}^{K}\sum_{k=p+1}^{K} L_\mathrm{k}^2\left(\omega_{Ip}-\omega_{Ik}\right)^4\right]} \\ &+\frac{A^2\left(\omega_z{}^2+\beta^2\right)^2\left(\beta\cos 2\phi-\omega_z\sin 2\phi\right)}{2T_p\left(\sum_{p=1}^{K}\sum_{k=p+1}^{K} L_\mathrm{k}^2\left(\omega_{Ip}-\omega_{Ik}\right)^4\right)\left(\omega_z^2+\beta^2\right)}\end{aligned} \tag{3.13}$$

Now, we examine the above SIR for two scenarios which cover most applications: a) the resonance frequency is approximately equal to the damping parameter, i.e., $\omega_z \approx \beta$, and b) the resonance frequency is substantially higher than the damping parameter, i.e., $\omega_z \gg \beta$.

For $\omega_z \approx \beta$, we obtain

$$\mathrm{SIR}\left(\mathrm{ADD}_2\left(r(t)\right)\right) \approx \frac{3A^2\left(\omega_z^2+\beta^2\right)^2}{4T_p\beta\left[\sum_{p=1}^{K}\sum_{k=p+1}^{K} L_k^2\left(\omega_{Ip}-\omega_{Ik}\right)^4\right]} \tag{3.14A}$$

For $\omega_z \gg \beta$, the SIR(ADD$_2$(t)) is

$$\mathrm{SIR}\left(\mathrm{ADD}_2\left(r(t)\right)\right) \approx \frac{A^2\left(\omega_z^2+\beta^2\right)^2}{2T_p\beta\left[\sum_{p=1}^{K}\sum_{k=p+1}^{K} L_k^2\left(\omega_{Ip}-\omega_{Ik}\right)^4\right]} \tag{3.14B}$$

Similarly, the SIR of the energy operator-processed signal with multiple interferences can be obtained based on Eqs. (3.10) and (3.11):

$$\mathrm{SIR}\left(\psi\left(r\left(t\right)\right)\right) = \frac{\left(\dfrac{1}{T_P}\right)\int_0^{T_P} A^4\omega_r^4 e^{-4\beta t}\,\mathrm{d}t}{\left(\dfrac{1}{T_k}\right)\sum_{k=1}^{K}\int_0^{T_k} L_k^4\omega_{Ik}^4\,\mathrm{d}t} \tag{3.15}$$

After the integral calculation, the SIR of the energy operator processed signal will be

$$\mathrm{SIR}\left(\psi\left(r\left(t\right)\right)\right) \approx \frac{A^4\omega_r^4}{4T_P\beta\sum_{k=1}^{K} L_k^4\omega_{Ik}^4} \tag{3.16}$$

From Eqs. (3.14) and (3.16), one obtains

For $\omega_z \approx \beta$

$$\frac{\mathrm{SIR}\left(\mathrm{ADD}_2\left(r(t)\right)\right)}{\mathrm{SIR}\left(\psi\left(r\left(t\right)\right)\right)} \approx \frac{3\left(\omega_z^2+\beta^2\right)^2\sum_{k=1}^{K} L_k^4\omega_{Ik}^4}{\omega_r^4\left[A^2\sum_{p=1}^{K}\sum_{k=p+1}^{K} L_k^2\left(\omega_{Ip}-\omega_{Ik}\right)^4\right]} \tag{3.17A}$$

For $\omega_z \gg \beta$

$$\frac{\mathrm{SIR}\left(\mathrm{ADD}_2\left(r(t)\right)\right)}{\mathrm{SIR}\left(\psi\left(r\left(t\right)\right)\right)} \approx \frac{2\left(\omega_z^2+\beta^2\right)^2\sum_{k=1}^{K} L_k^4\omega_{Ik}^4}{\omega_r^4\left[A^2\sum_{p=1}^{K}\sum_{k=p+1}^{K} L_k^2\left(\omega_{Ip}-\omega_{Ik}\right)^4\right]} \tag{3.17B}$$

Obviously, for $L_i > A$ and $L_i \approx A$, $\sum_{k=1}^{K} L_k^4 \omega_{Ik}^4$ is greater than $A^2 \sum_{p=1}^{K} \sum_{k=p+1}^{K} L_k^2 \left(\omega_{Ip} - \omega_{Ik}\right)^4$. Also, we have $(\omega_z + \beta) > \omega_r$. Therefore, Eq. (3.17) suggests that SIR(SM$_2$(t)) is always greater than SIR(ψ(r(t))). If we ignore the ratio of $\sum_{k=1}^{K} L_k^4 \omega_{Ik}^4$ to $A^2 \sum_{p=1}^{K} \sum_{k=p+1}^{K} L_k^2 \left(\omega_{Ip} - \omega_{Ik}\right)^4$, Eq. (3.17) leads to

$$\frac{2\left(\omega_z^2 + \beta^2\right)^2}{\omega_r^4} < \frac{\mathrm{SIR}\left(\mathrm{ADD}_2\left(r(t)\right)\right)}{\mathrm{SIR}\left(\psi\left(r(t)\right)\right)} < \frac{3\left(\omega_z^2 + \beta^2\right)^2}{\omega_r^4} \tag{3.18}$$

As $\omega_z \approx \omega_r$, $2\left(\omega_z^2 + \beta^2\right)^2 / \omega_r^4 \approx 8$ and $3\left(\omega_z^2 + \beta^2\right)^2 / \omega_r^4 \approx 12$ in the case $\omega_z \approx \beta$. Therefore, the SIR of the ADD processed signal is 8 to 12 times higher than that of the energy operator processed result when $\omega_z \approx \beta$. If $\omega_z \gg \beta$, the SIR of the ADD processed signal will be about 2 to 3 times higher than that of the energy operator processed result.

In addition to the improved SIR, the proposed ADD method is also computationally efficient because it is based on two data points which can be chosen backward or forward in the difference format.

3.5 Simulation evaluation

In this section, we evaluate the performance of the ADD method using the simulated faulty bearing signal shown in Fig. 2.1. This signal is mixed with four high-amplitude vibration interferences as well as white Gaussian noise with SNR= -9 dB. The mixed signal has a SIR of -44 dB (Note: the amplitudes of the interferences are automatically specified by MATLAB once the SIR is fixed) and is shown in Fig. 3.5 (The FCF is 50 Hz, and the frequencies of vibration interferences are 8 Hz, 35 Hz, 130 Hz, and 720 Hz). To generate white Gaussian noise, we use the 'awgn' MALAB command.

Fig. 3.6(a) and Fig. 3.6(b) display the frequency spectra of the signal mixture and the signal envelope, respectively. The obvious peaks in Fig. 3.6(a) can be detected at frequencies of 8 Hz, 35 Hz, 130 Hz, and 720Hz which are associated with vibration interferences. In Fig.

3.6(b), the high peaks are related to the combinations of vibration interferences at 26.88 Hz, 121.9 Hz, 590 Hz, 685 Hz, 711.9 Hz could attributes to the combined effects of the interferences. Neither of the results in Figs. 3.6(a) and (b) can reveal the fault characteristic frequency. Hence, the energy operator is then applied to this simulated signal and the result is presented in Fig. 3.7. Once again, the fault signature cannot be identified from this result; the several high peaks are related to the interferences and their artifacts.

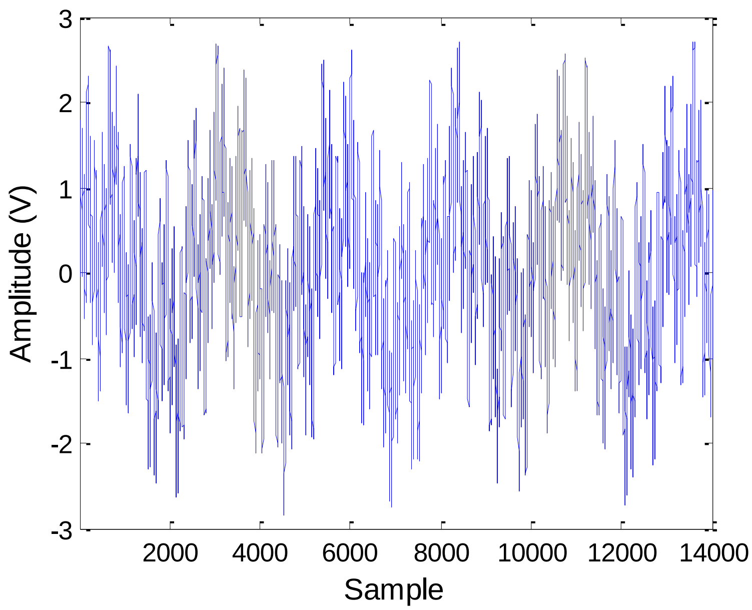

Fig. 3.5. Simulated faulty bearing signal mixed with large amplitude high- and low-frequency vibration interferences SIR=-44 dB and with white noise.

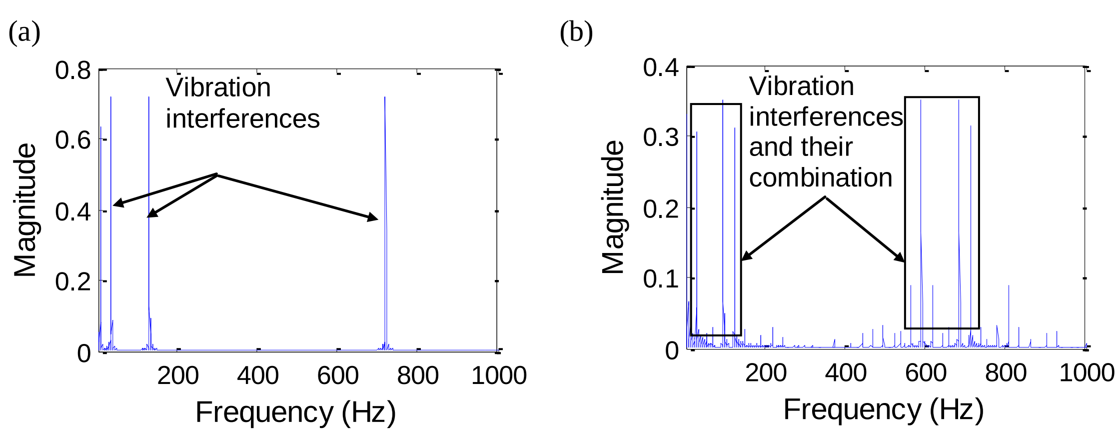

Fig. 3.6. Frequency domain representations of: (a) the signal mixture shown in Fig. 3.5, and (b) envelope of the signal mixture.

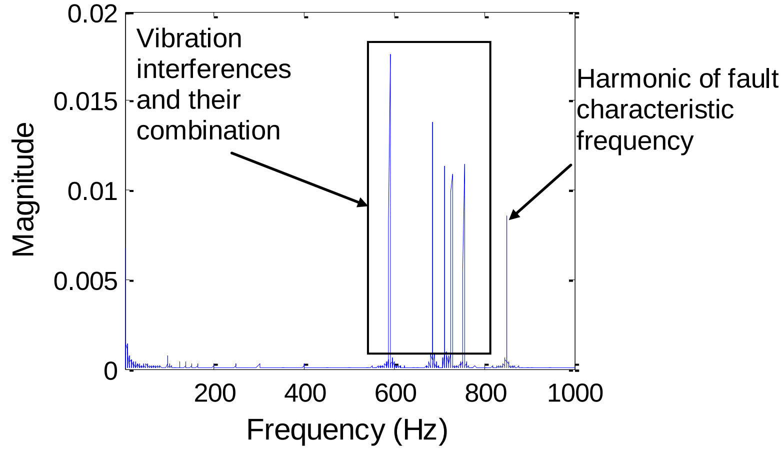

Fig. 3.7. Spectrum of energy operator applied to the signal mixture.

Then the same signal mixture is processed using the ADD method with the resulting envelope spectrum plotted in Fig. 3.8. The bearing fault at 50 Hz and more than ten of its harmonics can be clearly observed in Fig. 3.8. It should be noted that the result presented in Fig. 3.8 is obtained by directly applying the ADD approach to the simulated signal in Fig. 3.5 without any pre-filtering process.

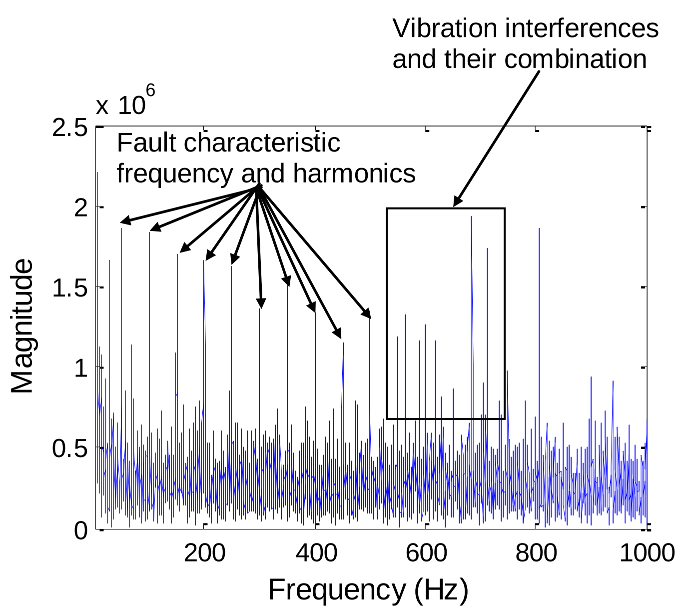

Fig. 3.8. Envelope spectrum of ADD result of the simulated signal in Fig. 3.5.

In the next section, the proposed method is further evaluated using experimental data.

3.6 Experimental evaluation of the ADD method

3.6.1 Detection of inner race bearing fault

The experimental data are collected from a Spectra Quest Machinery fault simulator (MKF-PK5M) as shown in Fig. 3.9. The vibration signal is acquired by an accelerometer. A 3-hp ac motor (ac motor 1) is used to drive the simulator. This ac motor is controlled by a PWM Hitachi drive. Two bearings support steel shaft and two well-balanced mass rotors are installed on the shaft. The vibration signal is transferred from sensor to DAQ card and then illustrated through LabVIEW. A PC is used to perform signal-processing with MATLAB.

The specification of various parts of experimental setup is mentioned below:

- Shaft: 5/8” in diameter
- Mass rotors: 2” thick, 4” in diameter and 11.1 lbs each
- Bearing: Type ER10K, inside, outside, pitch and ball diameters are, respectively, 0.625”, 1.8500”, 1.3190” and 0.3125”, eight roller elements (balls).
- Accelerometer: PCB sensor, model 623C01-100 Mv/g sensitivity and a 1-20 kHz sensitivity range.
- PWM Hitachi drive: SJ200-022NFU.
- DAQ card: NI PCI-6132 multi-function.
- PC: 4/2.52 GHz

The shaft speed is set at 1007 RPM (16.78 Hz). The right bearing has a pre-seeded fault (it was created by manufacture and the dimension of the fault are unknown) on the inner race with the characteristic frequency of 82.77 Hz (=4.9322f_r, specified in the simulator user’s manual).

To generate vibration interference, a gearbox is also connected to the driving shaft using a belt as shown in Fig. 3.9, and an extra motor (AC Motor 2) is placed on a table that is in contact with the test rig to produce additional interference signals. The gear meshing frequency is 116.56 Hz. The shaft rotor frequency of AC Motor 2 is 24 Hz. To make the problem more challenging, we added another inference of 1,000 Hz into the signal. The accelerometer is installed on the simulator base at a location away from the bearing but closer to the belt and the driven gearbox.

The vibration signal is sampled at 12,000 samples/s. Fig. 3.11(a) displays part of the raw date for the faulty bearing. The FFT results is shown in Fig. 3.11(b). As we can see from these plots, no impulse feature can be detected. For comparison, the counterpart plots of a healthy bearing are also presented (Fig. 3.10).

The envelope spectrum of the raw signal and the energy operator spectrum of the measured signal are shown in Fig. 3.12(a) and (b) respectively. Neither could reveal the inner race fault signature. Then the ADD method is applied to the same raw signal with the result presented in Fig. 3.13. As shown in this figure, the fault characteristic frequency as well as six of its harmonics at 82.77, 165.54, 248.31 ,331 Hz, 413.85 Hz, 496.62 Hz, and 579.39 Hz can be clearly observed from the result. This indicates that the performance of the proposed ADD method is substantially better than that of the plain enveloping method and the energy operator approach.

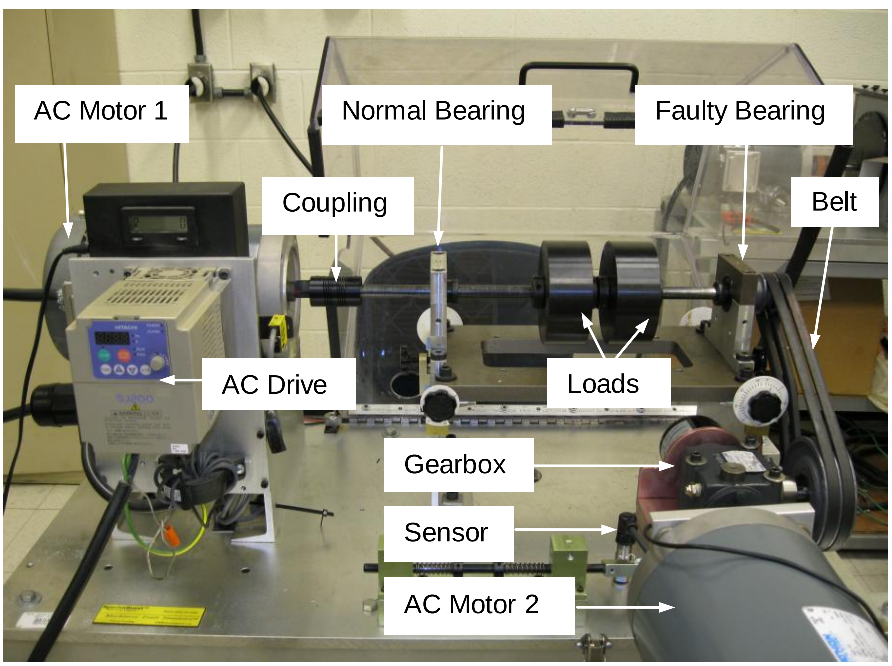

Fig 3.9. Experimental setup #1 (for inner race fault).

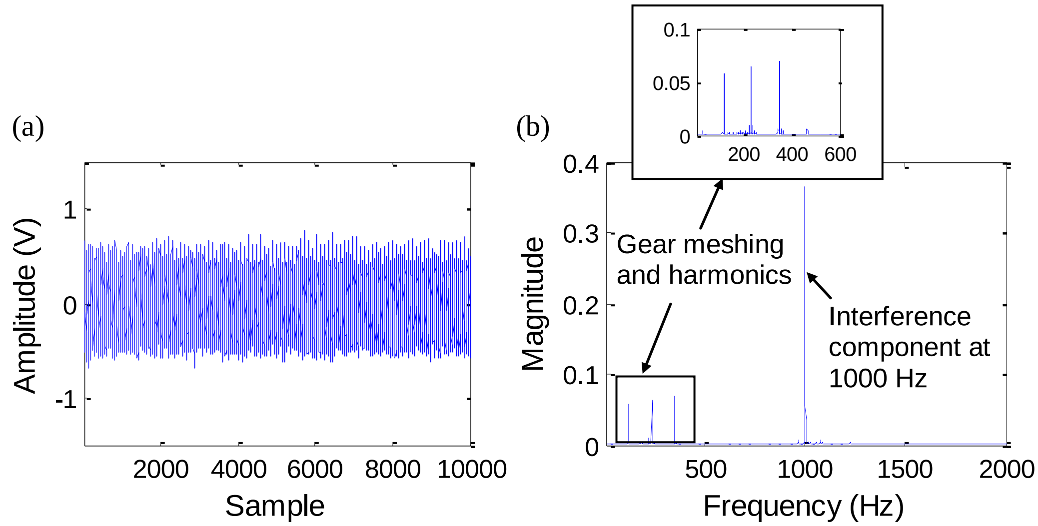

Fig 3.10. (a) A portion of the measured signal of healthy bearing, and (b) the spectrum of a healthy signal (Experimental setup #1).

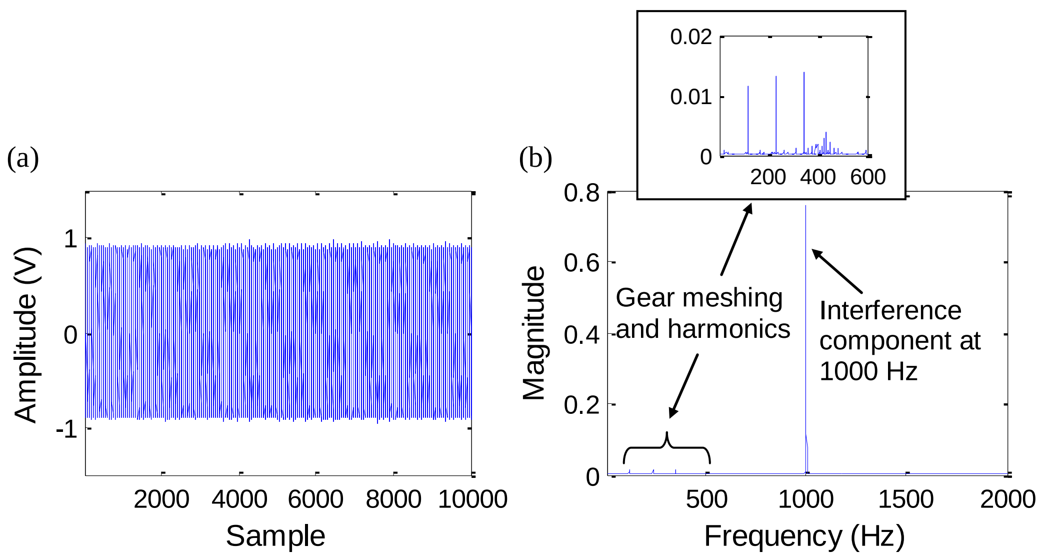

Fig 3.11. (a) A portion of the measured signal of inner race fault from Experiment # 1, and (b) the frequency spectrum of the fault signal.

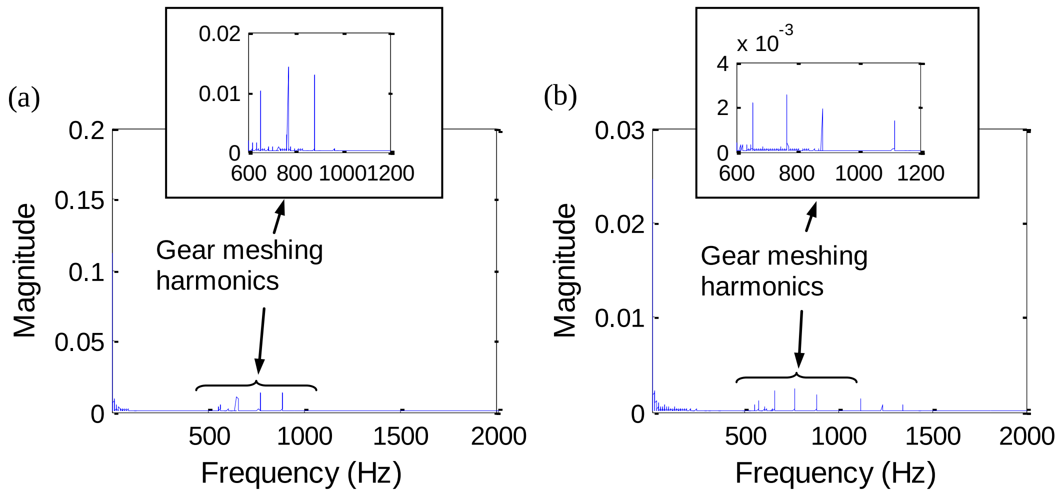

Fig 3.12. (a) Envelope spectrum of the inner race fault signal (Fig. 3.11(a)), and (b) The spectrum of the energy operator result of the same inner race fault signal.

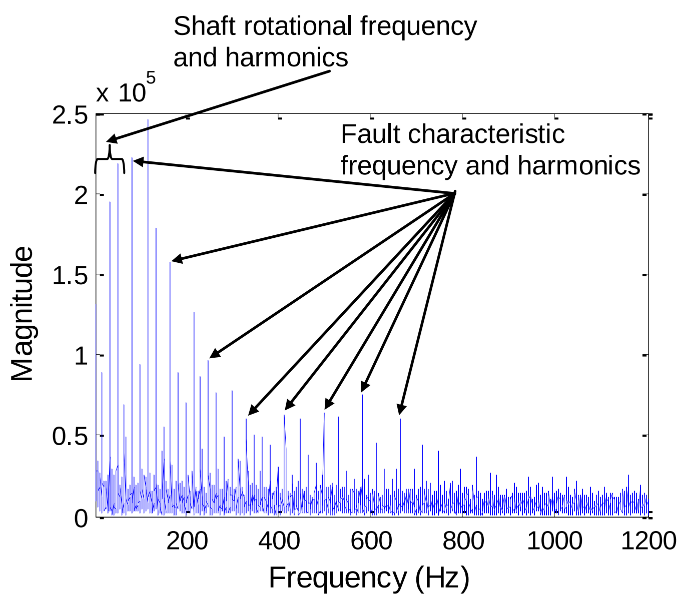

Fig 3.13. Envelope spectrum of the raw signal (shown in Fig. 3.11(a)) after applying ADD method (with two iterations).

3.6.2 Detection of outer race bearing fault (test 1)

The test rig is the same as the one used in the previous experimental set up (Experiment #1). However, the inner race faulty bearing is replaced by a bearing with an outer race fault and the two mass rotors are removed to examine the performance of the proposed method in a different test condition. The normal bearing is installed on the left side of the shaft with the same characteristics as in the previous experiment. Similar to the previous experiment, the gearbox is driven by the shaft through a belt connection.

The shaft speed is set at 993.6 RPM (16.56 Hz).The bearing has a pre-seeded fault (created by manufacture with unknown dimensions) on the outer race with a characteristic frequency of 50.54 Hz (=3.052f_r, specified in the simulator user's manual). The accelerometer is installed on the simulator base at a location away from the bearing but closer to the belt and the driven gearbox (Fig. 3.14). The interferences are added by motor 2 (24Hz) and the meshing frequency of the gearbox (117.1 Hz). We also added another interference at 1,000 Hz by MATLAB. Fig. 3.15(a) displays a part of the measured data from the outer race fault bearing. The spectrum of measured signal is plotted in Fig. 3.15(b) which shows only the interference frequencies.

The envelope spectrum of the raw signal (with no filtering) is shown in Fig. 3.16(a). Fig. 3.16(b) demonstrates the energy operator spectrum of the measured signal. Obviously, the outer race fault cannot be revealed from neither of the two figures. The result of the ADD method on the same experimental data is displayed in Fig. 3.17 which clearly shows the fault characteristic frequency at 50.54 Hz as well as four associated harmonics at 101.08, 151.6, 202.16 and 252.7 Hz.

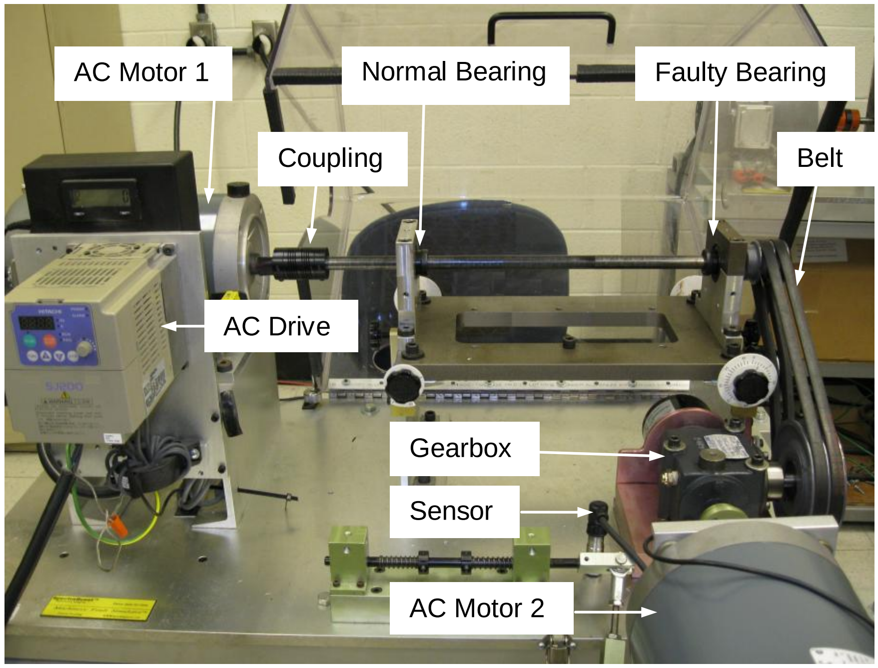

Fig 3.14. Experimental setup #2 (for outer race fault).

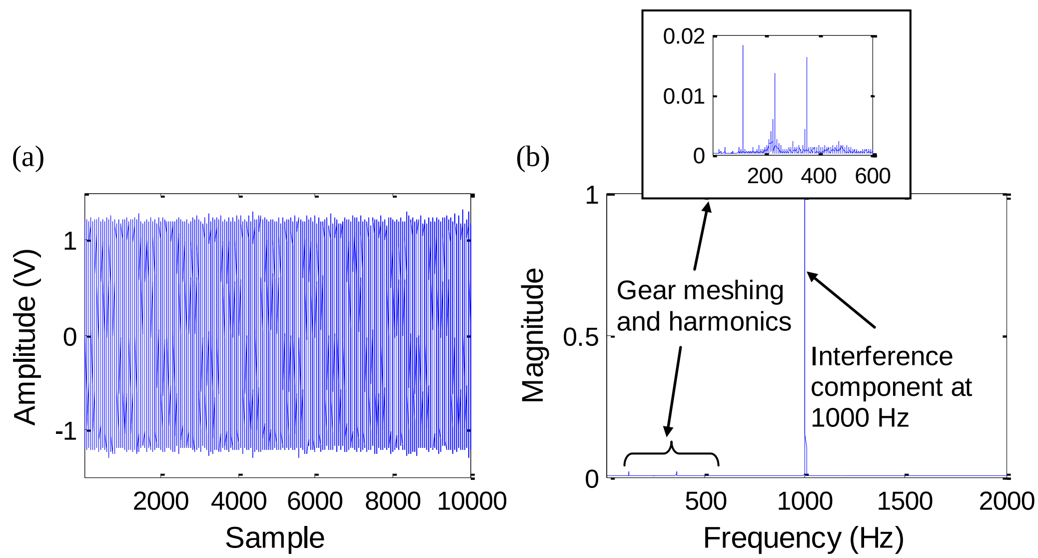

Fig 3.15. (a) A portion of the measured signal of outer race fault from same setup (experiment # 2), and (b) the spectrum of signal.

.

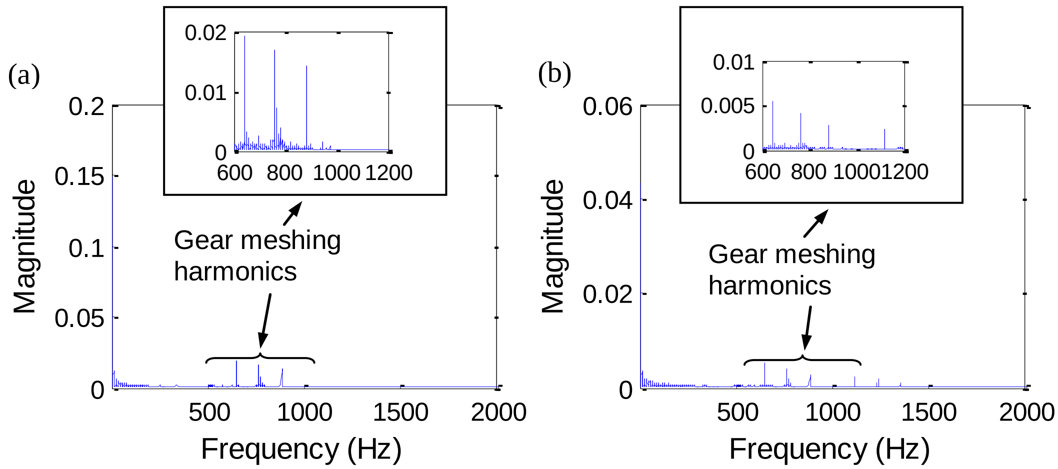

Fig 3.16. (a) Envelope spectrum of the outer race fault signal (from Fig. 3.15(a)), and (b) the spectrum of the energy operator result of the same outer race fault signal.

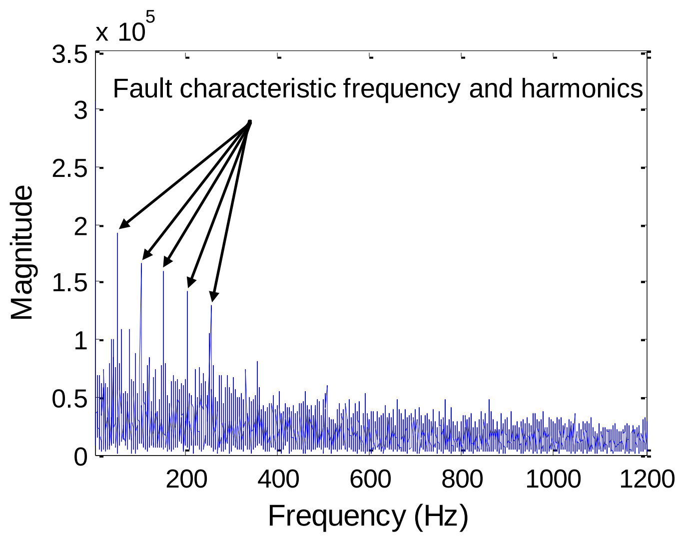

Fig. 3.17. Envelope spectrum of the raw signal after applying ADD method.

3.6.3 Detection of bearing outer race fault (test 2)

In this test, the test rig is the same the one used in experiment 2, except that two well-balanced rotors are installed on the shaft (Fig. 3.18), just like in the inner race case (Fig. 3.9). The vibration signal from sensor is fed to a USB DAQ device and then collected through LabVIEW at a sampling frequency of 12000 samples s^{-1}. The shaft speed is set at 1092 RPM (18.2 Hz). The bearing has a pre-seeded fault (created by the manufactures with unknown dimensions) on the outer race with a characteristic frequency of 55.54 Hz (=3.052 f_r, specified in the simulator user's manual). The data are acquired using an accelerometer installed nearby the driven gearbox on the simulator base at a location away from the faulty bearing. The interferences are added by motor 2 (24.65 Hz) and the meshing frequency of the gearbox (126.8 Hz). We also added an interference at 500 Hz by MATLAB.

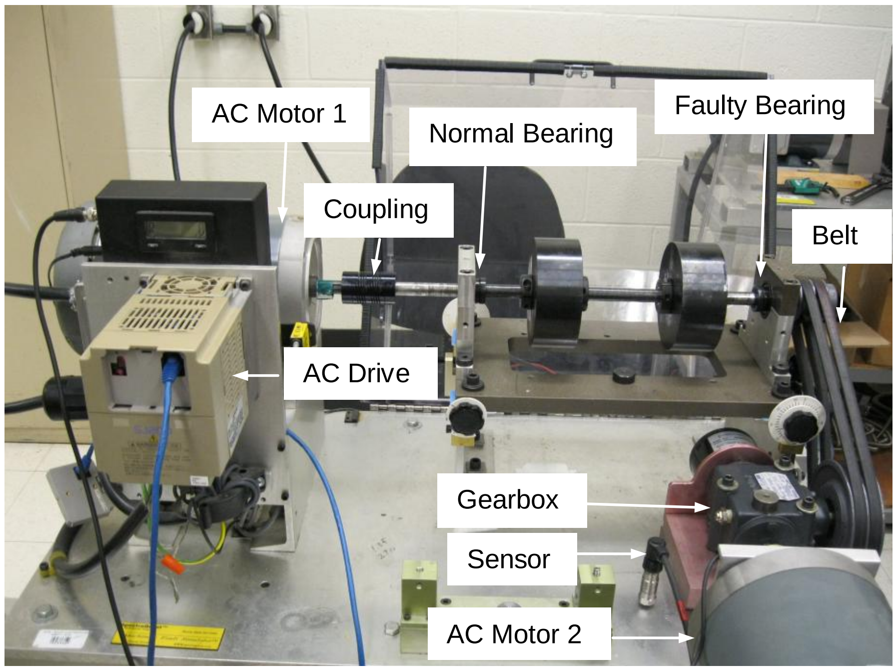

Fig. 3.18. Experimental setup #3.

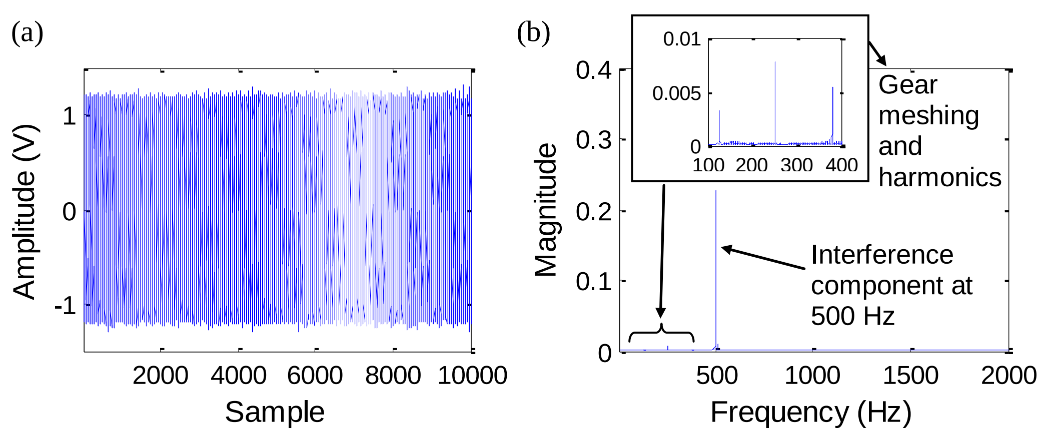

Fig. 3.19. (a) A portion of the measured signal of outer race fault from same setup (experiment # 3), and (b) the spectrum of signal.

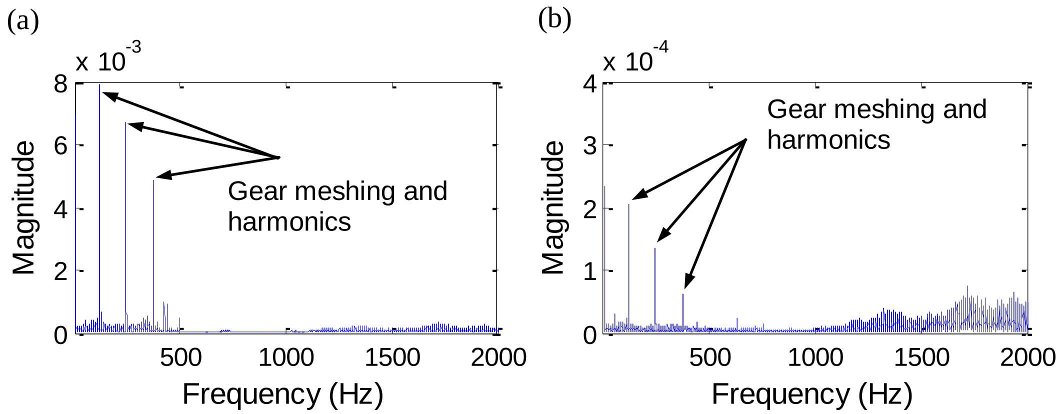

Fig. 3.20. (a) Envelope spectrum of the faulty bearing signal, and (b) the spectrum of energy operator applied to the original signal.

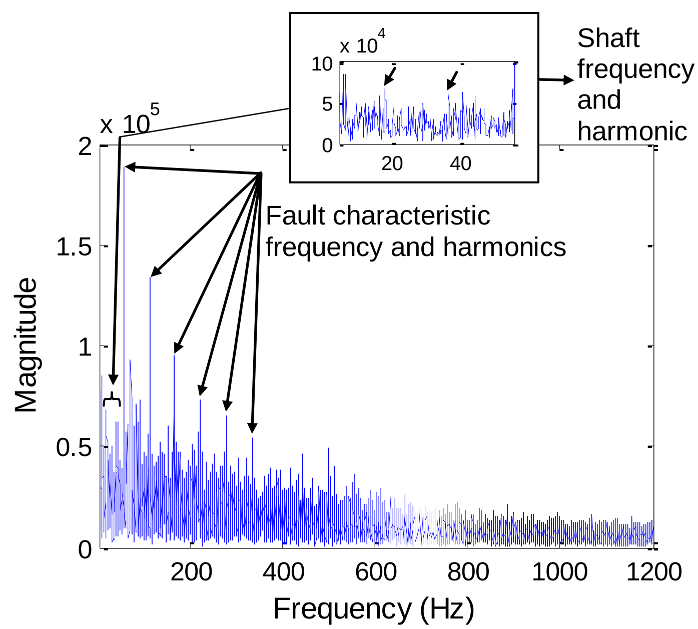

Fig. 3.21. Envelope spectrum of the raw signal after applying ADD method.

A portion of the measured data from the outer race fault bearing and its spectrum are shown in Fig. 3.19. Only the gear meshing frequencies and its harmonics can be recognized from the envelope spectrum of the raw signal (without filtering) in Fig. 3.20(a). Fig 3.20(b). shows the energy operator spectrum of the measured signal. Neither the envelope nor the energy operator can reveal signature of bearing defect. Then, the ADD method is applied to process the same data in the presence of high level of vibration interferences with the result in Fig. 3.21 clearly showing the FCF at 55.5 Hz as well as five of its harmonics at 111, 166.6, 222.1, 277.7, and 333.2 Hz.

3.6.4 Experimental evaluation using the experimental data from Case Western Reserve University

The proposed method is further tested using the data from the Bearing Data Center of the Case Western Reserve University. The fault was created by Electro-Discharge Machining (EDM).

3.6.4.1 Inner race fault detection

The experiment related information is summarized in Table 3.1.

Table 3.1 Specifications of the Case Western Reserve University experiments (for inner race fault)

Inner diameter	0.9843”	Motor load	0 HP
Outer diameter	2.0472”	Sampling frequency	12,000 samples/sec
Pitch diameter	1.5370”	BPFI	$5.4152f_r$ Hz
Fault diameter	0.007”	Shaft speed	1797 rpm
Fault depth	0.011”		

After employing the ADD method on the raw signal in Fig. 3.22(a), the fault characteristic frequency at 162.85 Hz, and its associated harmonics at 324.37 Hz, 486.55 Hz, 648.74 Hz, 810.92 Hz, and 973.11 Hz can be distinguished. However, the faulty features cannot be seen from spectrum of the raw signal in Fig. 3.22(b).

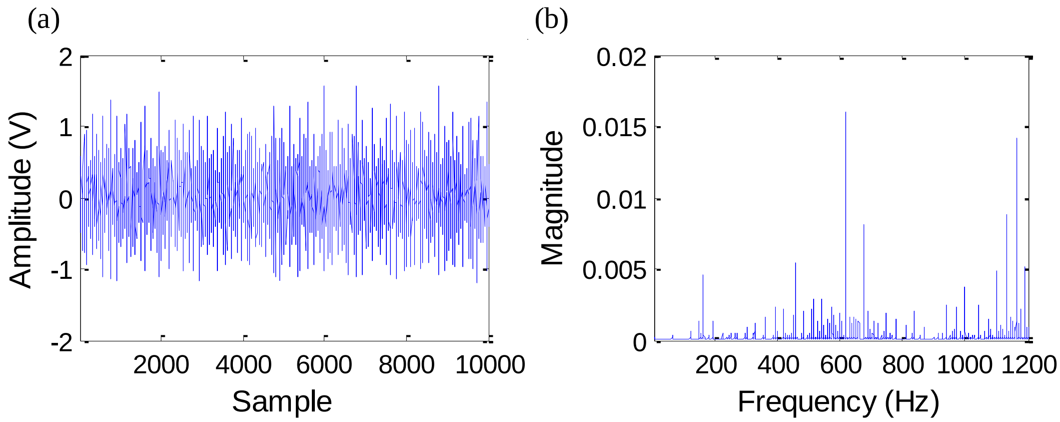

Fig 3.22. (a) A portion of the measured signal of inner race fault, and (b) the spectrum of signal.

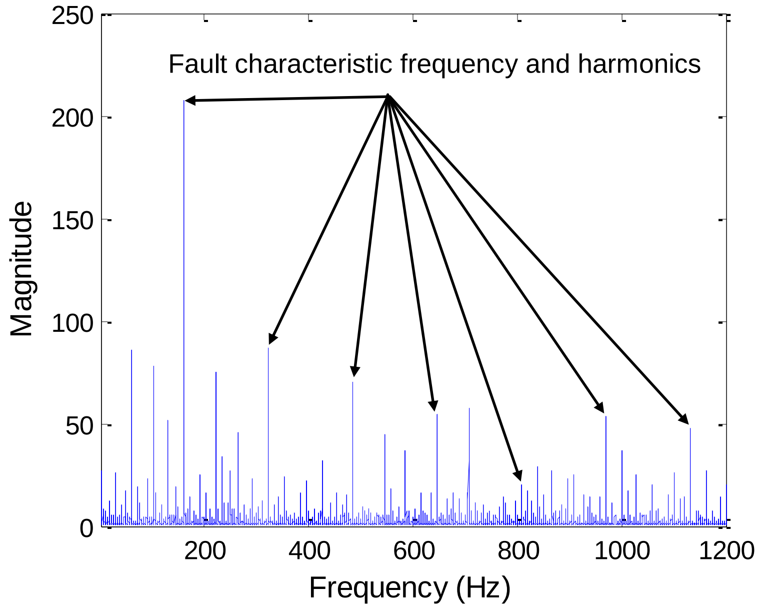

Fig 3.23. Envelope spectrum of the raw signal after applying the proposed method.

3.6.4.2 Outer race fault detection

The fault size, shaft speed, and load for out race fault test are the same as those specified for the inner race fault. The fault is at 6:00 o'clock position. The experimental information is summarized in Table 3.2.

Table 3.2 Specification of the Case Western Reserve University experiments (for outer race fault)

Inner diameter	0.9843”	Motor load	2 HP
Outer diameter	2.0472”	Sampling frequency	12,000 samples/sec
Pitch diameter	1.5370”	BPFO	3.5848 f_r Hz
Fault diameter	0.007”	Shaft speed	1750 rpm
Fault depth	0.011”		

The raw signal of faulty bearing and its spectrum are shown in Fig. 3.24. The fault characteristic frequency at 104.556 Hz, and its associated harmonics at 209.11 Hz, 313.67 Hz, 418.22 Hz, 522.78 Hz, 627.34 Hz, 731.89 Hz, 836.45 Hz, and 941 Hz can be detected by the proposed method. The result is shown in Fig. 3.25. The above results once again demonstrated the effectiveness of the proposed method in detection both inner and outer race faults, even when the fault size is very small (0.007” in diameter).

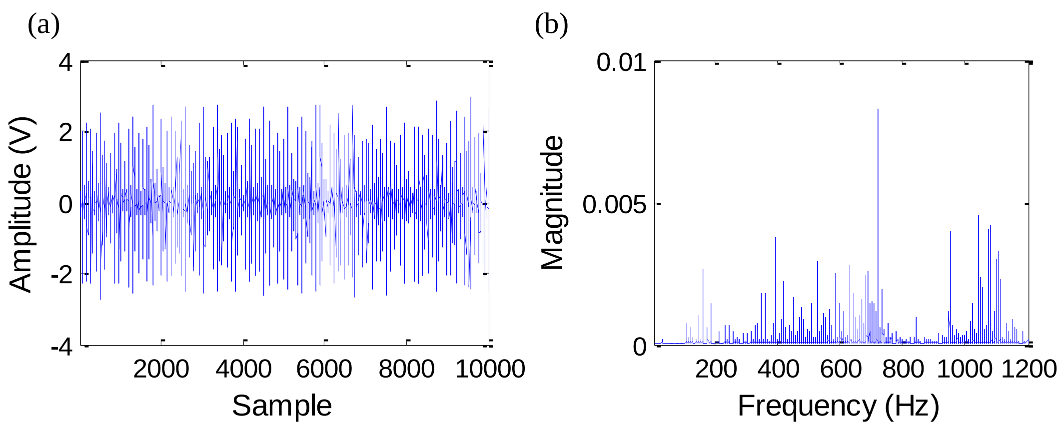

Fig 3.24. (a) A portion of the measured signal of outer race fault, and (b) the spectrum of signal.

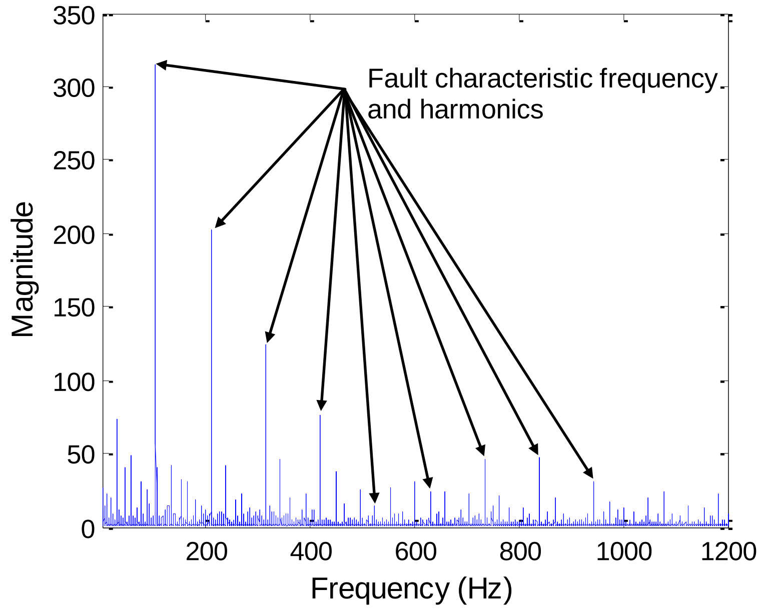

Fig 3.25. Envelope spectrum of the raw signal after applying the proposed method.

3.7 Conclusion

In this chapter, a new non-parametric approach, i.e., the amplitude demodulation differentiation (ADD) method has been developed to enhance fault delectability by increasing the signal-to-interference ratio (SIR). Depending on the damping characteristic of the system, the SIR could be boosted 2 to 12 times higher than that of the energy operator approach. The new algorithm is simple and easy to implement. Unlike the commonly adopted high-frequency resonance technique, the ADD method does not require a bandpass filter and thus eliminates the parameter selection step.

The ADD method has been evaluated using both simulated and experimental data against the enveloping and energy operator techniques. The results show that in the presence of multiple interferences, the ADD method outperform the enveloping and energy methods.

Chapter 4

Calculus enhanced energy operator (CEEO) for bearing fault detection in the presence of strong noise[2]

In the previous chapter, the ADD method has been developed to handle signals with multiple interferences. However, its performance may be affected by the noise because the differentiation step also amplifies the high frequency noise components. In this chapter, another non-parametric method with better noise handling capability will be developed to complement the ADD method. This method is based on the following observations (the details will be illustrated in later sections):

1. The differentiation of a signal can enhance the detectability of the impulsive fault signal but in the meantime also amplify the high frequency noise.
2. The integration of a signal can suppress the high frequency noise but may jeopardize the detection of the impulsive fault signal due to its "smoothing" effect.
3. The energy operator can reveal impulsive signal component without filtering.

Therefore, these observations motivate the development of a new method consisting of three associated main steps: a) differentiate the signal to boost the SIR especially in the presence of multiple strong interferences, b) integrate the result of step a) to improve the SNR particularly for the noisy signals, and c) apply the energy operator to the result of step b) to

[2] See Appendix B.2 for MATLAB script.

detect the fault. To facilitate applications, these steps will be incorporated into a single calculus enhanced energy operator (CEEO).

The principal work in this chapter is summarized as follows:

- Examine the effect of differentiation on the detectability of the fault from the faulty bearing signal with multiple vibration interferences.
- Examine the effect of integration on high frequency noise suppression.
- Derive the calculus enhanced energy operator and evaluate its performance using both simulated and experimental data, with comparison to other methods.

4.1 The effect of signal differentiation

This section starts with an illustrative example to explain that the low frequency signal components can be suppressed and the high frequency ones can be enhanced by differentiation. Then we quantify the level of signal enhancement by deriving the SIR. Next the effects of signal differentiation on interferences and noise are illustrated using simulation data.

For a discrete signal, the differentiation becomes difference as follows (step Δt=1). At time n, the discrete backward difference is written as

$$\mathrm{D}\big(x(n)\big) = x(n) - x(n-1) \tag{4.1}$$

Now we consider a signal with a low frequency component (0.1 Hz) and a high frequency component (10 Hz) of the same amplitude (Fig. 4.1(a)). The difference of the signal is shown in Fig. 4.1(b) which demonstrates that the low frequency component has been suppressed whereas the strength of high frequency one has been enhanced relative to that of the low frequency component. This effect is useful to suppress low frequency interferences and noise.

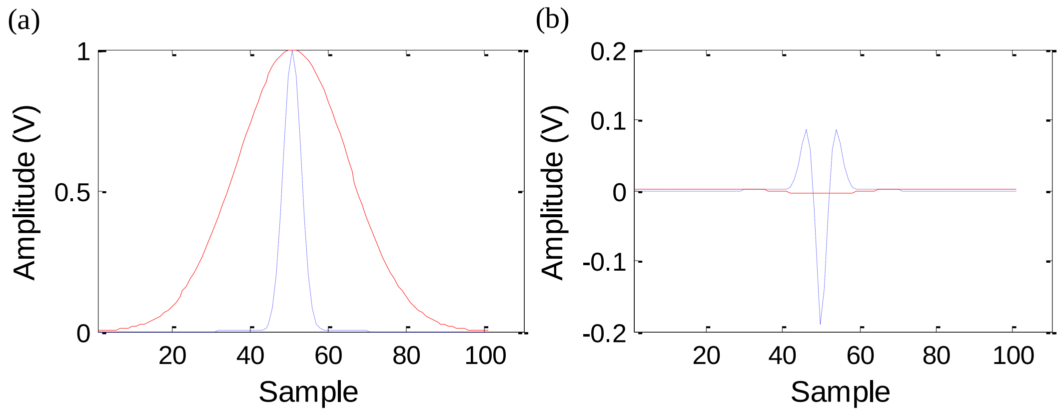

Fig 4.1. (a) Signals with a long period (solid line) and a short period (dash line), (b) their second differences (solid line: long period signal; dash line: short period signal).

4.1.1 Evaluation of the signal differentiation on the enhancement of SIR

To evaluate the effect of signal differentiation on SIR when the signal contains multiple interferences, we use the same bearing model as shown in Eq. (3.2) and present it below to facilitate discussions:

$$r(t) = x(t) + v(t) = Ae^{-\beta(t)} \cos(\omega_r t + \varphi) + \sum_{k=1}^{K} L_k \cos \omega_{Ik} t \tag{4.2}$$

where A is the amplitude of the fault signal, β is the structural damping characteristic frequency, ω_r is the frequency of the excited resonance, ω_{Ik} represents the frequency of kth interference component, L_k denotes the amplitude of the kth interference component, $x(t)$ is the vibration signal containing fault generated impulse, $v(t)$ contains multiple vibration interferences. Due to practical reason, it is reasonable to assume that the excited resonance frequency is much higher than interference signal frequency ω_{Ik} for all k's. The derivative of the signal shown in Eq. (4.2) in continuous form is

$$\mathrm{D}(r(t)) = -A\omega_r e^{-\beta t} \sin(\omega_r t + \varphi) - A\beta \cos(\omega_r t + \varphi) - \sum_{k=1}^{K} \omega_{Ik} L_k \sin \omega_{Ik} t \tag{4.3}$$

Eq. (4.3) can be written as

$$\mathrm{D}(r(t)) = -\lambda e^{-\beta t} \cos(\omega_r t + \varphi_\varsigma) - \sum_{k=1}^{K} \omega_{Ik} L_k \sin \omega_{Ik} t \tag{4.4}$$

where

$$\lambda = A\sqrt{\omega_r^2 + \beta^2}, \sin\varsigma = \frac{A\omega_r}{\lambda}, \cos\varsigma = \frac{A\beta}{\lambda}, \varphi_\varsigma = \varphi - \varsigma$$

The signal-to-interference ratio of the derivative of the faulty bearing signal is obtained)by using Eq. (3.11)) as follows

$$\mathrm{SIR}\left(\mathrm{D}\left(r\left(t\right)\right)\right) = \frac{\left(\frac{1}{T_P}\right)\int_0^{T_P} A^2\left(\omega_r^2 + \beta^2\right)e^{-2\beta t}\cos^2\left(\omega_r t + \varphi_\varsigma\right)\mathrm{d}t}{\left(\frac{1}{T_k}\right)\sum_{k=1}^{K}\int_0^{T_k} L_k^2\omega_{Ik}^2\sin^2\left(\omega_{Ik}t\right)\mathrm{d}t} \tag{4.5}$$

The above equation leads to

$$\begin{aligned}
\mathrm{SIR}\left(\mathrm{D}\left(r\left(t\right)\right)\right) &= \frac{\left(\frac{1}{T_P}\right)\int_0^{\infty} A^2\left(\omega_r^2 + \beta^2\right)e^{-2\beta t}\cos^2\left(\omega_r t + \varphi_\varsigma\right)\mathrm{d}t}{\left(\frac{1}{T_k}\right)\sum_{k=1}^{K}\int_0^{T_k} L_k^2\omega_{Ik}^2\sin^2\left(\omega_{Ik}t\right)\mathrm{d}t} \\
&= \left(\frac{A^2\left(\omega_r^2 + \beta^2\right)}{T_P}\right)\frac{\int_0^{\infty} e^{-2\beta t}\cos^2\left(\omega_r t + \varphi_\varsigma\right)\mathrm{d}t}{\left(\frac{1}{T_k}\right)\sum_{k=1}^{K}\int_0^{T_k} L_k^2\omega_{Ik}^2\sin^2\left(\omega_{Ik}t\right)\mathrm{d}t} \\
&= \left(\frac{A^2\left(\omega_r^2 + \beta^2\right)}{2T_P}\right)\left(\frac{(1/2)\left(\frac{1}{\beta} + \frac{(\beta\cos 2\varphi_\varsigma - \omega_r\sin 2\varphi_\varsigma)}{\left(\omega_r^2 + \beta^2\right)}\right)}{(1/2)\sum_{k=1}^{K} L_k^2\omega_{Ik}^2}\right) \\
&= \frac{A^2\left(\omega_r^2 + \beta^2\right)}{2T_p\beta\left[\sum_{k=1}^{K}\left(\omega_{Ik}L_k\right)^2\right]} + \frac{A^2(\beta\cos 2\varphi_\varsigma - \omega_r\sin 2\varphi_\varsigma)}{2T_p\left[\sum_{k=1}^{K}\left(\omega_{Ik}L_k\right)^2\right]}
\end{aligned} \tag{4.6}$$

According to Eqs. (3.11) and (4.2), the signal-to-interference ratio of the raw signal of a faulty bearing is obtained as

$$\mathrm{SIR}\left(r(t)\right)=\frac{\left(\frac{1}{T_P}\right)\int_0^{T_P} A^2 e^{-2\beta t}\cos^2\left(\omega_r t+\varphi\right)\mathrm{d}t}{\left(\frac{1}{T_k}\right)\sum_{k=1}^{K}\int_0^{T_k} L_k^2\cos^2\left(\omega_{Ik} t\right)\mathrm{d}t} \tag{4.7}$$

The above equation can be approximated by

$$\begin{aligned}
\mathrm{SIR}\left(r(t)\right)&=\frac{\left(\frac{1}{T_P}\right)\int_0^{\infty} A^2 e^{-2\beta t}\cos^2\left(\omega_r t+\varphi\right)\mathrm{d}t}{\left(\frac{1}{T_k}\right)\sum_{k=1}^{K}\int_0^{T_k} L_k^2\cos^2\left(\omega_{Ik} t\right)\mathrm{d}t}\\
&=\left(\frac{A^2}{T_P}\right)\frac{\int_0^{\infty} e^{-2\beta t}\cos^2\left(\omega_r t+\varphi\right)\mathrm{d}t}{\left(\frac{1}{T_k}\right)\sum_{k=1}^{K}\int_0^{T_k} L_k^2\cos^2\left(\omega_{Ik} t\right)\mathrm{d}t}=\left(\frac{A^2}{2T_P}\right)\left(\frac{\frac{1}{\beta}-\frac{\left(\beta\cos 2\varphi-\omega_r\sin 2\varphi\right)}{\left(\omega_r^2+\beta^2\right)}}{\sum_{k=1}^{K}\left(L_k\right)^2}\right)\\
&=\frac{A^2}{2T_p\beta\left[\sum_{k=1}^{K}\left(L_k\right)^2\right]}+\frac{A^2\left(\beta\cos 2\varphi-\omega_r\sin 2\varphi\right)}{2T_p\left[\sum_{k=1}^{K}\left(L_k\right)^2\right]\left(\omega_r^2+\beta^2\right)}
\end{aligned} \tag{4.8}$$

From Eqs. (4.6) and (4.8), we obtain

$$\frac{\mathrm{SIR}\left(\mathrm{D}\left(r(t)\right)\right)}{\mathrm{SIR}\left(r(t)\right)}\approx\frac{\left(\omega_r^2+\beta^2\right)\left[\sum_{k=1}^{K}\left(L_k\right)^2\right]}{\left[\sum_{k=1}^{K}\left(\omega_{Ik}L_k\right)^2\right]}>1 \tag{4.9}$$

SIR(D(r)) is greater than SIR(r) because of the resonance frequency is significantly greater than interference frequency, i.e., $\omega_z \gg \omega_{Ik}$. This SIR comparison shows that using the derivative of signal is better than using the original signal in terms of SIR when the signal contains multiple interferences.

4.1.2 Signal differentiation for bearing fault detection from simulated signal with multiple interferences

To illustrate how signal differentiation can help detect bearing fault, we use simulated data based on the following bearing fault model (Liang and Soltani Bozchalooi, 2010):

$$x(t) = \sum_{m=-M}^{M} A_m e^{-\beta(t-mT_p-\tau)} \cos\left(\omega_r \left(t - mT_p - \tau + \theta_m\right)\right) u\left(t - mT_p - \tau\right) \tag{4.10}$$

where A_m is the mth fault impulse, T_p is the time period corresponding to the fault characteristic frequency, β the structural damping characteristic frequency, ω_r the excited resonance frequency, τ represents the effect of random slippage of the rollers and $x(t)$ is the vibration signal containing $2M+1$ fault generated impulse. The sampling frequency is set to 20 kHz. The other parameters are set at A_m=1, β=1500, ω_r =2048 Hz, and T_p =0.008. Fig. 4.2 presents the simulated signal based on Eq. (4.12) and the above parameters.

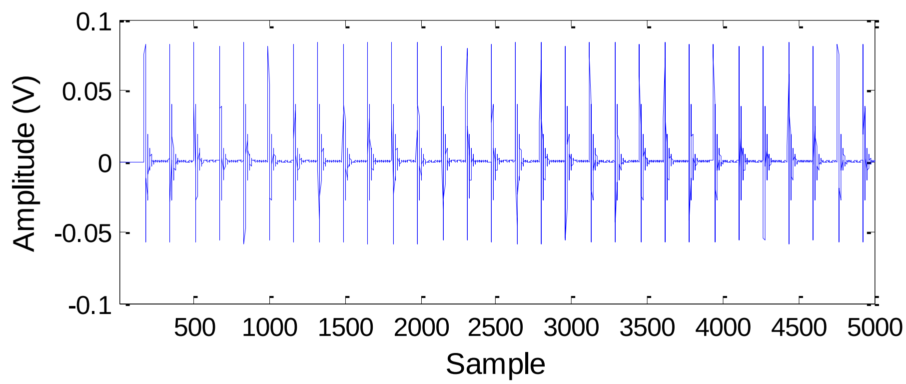

Fig. 4.2. Simulated signal of a faulty bearing.

Multiple vibration interferences with frequencies ω_{in} =5Hz, 27 Hz, 43 Hz, and 60 Hz are added to the simulated signal, rendering the signal mixture as shown in Fig. 4.3(a). The added interference signals can be easily distinguished from spectrum of the signal mixture in Fig. 4.3 (b) and (c) but the fault frequency cannot be seen. The signal-to-interference can be calculated by using fundamental definition of signal-to-noise ratio as follow

$$\text{SIR} = 10\log\frac{\sum x(t)^2}{\sum v(t)^2} \tag{4.11}$$

where $\sum x(t)^2$ and $\sum v(t)^2$ are respectively signal power and interference vibration power. Hence the SIR of the signal mixture in Fig. 4.3(a) is -20 dB. The interference components are added by using MATLAB.

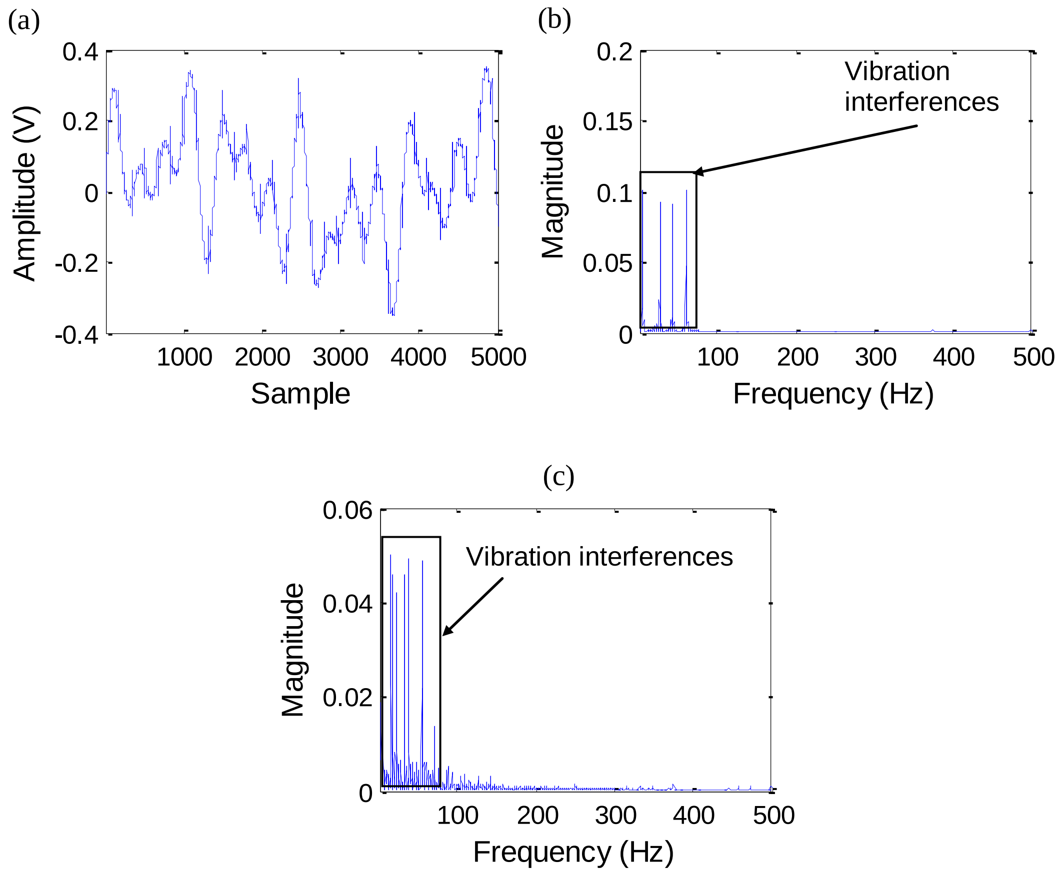

Fig. 4.3. (a) Faulty bearing vibration signal with vibration interferences, (b) the spectrum of the signal mixture, and (c) envelope spectrum of the signal.

The envelope spectrum of the signal difference is plotted in Fig. 4.4 in which the fault frequency and several of its harmonics can be observed clearly but the interferences cannot be easily seen due to the relatively low strength caused by the difference operation. This clearly demonstrates that the fault detectability in the presence of multiple interferences can be substantially improved by signal differentiation.

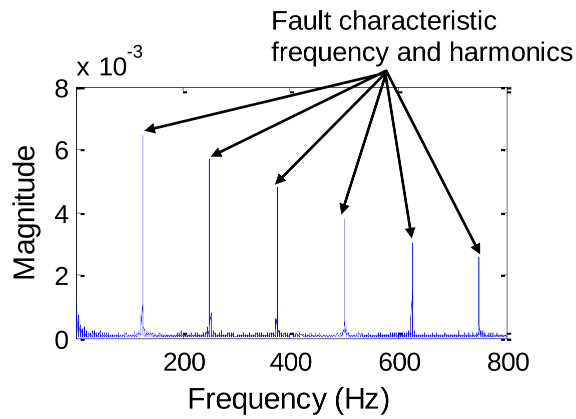

Fig. 4.4. Envelope spectrum of the signal difference.

4.1.3 Effect of signal differentiation on noisy signals

To examine the signal differentiation on noise, we compare the simulated noisy bearing signal in Fig. 4.5(a) and its differentiated version in Fig. 4.5(b). For the simulated signal, the SNR can be calculated by (Yoo et al., 2010)

$$\mathrm{SNR} = 10\log\frac{\sum_{X}|x(t)|^2}{\sum_{X}|ni(t)|^2} \tag{4.12}$$

where $\sum_{X}|x(t)|^2$ and $\sum_{X}|ni(t)|^2$ are, respectively, the estimated signal power and noise power.

Obviously, the relative strength of the noise has been amplified. The SNR has decreased from 10 dB for the signal in Fig. 4.5(a) to 5.5 dB for the signal shown in Fig. 4.5(b). This indicates that differentiation alone is not adequate to satisfy both high SIR and high SNR.

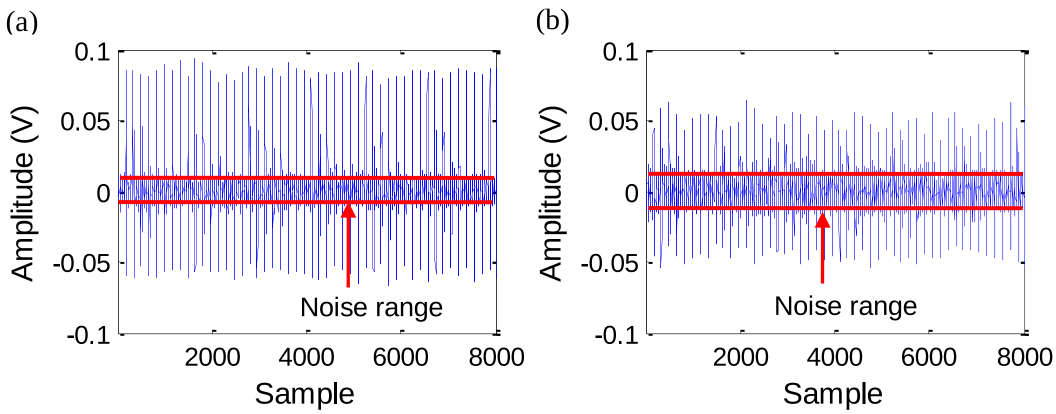

Fig 4.5. (a) The noisy signal of a faulty bearing (SNR = 10 dB), and (b) the signal after applying the differentiation operator (SNR = 5.5 dB).

4.2 The effect of signal integration

In the case of discrete signal, numerical integration should be performed. To save computing time, we simply use the trapezoidal rule for integration, i.e.

$$\mathrm{I}\left(x(n)\right) = \Delta t\left[x(n) + x(n - \Delta t)\right]/2 \tag{4.13A}$$

For the sampled data, we set step Δt=1 and omit the denominator 2 (this will further reduce computing time without affecting the final detection result). Then Eq. (4.13A) reduces to

$$\mathrm{I}\left(x(n)\right) = x(n) + x(n-1) \tag{4.13B}$$

Eq. (4.13B) will be used in the following analyses. Now we examine the effect of signal integration on noise using a simulated signal. The simulated signal with a SNR of 10 dB is shown in Fig. 4.6(a). After signal integration, the SNR has been increased to 12.5 dB with the signal displayed in Fig. 4.6(b). Table 4.1 compares the SNR values of the signals before and after signal integration by using the method of Cohen and Berdugo, (2002). It shows that the SNR has increased by 2.4 to 2.7 dB which is significant in the context of fault detection.

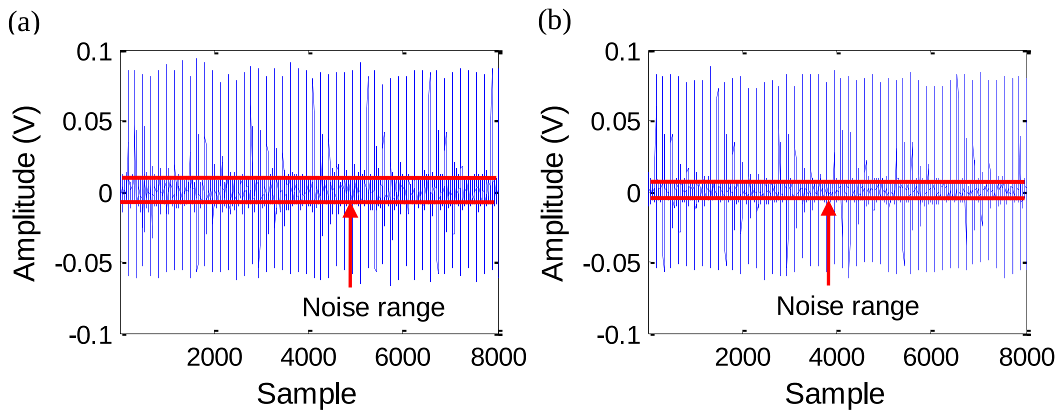

Fig. 4.6. (a) The noisy signal of a faulty bearing, and (b) the signal after integration.

Table 4.1 Comparison of the SNRs before and after signal integration.

SNR (dB) (Raw signal)	**SNR (dB)** (After integration)
10	12.5
12	14.7
15	17.4
17	19.5
20	22.6

4.3 Layer operator

The above discussions have shown that the differentiation can improve the SIR while the integration can enhance SNR. This leads to the development of a new operator called a layer operator (LO) consisting of sequential differentiation and integration operations to take advantages of both. The first order layer operator is defined as

$$\begin{aligned} \mathrm{LO}_1(x(n)) &= \mathrm{I}\left(\mathrm{D}\left(x(n)\right)\right) = \mathrm{I}\left(x(n)-x(n-1)\right) \\ &= \left(x(n)-x(n-1)\right)+\left(x(n-1)-x(n-2)\right) \\ &= x(n)-x(n-2) \end{aligned} \tag{4.14}$$

The first order layer operator is illustrated in Fig. 4.7. As shown in the figure, the layer operator is the backward integration of the differentiation result.

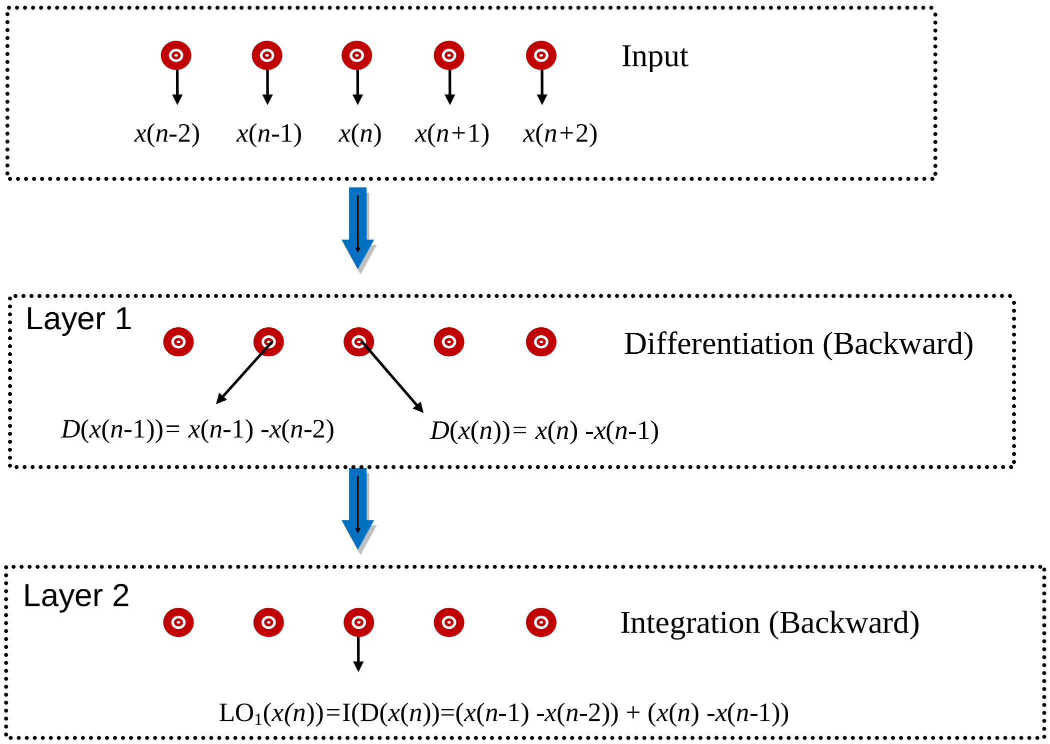

Fig. 4.7. Schematic operation of the layer operator (first order).

The layer operator has a commutative property, i.e., changing the order of differentiation and integration does not affect the result. This is shown by

$$\begin{aligned} \mathrm{LO}_1(x(n)) &= \mathrm{D}\Big(\mathrm{I}\big(x(n)\big)\Big) = \mathrm{D}\big(x(n)+x(n-1)\big) \\ &= \big(x(n)+x(n-1)\big)-\big(x(n-1)+x(n-2)\big) \\ &= x(n)-x(n-2) \end{aligned} \tag{4.15}$$

Similarly, a second order of LO can be defined:

$$\mathrm{LO}_2\big(x(n)\big)=\mathrm{LO}_1\Big(\mathrm{LO}_1\big(x(n)\big)\Big)=x(n)-2x(n-2)+x(n-4) \tag{4.16}$$

It should be emphasized that the differentiation and integration in the layer operator should both be done in one direction, i.e., either both are in backward or both are in forward direction, but not a mixed order.

4.4 The calculus enhanced energy operator

As discussed earlier, the conventional energy operator is sensitive to noise due to the differentiation operation. It is logic to expect that this shortcoming could be mitigated by a new version of the energy operator that incorporating both differentiation and integration. As such, the new energy operator is developed based on the layer operator. As the layer operator incorporates both the differentiation and integration elements, this new energy operator is named calculus enhanced energy operator (CEEO).

Analogous to the conventional energy operator but replacing the first and second order signal derivatives by the first order and second order LO's, we obtain the CEEO as follows:

$$\mathrm{CEEO}\left(x(n)\right)=\mathrm{LO}_1^{\,2}\left(x(n)\right)-\mathrm{LO}_2\left((n)\right)x\left(n\right)=x^2\left(n\right)-x\left(n-2\right)x\left(n+2\right) \qquad (4.17)$$

The flowchart of applying the CEEO for bearing fault detection is shown in Fig. 4.8.

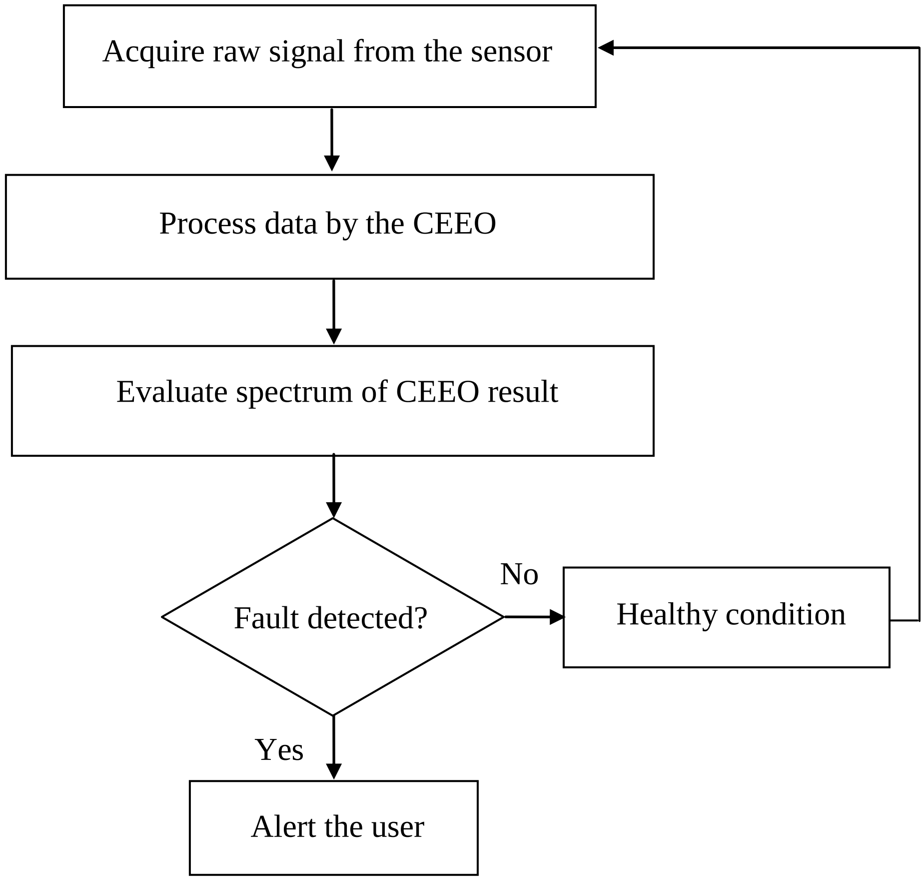

Fig. 4.8. Flowchart of the CEEO method.

4.4.1 Comparison of the CEEO with the conventional energy operator, envelope and ADD methods in handling noise

To examine the noise handling ability of the proposed CEEO, we compare it with the conventional energy operator, enveloping and ADD methods using a simulated signal (Fig. 4.9) blended with noise (No vibration interferences). The initial SNR of raw signal is determined when the signal is directly mixed by a specific power of noise, and final SNR is the signal-to-noise ratio estimation after being processed by an associated method. The comparisons are summarized in Table 4.2.

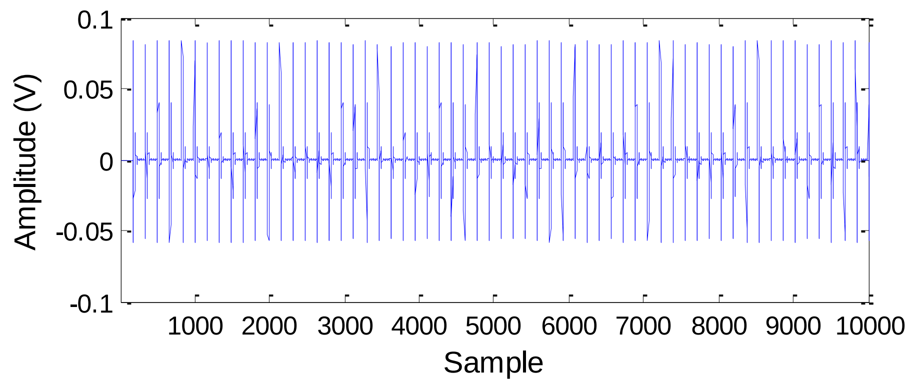

Fig. 4.9. A Simulated of faulty bearing signal.

Table 4.2 Comparison of noise handling capabilities of four methods.

Initial SNR (dB)	Methods	Final SNR (dB)
10 dB	Energy operator method	9.3 dB
	Envelope method	12.1 dB
	CEEO method	14.1 dB
	ADD method	3.9 dB
12 dB	Energy operator method	11.5 dB
	Envelope method	13.9 dB
	CEEO method	16.2 dB
	ADD method	5.5 dB
15 dB	Energy operator method	14.4 dB
	Envelope method	17.0 dB
	CEEO method	19.3 dB
	ADD method	8.2 dB
17 dB	Energy operator method	16.4 dB
	Envelope method	18.9 dB
	CEEO method	21.1 dB
	ADD method	9.8 dB
20 dB	Energy operator method	19.3 dB
	Envelope method	22.0 dB
	CEEO method	24.1 dB
	ADD method	12.4 dB

As shown in Table 4.2, the noise handling capability of the CEEO is much better than the conventional EO with an SNR improvement in the range of 4.7 to 4.9 dB. The CEEO also outperforms the enveloping method by 2.3 to 2.8 dB.

4.5 Simulation evaluation of the CEEO method

In this section, the performance of the CEEO method is further investigated for bearing fault detection using simulation data with ***both*** noise and multiple interferences. Here, we again use the signal with multiple interferences shown in Fig. 4.2 that is generated using Eq. (4.10) with parameters A_m=1, β=1500, ω_r =2048 Hz, and T_p =0.008 and sampling frequency of 20,480 Hz. The fault frequency is $1/T_p$ =125 Hz. To test the CEEO method, the signal is mixed with Gaussian noise (SNR=-15 dB) and four interferences with frequencies ω_{in} =5Hz, 27 Hz, 43 Hz, and 810 Hz respectively to reach an SIR of -20 dB. The signal mixture is shown in Fig. 4.10(a).

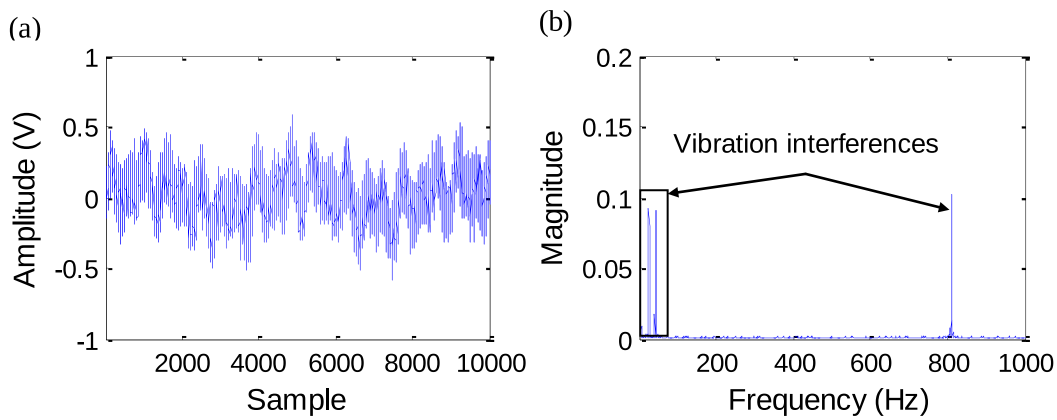

Fig. 4.10. (a) Simulated signal of a faulty bearing with noise and multiple interfering components, and (b) the spectrum of the simulated signal.

Fig. 4.10(b) shows the spectrum of the simulated signal. It can be seen that the interference components and noise dominate the entire spectrum. The results of the enveloping, energy operator and ADD methods for this signal are shown respectively in Figs. 4.11(a), (b) and (c). In Figs. 4.11(a) and (c), the spectra are dominated by the interferences whereas in Fig. 4.11(b) the landscape is masked by heavy noise with some artifacts of the interferences. The fault frequency cannot be easily identified. These are expected because it is known that the amplitude demodulation becomes ineffective in the enveloping method does not work well in the presence of strong interferences and the energy operator method is susceptible to noise.

The proposed CEEO method is then used to process the same data and yields the result of Fig. 4.12. The fault characteristic frequency and its harmonics can be easily recognized, indicating that the CEEO can effectively suppress noise and enhance the detectability of the fault.

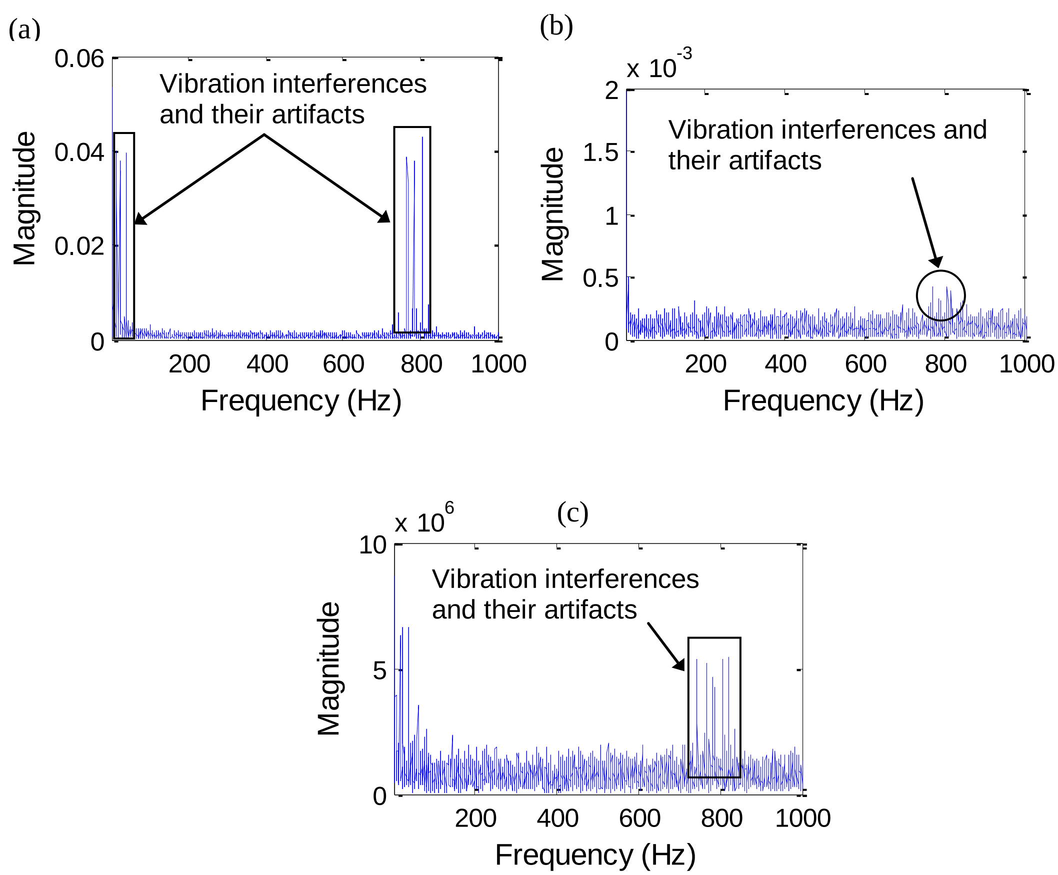

Fig. 4.11. (a) The envelope spectrum of the simulated signal (Fig 4.10(a)), (b) spectrum of the energy operator result of the signal, and (c) spectrum of ADD result of the same signal.

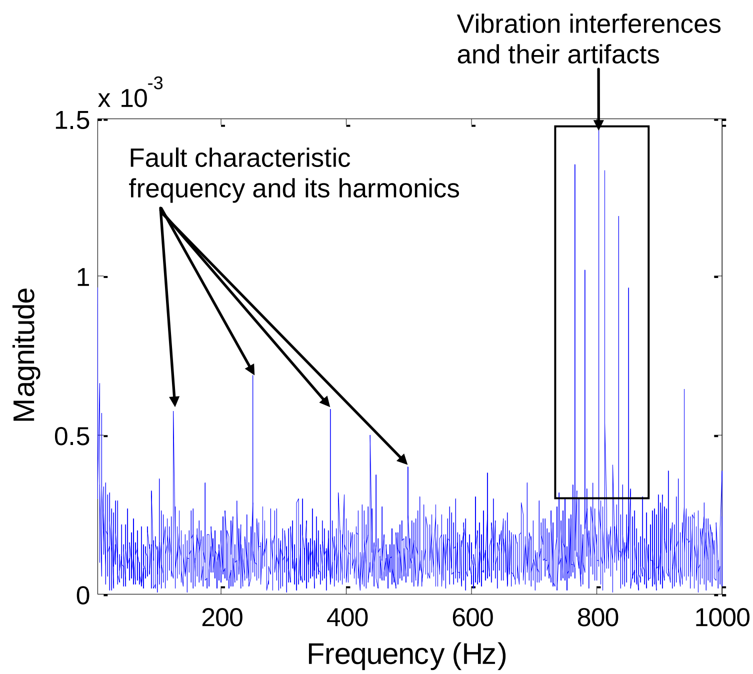

Fig. 4.12. Spectrum of the CEEO result (the raw signal is shown in Fig. 4.10(a).

4.6 Experimental evaluation of the CEEO method

4.6.1 Detection of inner race bearing fault

The experimental setup, test rig, bearing type, accelerometer, and loads are the same as those in section 3.6.1 except that AC Motor 2 is removed (Fig. 4.13). The shaft speed is set at 1503 RPM (25.1 Hz). The right bearing has a pre-seeded fault (created by manufacturer with unknown dimensions) on the inner race with the characteristic frequency of 124.19 Hz (=4.948 f_r, specified in the simulator user's manual).

The gear meshing frequency is 174.1 Hz. To make the situation more complex, white noise (SNR=1dB) is added to both the healthy and faulty bearing signals. The accelerometer is installed on the simulator base at a location away from the bearing but closer to the gearbox and belt pulley (Fig. 4.13). The vibration signal is sampled at 12,000 samples/s. The healthy bearing signal is plotted in Fig. 4.14. The raw signal and its frequency spectrum of the bearing with an inner race fault are shown in Figs. 4.15(a) and (b) respectively. The fault characteristic frequency of 124.19 Hz cannot be detected from Fig. 4.15.

The vibration signal is acquired using an accelerometer and an NI DAQ card. The vibration data is stored in a PC with sampling frequency and other parameters specified by LabVIEW. Signal-processing is carried out using MATLAB on the PC.

Other details of the experiment are as follows:

- Shaft: 5/8” in diameter
- Mass rotors: 2” thick, 4” in diameter and 11.1 lbs each
- Bearings: Type ER10K with eight roller elements (balls). The inside, outside, pitch and ball diameters are respectively 0.625”, 1.8500”, 1.3190” and 0.3125”.
- Accelerometer: PCB sensor, model 623C01 with sensitivity of 100 Mv/g and a sensitivity range of 1 Hz to 20 kHz.
- PWM Hitachi drive: SJ200-022NFU.
- DAQ card: NI PCI-6132 multi-function.
- PC: Pentium 4 of 2.52 GHz speed.

The envelope spectrum of the raw signal, and the spectra of the energy operator and ADD processed results of the same signal are shown in Figs. 4.16(a), (b) and (c) respectively. In all the three cases, the fault signature cannot be easily observed. The CEEO result is presented in Fig. 4.17 where the fault characteristic frequency at 124.19 as well as two of its harmonics at 248.3 and 372.5 Hz can be clearly seen. This suggests that the CEEO method is more effective than the enveloping and conventional energy operator methods in detecting inner race fault in the presence of both noise and interferences.

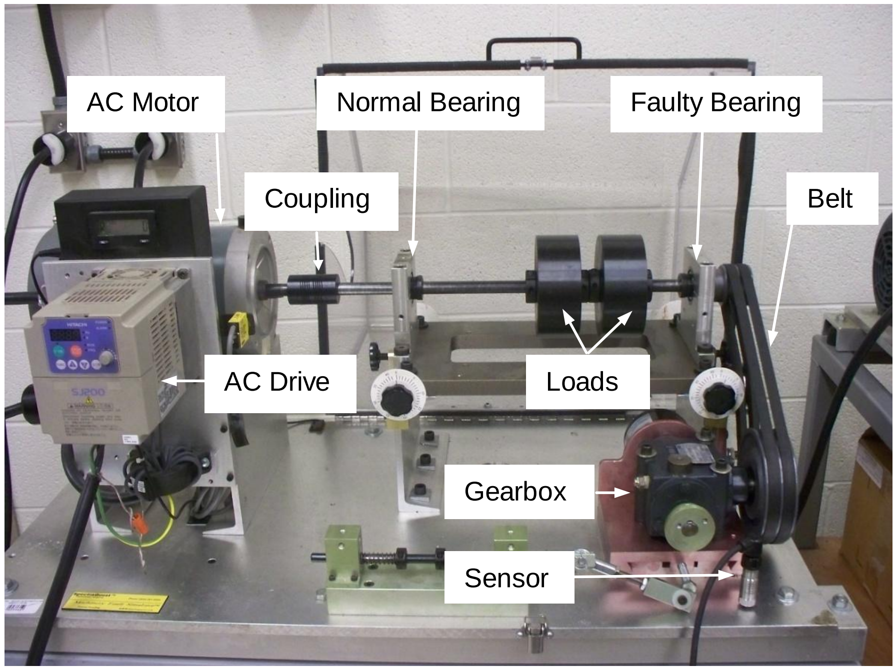

Fig. 4.13. Experimental setup #1 (inner race fault).

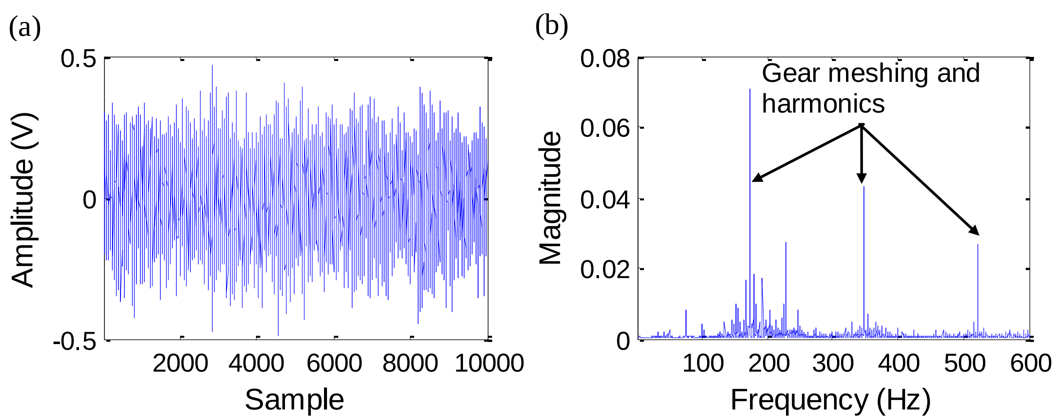

Fig. 4.14. (a) A part of the measured signal of a healthy bearing, and (b) the spectrum of the signal (Experimental setup #1).

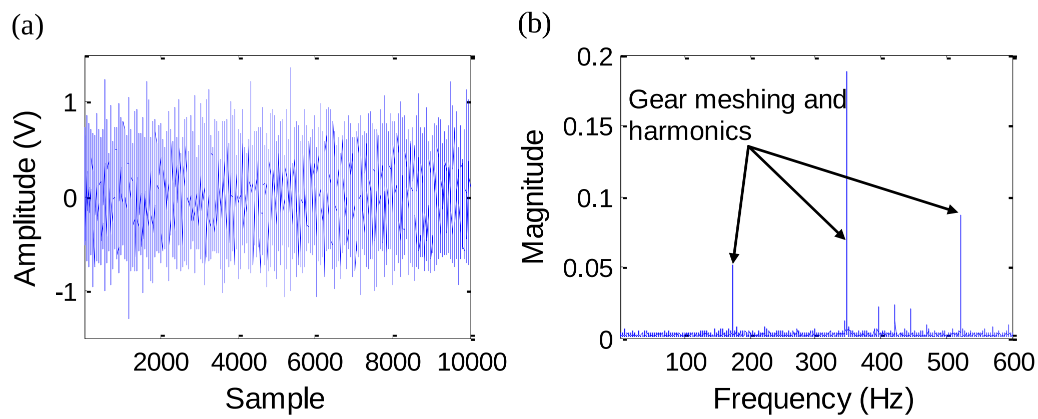

Fig. 4.15. (a) A part of the measured signal of inner race fault from Experimental setup # 1, and (b) the spectrum of a faulty bearing signal.

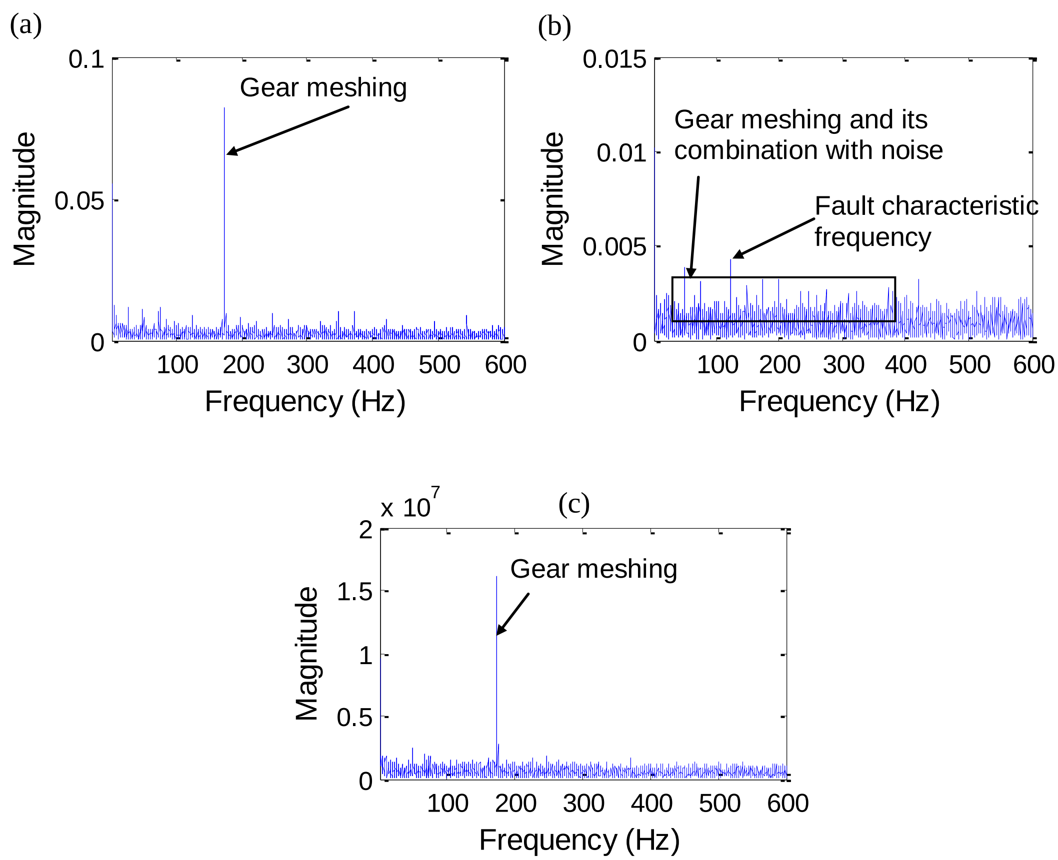

Fig. 4.16. (a) Envelope spectrum of the same faulty bearing signal shown in Fig. 4.15(a), (b) the spectrum of the energy operator result, and (c) spectrum of the ADD method.

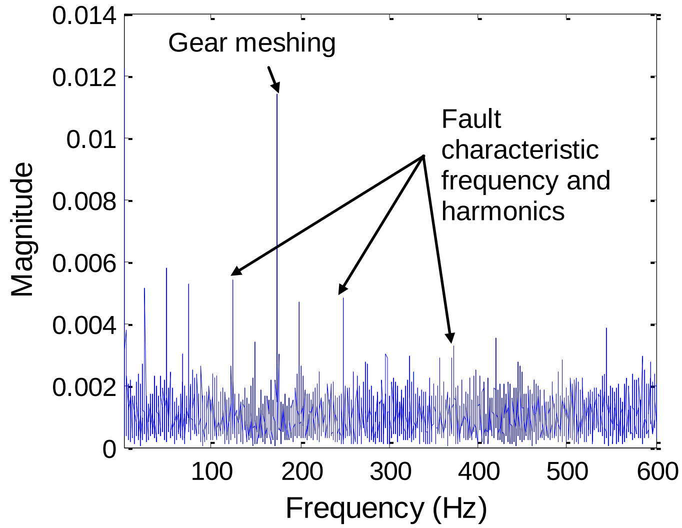

Fig. 4.17. Spectrum of the faulty bearing signal (shown in Fig. 4.15(a)) obtained by the CEEO method.

4.6.2 Detection of outer race bearing fault

In this test the inner race faulty bearing is replaced by one (also type ER10K) with an outer race fault on the right side of shaft, and a single balanced load rotor (2” thick, 4” in diameter and 11.1 lb) is mounted on the same shaft. Like in the previous experiment, the gearbox is driven by the shaft through a belt connection and the accelerometer is installed on the simulator base at a location close to the belt pulley and the gearbox but far from the bearing. The setup is shown in Fig. 4.18. The shaft speed is set at 990 RPM (16.5 Hz). The outer race fault is created by the manufacturer with unknown dimensions. The outer race fault characteristic frequency is 50.5 Hz (=3.052 f_r,, specified in the simulator user’s manual). The meshing frequency of gearbox associated with the above shaft speed is 116.2 Hz. The reference healthy bearing signal and spectrum are displayed in Fig. 4.19(a) and (b) respectively. Figs. 4.20(a) and (b) respectively present the raw signal of the faulty bearing and its spectrum. Figs. 4.19(b) and 4.20(b) are almost identical and thus the outer race fault cannot be detected by looking at the FFT result.

The envelope spectrum of the raw signal, the spectra of the signal processed by the conventional energy operator and ADD methods are shown in Figs. 4.21(a), (b), and (c). The three figures are dominated by the meshing frequency and noise while the fault signature can be barely seen in the enveloping result. Fig. 4.22 presents the spectrum of the CEEO result in which the fault frequency at 50.54 Hz as well as two of its associated harmonics at 101.08, 151.6, can be clearly distinguished. This once again demonstrates that the proposed CEEO method performs better than both the enveloping and conventional energy operator approaches.

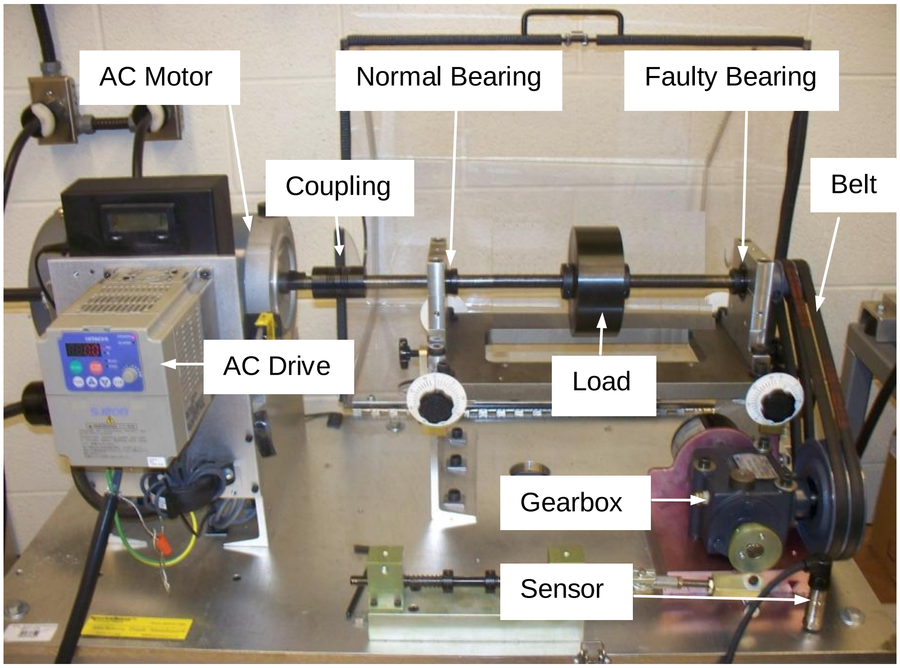

Fig. 4.18. Experimental setup #2 (outer race fault).

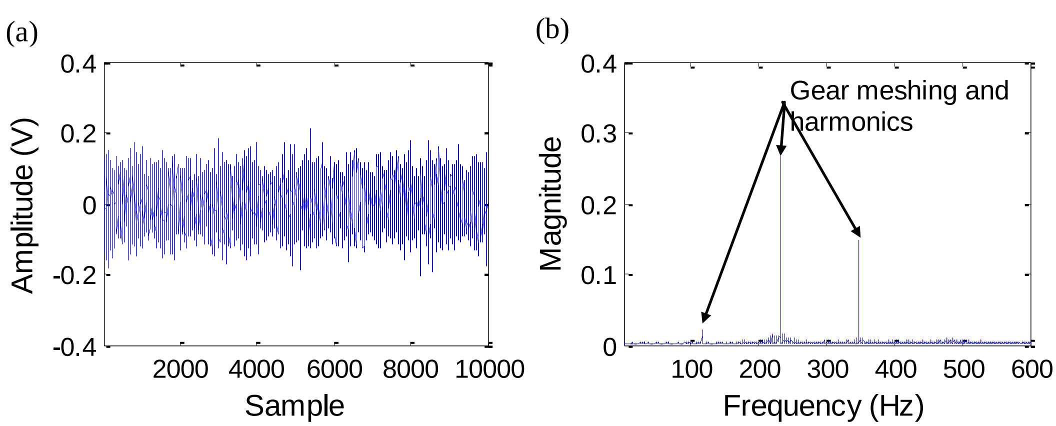

Fig. 4.19. (a) A part of the measured healthy bearing signal, and (b) the spectrum of a healthy signal (Experimental setup #2).

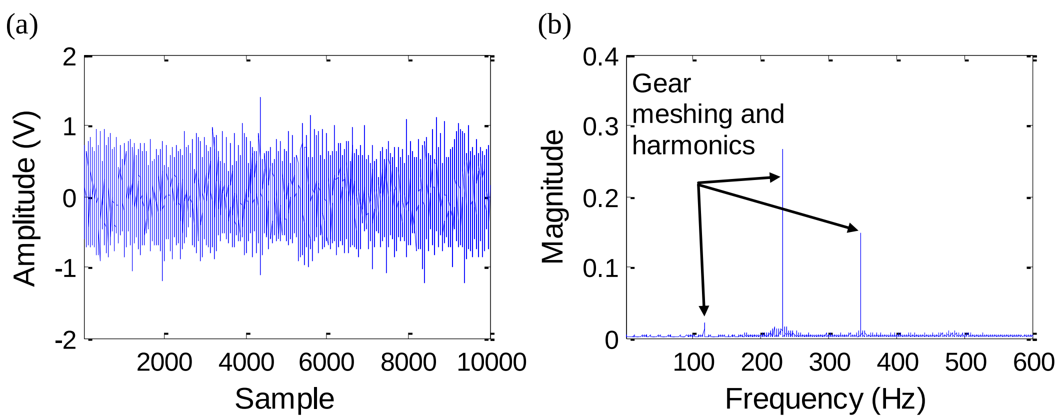

Fig. 4.20. (a) A part of the measured signal of outer race fault from Experiment # 2, and (b) the spectrum of the faulty bearing signal.

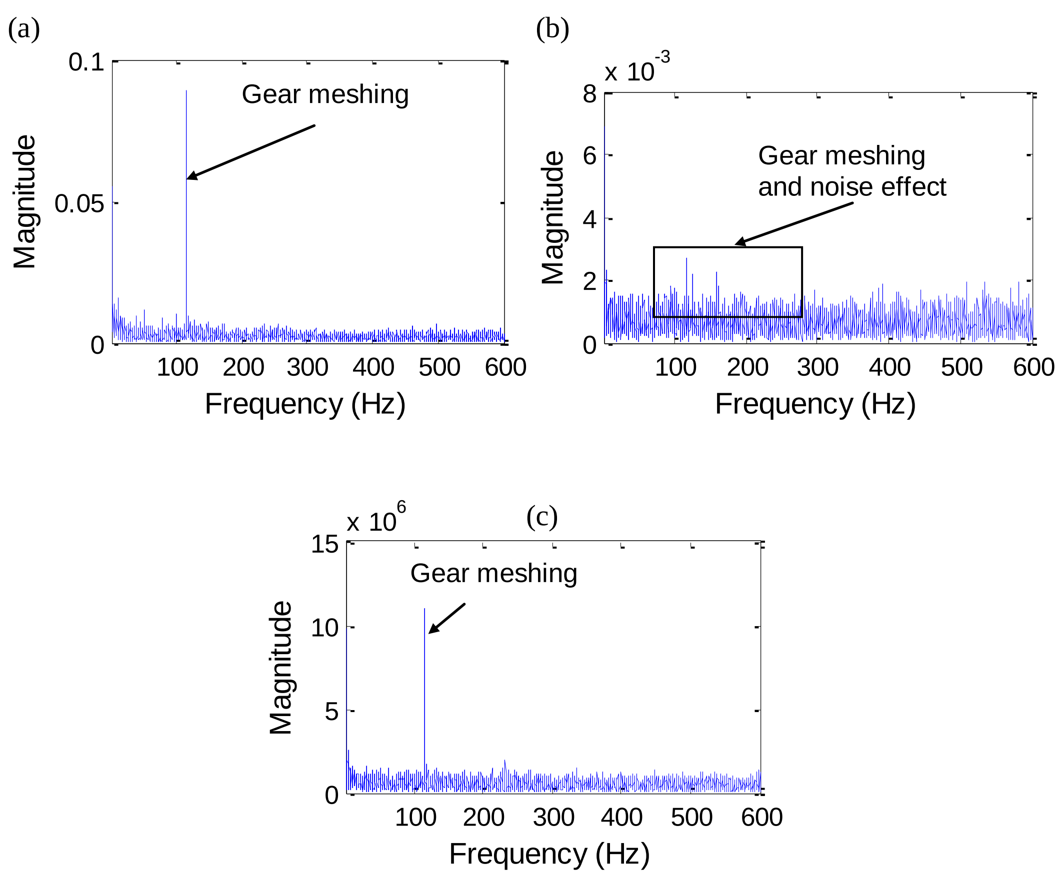

Fig. 4.21. (a) Envelope spectrum of the faulty bearing signal (shown in Fig. 4.20(a)), (b) the spectrum of the energy operator result of the same raw signal, and (c) spectrum of the ADD method.

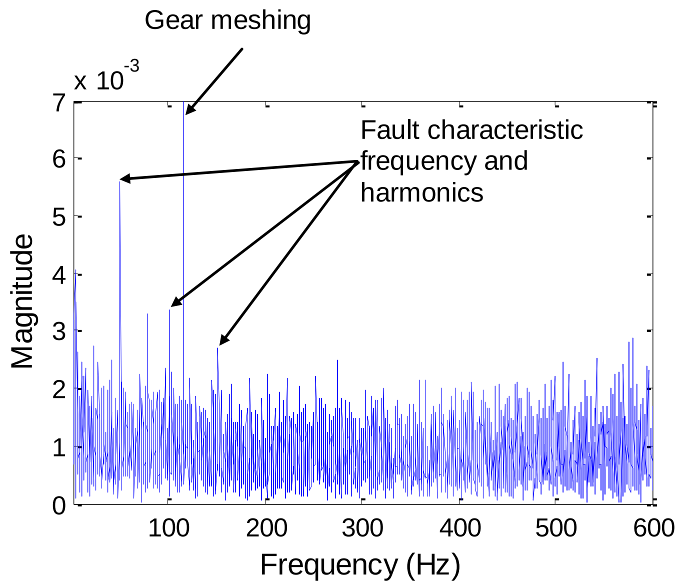

Fig. 4.22. Spectrum of the CEEO processed faulty bearing signal.

4.6.3 Experimental evaluation using the experimental data from Case Western Reserve University

The proposed method is further tested using the data from the Bearing Data Center of the Case Western Reserve University. The fault was created by Electro-Discharge Machining (EDM).

4.6.3.1 Inner race fault detection

The experiment related information is summarized in Table 4.3.

Table 4.3 Specifications of the Case Western Reserve University experiments (for inner race fault)

Inner diameter	0.9843”	Motor load	1 HP
Outer diameter	2.0472”	Sampling frequency	12,000 samples/sec
Pitch diameter	1.5370”	BPFI	5.4152f_r Hz
Fault diameter	0.007”	Shaft speed	1772 rpm
Fault depth	0.011”		

The CEEO method can reveal the fault characteristic frequency at 159.93.85 Hz (=(1772/60)×5.4152), and its associated harmonics at 319.86 Hz, 479.79 Hz, 639.72 Hz, 799.65 Hz, and 959.58 Hz as shown in Fig 4.24. However, the faulty features cannot be detected from spectrum of the raw signal in Fig 4.23(b).

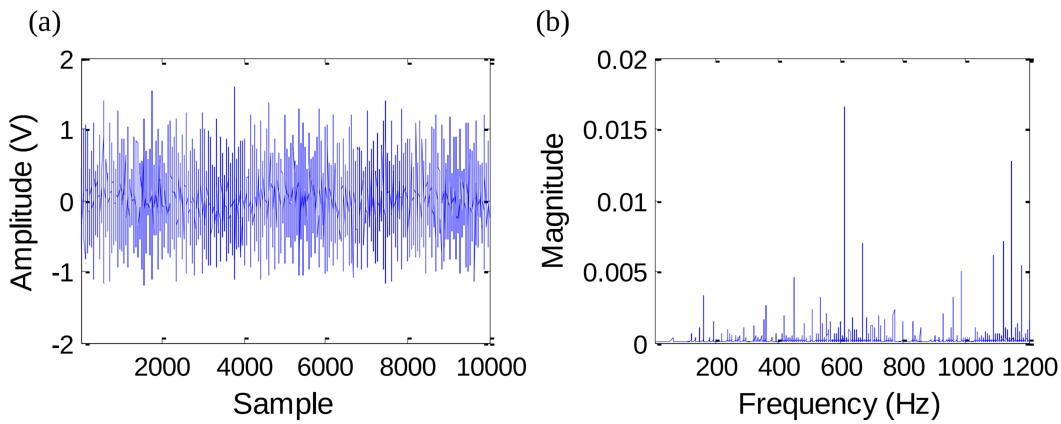

Fig 4.23. (a) A portion of the measured inner race fault signal, and (b) the spectrum of the signal.

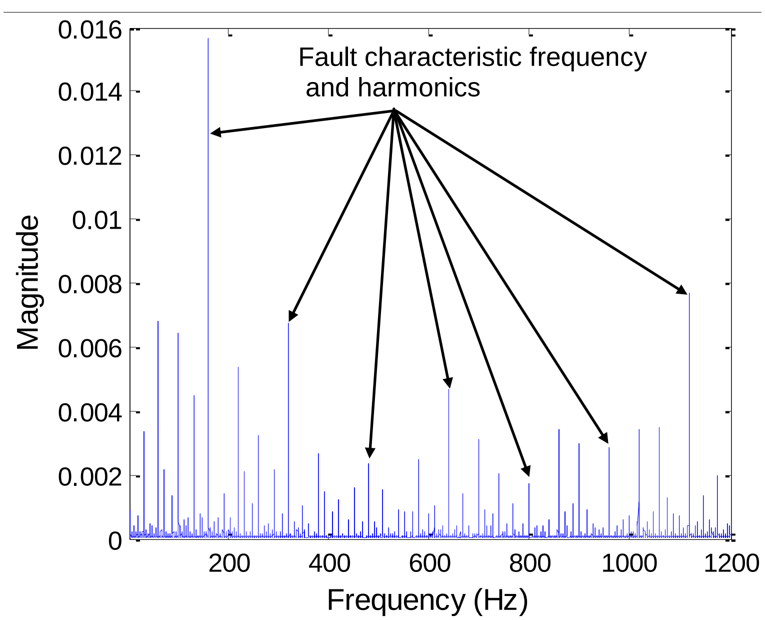

Fig 4.24. Envelope spectrum of the raw signal after applying the proposed method.

4.6.3.2 Outer race fault detection

The fault size, shaft speed, and load for out race fault test are the same as those specified for the inner race fault; related experimental information is summarized in Table 4.2. The fault is at 6:00 o'clock position.

Table 4.4 Specification of the Case Western Reserve University experiments (for outer race fault)

Inner diameter	0.9843"	Motor load	2 HP
Outer diameter	2.0472"	Sampling frequency	12,000 samples/sec
Pitch diameter	1.5370"	BPFO	3.5848 f_r Hz
Fault diameter	0.007"	Shaft speed	1750 rpm
Fault depth	0.011"		

The raw signal of faulty bearing and its spectrum are shown in Fig 4.25. With the proposed method, the fault characteristic frequency at 104.556 Hz (=(1750/60)×3.5848), and its associated harmonics at 209.11 Hz, 313.67 Hz, 418.22 Hz, 522.78 Hz, 627.34 Hz, 731.89 Hz, 836.45 Hz, and 941 Hz can be easily detected. The result is shown in Fig 4.26.

The above results once again demonstrated the effectiveness of the proposed method in detecting both inner and outer race faults, even when the fault size is very small (0.007" in diameter).

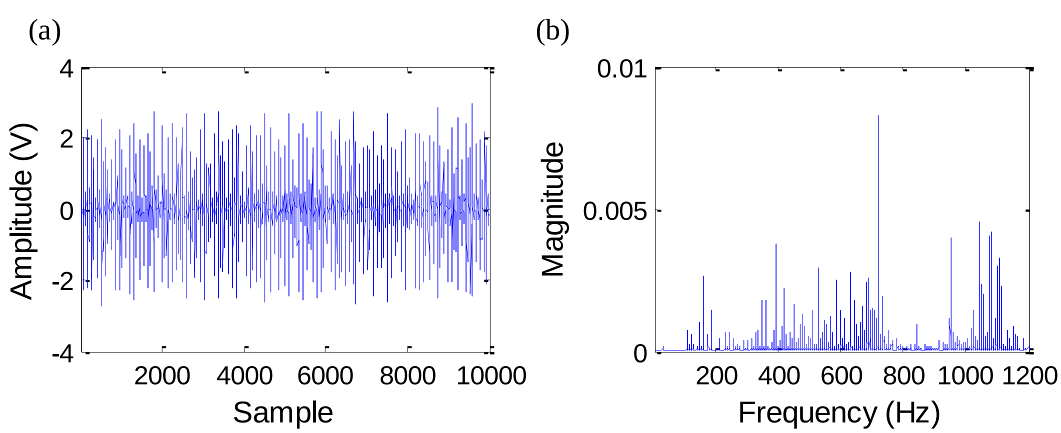

Fig 4.25. (a) A portion of the measured signal of outer race fault, and (b) the spectrum of signal.

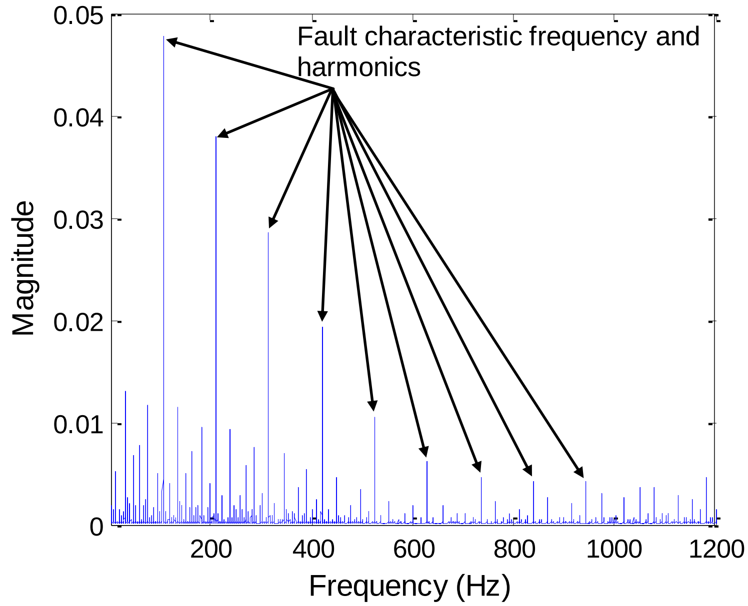

Fig 4.26. Envelope spectrum of the raw signal after applying the proposed CEEO method.

4.7 Conclusion

In this chapter, it has been demonstrated that SIR can be improved by differentiation and SNR can be boosted by integration. However, using differentiation alone leads to amplified noise level whereas applying only integration may diminish the impulsiveness of the fault signal. As such, the two are jointly applied to develop a calculus enhanced energy operator to take advantage of both differentiation and integration for improved SIR as well as SNR. In the form of an energy operator, the proposed method is also fast since it requires only three points of data and easy to implement because of its structural simplicity. The performance of the CEEO method has been compared favourably with the enveloping and the conventional energy operator methods using simulated data. The effectiveness of the CEEO method is further confirmed in detecting both inner and outer race faults from our experimental data and the data from the literature.

Chapter 5

A higher order analytic energy operator (HO_AEO) approach to extraction of bearing fault signature from heavily contaminated signals[3]

Though the CEEO method can improve signal-to-noise ratio, it cannot enhance the signal in comparing with conventional energy operator in the presence of high level interfering components. On the other hand, the ADD method shows reasonable ability to improve signal-to-interference ratio. Therefore, we need to propose a new non-parametric, non-filtering approach with superior capability of dealing with intense noise and interfering components for bearing fault detection simultaneously. The major work in this chapter is derived based on the following observations:

- The analytic energy operator will be introduced based on exploiting the information in both the real and imaginary part of the analytic signal and is hence named analytic energy operator (AEO). It is well suited for detecting the impulsive signatures from faulty bearing signals as it can extract both the amplitude and frequency modulations.
- The higher orders of the analytic energy operator can boost the signal-to-interference ratio due to differentiation characteristic. However, higher orders transformation cause to intensify high frequency noise.

[3] See Appendix B.3 for MATLAB script.

- A joint use of multiple higher order AEOs can boost the signal-to-interference and signal-to-noise ratio at the same time, because each higher order can be considered as a distinct transformation with individual effect on noise and vibration interference level.

Therefore, we further propose to use the combination of multiple higher order AEOs to better handle noise by offsetting the effects of positive and negative amplitude noise. With the proposed higher order analytic energy operator (HO_AEO), the filtering and enveloping steps are eliminated.

It is illustrated that the proposed method can effectively boost the signal-to-interference ratio (SIR) and signal-to-noise ratio (SNR). The proposed method is also parameter-free and filter-free. Unlike the HFR techniques, it does not require the information of resonance excited by bearing faults. Moreover, it is simple and computationally efficient and therefore is suited for on-line applications.

The principal work in this chapter is summarized as follows:

- Mathematical expansion of analytic energy operator for a faulty bearing signal with multiple vibration interferences, and mathematical assessment in terms of SIR.
- Development of higher order AEOs and show its capability to reduce effect of vibration interference.
- Development of the HO_AEO technique and comparison ofare it with the conventional energy operator in terms of SIR.
- Performance evaluation of HO_AEO method using both simulated and experimental data.

5.1 Analytic energy operator

According to the analytic signal theory, an acquired vibration signal from bearing, gearbox, and different components of a system can be transformed into a new function by applying the Hilbert transform. Furthermore, the analytic of a signal can be represented as the amplitude demodulation, and instantaneous frequency to reveal some characteristics of the signal. The Hilbert transform provides an imaginary translation of a signal. A new contribution between real part and imaginary part of signal attributes to a new operator, namely analytic energy operator. The analytic energy operator retains functional characteristics such as amplitude demodulation and phase demodulation.

For a simple representation and better understanding of the analytic energy operator, consider a simple mono-component signal as follows

$$z(t) = U(t)\cos(\eta(t)) \tag{5.1}$$

The analytical form of the signal is

$$Z(t) = z(t) + i\hat{z}(t) \tag{5.2}$$

With its exponential form as follow

$$Z(t) = U(t)\exp(i\eta(t)) \tag{5.3}$$

where $U(t)$ represents amplitude of envelope or amplitude-modulation, $\eta(t)$ is instantaneous phase or phase-modulation. The function $\hat{z}(t)$, i.e., the imaginary part of the analytic form of the signal is defined as the Hilbert transform of signal $z(t)$ (Feldman, 1994a, 1994b, 2011; Potamianos and Maragos, 1994)

$$\hat{z}(t) = H(z(t)) = \frac{1}{\pi t} * z(t) = \frac{1}{\pi}\int_{-\infty}^{+\infty} \frac{z(\tau)}{t-\tau}\,\mathrm{d}\tau \tag{5.4}$$

A new operator can be developed as a difference between the product of the derivative and Hilbert transform of the signal, and the product of the signal and the derivative of its Hilbert transform, i.e.,

$$\mathrm{S}(z(t)) = z'(t)\hat{z}(t) - \hat{z}'(t)z(t) \tag{5.5}$$

As the new operator explores the information of both the real and imaginary parts of the signal, it is named analytic energy operator (AEO). The rationale of this new operator lies in:

a) in the presence of interferences, the relative strength of the impulsive signal component can be enhanced by differentiating the signal, though the enhancing effect may be adversely affected by heavy noise; b) as illustrated later, the AEO has can extract both amplitude and frequency modulations, thus making it suited to the detection of impulsive fault signatures and eliminating the enveloping step required by many HFR methods; and c) both the amplitude demodulation (AD) and frequency demodulation (FD) capability inherent in the analytic energy operator have certain noise reduction ability (Reed, 2005). As a result, the combined effect of differentiation and AD/FD can boost the detectability of the impulsive fault signature in the presence of both noise and interferences.

Here we illustrate that the analytic energy operator has the AD and FD effects by applying it to the signal $z(t)$ in the form of Eq. (5.5):

$$\begin{aligned} \mathrm{S}(z(t)) &= \left[U(t)\cos(\eta(t))\right]\left[U'(t)\sin(\eta(t)) + \eta'(t)U(t)\cos(\eta(t))\right] \\ &\quad - \left[U(t)\sin(\eta(t))\right]\left[U'(t)\cos(\eta(t)) - \eta'(t)U(t)\sin(\eta(t))\right] \\ &= U^2(t)\eta'(t) \end{aligned} \tag{5.6}$$

where $U^2(t)$ is squared of amplitude-modulation, and $\eta'(t)$ represents frequency-modulation

According to Eq. (5.6), the analytic energy operator contains information of both the amplitude-modulation (AM) and frequency-modulation (FM), which is important for the extraction of transient impulses associated with the bearing faulty. In the next three sections we illustrate the noise and interference handling capabilities of the analytic energy operator.

5.2 Mathematical expression of the analytic energy operator for a faulty bearing signal with multiple vibration interferences

To examine the interference handling ability of the analytic energy operator, we derive its explicit mathematical expression for a faulty bearing signal containing multiple interferences. The vibration model of a faulty bearing with multiple interference components used same bearing model as shown in Eq. (3.2) and present it below to facilitate discussions (Bozchalooi and Liang, 2009; Liang and Soltani Bozchalooi, 2010):

$$r(t) = x(t) + v(t) = Ae^{-\beta(t)} \cos(\omega_r t + \varphi) + \sum_{k=1}^{K} L_k \cos \omega_{Ik} t \tag{5.7}$$

where A is the amplitude of the fault signal, β is the structural damping characteristic frequency, ω_r is the frequency of the excited resonance, ω_{Ik} represents the frequency of kth interference component, L_k denotes the amplitude of the kth interference component, $x(t)$ is the vibration signal containing the fault generated impulses, and $v(t)$ represents multiple vibration interferences. Once again, it is reasonable to assume that the excited resonance frequency is much higher than interference signal frequency ω_{Ik} for all k's.

The analytical version of the signal is

$$\text{Analytic}(r(t)) = r(t) + i\hat{r}(t) = \text{Re}(t) + i\,\text{Im}(t) \tag{5.8}$$

where $\hat{r}(t)$ is the Hilbert transform of signal $r(t)$, Re(t) (= $r(t)$) and Im(t)(= $\hat{r}(t)$) are respectively the real and imaginary parts of the analytical signal. Eq. (5.8) can be expanded as

$$\begin{aligned}\text{Analytic}(r(t)) = &\left[Ae^{-\beta t} \cos(\omega_r t + \varphi) + \sum_{k=1}^{K} L_k \cos \omega_{Ik} t \right] \\ &+ i\left[Ae^{-\beta t} \sin(\omega_r t + \varphi) + \sum_{k=1}^{K} L_k \sin \omega_{Ik} t \right]\end{aligned} \tag{5.9}$$

The analytic energy operator is defined as

$$\text{S}(r(t)) = \text{Re}'(r(t))\,\text{Im}(r(t)) - \text{Im}'(r(t))\,\text{Re}(r(t)) \tag{5.10}$$

To represent the first order of the analytic energy operator, the derivatives of the real part (i.e., the raw signal) of Eq. (5.9) and the imaginary part (i.e., the Hilbert transform of the raw signal) of Eq. (5.9) are respectively obtained as follows

$$\text{Re}'(t) = -\beta Ae^{-\beta t} \cos(\omega_r t + \varphi) - \omega_r Ae^{-\beta t} \sin(\omega_r t + \varphi) - \sum_{k=1}^{K} L_k \omega_{Ik} \sin \omega_{Ik} t \tag{5.11}$$

$$\mathrm{Im}'(t) = -\beta A e^{-\beta t} \sin\left(\omega_r t + \varphi\right) + \omega_r A e^{-\beta t} \cos\left(\omega_r t + \varphi\right) + \sum_{k=1}^{K} L_k \omega_{Ik} \cos \omega_{Ik} t \tag{5.12}$$

According to the result of the imaginary and the real parts of the signal as expressed by Eqs. (5.9), (5.11) and (5.12), the expression of the analytic energy operator for a signal with multiple interferences is obtained as

$$\begin{aligned} \mathrm{S}\left(r\left(t\right)\right) &= \left(A^2 \omega_r\right) e^{-2\beta t} - \sum_{k=1}^{K} \left(A\beta L_k\right) e^{-\beta t} \sin\left(\left(\omega_r - \omega_{Ik}\right) t + \varphi\right) \\ &+ \sum_{k=1}^{K} \left(A\omega_r L_k + A\omega_{Ik} L_k\right) e^{-\beta t} \cos\left(\left(\omega_r - \omega_{Ik}\right) t + \varphi\right) + \sum_{k=1}^{K} L_k^2 \omega_{Ik} \\ &= \left(A^2 \omega_r\right) e^{-2\beta t} + c_1\left(t\right) e^{-\beta t} + \sum_{k=1}^{K} L_k^2 \omega_{Ik} \end{aligned} \tag{5.13}$$

where $c_1(t)$ is given below

$$\begin{aligned} c_1\left(t\right) &= \sum_{k=1}^{K} \left(A\omega_r L_k + A\omega_{Ik} L_k\right) \cos\left(\left(\omega_r - \omega_{Ik}\right) t + \varphi\right) \\ &- \sum_{k=1}^{K} \left(A\beta L_k\right) \sin\left(\left(\omega_r - \omega_{Ik}\right) t + \varphi\right) \end{aligned}$$

As shown above, the analytic energy operator transformed faulty bearing signal with multiple interferences consists of three terms. The first term is an amplitude-demodulated term denoted by ADM. The second are high-frequency components. The third term represents interfering components. The first term $A^2\omega_r$, the squared envelope scaled by a factor of ω_r at the fault impulse, illustrates that the analytic energy operator can amplitude demodulate the fault signature in the presence of multiple vibration interferences.

5.3 Interference handling capability of the AEO

With the above result, the interference handling capability of the analytic energy operator can be assessed by comparing the signal-to-inference ratios of the raw signal and of the AEO processed signal.

The SIR of a faulty bearing signal with multiple interferences can be defined as (reproduced from Eq. (3.11) for convenience) (Bozchalooi and Liang, 2009; Liang and Soltani Bozchalooi, 2010)

$$\mathrm{SIR}\left(r\right)=\frac{\left(1/T\right)\int_{0}^{T}x^{2}\left(t\right)\mathrm{d}t}{\left(1/T\right)\int_{0}^{T}\sum_{k=1}^{K}v_{k}^{2}\left(t\right)\mathrm{d}t}=\frac{P_{x}}{P_{v}} \tag{5.14}$$

where $x(t)$ is the faulty bearing impulse signal, and $\sum_{k=1}^{K}v_{k}\left(t\right)$ represents the multiple vibration interferences.

Referring to Eqs. (5.7) and (5.14), one obtains the signal-to-interference ratio of the raw signal of the faulty bearing with multiple periodic interference components as

$$\mathrm{SIR}\left(r\left(t\right)\right)=\frac{\left(\frac{1}{T_{P}}\right)\int_{0}^{T_{P}}A^{2}e^{-2\beta t}\cos^{2}\left(\omega_{r}t+\varphi\right)\mathrm{d}t}{\left(\frac{1}{T_{k}}\right)\sum_{k=p+1}^{K}\int_{0}^{T_{k}}L_{k}^{2}\cos^{2}\left(\omega_{Ik}t\right)\mathrm{d}t} \tag{5.15}$$

where T_k is the time period corresponding to k^{th} element of vibration interference, and T_p is the time period associated with fault characteristic frequency.

Eq. (5.15) leads to

$$\mathrm{SIR}\left(r\left(t\right)\right)=\frac{A^{2}}{2T_{P}\beta\sum_{k=1}^{K}L_{k}^{2}}+\frac{A^{2}\left(\beta\cos 2\varphi-\omega_{r}\sin 2\varphi\right)}{2T_{P}\left(\omega_{r}^{2}+\beta^{2}\right)\sum_{k=1}^{K}L_{k}^{2}} \tag{5.16}$$

One can then evaluate Eq. (5.16) for limiting cases

Case (1) $\omega_r \approx \beta$:

$$\mathrm{SIR}\left(r\left(t\right)\right)=\frac{3A^{2}}{4T_{P}\beta\sum_{k=1}^{K}L_{k}^{2}} \tag{5.17A}$$

and case (2) $\omega_r \gg \beta$:

$$\mathrm{SIR}\left(r\left(t\right)\right)=\frac{A^2}{2T_P\beta\sum_{k=1}^{K}L_k^2} \tag{5.17B}$$

From Eqs. (5.13) and (5.14), the signal-to-interference ratio of the AEO processed signal is

$$\mathrm{SIR}\left(\mathrm{S}\left(r\left(t\right)\right)\right)=\frac{\left(\frac{1}{T_P}\right)\int_0^{T_P}A^4\omega_r^2e^{-4\beta t}\,\mathrm{d}t}{\left(\frac{1}{T_k}\right)\sum_{k=1}^{K}\int_0^{T_k}L_k^4\omega_{Ik}^2\,\mathrm{d}t} \tag{5.18}$$

After simplification of the integral calculation, Eq. (5.18) becomes

$$\mathrm{SIR}\left(\mathrm{S}\left(r\left(t\right)\right)\right)=\frac{A^4\omega_r^2}{4T_P\beta\sum_{k=1}^{K}L_k^4\omega_{Ik}^2} \tag{5.19}$$

As the resonance frequency is substantially higher than those of the interference components, i.e., $\omega_r \gg \omega_{Ik}$, then from Eqs. (5.17) and (5.19), SIRs of raw signal and AEO processed version can be compared as follows:

$$\frac{\sum_{k=1}^{K}A^2L_k^2\omega_r^2}{3\sum_{k=p+1}^{K}L_k^4\omega_{Ik}^2}<\frac{\mathrm{SIR}\left(\mathrm{S}\left(t\right)\right)}{\mathrm{SIR}\left(r\left(t\right)\right)}<\frac{\sum_{k=1}^{K}A^2L_k^2\omega_r^2}{2\sum_{k=p+1}^{K}L_k^4\omega_{Ik}^2} \tag{5.20}$$

To illustrate, suppose $L_k=L=3A$, $\omega_r=10\omega_{Ik}$ and $K=5$. Then we have $3.7<\mathrm{SIR}(\mathrm{S}(t))/\mathrm{SIR}(r(t))<5.5$. As a result, the analytic energy operator can enhance the signal effectively in many cases. However, this SIR improvement alone may not be sufficient in the presence of very strong vibration interferences. Hence, higher orders of the analytic energy operator will be considered to further improve the signal-to-interference ratio. As the analytic energy operator is based on differentiation, the derivation operators in higher orders decrease the effect of vibration interferences but increase noise level at the same time, particularly the level of high frequency noise which is obviously undesirable for bearing defect detection. Therefore, to tackle the noise problem, we jointly employ multiple higher order analytic energy operators such that the effects of the positive and negative noise values can be offset to a certain degree.

5.4 The higher order analytic energy operator (HO_AEO) method

In this section, the higher order analytic energy operators are first introduced in both continuous and discrete forms. The noise handling capability of the HO_AEO method is then examined. Its interference handling ability is also evaluated and compared with that of the EO method.

5.4.1 Expression of the HO_AEO

The continuous form of the first order analytic energy operator has been defined in Eq. (5.10). Its discrete version in the forward format is

$$S_1\left(r(n)\right)=\mathrm{Re}(n+1)\,\mathrm{Im}(n)-\mathrm{Im}(n+1)\,\mathrm{Re}(n) \tag{5.21}$$

where the real part of signal is represented by Re and the imaginary part of signal is denoted by Im. For simplicity, we omitted $r(\cdot)$ and replace $\mathrm{Re}(r(n))$ by $\mathrm{Re}(n)$, and $\mathrm{Im}(r(n))$ by $\mathrm{Im}(n)$. The second order analytic energy operator is expressed in terms of the second derivatives of the signal and its Hilbert transform, i.e.

$$S_2\left(r(t)\right)=\mathrm{Re}^{(2)}\left(r(t)\right)\mathrm{Im}\left(r(t)\right)-\mathrm{Im}^{(2)}\left(r(t)\right)\mathrm{Re}\left(r(t)\right) \tag{5.22}$$

The discrete form of the second order analytic energy operator is expressed as a combination of real and imaginary parts of the analytic signal, their two-point shifted versions, and the first order AEO, i.e.,

$$\begin{aligned} S_2\left(r(n)\right)&=\left[\mathrm{Re}(n+2)-2\,\mathrm{Re}(n+1)+\mathrm{Re}(n)\right]\mathrm{Im}(n)\\ &\quad-\left[\mathrm{Im}(n+2)-2\,\mathrm{Im}(n+1)+\mathrm{Im}(n)\right]\mathrm{Re}(n)\\ &=\mathrm{Re}(n+2)\,\mathrm{Im}(n)-\mathrm{Im}(n+2)\,\mathrm{Re}(n)-2S_1\left(r(n)\right) \end{aligned} \tag{5.23}$$

The third order analytic energy operator in the continuous format is

$$S_3\left(r(t)\right)=\mathrm{Re}^{(3)}\left(r(t)\right)\mathrm{Im}\left(r(t)\right)-\mathrm{Im}^{(3)}\left(r(t)\right)\mathrm{Re}\left(r(t)\right) \tag{5.24}$$

Similarly, the third order of the analytic energy operator is defined based on the real and imaginary parts of the analytic signal, their three-point shifted versions, and the lower order AEOs, i.e.,

$$\begin{aligned} \mathrm{S}_3\left(r(n)\right) &= \left[\mathrm{Re}(n+3) - 3\,\mathrm{Re}(n+2) + 3\,\mathrm{Re}(n+1) - \mathrm{Re}(n)\right]\mathrm{Im}(n) \\ &\quad - \left[\mathrm{Im}(n+3) - 3\,\mathrm{Im}(n+2) + 3\,\mathrm{Im}(n+1) - \mathrm{Im}(n)\right]\mathrm{Re}(n) \\ &= \mathrm{Re}(n+3)\,\mathrm{Im}(n) - \mathrm{Im}(n+3)\,\mathrm{Re}(n) \\ &\quad -3\left(\mathrm{S}_1\left(r(n)\right) + \mathrm{S}_2\left(r(n)\right)\right) \end{aligned} \tag{5.25}$$

Proceeding following the same logic, the fourth order continuous AEO is defined as

$$\mathrm{S}_4\left(r(t)\right) = \mathrm{Re}^{(4)}\left(r(t)\right)\mathrm{Im}\left(r(t)\right) - \mathrm{Im}^{(4)}\left(r(t)\right)\mathrm{Re}\left(r(t)\right) \tag{5.26}$$

Likewise, the fourth order discrete AEO involves the real and imaginary parts of the analytic signal, their 4-point shifted versions, and lower order AEOs:

$$\begin{aligned} \mathrm{S}_4\left(r(n)\right) &= \left[\mathrm{Re}(n+4) - 4\,\mathrm{Re}(n+3) + 6\,\mathrm{Re}(n+2) - 4\,\mathrm{Re}(n+1) + \mathrm{Re}(n)\right]\mathrm{Im}(n) \\ &\quad - \left[\mathrm{Im}(n+4) - 4\,\mathrm{Im}(n+3) + 6\,\mathrm{Im}(n+2) - 4\,\mathrm{Im}(n+1) + \mathrm{Im}(n)\right]\mathrm{Re}(n) \\ &= \mathrm{Re}(n+4)\,\mathrm{Im}\left(r(n)\right) - \mathrm{Im}(n+4)\,\mathrm{Re}\left(r(n)\right) \\ &\quad -4\left(\mathrm{S}_1\left(r(n)\right) + \mathrm{S}_3\left(r(n)\right)\right) - 6\,\mathrm{S}_2\left(r(n)\right) \end{aligned} \tag{5.27}$$

In general, the Qth order continuous AEO is expressed as

$$\mathrm{S}_Q\left(r(t)\right) = \mathrm{Re}^{(Q)}\left(r(t)\right)\mathrm{Im}\left(r(t)\right) - \mathrm{Im}^{(Q)}\left(r(t)\right)\mathrm{Re}\left(r(t)\right) \tag{5.28}$$

and its discrete counterpart is written as

$$\mathrm{S}_Q\left(r(n)\right) = \sum_{q=1}^{Q} \left[\begin{aligned} &\frac{(-1)^{(q-1)}\,Q!}{\left(Q-(q-1)\right)!}\mathrm{Re}\left(n+\left(Q-(q-1)\right)\right)\mathrm{Im}(n) \\ &-\frac{(-1)^{(q-1)}\,Q!}{\left(Q-(q-1)\right)!}\mathrm{Im}\left(n+(Q-(q-1))\right)\mathrm{Re}(n) \end{aligned} \right] \tag{5.29}$$

It will be illustrated that higher order AEOs can better boost the signal-to-interference ratio compared to the lower order AEOs. However, the noise level may also be amplified by the higher order AEOs because of the differentiation operation. This undesirable consequence of differentiation can be suppressed using a combination of higher order AEOs because averaging has a noise reduction effect.

A combination of higher order AEOs leads to a new version of the analytic energy operator called higher order analytic energy combination operator (HO_AEO). The purpose is to take advantage of the useful information in each AEO whereas reducing the noise level by offsetting the positive and negative noise values. Simple time-normalized can yield to a natural unit for cross-order application (Nelson, 2006). The HO_AEO operator is defined below in the general continuous format:

$$\mathrm{HO\_AEO}\left(r\left(t\right)\right)=\frac{1}{J}\sum_{j=1}^{J}F_j S_{j_N}\left(r(t)\right) \tag{5.30}$$

where subscript N indicates the normalized analytic energy operator, F_j is the weight of the jth order AEO, and J is total number of orders of AEOs considered. It is difficult to specify the optimal weight coefficients. Here the coefficients are determined using the expressions given in Eqs. (5.23), (5.25), and (5.27). To do so, we denote integer J as the maximum time shift to be considered. In general form, the HO_AEO is expressed in discrete format as

$$\mathrm{HO\_AEO}\left(r\left(n\right)\right)=\frac{1}{J}\sum_{j=1}^{J}\left(\mathrm{Re}(n+j)\,\mathrm{Im}(n)-\mathrm{Im}(n+j)\,\mathrm{Re}(n)\right) \tag{5.31}$$

For example, for J=4, we have the higher order analytic energy combination operator as

$$\begin{aligned}\mathrm{HO\_AEO}\left(r\left(n\right)\right)&=\frac{1}{4}\sum_{j=1}^{4}\left(\mathrm{Re}(n+j)\,\mathrm{Im}(n)-\mathrm{Im}(n+j)\,\mathrm{Re}(n)\right)\\&=\left(1/4\right)\left[\mathrm{S}_{4_N}\left(n\right)+5\mathrm{S}_{3_N}\left(n\right)+10\mathrm{S}_{2_N}\left(n\right)+10\mathrm{S}_{1_N}\left(n\right)\right]\end{aligned} \tag{5.32}$$

5.4.2 The HO_AEO method for SNR improvement

This subsection illustrates that HO_AEO can effectively improve the SNR of a signal and the HO_AEO method using different J values (i.e., orders) results in various SNR improvements. The test is done using a simulated signal generated using the following bearing signal model (reproduced from Eq. (3.1) for convenience) (Bozchalooi and Liang, 2009; Liang and Soltani Bozchalooi, 2010)

$$x(t)=\sum_{m=-M}^{M} A_m e^{-\beta\left(t-mT_p-\tau\right)} \cos\left(\omega_r\left(t-mT_p-\tau+\theta_m\right)\right) u\left(t-mT_p-\tau\right) \tag{5.33}$$

where $x(t)$ is the vibration signal with $2M+1$ fault generated impulses, A_m represents amplitude of faulty signature, β is the structural damping characteristic frequency, ω_r is the excited resonance frequency, T_p represents the time period corresponding fault characteristic frequency, τ is the amount of deviation from the period T_p caused by random slippage of the rolling elements with a zero mean and a standard deviation of 0.01 T_p ~0.02 T_p.

The simulated pure fault signal is plotted in Fig. 5.1 with the following parameters.

Parameter	A_m	β	T_p	ω_r	θ_m
Value	1	1500	0.008	2048	π/8

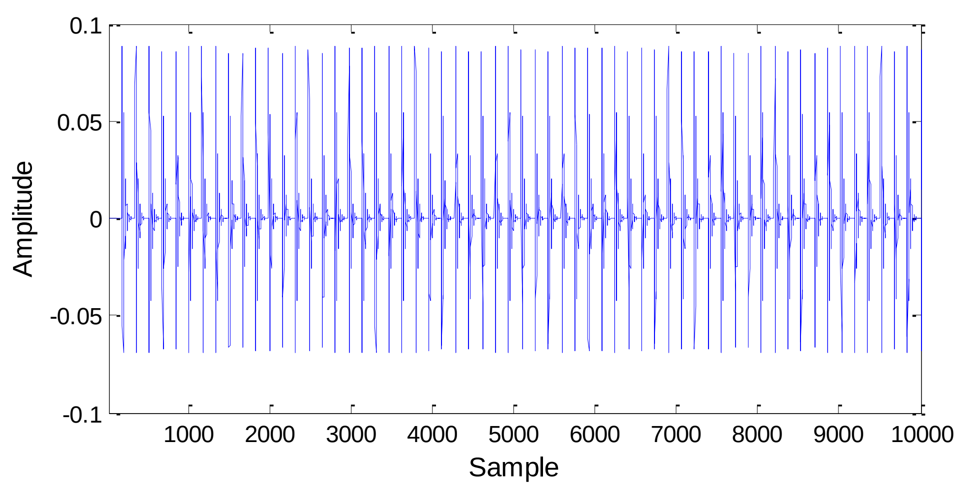

Fig 5.1. Simulated signal of a faulty bearing.

Signal mixtures of different SNRs are then obtained by adding different levels of Gaussian noise to the simulated pure faulty bearing signal. Then the signal mixtures are processed by the HO_AEO transformation. The signal-to-noise ratio is estimated (Cohen and Berdugo, 2002) after applying HO_AEO method and results are summarized in Table 5.1. Apparently, the SNR can be boosted using the HO_AEO approach for all the six different J

values with a minimum of 2 dB improvement. Among them, the third-order and fourth-order HO_AEO yield the best results for the simulated signal with all the four initial SNRs with an average of improvements 6 dB. It should be noted that though order may exist for a particular signal, it may be difficult to be generalized. Nevertheless, considering the similarity of the faulty bearing signals, it is reasonable to fix the HO_AEO order to 3.

Table 5.1 Results of SNR improvement using the HO_AEO method of different orders (i.e., *J* values).

Before applying HO_AEO method Initial SNR (dB)	After applying HO_AEO method Final SNR (dB)					
	J=1	*J*=2	*J*=3	*J*=4	*J*=5	*J*=6
10	12.1	14.3	**16.1**	**15.9**	13.8	12.8
12	14.4	16.5	**18**	**18.1**	15.7	14.5
15	17.1	19.3	**21.5**	**21.9**	18.8	17.7
17	19	21.5	**23.3**	**23.1**	20.6	19.5

5.4.3 Comparison of the HO_AEO method and the energy operator method in terms of signal-to-interference ratio

The energy operator has shown to be an effective tool for machinery fault detection because it can boost the signal-to-interference ratio and hence identify the faulty characteristic frequency (Liang and Soltani Bozchalooi, 2010). Subsequently, in this section, a comparison will be carried out between the HO_AEO and the energy operator methods in terms of their interference handling capabilities. It will be shown that the HO_AEO method performs better than energy operator in the presence of interfering components. In the comparison of the SIRs, we consider only the continuous forms of the HO_AEO.

5.4.3.1 Deriving the HO_AEO expression for faulty bearing signal with multiple vibration interferences

According to the results of section 5.4.2, we fix the HO_AEO order to 3 and derive the associated HO_AEO expression for bearing signal containing multiple interferences and then determine the signal-to-interference ratio of the HO_AEO processed signal. For this purpose, mathematical expressions of the second and third order AEOs are first obtained in the following.

From Eq. (5.28), the second order symmetric operator of the faulty bearing signal is obtained as

$$\begin{aligned}
\mathrm{S}_{2_N}\left(r(t)\right) &= \left(2A^2\beta\omega_r\right)e^{-2\beta t} + \sum_{k=1}^{K} L_k\left(2A\beta\omega_r\right)e^{-\beta t}\cos\left(\left(\omega_r-\omega_{Ik}\right)t+\varphi\right) \\
&\quad + \sum_{k=1}^{K}\left[L_k\left(A^2\omega_r + A\omega_{Ik}^2\right) + A\beta^2\right]e^{-\beta t}\sin\left(\left(\omega_r-\omega_{Ik}\right)t+\varphi\right) \\
&= \left(2A^2\beta\omega_r\right)e^{-2\beta t} + k_2(t)e^{-\beta t}
\end{aligned} \tag{5.34}$$

where $c_2(t)$ is given below

$$\begin{aligned}
c_2(t) &= \sum_{k=1}^{K} L_k\left(2A\beta\omega_r\right)\cos\left(\left(\omega_r-\omega_{Ik}\right)t+\varphi\right) \\
&\quad + \sum_{k=1}^{K}\left[L_k\left(A^2\omega_r + A\omega_{Ik}^2\right) + A\beta^2\right]\sin\left(\left(\omega_r-\omega_{Ik}\right)t+\varphi\right)
\end{aligned}$$

Similarly, the third order analytic operator is calculated from Eq. (5.28) as follow

$$\begin{aligned}
\mathrm{S}_{3_N}\left(r(t)\right) &= \left(A^2\omega_r^3 - 3A^2\omega_r\beta^2\right)e^{-2\beta t} \\
&\quad + \sum_{k=1}^{K}\left(AL_k\omega_{Ik}^3 + L_k\left(3A\omega_r\beta^2 - A\omega_r^2\right)\right)e^{-\beta t}\cos\left(\left(\omega_r-\omega_{Ik}\right)t+\varphi\right) \\
&\quad - \sum_{k=1}^{K} L_k\left(A\beta^3 - 3A\omega_r^2\beta\right)e^{-\beta t}\sin\left(\left(\omega_r-\omega_{Ik}\right)t+\varphi\right) + \sum_{k=1}^{K} L_k^2\omega_{Ik}^3 \\
&= \left(A^2\omega_r^3 - 3A^2\omega_r\beta^2\right)e^{-2\beta t} + k_3(t)e^{-\beta t} + \sum_{k=1}^{K} L_k^2\omega_{Ik}^3
\end{aligned} \tag{5.35}$$

where $c_3(t)$ is given below

$$\begin{aligned}
c_3(t) &= \sum_{k=1}^{K}\left(AL_k\omega_{Ik}^3 + L_k\left(3A\omega_r\beta^2 - A\omega_r^2\right)\right)\cos\left(\left(\omega_r-\omega_{Ik}\right)t+\varphi\right) \\
&\quad - \sum_{k=1}^{K} L_k\left(A\beta^3 - 3A\omega_r^2\beta\right)\sin\left(\left(\omega_r-\omega_{Ik}\right)t+\varphi\right)
\end{aligned}$$

The third order HO_AEO of the bearing signal is then determined based on Eqs. (5.13), (5.30), (5.34), and (5.35) as follows

$$\mathrm{HO\_AEO}\big(r(t)\big)=\begin{bmatrix}\left[F_1\left(A^2\omega_r\right)+F_2\left(2A^2\beta\omega_r\right)+F_3\left(A^2\omega_r^3-3A^2\omega_r\beta^2\right)\right]e^{-2\beta t}\\ +\left[c_1(t)+c_2(t)+c_3(t)\right]e^{-\beta t}+F_1\sum_{k=1}^{K}L_k^2\omega_{Ik}+F_3\sum_{k=1}^{K}L_k^2\omega_{Ik}^3\end{bmatrix} \quad (5.36)$$

$$\begin{cases}\text{ADM of the faulty bearing signal}\rightarrow\left[F_1\left(A^2\omega_r\right)+F_2\left(2A^2\beta\omega_r\right)+F_3\left(A^2\omega_r^3-3A^2\omega_r\beta^2\right)\right]e^{-2\beta t}\\ \text{High-frequency components}\rightarrow\left[c_1(t)+c_2(t)+c_3(t)\right]e^{-\beta t}\\ \text{Vibration interferences}\rightarrow F_1\sum_{k=1}^{K}L_k^2\omega_{Ik}+F_3\sum_{k=1}^{K}L_k^2\omega_{Ik}^3\end{cases}$$

where F_1, F_2, and F_3 are coefficients of orders 1 to 3 respectively, and $c_1(t)$ is defined in Eq. (5.13).

According to Eqs. (5.36), the HO_AEO result consists of three main terms: the amplitude demodulation of faulty bearing signal (the first term), high-frequency components (the second term), and vibration interferences (the third term). The amplitude demodulation term is a product of the squared envelope of the fault signal (A^2) (A represents amplitude demodulation or envelope of the faulty bearing signal), resonant frequency and an exponentially decaying factor. Obviously it contains the fault related information (amplitude demodulation, damping and resonant frequency) and is not affected by the interferences. The high-frequency term represents a combination of an exponential decaying factor of the fault signature and the interfering signal contents. It is will not be used for fault detection because of its high-frequency components (Liang and Soltani Bozchalooi, 2010) and more importantly the interaction with the vibration interferences. The third term reflects only the interference information. Therefore, to calculate the signal-to-interference ratio in the following, the first term is considered as a fault-induced vibration signal and the third term as vibration interferences.

5.4.3.2 Comparison of the SIRs of the signals processed by the HO_AEO and the energy operator method

With the results in the previous subsection, the SIR of the HO_AEO processed signal can be calculated according to definition equation of SIR, i.e., Eq. (5.14). Then the comparison can be made with that of the energy operator.

From Eqs. (5.14) and (5.36), the SIR of the HO_AEO method can be written as

$$\mathrm{SIR}\left(\mathrm{HO\_AEO}\left(r(t)\right)\right)=\frac{\left(\frac{1}{T_P}\right)\int_0^{T_P}\left[F_1\left(A^2\omega_r\right)+F_2\left(2A^2\beta\omega_r\right)+F_3\left(A^2\omega_r^3-3A^2\omega_r\beta^2\right)\right]^2 e^{-4\beta t}\,\mathrm{d}t}{\left(\frac{1}{T}\right)\int_0^{T}\left[F_1\sum_{k=1}^{K}L_k^2\omega_{Ik}+F_3\sum_{k=1}^{K}L_k^2\omega_{Ik}^3\right]^2\mathrm{d}t}$$
$$\approx\frac{\left(\frac{1}{T_P}\right)\int_0^{\infty}\left[F_1\left(A^2\omega_r\right)+F_2\left(2A^2\beta\omega_r\right)+F_3\left(A^2\omega_r^3-3A^2\omega_r\beta^2\right)\right]^2 e^{-4\beta t}\,\mathrm{d}t}{\left(\frac{1}{T}\right)\int_0^{T}\left[F_1\sum_{k=1}^{K}L_k^2\omega_{Ik}+F_3\sum_{k=1}^{K}L_k^2\omega_{Ik}^3\right]^2\mathrm{d}t} \tag{5.37}$$

After integrations and simplification, Eq. (5.37) reduces to

$$\mathrm{SIR}\left(\mathrm{HO\_AEO}\left(r(t)\right)\right)\approx\frac{A^4\omega_r^6}{4T_P\beta\sum_{k=1}^{K}L_k^4\omega_{Ik}^6} \tag{5.38}$$

To evaluate the proposed method, it will be compared with the energy operator method in terms of SIR. The SIR of the EO processed signal is obtained as (reproduced from Eq. (3.15) for convenience)

$$\mathrm{SIR}\left(\psi\left(r(t)\right)\right)\approx\frac{A^4\omega_r^4}{4T_P\beta\sum_{k=1}^{K}L_k^4\omega_{Ik}^4} \tag{5.39}$$

Using Eqs. (5.38) and (5.39), we can compare the two methods in terms of SIR as follows

$$\frac{\mathrm{SIR}\left(\mathrm{HO\_AEO}\left(r(t)\right)\right)}{\mathrm{SIR}\left(\psi\left(r(t)\right)\right)}=\frac{\omega_r^2\sum_{k=1}^{K}L_k^4\omega_{Ik}^4}{\sum_{k=1}^{K}L_k^4\omega_{Ik}^6}>1 \tag{5.40}$$

As the resonant frequency is much higher than the interference frequencies, the SIR yielded by the HO_AEO is, in the presence of multiple vibration interferences, much higher than that obtained by the energy operator.

The whole process of the HO_AEO method for online monitoring and bearing fault detection is summarized by a flowchart shown in Fig. 5.2. In the case of very low SIR, a faulty bearing signal can be enhanced by repeatedly applying the HO_AEO method because the amplitude-demodulated term can be further magnified.

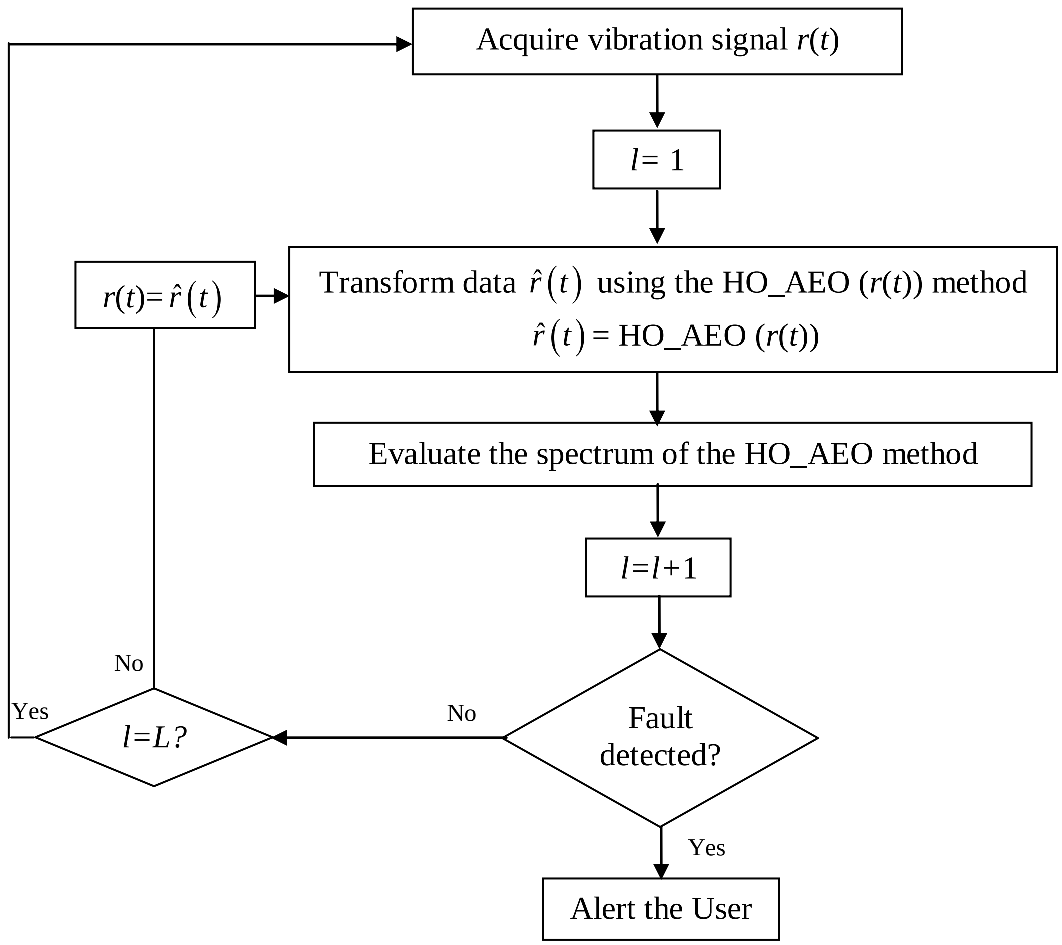

Fig. 5.2. Flowchart of the HO_AEO method.

5.5 Performance Simulation evaluation of the HO_AEO method

In this section, the HO_AEO method will be tested and compared with the energy operator method using simulation data for the following cases:

1) Simulate impulsive faulty bearing signal with high level of noise and medium level of vibration interferences.

2) Simulate impulsive faulty bearing signal with high level of vibration interferences and medium level of noise.
3) Simulate impulsive faulty bearing signal with fairly high level of noise and vibration interferences.

The signal mixture containing a bearing fault, multiple interferences and noise can be expressed as

$$\begin{aligned} r(t) = & \sum_{m=-M}^{M} A_m e^{-\beta\left(t-mT_p-\tau\right)} \cos\left(\omega_r\left(t-mT_p-\tau+\theta_m\right)\right) u\left(t-mT_p-\tau\right) \\ & +\sum_{k=1}^{K} L_k \cos\left(\omega_{ik} t\right) + w(t) \end{aligned} \tag{5.41}$$

where $w(t)$ represents noise and the other symbols have been explained previously.

The simulated signal is generated with four vibration interferences as well as white Gaussian noise. The fault characteristic frequency is 125 Hz, and the frequencies of vibration interferences are 5 Hz, 27 Hz, 43 Hz, and 650 Hz. To generate white Gaussian noise, we use the 'awgn' MATLAB command.

5.5.1 Simulated faulty bearing in the presence of high level of interference components and medium level of noise

The simulated signal of a faulty bearing with interference components and noise is shown in Fig. 5.3(a). The signal-to-noise ratio is -5 dB, and signal-to-interference ratio is -35 dB. The spectrum of the signal is presented in Fig. 5.3(b) which shows mostly the four interferences. Fig. 5.4 shows the envelope spectrum, and spectrum of the energy operator processed signal. The fault signature cannot be detected by either the envelope method or the energy operator method. In addition, no evidence of fault can be seen from the results of the ADD and CEEO (from Fig. 5.4) either. However, the HO_AEO method can successfully extract fault features with the result displayed in Fig. 5.5.

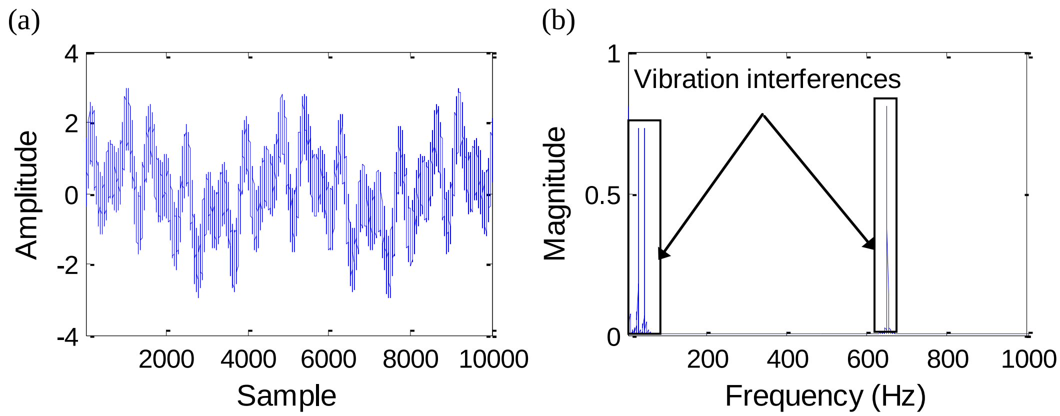

Fig. 5.3. (a) Simulated of faulty bearing signal with vibration interferences and noise (SIR= -35 dB, SNR= -5 dB), and (b) spectrum of the simulated signal.

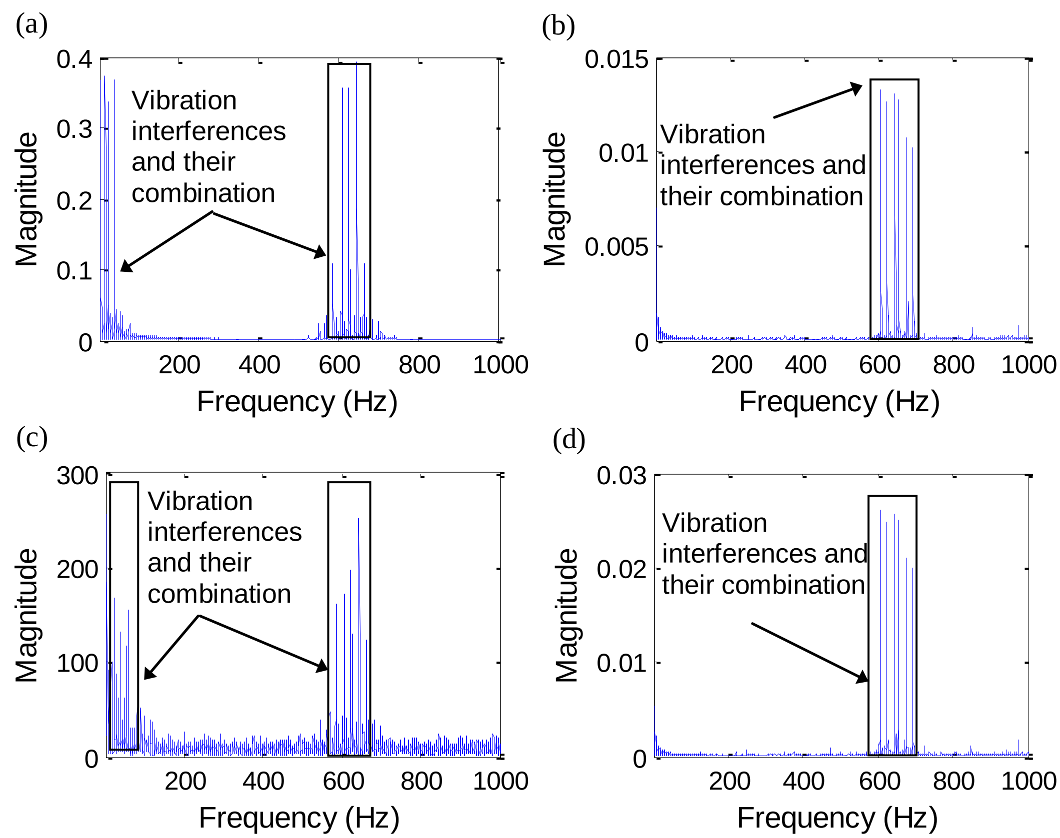

Fig. 5.4. (a) Envelope spectrum of the signal, (b) spectrum of the energy operator, (c) envelope spectrum of the ADD method, and (d) spectrum of the CEEO method.

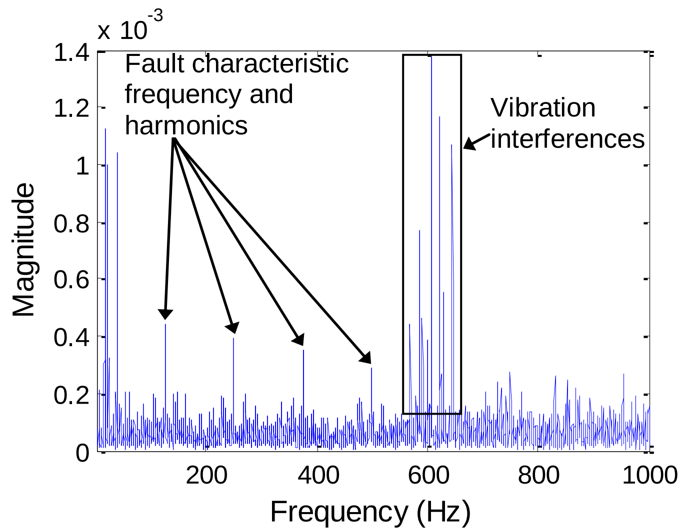

Fig. 5.5. Spectrum of the HO_AEO processed signal.

5.5.2 Simulated faulty bearing with high level of noise and medium level of interferences

In this case, the simulated signal of faulty bearing is masked with harsh noise (SNR=-17dB) and interfering components (SIR=5dB). This simulated signal and its spectrum are shown in Fig. 5.6. The landscape of Fig. 5.6(b) is dominated by the noise and interferences. The envelope and operator results as shown in Fig. 5.7 (a) and (b) are clouded mainly by noise and the fault signature cannot be detected.

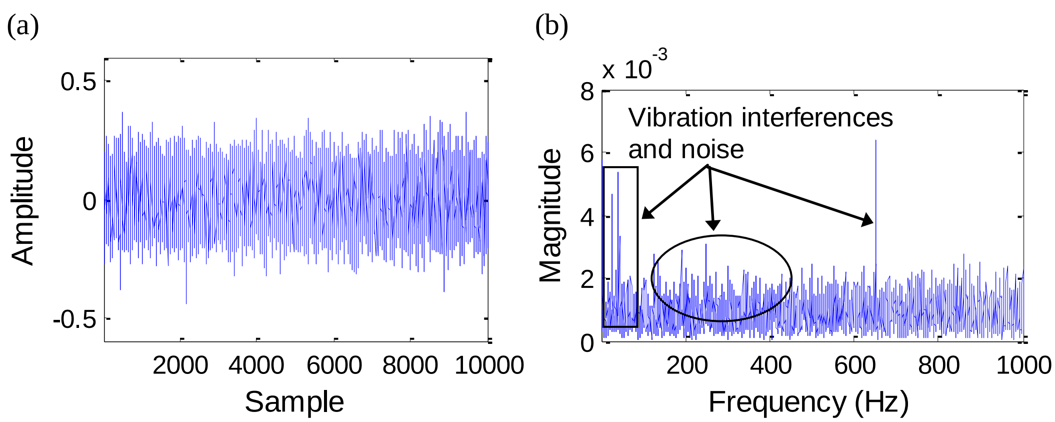

Fig.5.6. (a) Simulated of faulty bearing signal with harsh noise and interfering components (SIR= 5 dB, SNR= -17 dB), and (b) spectrum of the simulated signal.

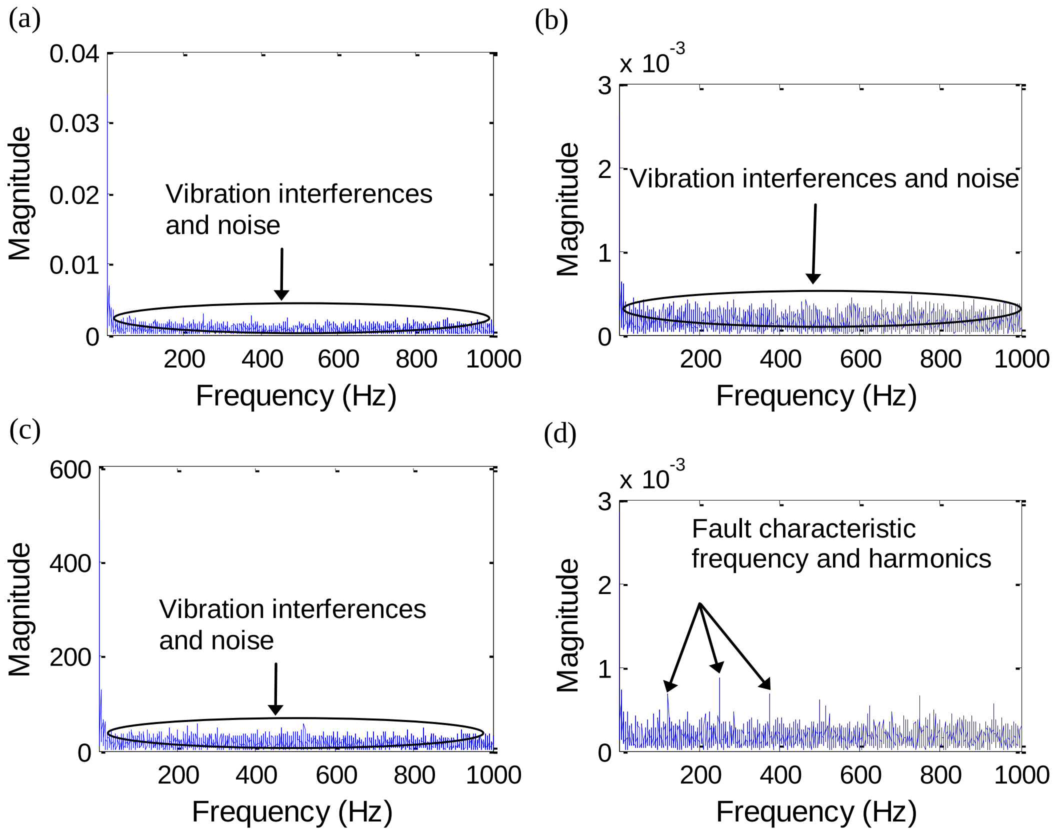

Fig. 5.7. (a) Envelope spectrum of the signal, (b) spectrum of the energy operator, (c) envelope spectrum obtained by the ADD method, and (d) spectrum obtained by the CEEO method.

Furthermore, the ADD and CEEO results are presented in Fig. 5.7 (c) and (d). Due to the presence of high level of noise in the signal, only the CEEO method can identify FCF and two of its harmonics at low magnitude. Then the HO_AEO is applied to the same signal mixture. The fault frequency at 125 Hz and several of its harmonics can be clearly identified the HO_AEO result (Fig. 5.8).

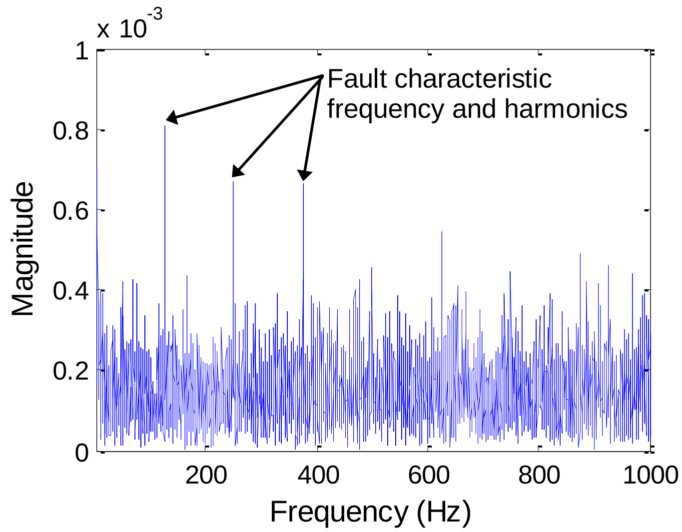

Fig. 5.8. Spectrum of the HO_AEO processed signal.

5.5.3 Simulated faulty bearing with high level of noise and vibration interferences

In this test, the signal-to-noise ratio and signal-to-interference ratio are both fixed at -15 dB. The signal mixture and its spectrum are shown in Fig. 5.9 which is dominated by the interferences. Obviously the envelope result is obscured mainly by the interferences (Fig. 5.10 (a)). On the other hand, though the relative strengths of the interferences are suppressed by the energy operator, the spectrum is overwhelmed by noise and the fault feature cannot be extracted.

Similarly, the results of the ADD and CEEO methods are plotted in Fig. 5.10. As we can see, noise and interfering components have obscured the fault signature, and only can the CEEO method reveal fault features with low magnitude. The same signal mixture is then processed by the HO_AEO and the fault characteristic frequency as well as multiple of its harmonics can be detected as shown in Fig. 5.11.

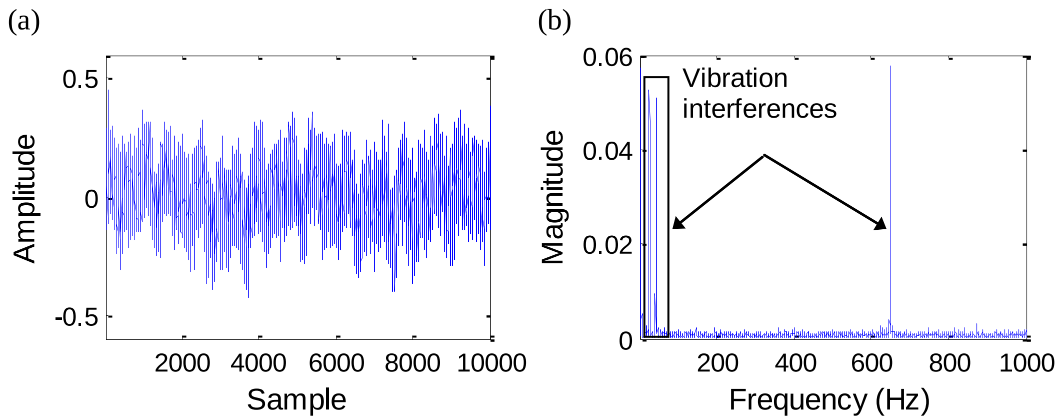

Fig. 5.9. (a) Simulated of faulty bearing signal with harsh noise and interfering components (SIR= -15 dB, SNR= -15 dB) and (b) spectrum of this simulated signal.

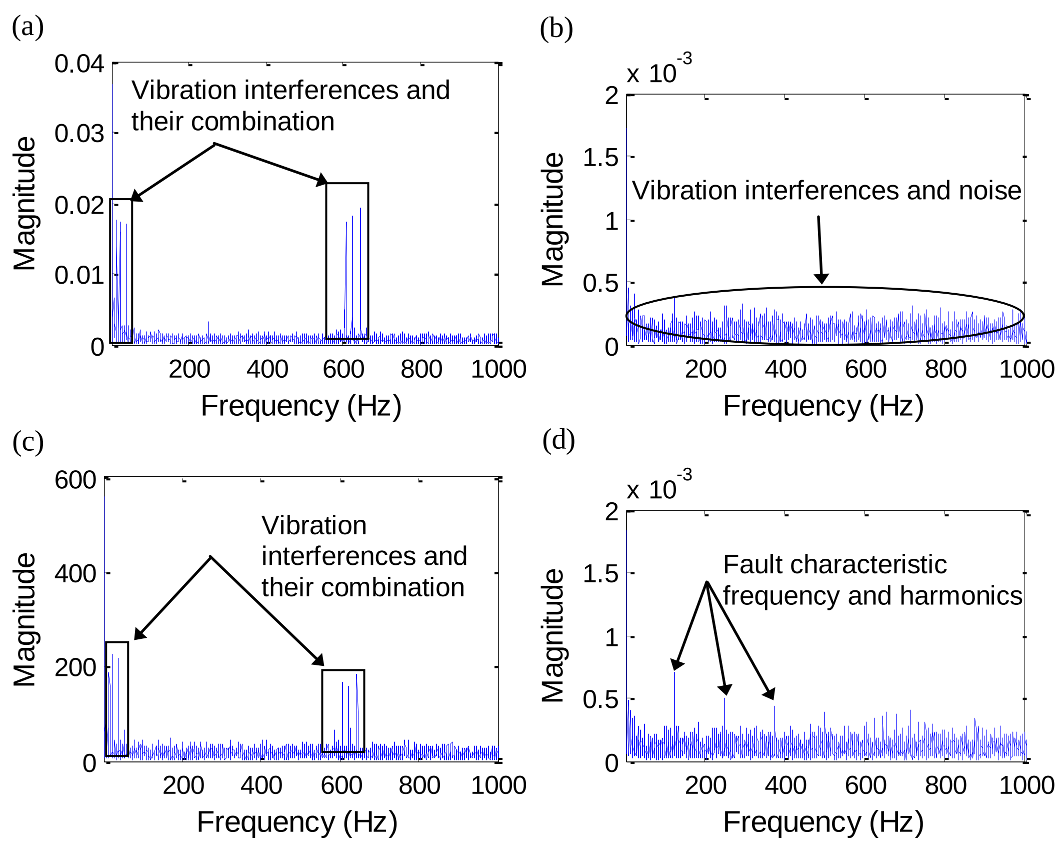

Fig. 5.10. (a) Envelope spectrum of the signal, (b) spectrum of the energy operator, (c) envelope spectrum of the ADD result, and (d) spectrum of the CEEO result.

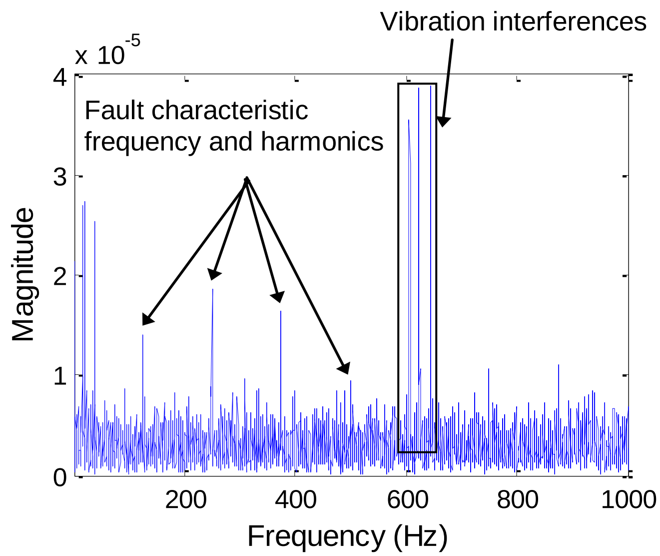

Fig. 5.11. Spectrum of the HO_AEO processed signal.

5.6 Experimental evaluation of the HO_AEO method

5.6.1 Detection of inner race bearing fault

A Spectra Quest Machinery fault simulator (MKF-PK5M) is used to collect data in this experiment as shown in Fig. 5.12. The AC motor is employed to dive the simulator that is controlled by a PWM Hitachi drive. Two bearings are mounted to support a steel shaft and two well-balanced mass rotors are installed on the shaft. The vibration signal is collected by using the accelerometer sensor and then fed to a DAQ card. Vibration data are saved in a PC with determined sampling frequency and specified parameters through LabVIEW. Processing on signal is exploited by using MATLAB on a PC.

Information of experimental elements is as follows:

- Shaft: 5/8” in diameter
- Mass rotors: 2” thick, 4” in diameter and 11.1 lbs each
- Bearings: Type ER10K with eight roller elements (balls). The inside, outside, pitch and ball diameters are, respectively, 0.625”, 1.8500”, 1.3190” and 0.3125”.
- Accelerometer: PCB sensor, model 623C01 with sensitivity of 100 Mv/g and a sensitivity range of 1 to 20 kHz.

- PWM Hitachi drive: SJ200-022NFU.
- DAQ card: NI PCI-6132 multi-function.
- PC: Pentium 4 of 2.52 GHz speed.

The shaft speed is set at 1503 RPM (25.1 Hz). The right bearing has a pre-seeded fault (created by manufacturer with unknown dimensions) on the inner race with the characteristic frequency of 124.19 Hz (=4.948 f_r, specified in the simulator user's manual). The gear meshing frequency is 174.1 Hz. To make the situation more complex, white noise (SNR=1dB), and also another interference at 800Hz is added to both the healthy and faulty bearing signals. The accelerometer is installed on the simulator base at a location away from the bearing but closer to the gearbox and belt pulley (Fig. 5.12). The vibration signal is sampled at 12,000 samples/s.

The healthy bearing signal is plotted in Fig. 5.13. The raw signal and its frequency spectrum of the bearing with an inner race fault are shown in Figs. 5.14(a) and (b) respectively. The fault characteristic frequency at 124.19 Hz cannot be detected from Fig. 5.14. The envelope spectrum of acquired signal, spectrum of the energy operator, ADD, and CEEO method result are illustrated in Figs. 5.15(a)-(d). Among mentioned methods, only the CEEO method could extract fault characteristic frequency. However, in the spectrum of the HO_AEO result (Fig. 5.16), the fault characteristic frequency and two of its associated harmonics can be clearly distinguished.

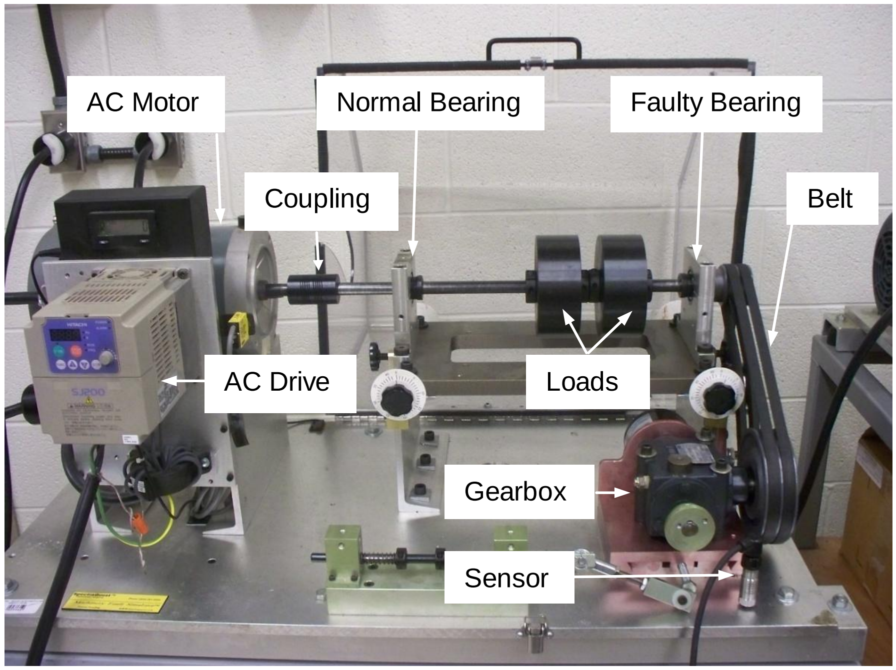

Fig. 5.12. Experimental setup #1 (inner race fault).

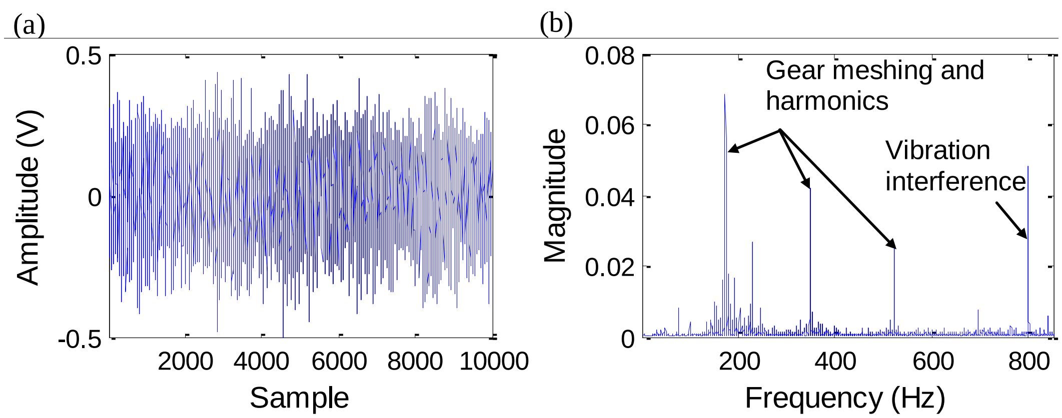

Fig. 5.13. (a) Part of the measured signal of a healthy bearing, and (b) the spectrum of the signal (Experimental setup #1).

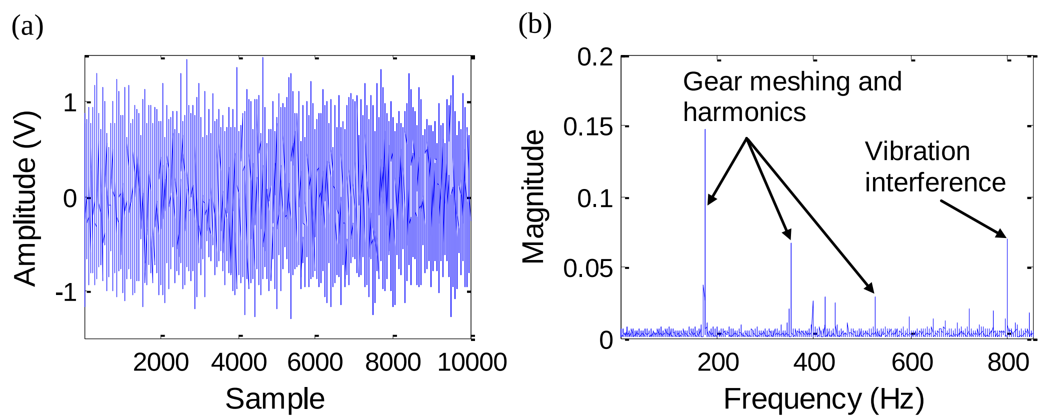

Fig. 5.14. (a) Part of the measured signal of a bearing with inner race fault from Experimental setup # 1, and (b) the spectrum of the faulty bearing signal.

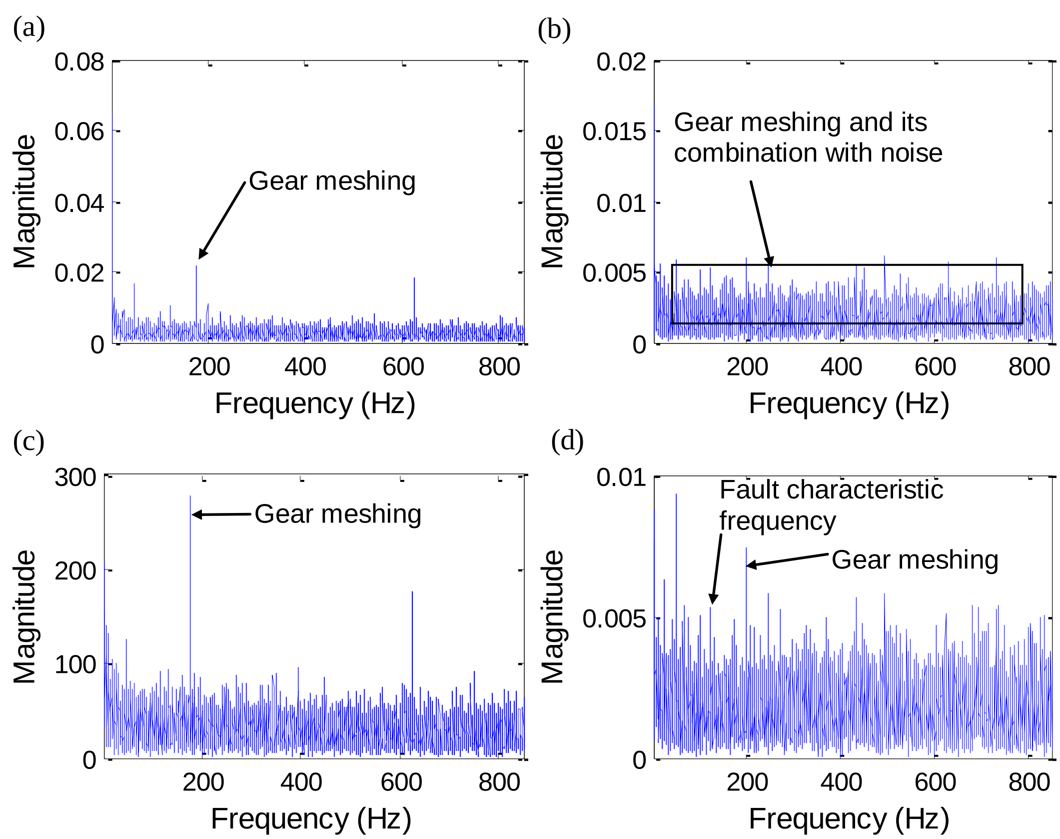

Fig. 5.15. (a) Envelope spectrum of the same faulty bearing signal shown in Fig. 5.14(a), (b) the spectrum of the energy operator result, (c) envelope spectrum obtained by the ADD method, and (d) spectrum obtained by the CEEO method.

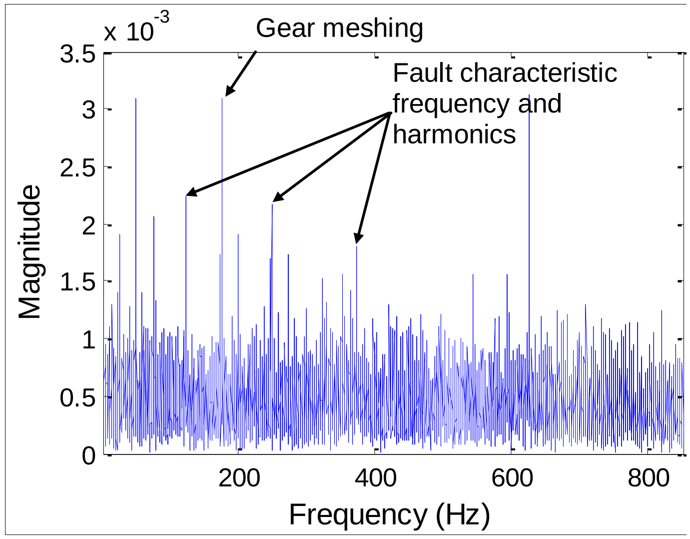

Fig. 5.16. Spectrum of the HO_AEO processed faulty bearing signal (shown in Fig. 5.14 (a)).

5.6.2 Detection of outer race bearing fault

In this case, the test rig is the same as in the previous experimental setup but The inner race faulty bearing is replaced by one (also type ER10K) with an outer race fault on the right side of the shaft. The shaft now carries one balanced load rotor (2" thick, 4" in diameter and 11.1 lbs). Similar to the previous experiment, the gearbox is driven by the shaft through a belt connection and the accelerometer is installed on the simulator base at a location close to the belt pulley and the gearbox but far from the bearing. Same as Inner race fault test, to provide more complex situation, white noise (SNR=1dB), and also another interference at 800Hz is added to both the healthy and faulty bearing signals. The setup is shown in Fig. 5.17. The shaft speed is set at 990 RPM (16.5 Hz).

The outer race fault is created by the manufacturer with unknown dimensions. The outer race fault characteristic frequency is 50.5 Hz (=3.052 f_r, specified in the simulator user's manual). The meshing frequency of gearbox associated with the above shaft speed is 116.2 Hz. The reference healthy bearing signal and spectrum are demonstrated in Figs. 5.18(a) and (b) respectively. Figs. 5.19(a) and (b) respectively show the raw signal of the faulty bearing and its spectrum without any sign of the outer race fault.

The results of the enveloping method, the energy operator, the ADD and CEEO methods are plotted in Figs. 5.20(a)-(d), respectively. Obviously, the meshing frequency and noise mask a whole range of spectra while the fault signature can be hardly observed in the enveloping, energy operator, and ADD results. The CEEO method can extract only one frequency associated with outer race fault. The spectrum of the proposed method is displayed in Fig. 5.21. It clearly indicates the fault characteristic frequency at 50.54 Hz and its associated harmonics at 101.08, 151.6. These results determine that performance of the proposed method better than the enveloping, conventional energy operator, ADD and CEEO methods approaches.

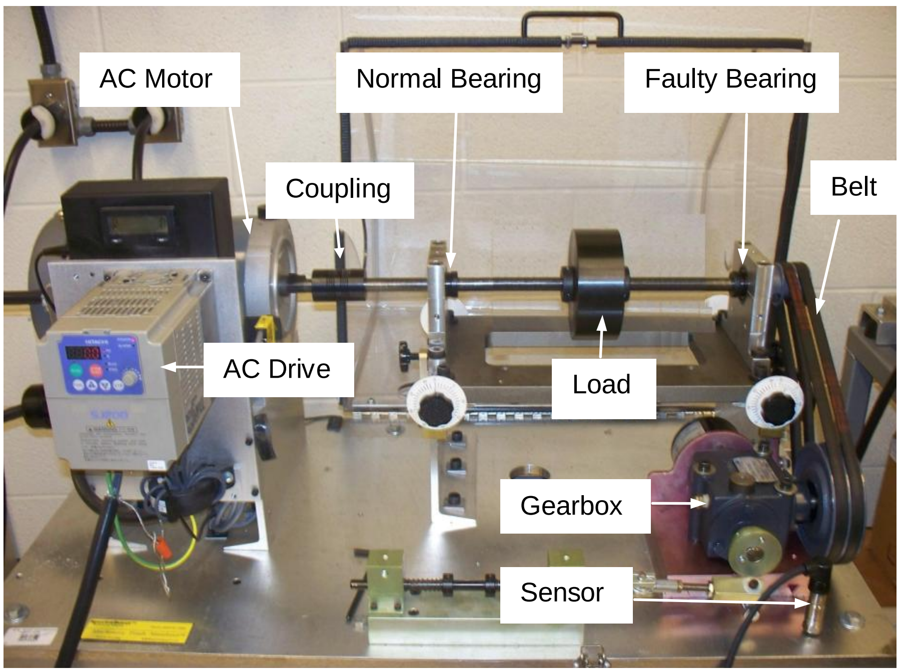

Fig. 5.17. Experimental setup #2 (outer race fault).

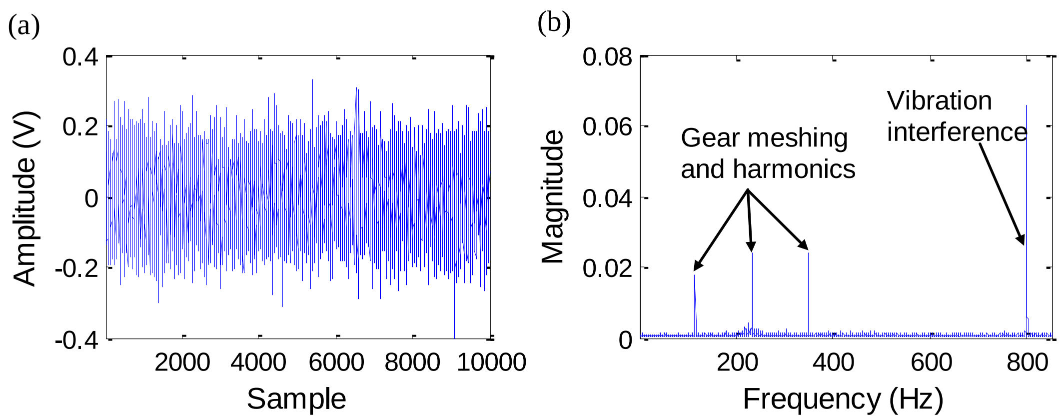

Fig. 5.18. (a) Part of the measured healthy bearing signal, and (b) the spectrum of a healthy bearing signal (Experimental setup #2).

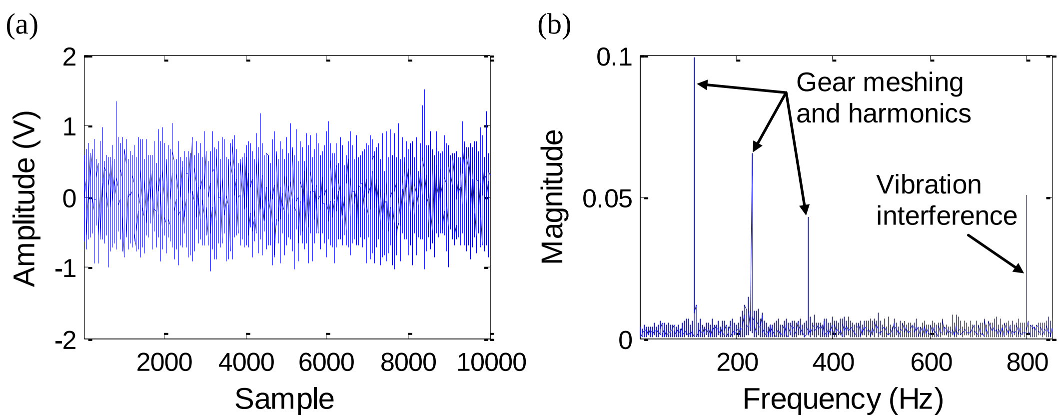

Fig. 5.19. (a) Part of the measured signal of outer race fault from Experiment # 2, and (b) the spectrum of the faulty bearing signal.

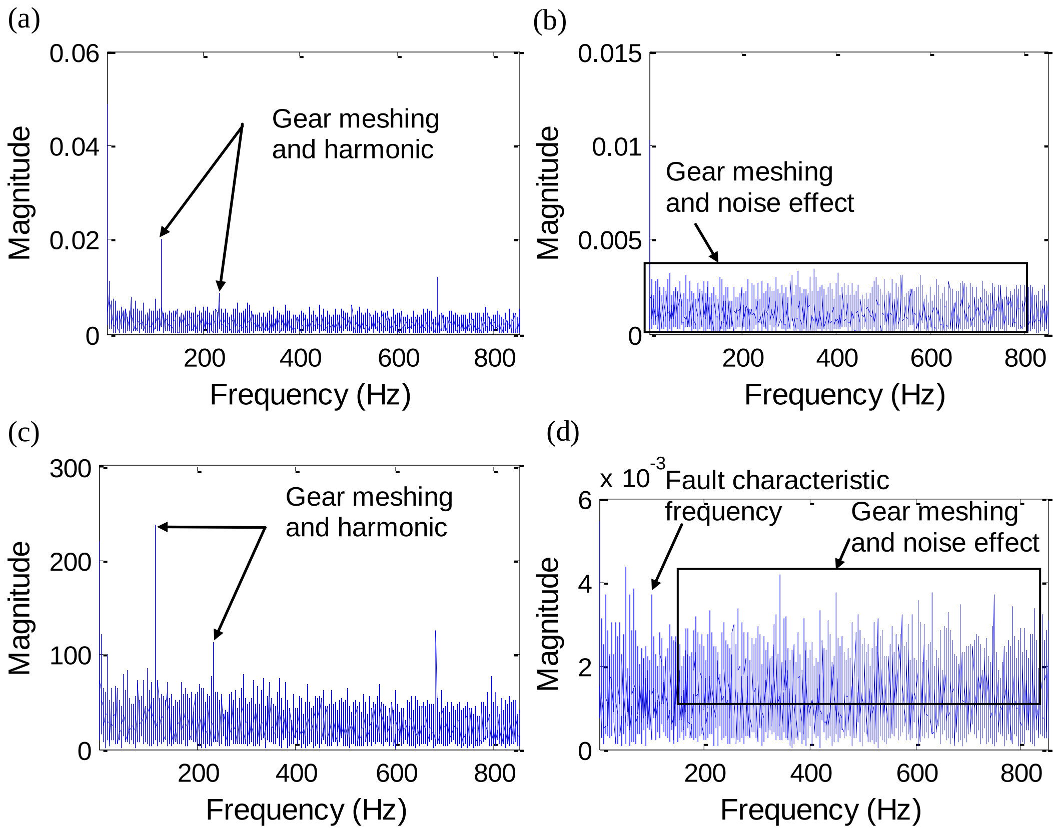

Fig. 5.20. (a) Envelope spectrum of the faulty bearing signal (shown in Fig. 5.19(a)), (b) the spectrum of the energy operator result of the same raw signal, (c) envelope spectrum obtained by the ADD method, and (d) spectrum obtained by the CEEO method.

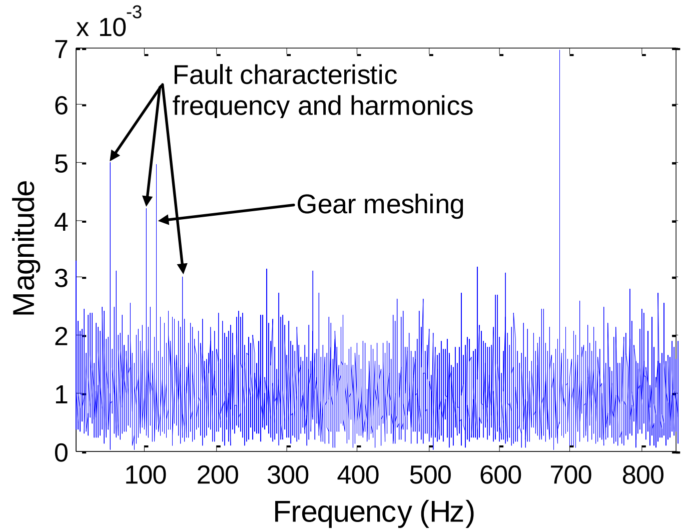

Fig. 5.21. Spectrum of the HO_AEO processed faulty bearing signal.

5.7 Conclusion

A higher order AEO method has been developed to detect bearing fault from vibration signals heavily contaminated by both noise and multiple interferences. The new AEO is a balanced combination of the signal, its Hilbert transform, and their derivatives. It works by exploring the information in both the real and imaginary parts of the signal and extracting both the amplitude and frequency modulations. In this study, we have mathematically shown that the HO_AEO yields higher SIR compared to the conventional EO. The use of the combined multiple higher order AEOs can further counterweigh the noise effects. The effectiveness of the proposed method has been illustrated using both simulated and experimental signals and compared favorably with the conventional EO. It should be noted that the proposed method does not require the information of the fault excited resonance and thus eliminated the filtering and enveloping steps that are needed in many existing HFR methods. The computation is straightforward and less burdensome as compared other methods that require various transformations. As such, it is suited for on-line applications.

Chapter 6

A non-resonance based method for bearing fault identification by higher order energy operator fusion[4]

In this chapter, another non-parametric, non-filtering approach is proposed based on higher orders of energy operator for more reliable and robust bearing fault detection. This method is based on the fusion of multiple higher order energy operators and hence abbreviated as HOEO_F. It performs better than the methods presented in the previous three chapters in handling intense noise and interfering components. This method applies higher order EO fusion to handle intense noise and strong interferences. The rationales of this method are:

a) Comparing with the second order (traditional) energy operator (to simplify discussion, the second order energy operator will simply called energy operator hereafter), the signal-to-interference ratio (SIR) can be further improved by higher order EOs.
b) The application of higher order EOs may also amplifies the higher frequency noise..
c) The difficulty in b) can be mitigated by using the fused higher order EOs due to the noise cancelling effect of the different higher order EOs.

[4] See Appendix B.4 for MATLAB script.

The proposed new method is simple, easy to implement and has good capability to handle both noise and interferences. It should be noted that even though several higher order EOs are incorporated in this method, they are not applied sequentially. Instead, they are fused into a single step transform, which makes it computationally efficient.

The principal work in this chapter is summarized as follows:

- Illustration of the effect of applying higher order EOs on SIR.
- Development of the HOEO_F method, and examination of its effects on SIR and SNR.
- Evaluation of the HOEO_F performance for bearing defect detection using both simulated and experimental data.

6.1 The higher order EO and its effect on SIR

The generalized energy operator is defined in continuous format as follows (Maragos and Potamianos, 1995)

$$\mathrm{EO}_J\left(r\left(t\right)\right)=\dot{r}r^{(J-1)}-rr^{(J)} \tag{6.1}$$

and its discrete counterpart is written as

$$\mathrm{EO}_J\left(r\left(n\right)\right)=r_n r_{(n+J-2)}-r_{(n-1)}r_{(n+J-1)} \tag{6.2}$$

To illustrate the performance of the higher order energy operators, the same bearing model as shown in Eq. (3.2) is considered (Bozchalooi and Liang, 2009; Liang and Soltani Bozchalooi, 2010), i.e.,

$$r\left(t\right)=x(t)+v\left(t\right)=Ae^{-\beta(t)}\cos\left(\omega_r t+\varphi\right)+\sum_{k=1}^{K}L_k\cos\omega_{Ik}t \tag{6.3}$$

where A is the amplitude of the fault signal, β is the structural damping characteristic frequency, ω_r is the frequency of the excited resonance, ω_{Ik} represents the frequency of kth interference component, L_k denotes the amplitude of the kth interference component, $x(t)$ is the vibration signal containing fault generated impulse, $v(t)$ contains multiple vibration interferences. Due to practical reason, we assume that the excited resonance frequency is much higher than interference signal frequency ω_{Ik} for all k's.

In the following, we use the fourth order EO to illustrate that the SIR can be further improved by higher order EO in comparison to that already improved by the traditional EO. The fourth order EO for a signal mixture containing an impulsive bearing fault signal component and multiple vibration interferences (based on Eq. (6.3)) is expressed as

$$\begin{aligned}\mathrm{EO}_4\left(r\left(t\right)\right) &= \dot{r}r^{(3)} - rr^{(4)} \\ &= A^2\left(3\beta^2\omega_r{}^2 - \omega_r{}^4\right)e^{-2\beta t} + AG_c\left(t\right)e^{-\beta t} + \sum_{k=1}^{K} L_k^2\omega_{Ik}^4\end{aligned} \tag{6.4}$$

where $G_c(t)$ is given by

$$\begin{aligned}G_c\left(t\right) = \cos\left(\omega_r t + \theta\right) &\sum_{k=1}^{K} L_k\left(\left(\beta^3 - 3\beta\omega_r^2\right)\omega_{Ik} - \left(\beta\right)\omega_{Ik}^3\right)\sin\omega_{Ik}t \\ &+ \sin\left(\omega_r t + \theta\right)\sum_{k=1}^{K} L_k\left(\left(3\beta^2\omega_r - \omega_r^3\right)\omega_{Ik} - \left(\omega_r\right)\omega_{Ik}^3\right)\sin\omega_{Ik}t \\ &+ \cos\left(\omega_r t + \theta\right)\sum_{k=1}^{K} L_k\left(\left(\beta^4 - 6\beta^2\omega_r^2 + \omega_r^4\right) - \omega_{Ik}^4\right)\cos\omega_{Ik}t \\ &+ \sin\left(\omega_r t + \theta\right)\sum_{k=1}^{K} L_k\left(4\omega_r\beta^3 - 4\beta\omega_r^3\right)\cos\omega_{Ik}t\end{aligned}$$

The basic definition of the signal-to-interference ratio in the context of bearing fault detection is expressed as (reproduced from Eq. (3.11) for convenience)

$$\mathrm{SIR}\left(r\right) = \frac{\left(1/T\right)\int_0^T x^2\left(t\right)\mathrm{d}t}{\left(1/T\right)\int_0^T \sum_{k=1}^{K} v_k{}^2\left(t\right)\mathrm{d}t} = \frac{P_x}{P_v} \tag{6.5}$$

where $x(t)$ is the faulty bearing vibration, and $\sum_{k=1}^{K} v_k\left(t\right)$ represents multiple vibration interferences.

According to Eqs. (6.4) and (6.5), the signal-to-interference ratio of the fourth order EO of the signal mixture defined by Eq. (6.5) can be calculated as follows

$$\operatorname{SIR}\left(\mathrm{EO}_4\left(r\left(t\right)\right)\right)=\frac{\left(\dfrac{1}{T_P}\right)\int_0^{T_P}A^4\left(3\beta^2\omega_r{}^2-\omega_r{}^4\right)^2e^{-4\beta t}\,\mathrm{d}\,t}{\left(\dfrac{1}{T}\right)\int_0^T\sum_{k=1}^K L_k^4\omega_{Ik}^8\,\mathrm{d}\,t}$$
$$\approx\frac{\left(\dfrac{1}{T_P}\right)\int_0^{\infty}A^4\left(3\beta^2\omega_r{}^2-\omega_r{}^4\right)^2e^{-4\beta t}\,\mathrm{d}\,t}{\left(\dfrac{1}{T}\right)\int_0^T\sum_{k=1}^K L_k^4\omega_{Ik}^8\,\mathrm{d}\,t} \tag{6.6}$$

After the integral calculations, the above SIR can be simplified as

$$\operatorname{SIR}\left(\mathrm{EO}_4\left(r\left(t\right)\right)\right)\approx\frac{A^4\omega_r^8}{4T_P\beta\sum_{k=1}^K L_k^4\omega_{Ik}^8} \tag{6.7}$$

The SIR of the EO is (reproduced from Eq. (3.15) for convenience)

$$\operatorname{SIR}\left(\psi\left(r\left(t\right)\right)\right)\approx\frac{A^4\omega_r^4}{4T_P\beta\sum_{k=1}^K L_k^4\omega_{Ik}^4} \tag{6.8}$$

From Eqs. (6.7) and (6.8), a comparison between the SIR of fourth order EO and the energy operator of the signal mixture is obtained as follows

$$\frac{\operatorname{SIR}\left(\mathrm{EO}_4\left(r\left(t\right)\right)\right)}{\operatorname{SIR}\left(\psi\left(r\left(t\right)\right)\right)}\approx\frac{\omega_r^4\sum_{k=1}^K L_k^4\omega_{Ik}^4}{\sum_{k=1}^K L_k^4\omega_{Ik}^8} \tag{6.9}$$

As the interference frequencies ω_{Ik} are usually much lower than the resonant frequency ω_r, the SIR of the fourth order EO of the signal is much higher than that of the energy operator as shown in Eq. (6.9). Hence, it can be concluded that a higher order EO can significantly improve the relative strength of the faulty bearing signal with respect to interferences. Such a property is useful for bearing fault detection in the presence of high level vibration interferences generated from different parts of the mechanical system. However, as a high order EO involves differentiation operations, the relative strength of the high-frequency noise is also amplified at the same time. Therefore, a high order EO may not be directly applicable to processing bearing signals.

6.2 The higher order energy operator fusion (HOEO_F) method and its effects on SNR and SIR

6.2.1 The high order EO fusion (HOEO-F) method

As mentioned in the previous section, the SIR of the bearing fault signal can be boosted by applying a higher order EO but this also leads to the amplified relative strength of the high frequency noise. In addition, it is difficult to predict which order of EO will yield the best result. To mitigate this difficulty, we treat the result from each EO of a different order as a distinct dataset from a different virtual sensor and then use their fused result for bearing fault detection. The rationale is that the fusion process has a cancelling effect of the random noise from different virtual sensors whereas in the meantime the peaks at the fault characteristic frequency and its harmonics should remain after fusion. Therefore, the fusion step can lead to signal-to-noise ratio enhancement and also take advantage of each order EO's contribution to the signal-to-interference ratio improvement simultaneously.

The continuous HOEO_F is defined as follows

$$\mathrm{HOEO\_F}\left(r(t)\right)=\sum_{j=2}^{J}\alpha_j\left[\mathrm{EO}_j\left(r(t)\right)\right] \tag{6.10}$$

and its discrete counterpart is

$$\mathrm{HOEO\_F}\left(r(n)\right)=\sum_{j=2}^{J}\alpha_j\left[r_n r_{(n+j-2)}-r_{(n-1)}r_{(n+j-1)}\right] \tag{6.11}$$

where j is order number, J is the total number of orders considered, and α_j is coefficient associated with order j.

To incorporate multiple higher orders of EO, the minimum entropy data fusion is used. We consider the fusion technique in linear combination of higher order EOs (Eq. 6.10). The fused information is represented as the weighted sum of outputs of different orders. Consider the J-order fusion as shown in Fig. 6.1. We assume that each order has its own specific noise level. The jth order result can be expressed as

$$\mathrm{EO}_j\left(r(t)\right) = OX_j(t) + n_j(t) \tag{6.12}$$

where the $OX_j(t)$ represents output of higher order energy operator of impulsive faulty bearing signal related to j order, and $n_j(t)$ indicates to noise associated to j order. The objective of fusion is to combine different order output in a symmetric manner to obtain proper consensus $OX_j(t)$.

The minimum entropy fusion is designed to reduce the spread of impulse response frequencies to obtain desired feature related to the original signature of impulsive fault. It is known that the Gaussian processes are characterized by second order moment (Variance) statistics while non-Gaussian process contains valuable information in their higher orders moment, especially in fourth order. Furthermore, maximizing kurtosis is equivalent to minimizing entropy (Hall and Llinas, 1997; Sawalhi et al., 2007; Zhou and Leung, 1997).Therefore, we use kurtosis of the higher order EO fusion as the information measure, i.e., the criterion to assign optimum coefficients in (Eq. (6.11)).

In general, the kurtosis of time series y is defined as (Caviedes and Oberti, 2004; Dron et al., 2004; Papoulis, 1991)

$$Kurt(y) = \frac{(1/N)\sum_{n=1}^{N}\left(y_n - \bar{y}\right)^4}{\left[(1/N)\sum_{n=1}^{N}\left(y_n - \bar{y}\right)^2\right]^2} \tag{6.13}$$

where N is the number of data points and $\bar{y}$ is the mean value of y_n (n=1,2,…,N) respectively.

Similarly, the kurtosis of the HOEO_F function can be expressed as

$$Kurt\left(\mathrm{HOEO\_F}(r(n))\right) = \frac{(1/N)\sum_{n=1}^{N}\left(\mathrm{HOEO\_F}(r(n)) - \bar{\mathrm{B}}\right)^4}{\left[(1/N)\sum_{n=1}^{N}\left(\mathrm{HOEO\_F}(r(n)) - \bar{\mathrm{B}}\right)^2\right]^2} \tag{6.14}$$

where $\bar{\mathrm{B}}$ is the mean value of HOEO_F($r(n)$).

Then, the optimum coefficients $(\alpha_1^*, \alpha_2^*, \ldots, \alpha_J^*)$ can be obtained as follows

$$\boldsymbol{\alpha}^* = \arg\max_{\boldsymbol{\alpha}} \left(Kurt\left(\text{HOEO\_F}(r(n)) \right) \right) \tag{6.15}$$

where $\boldsymbol{\alpha} = (\alpha_1, \alpha_2, ..., \alpha_J)$ and $\boldsymbol{\alpha}^* = (\alpha_1^*, \alpha_2^*, ..., \alpha_J^*)$.

The optimization step in Eq. (6.15) needs numerical and non-linear technique to find proper coefficients. Such optimization process is carried out by MATLAB program.

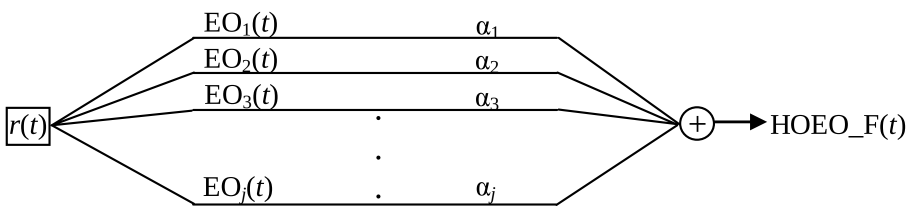

Fig 6.1. Model of minimum entropy fusion of higher order energy operator.

In the following section, the proposed method will be examined in different EO orders for different noise levels to determine the optimum EO order for bearing fault detection.

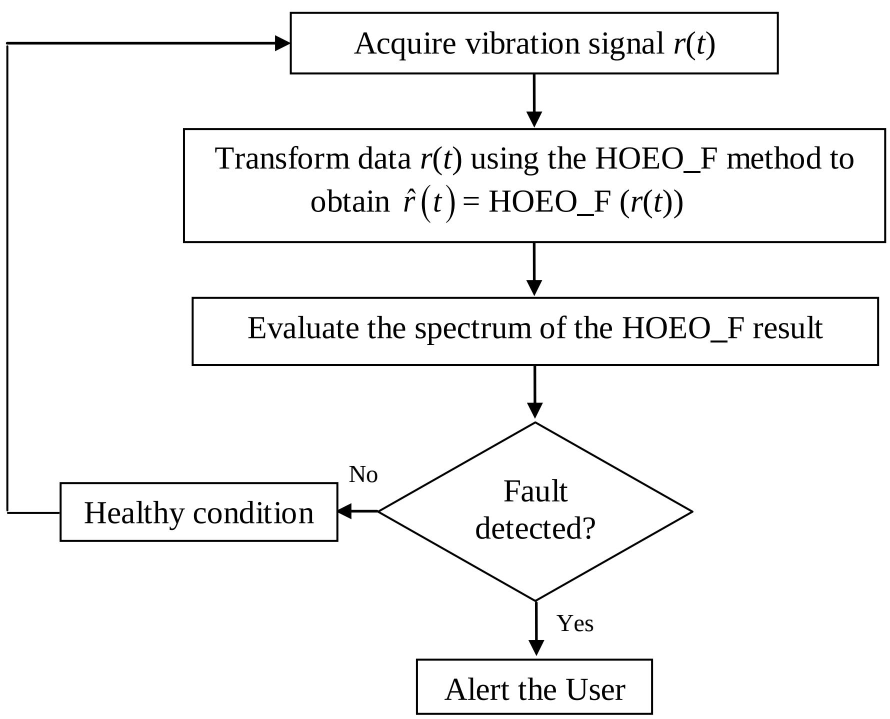

Fig. 6.2. Flowchart of the proposed method.

6.2.2 SNR gain from HOEO_F

In this section, the performance of HOEO_F is evaluated in the presence of noise to determine the optimum order level (*J*). For this purpose, we blend the variety simulated signal of a faulty bearing with different levels of noise. A typical signal of a faulty bearing is plotted in Fig 6.3. Then, the signal-noise mixtures are processed by the HOEO_F method in different order, *J*. Based on the method reported in (Cohen and Berdugo, 2002), the SNR results are obtained after processing the signal mixtures with different initial SNR's using the proposed method as shown in Table 6.1.

Note that in Table 6.1, the result for each case is the average of 100 simulation trials of different faulty bearing signals. As we can see from the table, the SNR can be boosted using the HOEO_F approach for all the five different *J*'s comparing with the conventional energy operator which is indicated by J=2. Among them, the fifth-order and sixth-order HOEO_F results are the best for all initial signal mixtures with SNR improved by more than 5 dB for all cases. It should be noted that the best EO order may vary for signals of different natures. However, as faulty bearing signals are mostly composed of impulses and random noise similar to the above simulated case, we will choose the sixth order HOEO_F for further analysis in the following sections.

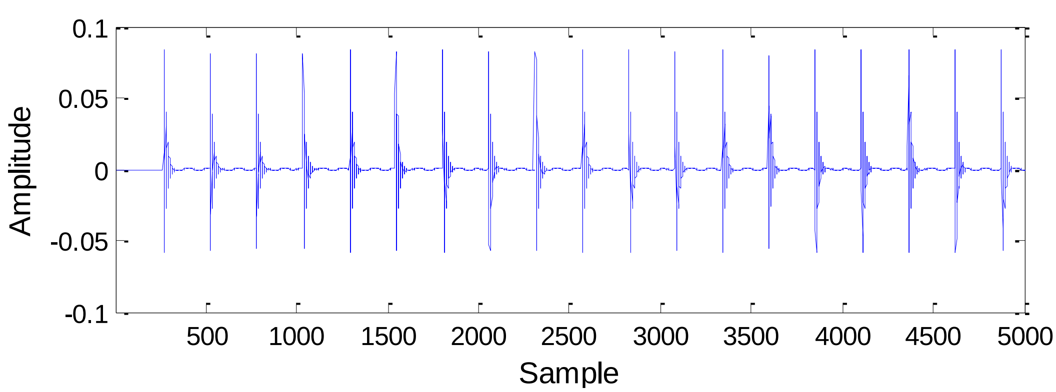

Fig. 6.3. Typical simulated of faulty bearing signal.

Table 6.1 SNR results obtained using the HOEO_F with different *J*'s (Note: the result presented for each initial SNR and J combination is the average of 100 simulation trials of different simulated faulty bearing signals).

Initial SNR (dB) (Before applying the HOEO_F method)	Final SNR (dB) (After applying the HOEO_F method)						
	J=2	*J*=3	*J*=4	***J*=5**	***J*=6**	*J*=7	*J*=8
10	9.36	14.11	15.83	**16.2**	**16.41**	15.61	13.95
12	11.16	15.9	17.05	**17.79**	**17.5**	16.77	15.21
14	13.25	18.26	20.25	**21.13**	**21.07**	19.39	17.9
16	14.8	20.32	21.97	**22.34**	**22.4**	21.32	19.86
18	16.9	21.87	24.16	**24.8**	**24.93**	23.63	21.59

6.2.3 SIR gain from HOEO_F

According to the results of Section 6.2.2, we examine the effect of HOEO_F on SIR improvement using up to six orders of EO's. Accordingly, the signal-to-interference ratio of the HOEO_F processed faulty bearing signal is (based on Eq. (6.5))(See Appendix A for derivation)

$$\mathrm{SIR}\left(\mathrm{HOEO\_F}\left(r(t)\right)\right)=\frac{\left(\dfrac{1}{T_P}\right)\int_0^{T_P}\left[\alpha_2^*\,\mathrm{EO}_{2_x}{}^2+\alpha_3^*\,\mathrm{EO}_{3_x}{}^2+\alpha_4^*\,\mathrm{EO}_{4_x}{}^2+\alpha_5^*\,\mathrm{EO}_{5_x}{}^2+\alpha_6^*\,\mathrm{EO}_{6_x}{}^2\right]e^{-4\beta t}\,\mathrm{d}t}{\left(\dfrac{1}{T}\right)\int_0^{T}\left[\sum_{k=1}^{K}\alpha_2^*L_k^4\omega_{Ik}^4+\sum_{k=1}^{K}\alpha_4^*L_k^4\omega_{Ik}^8+\sum_{k=1}^{K}\alpha_6^*L_k^4\omega_{Ik}^{12}\right]\mathrm{d}t}$$
$$\approx\frac{\left(\dfrac{1}{T_P}\right)\int_0^{\infty}\left[\alpha_2^*\,\mathrm{EO}_{2_x}{}^2+\alpha_3^*\,\mathrm{EO}_{3_x}{}^2+\alpha_4^*\,\mathrm{EO}_{4_x}{}^2+\alpha_5^*\,\mathrm{EO}_{5_x}{}^2+\alpha_6^*\,\mathrm{EO}_{6_x}{}^2\right]e^{-4\beta t}\,\mathrm{d}t}{\left(\dfrac{1}{T}\right)\int_0^{T}\left[\sum_{k=1}^{K}\alpha_2^*L_k^4\omega_{Ik}^4+\sum_{k=1}^{K}\alpha_4^*L_k^4\omega_{Ik}^8+\sum_{k=1}^{K}\alpha_6^*L_k^4\omega_{Ik}^{12}\right]\mathrm{d}t} \tag{6.16}$$

where the subscript x indicates the amplitude demodulation result of each order, and EO_{jx} (j=1,2,…,6) are respectively

$$\mathrm{EO}_{2_x}\left(r\left(t\right)\right)=A^2\omega_r{}^2$$

$$\mathrm{EO}_{3_x}\left(r(t)\right) = 2A^2\beta\omega_r{}^2$$

$$\mathrm{EO}_{4_x}\left(r(t)\right) = A^2\left(3\beta^2\omega_r{}^2 - \omega_r{}^4\right)$$

$$\mathrm{EO}_{5_x}\left(r(t)\right) = A^2\left(4\beta\omega_r{}^4 - 4\beta^3\omega_r{}^2\right)$$

$$\mathrm{EO}_{6_x}\left(r(t)\right) = A^2\left(\omega_r{}^6 + 5\beta^4\omega_r{}^2 - 10\beta^2\omega_r{}^4\right)$$

The above EO_{jX}'s are only the amplitude demodulated parts of the corresponding EO_j's. It should be mentioned again that to calculate SIR, we consider the amplitude demodulation term (i.e., the first term of Eqs. (3.10) and (6.4)) and the interference signal contents (i.e., the third term of Eqs. (3.10) and (6.4)) will be taken into account in calculating the powers associated with the fault impulsive signal component and the interference component respectively for obtaining the signal-to-interference ratio of the transformed signal (Liang and Soltani Bozchalooi, 2010).

After integrations and some simplifications, we have

$$\mathrm{SIR}\left(\mathrm{HOEO\_}F\left(r(t)\right)\right) \approx \frac{A^4\omega_r{}^4\left(\left(\alpha_2^* + 4\alpha_3^*\beta^2\right) + \left(\alpha_4^* + 16\alpha_5^*\beta^2\right)\omega_r^4 + \alpha_6^*\omega_r^8\right)}{4T_P\beta\left(\sum_{k=1}^{K} L_k^4\omega_{Ik}^4\left(\alpha_2^* + \alpha_4^*\omega_{Ik}^4 + \alpha_6^*\omega_{Ik}^8\right)\right)} \tag{6.17}$$

Finally, the SIR of the HOEO_F processed signal and that of the traditional EO processed signal are compared using Eqs. (6.7) and (6.17).

$$\frac{\mathrm{SIR}\left(\mathrm{HOEO\_F}\left(r(t)\right)\right)}{\mathrm{SIR}\left(\psi\left(r(t)\right)\right)} \approx \frac{\sum_{k=1}^{K} L_k^4\omega_{Ik}^4\left(\left(\alpha_2^* + 4\alpha_3^*\beta^2\right) + \left(\alpha_4^* + 16\alpha_5^*\beta^2\right)\omega_r^4 + \alpha_6^*\omega_r^8\right)}{\sum_{k=1}^{K} L_k^4\omega_{Ik}^4\left(\alpha_2^* + \alpha_4^*\omega_{Ik}^4 + \alpha_6^*\omega_{Ik}^8\right)} \gg 1 \tag{6.18}$$

As β>>1, and resonant frequency ω_r is generally much higher than the interference frequency ω_{Ik}, Eq. (6.18) indicates that the SIR of the HOEO_F processed signal is much higher than that of the signal processed by the traditional EO. In view that the HOEO_F can improve both the SNR and SIR, we will use it to extract bearing fault signature. The associated procedure can be summarized in the flowchart shown in Fig. 6.2.

6.3 Simulation evaluation

In this section, the HOEO_F method is examined using simulation data of a faulty bearing in the following three cases:

Case (a): A faulty bearing signal with high level of vibration interferences and low level of noise.

Case (b): A faulty bearing signal with high level of noise and low level of vibration interferences.

Case (c): A faulty bearing signal with high levels of noise and vibration interferences.

The vibration of a faulty bearing can be represented by sequences of fault impulses as follow [reproduced from Eq. (3.1) for convenience] (Bozchalooi and Liang, 2010; Liang and Soltani Bozchalooi, 2010)

$$x(t) = \sum_{m=-M}^{M} A_m e^{-\beta\left(t-mT_p-\tau\right)} \cos\left(\omega_r\left(t-mT_p-\tau+\theta_m\right)\right) u\left(t-mT_p-\tau\right) \tag{6.19}$$

where A_m represents the amplitude of faulty signature, β is the structural damping characteristic frequency, ω_r is the excited resonance frequency, T_p represents the time period corresponding fault characteristic frequency, τ is the factor of random slippage with standard deviation of 0.01 T_p ~0.02 T_p, and $x(t)$ is the vibration signal corresponding to fault generated impulses (2M+1). Such faulty bearing model is plotted in Fig. 6.3.

To simulate the above cases, the signal model is obtained by adding both interferences and noise to the faulty bearing model (Eq. (6.19)), i.e.

$$\begin{aligned} r(t) = & \sum_{m=-M}^{M} A_m e^{-\beta\left(t-mT_p-\tau\right)} \cos\left(\omega_r\left(t-mT_p-\tau+\theta_m\right)\right) u\left(t-mT_p-\tau\right) \\ & +\sum_{k=1}^{K} L_k \cos\left(\omega_{Ik} t\right) + w(t) \end{aligned} \tag{6.20}$$

where L_k and ω_{Ik} are respectively the amplitude and frequency of kth interfering component, and $w(t)$ represents noise.

In the following simulation tests, the fault characteristic frequency is 80 Hz, β is 1500 Hz, four vibration interferences with frequencies of 33 Hz, 43 Hz, 50 Hz, and 310 Hz are employed. In addition, the signal is further blended with white Gaussian noise for examinations. For this purpose, the 'awgn' MATLAB command is used to generate white Gaussian noise.

6.3.1 Simulated faulty impulse bearing in the presence of high levels of interference components-Case (a)

In this case, the signal mixture is shown in Fig. 6.4(a) with a SNR of 5 dB, and a SIR of -45 dB. The frequency representation of the signal is plotted in Fig. 6.4(b) where the four interferences dominate the spectrum and the fault frequency cannot be observed. The envelope and EO spectra presented in Figs. 6.5(a) and (b) cannot reveal the fault signature at 80 Hz either. The ADD, CEEO and HO_AEO results are displayed respectively in Figs. 6.5(c), (d) and (e). No fault signature can be detected by the CEEO method. Though the ADD and HO_AEO methods can extract FCF and its harmonics, they are of low magnitude and are clouded by noise and interferences. It should be clarified that the high magnitude of the ADD method is because that the multiplication of the second order differentiation of the AD by the square of the sampling frequency in the ADD process. The HOEO_F method is then applied to the signal mixture with the result shown in Fig. 6.6 where the peaks at the fault characteristic frequency and several of its harmonics clearly stand out.

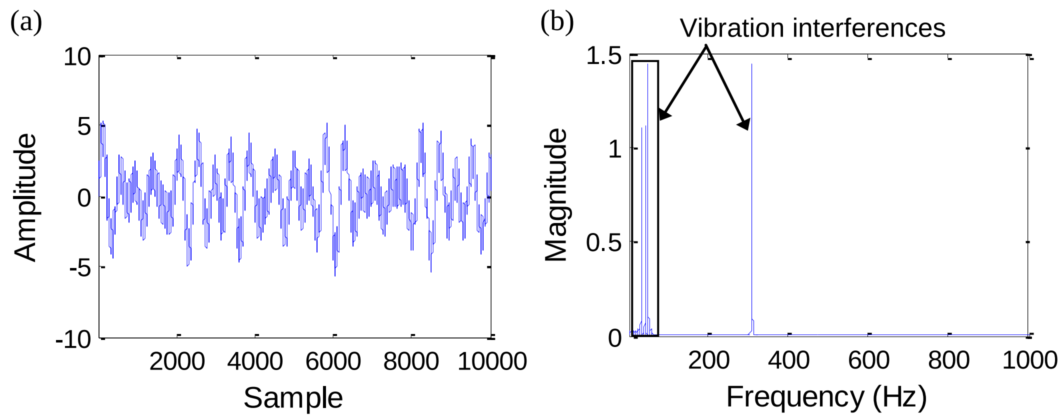

Fig. 6.4. (a) Simulated faulty bearing signal with high level of vibration interferences (SIR= -45 dB) and low level of noise (SNR= 5 dB), and (b) spectrum of the simulated signal.

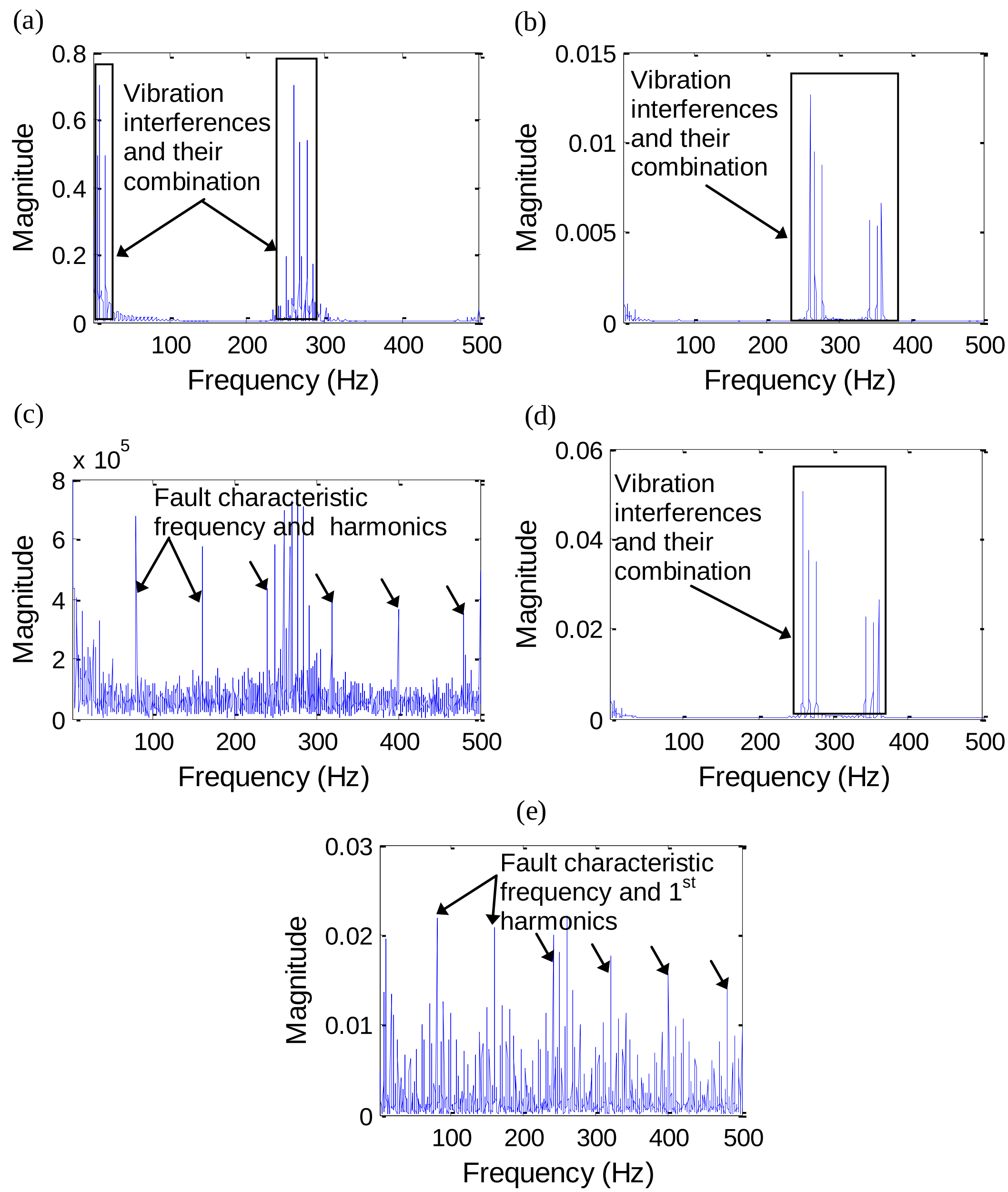

Fig. 6.5. (a) Envelope spectrum of the signal, (b) spectrum of the energy operator processed signal, (c) envelope spectrum obtained by the ADD method, (d) spectrum obtained by the CEEO method, and (e) Spectrum of the HO_AEO processed simulation signal.

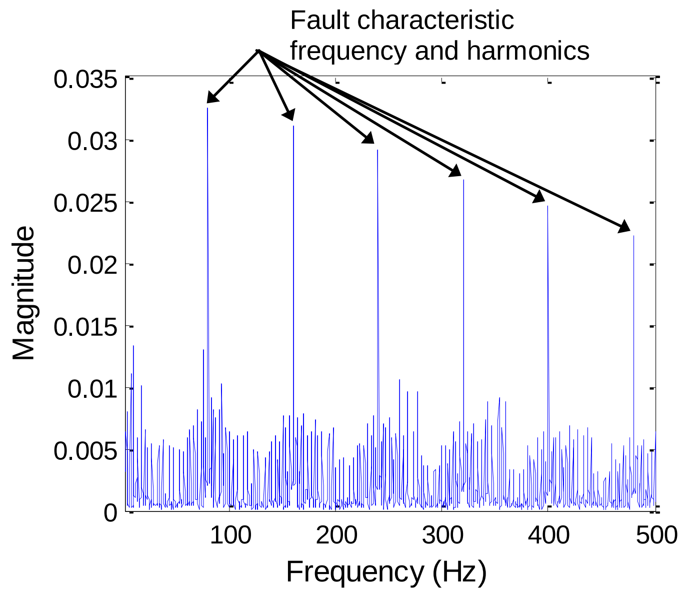

Fig. 6.6. Spectrum of the HOEO_F processed simulation signal.

6.3.2 Simulated signal of a faulty bearing with high level of noise – Case (b)

The focus of this case is on the performance of the HOEO_F method in handling high-level noise. As such, the noise level is increased in the signal mixture (SNR=-19dB) and the strength of the interfering components is reduced (SIR=5dB). The time- and frequency-domain representations of the signal mixture are displayed in Figs. 6.7(a) and (b) respectively. The fault signature cannot be identified form Fig. 6.7.

Applying the envelope method and energy operator method to the same signal mixture leads to the results illustrated in Figs. 6.8 (a) and (b), respectively, but neither can extract the fault signature.

Then the signal is processed by the ADD, CEEO, and HO_AEO methods with results shown respectively in Figs. 6.8(c), (d) and (e). Obviously the ADD and CEEO methods are not effective. The HO_AEO method can extract defect frequencies, reflecting its noise handling capability.

Next, the proposed method is employed to process the signal mixture with the output plotted in Fig. 6.9 which clearly shows the fault characteristic frequency at 80 Hz and its harmonics. This result demonstrates that the proposed method can better handle strong noise than the enveloping, traditional EO, ADD and CEEO methods.

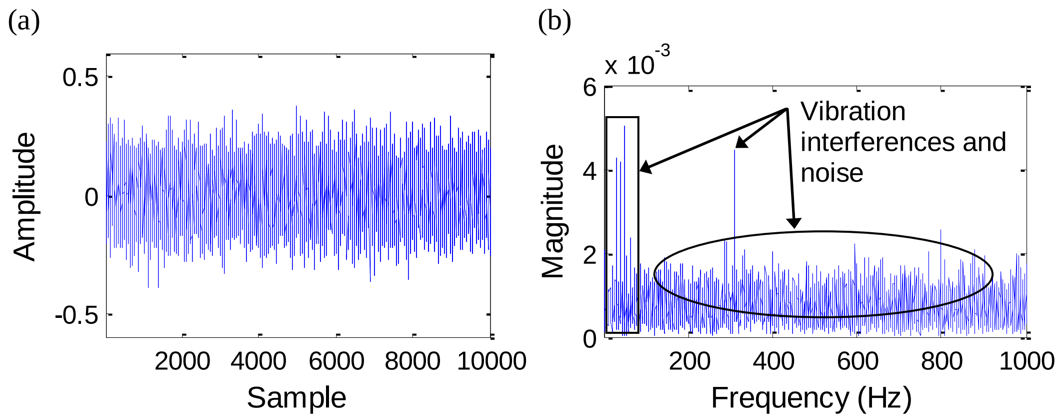

Fig. 6.7. (a) Simulated faulty bearing signal with harsh noise (SNR= -19 dB) and low level of interferences (SIR= 5 dB), and (b) spectrum of this simulated signal.

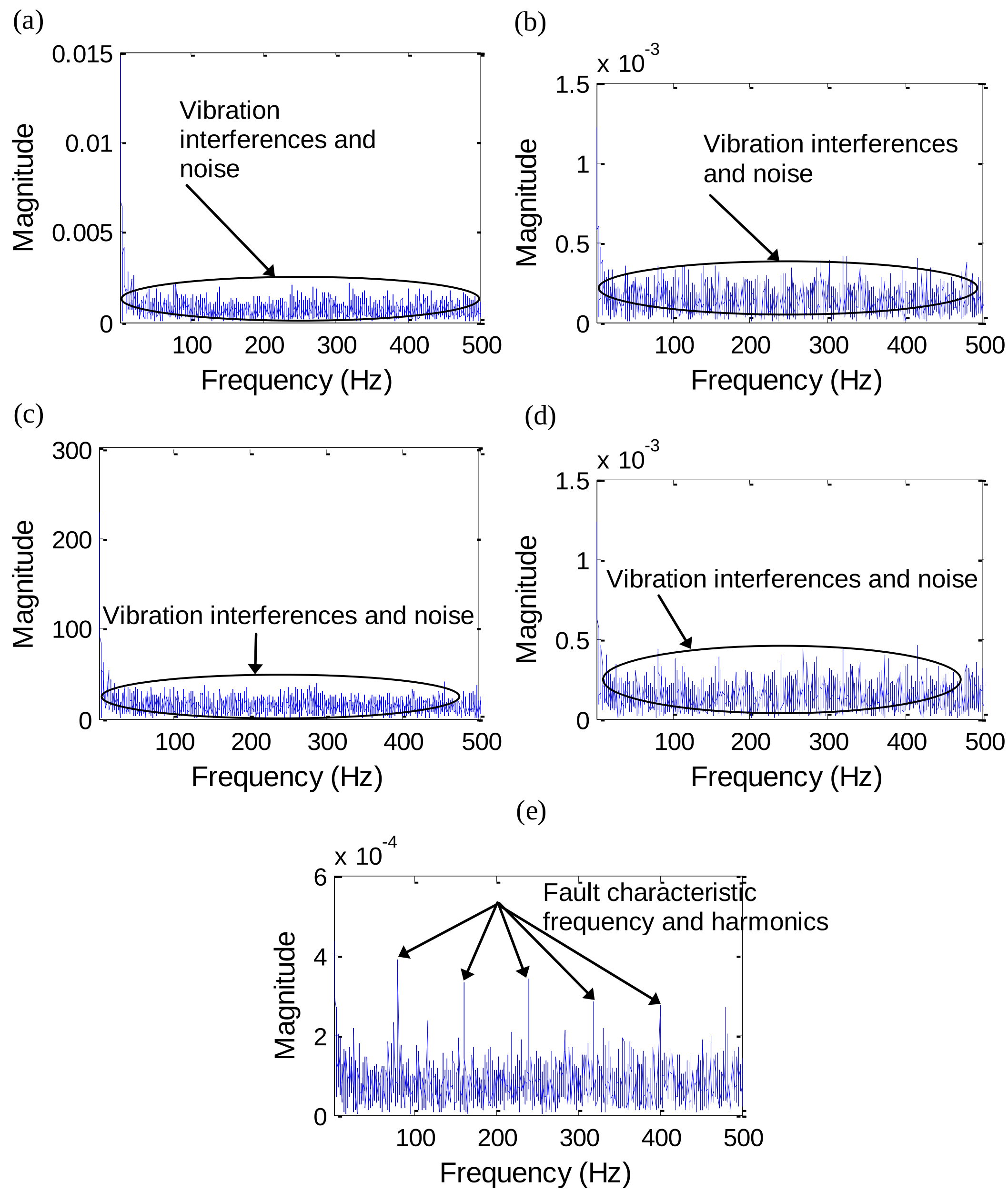

Fig. 6.8. (a) Envelope spectrum of the signal, (b) spectrum of the energy operator processed signal, (c) envelope spectrum obtained by the ADD method, (d) spectrum obtained by the CEEO method, and (e) spectrum obtained by the HO_AEO method.

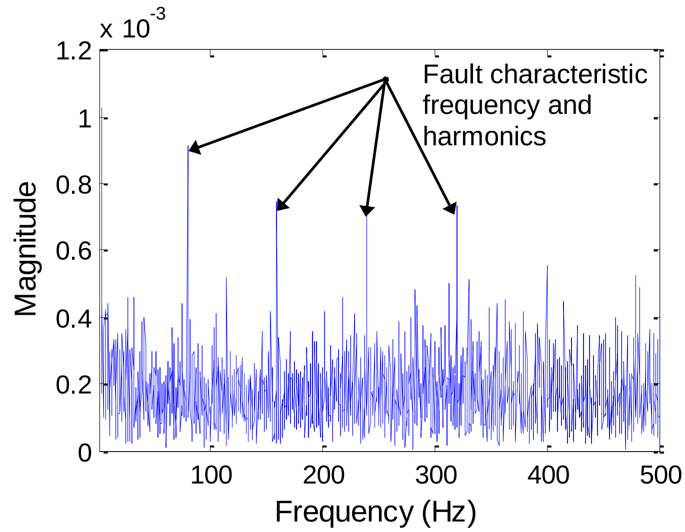

Fig. 6.9. Spectrum of the HOEO_F processed simulation signal.

6.3.3 Simulated signal of a faulty bearing with high level of noise and vibration interferences

In this subsection, the proposed method is tested by a signal which contains impulsive faulty bearing feature, harsh noise (-18 dB) and multiple strong vibration interferences (-20 dB). The mixed signal and its spectrum are plotted in Fig. 6.10. The results of envelope, energy operator, ADD, CEEO and HO_AEO methods are presented in Figs. 6.11 (a), (b), (c), (d) and (e), respectively. In all the above results except the case of HO_AEO, the fault signature is severely obscured by the heavy noise and strong interfering components, making it impossible to detect the bearing fault. The HO_AEO method can reveal only the second and third harmonics of FCF.

In contrast, the HOEO_F method can still clearly reveal the fault characteristic frequency and multiple of its harmonics as shown in Fig. 6.12. It should be noted that the new method has been applied without using any filter and pre-processing.

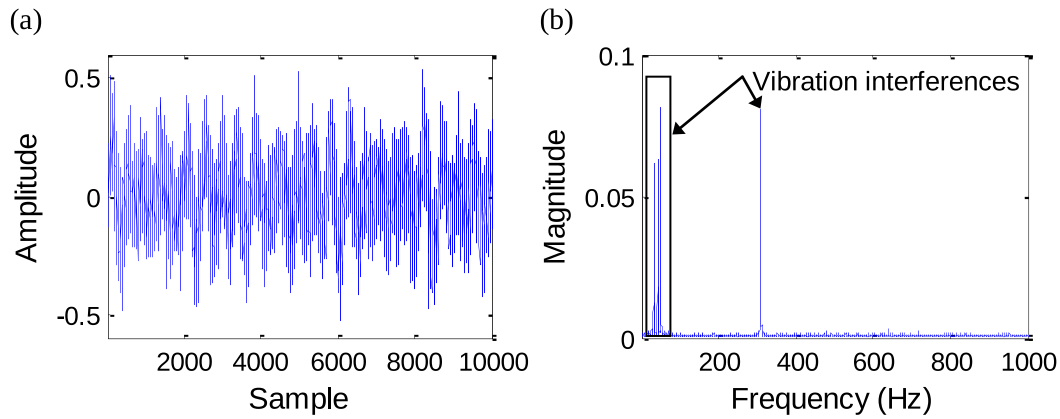

Fig. 6.10. (a) Simulated faulty bearing signal with harsh noise (SNR= -18 dB) and strong interfering components (SIR= -20 dB), and (b) spectrum of this simulated signal.

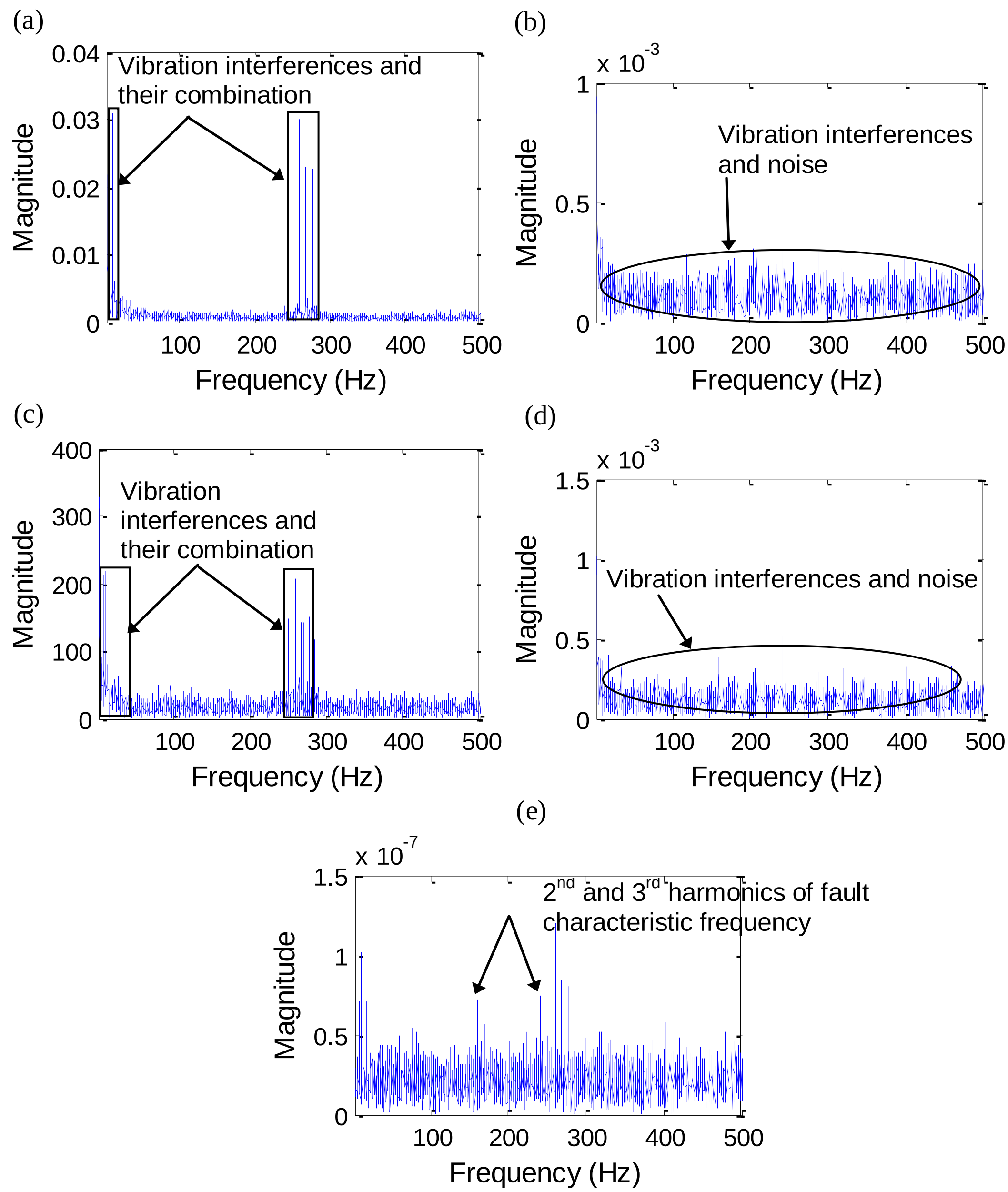

Fig. 6.11. (a) Envelope spectrum of the signal, and (b) spectrum of the energy operator processed signal, (c) envelope spectrum obtained by the ADD method, (d) spectrum obtained by the CEEO method , and (e) spectrum obtained by the HO_AEO method.

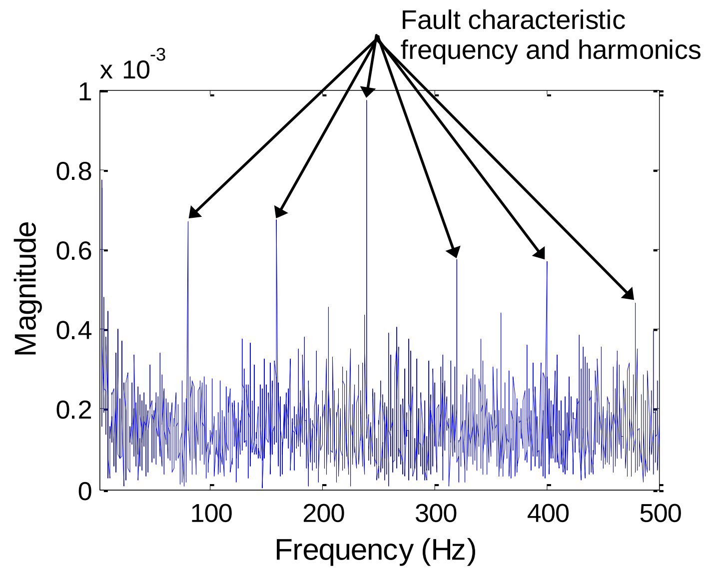

Fig. 6.12. Spectrum of the HOEO_F processed simulation signal.

6.4 Experimental evaluation

6.4.1 Detection of inner race bearing fault (experimental data from Machinery fault simulator)

Experimental data is obtained from a Spectra Quest Machinery fault simulator (MKF-PK5M) shown in Fig. 6.13. The simulator is driven by an AC motor and is controlled by a PWM Hitachi drive. Two bearings are mounted to support a steel shaft and a well-balanced mass rotor is fixed on the shaft. The normal bearing is installed on the left hand side, and a faulty bearing on the right hand side.

The vibration signal is collected by only one accelerometer mounted far away from both bearings but near a gearbox acting as a source of interference signal. The accelerometer signal is then fed to a PC through a DAQ card. The sampling frequency and other parameters are set up through LabVIEW. The vibration signal is sampled at 12,000 samples/s. Afterwards the measured signal is processed using MATLAB on a PC.

Other information of the experimental setup is as follows:

- Shaft: 1” in diameter.

- Mass rotors: 2” thick, 4” in diameter and 11.1 lbs.
- Bearings: Type ER16K with nine roller elements (balls). The inside, outside, pitch and ball diameters are, respectively, 1”, 2.0472”, 1.548” and 0.3125”.
- Accelerometer: PCB sensor, model 623C01 with sensitivity of 100 Mv/g and a sensitivity range of 1 to 20 kHz.
- PWM Hitachi drive: SJ200-022NFU.
- DAQ card: USB DAQ device.
- PC: Pentium 4 of 2.52 GHz speed.

The right bearing has a pre-seeded fault (created by manufacturer with unknown dimensions) on the inner race with the characteristic frequency of 137.3 Hz (=5.4152 f_r, specified in the simulator user’s manual). The shaft speed is fixed at 1518 RPM (25.3 Hz). The gearbox is connected to the main shaft with associated gear meshing frequency at174.6 Hz. In addition, white Gaussian noise (SNR= -3dB) and also another interference at 800 Hz are added to both the healthy and faulty bearing signals to provide much more complex signal. As shown in Fig. 6.13, the accelerometer is placed on the simulator base close to the gearbox but a location away from the bearing.

The faulty bearing signal and its spectrum are illustrated in Fig. 6.14. The fault characteristic frequency of inner race fault, 137.3 Hz, cannot be identified from Fig. 6.14 (b). The results of envelope, energy operator, ADD, CEEO and HO_AEO methods are demonstrated in Figs. 6.15(a)-(e). As one can see, only can the CEEO and HO_AEO methods vaguely reveal the frequency related to inner race fault. However, the fault characteristic frequency and two of its harmonics are evidently distinguished from other signal components after applying the HOEO_F method as illustrated in Fig. 6.16.

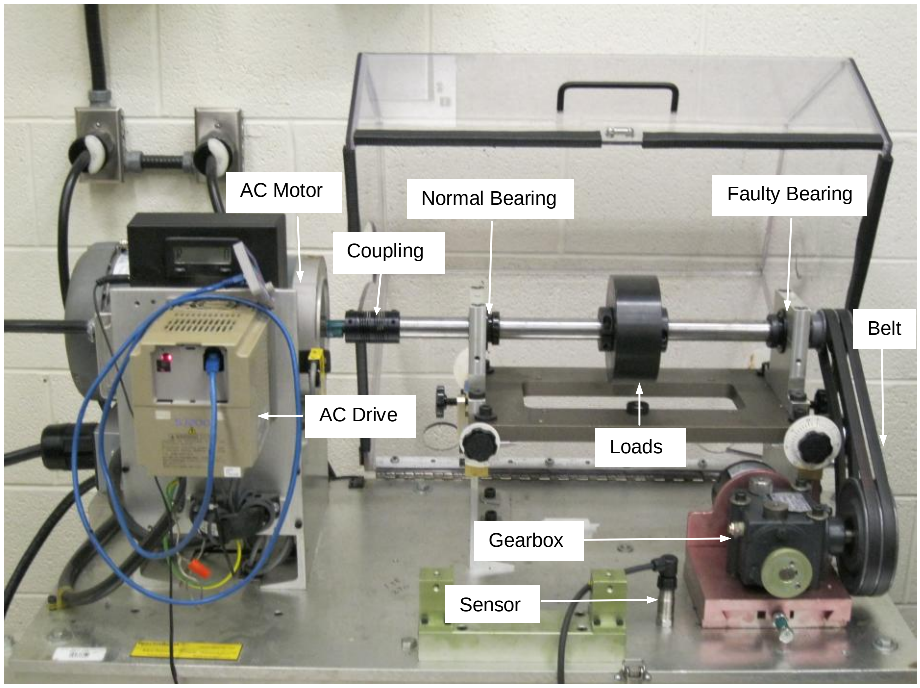

Fig. 6.13. Experimental setup.

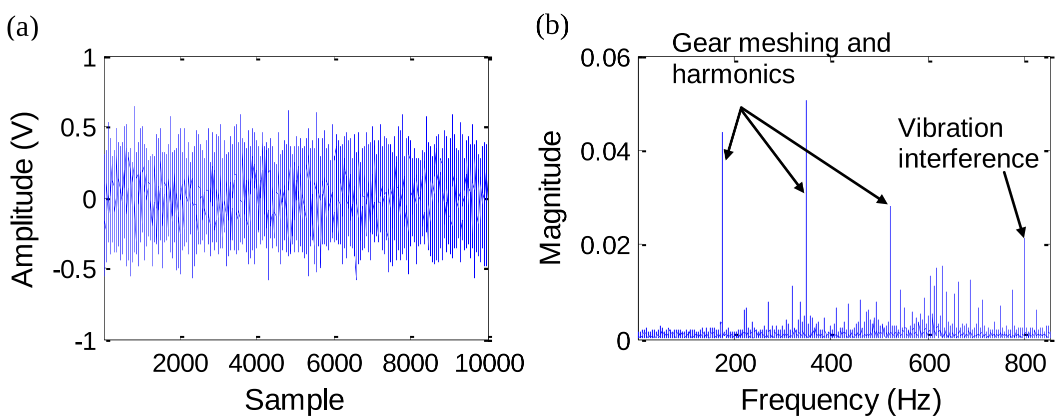

Fig. 6.14. (a) Measured signal of inner race fault, and (b) spectrum of a faulty bearing signal.

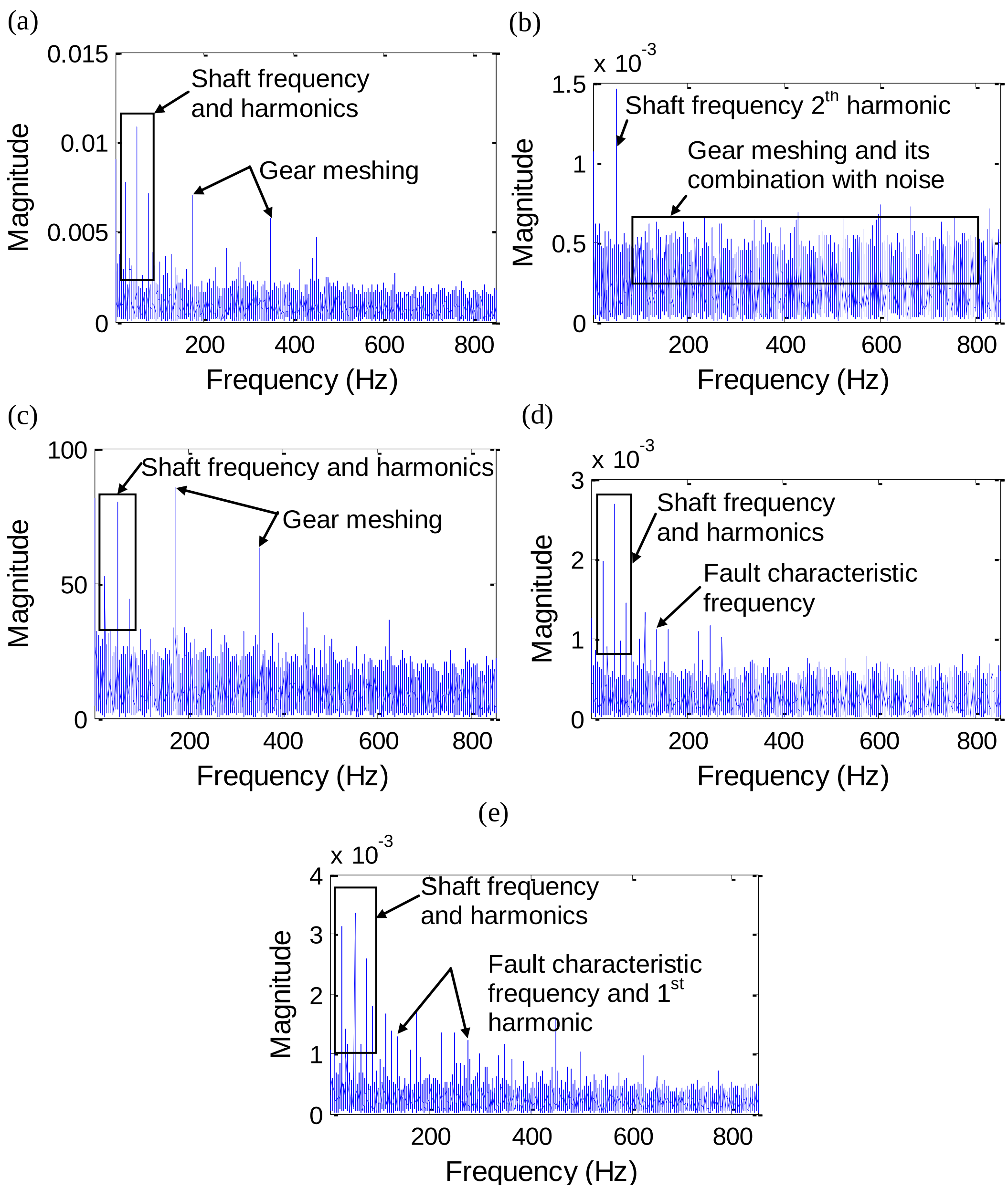

Fig. 6.15. (a) Envelope spectrum of the outer race faulty bearing signal shown in Fig. 6.14(a), and (b) the spectrum of the energy operator result, (c) envelope spectrum obtained by the ADD method, (d) spectrum obtained by the CEEO method, and (e) spectrum obtained by the HO_AEO method.

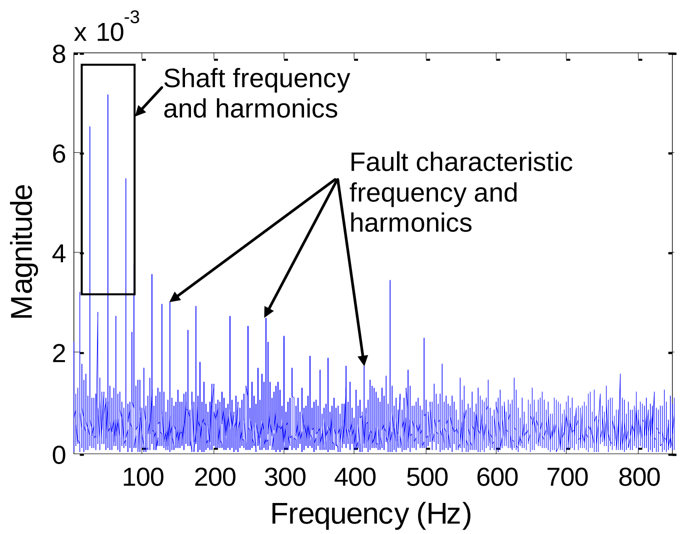

Fig. 6.16. Spectrum of the faulty inner race bearing signal (shown in Fig. 6.14(a)) obtained by the HOEO_F method.

6.4.2 Detection of outer race bearing fault (experimental data from Machinery fault simulator)

In this test, the setup is the same as in the previous test except that the inner race faulty bearing is replaced by one (also type ER16K) with an outer race fault on the right side of the shaft. Like in the inner race fault test, the gearbox is driven by the shaft through a belt connection and the accelerometer is kept in the same place. The shaft speed is set at 888 RPM (14.8 Hz). The outer race fault is created by the manufacturer with unknown dimensions. The related frequency of outer race fault is 53.1 Hz (=3.5848 f_r, specified in the simulator user's manual). The meshing frequency of gearbox is 104.2 Hz. White Gaussian noise (SNR= -3dB) is also added to the collected signal. Figs. 17(a) and (b) respectively show the raw signal of the outer race fault and its spectrum without any indication of the outer race fault feature.

The results of the envelope, energy operator, ADD, CEEO, and HO_AEO methods are shown in Figs. 6.18(a)-(e), respectively. Obviously, in the cases of the envelope, energy operator, ADD, CEEO methods, the faulty bearing signatures cannot be detected through their spectra because the meshing frequency and noise cover a whole range of spectra. Only the HO_AEO method could recognize fault characteristic frequency and three of its harmonics. However, as compared with the HOEO_F results shown in Fig. 6.19, the noise floor in the result of the HO_AEO is higher than that in the HOEO_F results.

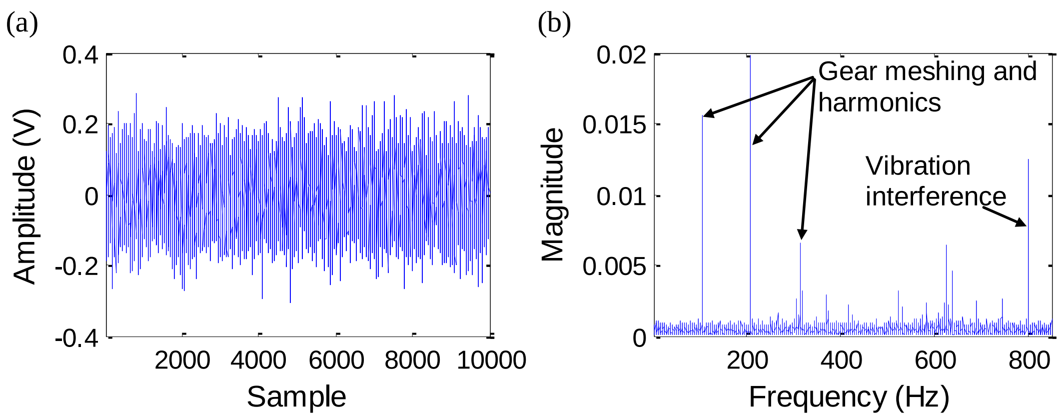

Fig. 6.17. (a) Measured signal of outer race fault, and (b) spectrum of the faulty bearing signal.

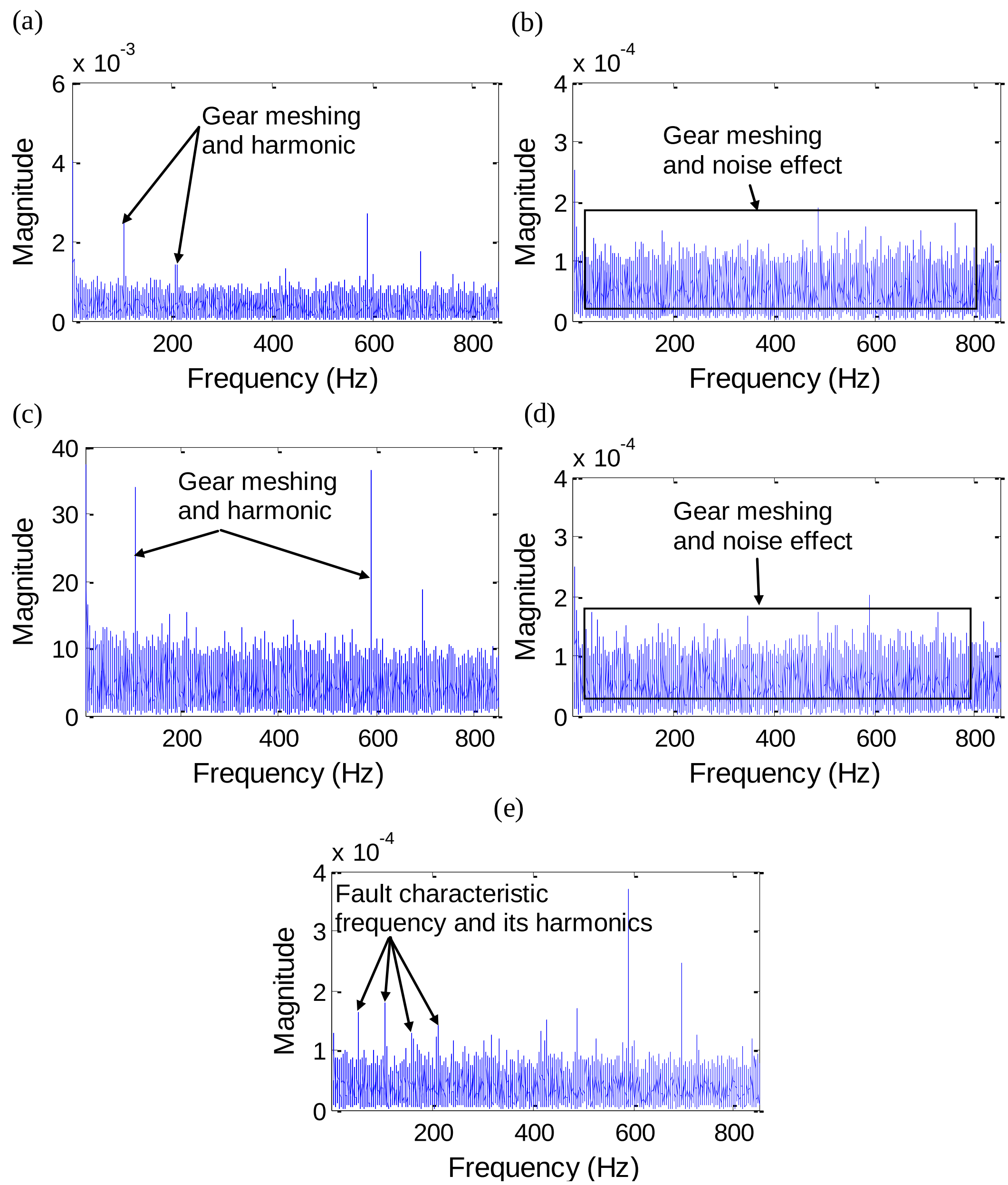

Fig. 6.18. (a) Envelope spectrum of the faulty bearing signal (shown in Fig. 6.17(a)), and (b) the spectrum of the energy operator result of the same raw signal, (c) envelope spectrum obtained by the ADD method, (d) spectrum obtained by the CEEO method, and (e) spectrum obtained by the HO_AEO method.

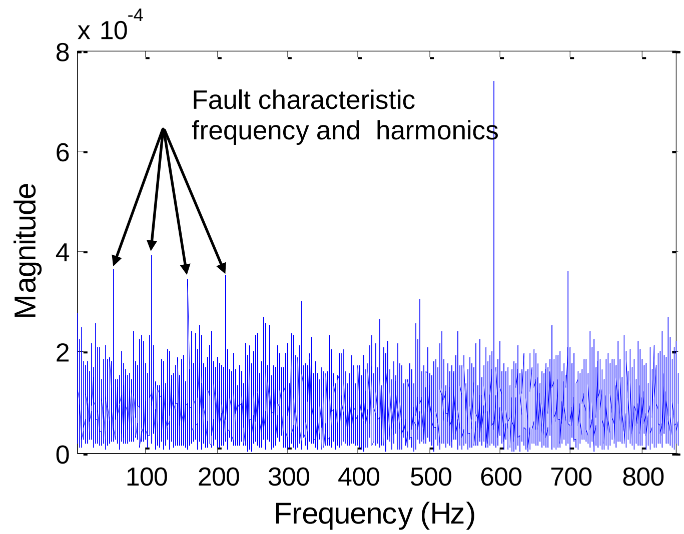

Fig. 6.19. Spectrum of the HOEO_F processed faulty outer race bearing signal.

The above experimental results demonstrate that the HOEO_F approach is much more effective than the envelope, energy operator, ADD and CEEO methods in detecting both inner and outer race bearing faults from signals obscured by both harsh noise and strong vibration interferences. Comparing Figs. 6.19 and 6.18 (e) indicates that the HOEO_F method also outperforms the HO_AEO method.

6.5 Conclusion

A non-resonance based method has been developed using the information from multiple higher order EOs. It is demonstrated that higher order EOs can diminish effect of interfering vibration signal components. However, due to differentiation operator inherent in the EOs, the noise effect may also be amplified level in the EO transformed signal. It is illustrated that averaging the higher order EOs can alleviate this difficulty. The effectiveness of the proposed method in extracting bearing fault from signals contaminated by both strong noise and interferences have been validated using both simulated and experimental data. For comparison, the same datasets are also processed by the envelope and plain energy operator methods but neither can extract any fault signature. As this method does not rely on the excitation resonance information and can be implemented in a single simple step, it is suited for on-line bearing fault detection.

Chapter 7

Comparison of non-parametric, non-filtering methods using fault detection map (FDM)[5]

This chapter first proposes fault detectability map (FDM) to compare several non-parametric, non-filtering fault detection methods in terms of their interference and noise handling capabilities. The FDM provides a comprehensive view of the fault detection capability of each method under different SNR and SIR levels. Hence fair comparison could be made between the existing and proposed non-parametric and non-filtering methods. In this chapter, the comparisons will be conducted using a simulation model, followed by discussions.

7.1 The fault detectability map (FDM)

The FDM is a two dimensional representation of the fault detection capability of a given method at different SNR and SIR levels. Generally, a fault is considered as detected if its characteristic frequency and a few of its harmonics are observed in the frequency spectrum. In this chapter, the fault is said detected if the amplitudes of the fault characteristic frequency and its first two harmonics (of course, more harmonics could be used) are all higher than the universal threshold. Hence an important step is to apply the threshold function over the frequency domain.

In this research, the widely used universal threshold is adopted due to its simplicity which is expressed as

[5] See Appendix B.5 for MATLAB script.

$$\Gamma = \sigma\sqrt{2\log N}, \qquad \sigma = MAD / 0.6745 \tag{7.1}$$

where N is a length of a given signal sample, and MAD represents the median absolute deviation.

In addition, there are two typical thresholding methods, i.e., hard and soft thresholding. The hard thresholding method can be expressed by (Wang and Liang, 2009)

$$\delta_\Gamma = \begin{cases} 0 & \left|d_{jk}\right| < \Gamma \\ d_{jk} & \left|d_{jk}\right| \ge \Gamma \end{cases} \tag{7.2}$$

In order to find the number of peaks associated with fault characteristic frequency, the hard thresholding is applied in the frequency domain. To illustrate the FDM and compare different non-parametric fault detection methods, the following model is used to simulate bearing fault vibration signal with noise and interferences

$$\begin{aligned} r(t) = &\sum_{m=-M}^{M} A_m e^{-\beta\left(t-mT_p-\tau\right)} \cos\left(\omega_r\left(t-mT_p-\tau+\theta_m\right)\right)u\left(t-mT_p-\tau\right) \\ &+\sum_{k=1}^{K} L_k \cos\left(\omega_{Ik}t\right)+w(t) \end{aligned} \tag{7.3}$$

where A_m is the mth fault impulse amplitude, T_p is the time period corresponding to the fault characteristic frequency, β the structural damping characteristic frequency, ω_r the excited resonance frequency, τ represents the effect of random slippage of the rollers, L_k is the amplitude of the kth vibration interference, ω_{Ik} is the frequency of the kth vibration interference, and $w(t)$ is white Gaussian noise.

In the simulation, the parameters in the above model are as follows: K=4, A_m=1, β=1500, ω_r =2048 Hz, T_p =0.008, 0<τ<0.02, ω_{I1} =5Hz, ω_{I2} =27 Hz, ω_{I3} =43 Hz, and ω_{I4} =600 Hz. In addition, A_m is set to 1 for all m. The amplitudes of the interferences L_k are automatically specified by MATLAB based on the specified SIR level. The sampling frequency is 20 kHz.

The simulated signal is plotted in Fig. 7.1. The frequency spectrum of the simulated signal with SNR=-1 and SIR=-1 is shown in Fig. 7.2. As the fault characteristic frequency at

125 Hz and at least two of its harmonics can be identified, this can be plotted as a point at (SIR=-1, SNR=-1) in an FDM. White Gaussian noise is added to the simulated signal by using MATLAB command ‘awgn’.

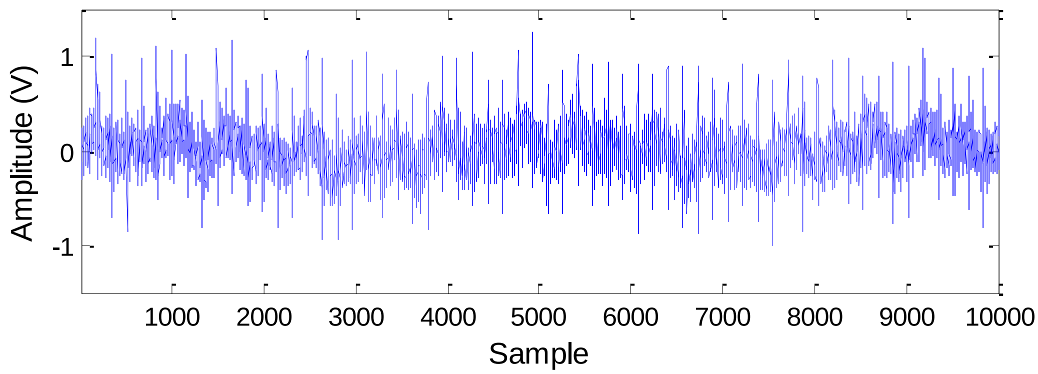

Fig. 7.1. Simulated signal of a faulty bearing with noise and vibration interference.

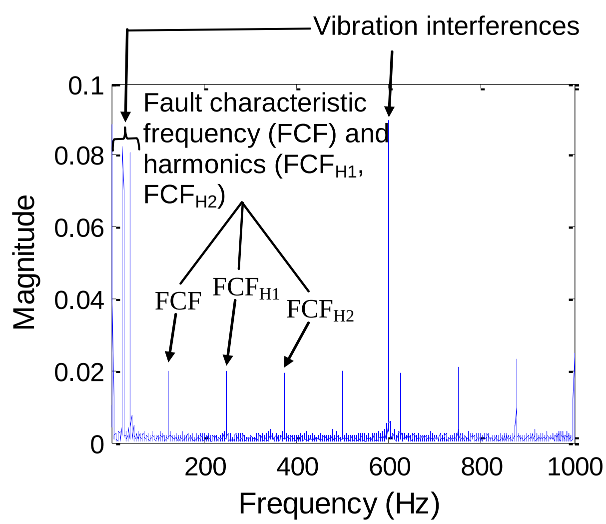

Fig. 7.2. Spectrum of the simulated signal in Fig 7.1.

7.2 Evaluation of non-parametric methods using FDM

In this section, eight methods, i.e., FT, envelope analysis, differentiation, energy operator, ADD, CEEO, HO_AEO, and HOEO_F will be evaluated using the FDM. For each (SIR, SNR) point in the map associated with each of the eight methods, the signal mixture of fault, noise and interference components will be generated by the model in Eq. (7.3) with the same parameters specified in section 7.1.

The FDMs for the eight methods, i.e., FT, envelope analysis, differentiation, energy operator, ADD, CEEO, HO_AEO, and HOEO_F can be plotted in Figs. 7.3 to 7.10, respectively. In all the eight figures, the FDM is plotted in the range of -60dB≤ SIR ≤5dB, -20dB≤ SNR ≤45 dB. The levels of detectability are represented by four levels of grayness. The white area means that the fault characteristic frequency and at least its first two harmonics have been detected. The light grey area indicates that only the fault characteristic frequency and its first harmonic can be identified. The dark grey zone represents the area where only the fault characteristic is detected and none of its harmonics can be identified. The black region is the area where the applied method cannot detect fault at all. Though the upper limits of the SIR and SNR in the eight figures are respectively 5 and 45 dB, it should be understood that, for areas where SIR>5 dB and SNR>45dB, all the eight methods are also effective (i.e., the fault characteristic frequency and at least its first two harmonics can be detected).

For example, the detection performance of the Fourier transform is shown in Fig. 7.3. This figure shows that the effective region of the Fourier transform method is limited to an irregular area roughly bounded by -33 dB< SIR <∞ dB, and -9 dB < SNR < ∞ dB.

Table 7.1 lists the effective areas of the eight methods. Of the four existing methods, i.e., FT, envelope, differentiation and energy operator, the differentiation method has the moderate interference handling capability but is the worst in dealing with noise. The energy operator offers better noise handling ability than the differentiation method but falls behind it in processing signals severely contaminated by noise. As expected, in comparison with the CEEO, the ADD is stronger in handling interferences but weaker in dealing with noise. On the other hand, the HO_AEO method can deal with noise and vibration interferences better than even the CEEO, and ADD methods. Finally, by developing the HOEO_F method, we could broaden the horizon of fault detectability, especially to achieve higher SIR comparing with the HO_AEO method. The performances of above methods are compared in Fig. 7.11.

Table 7.1 Approximate effective areas of eight non-parametric fault detection methods.

Detection method	**SIR limits (dB)**	**SNR limits (dB)**
FT (Fig 7.3)	SIR > -33	SNR≈ -9
Envelope analysis (Fig 7.4)	SIR > -20	SNR≈ -13
Differentiation (Fig 7.5)	SIR > -50	SNR≈ +2.5
Energy operator (Fig 7.6)	-33 > SIR > -40 SIR > -33	SNR≈ -11 SNR≈ -12
ADD (Fig 7.7)	-35 > SIR > -43 -10 > SIR > -35 SIR > -10	SNR≈ -5 SNR≈ -9 SNR≈ -15
CEEO (Fig 7.8)	-32 > SIR > -38 SIR > -32	SNR≈ -12 SNR≈ -16
HO_AEO (Fig 7.9)	--50 > SIR > -44 -44 > SIR > -32 -32 > SIR > -22 SIR > -22	SNR≈ -10 SNR≈ -15 SNR≈ -17 SNR≈ -19
HOEO_F (Fig 7.10)	-58 > SIR > -50 -50 > SIR > -25 SIR > -25	SNR≈ -2 SNR≈ -14 SNR≈ -19

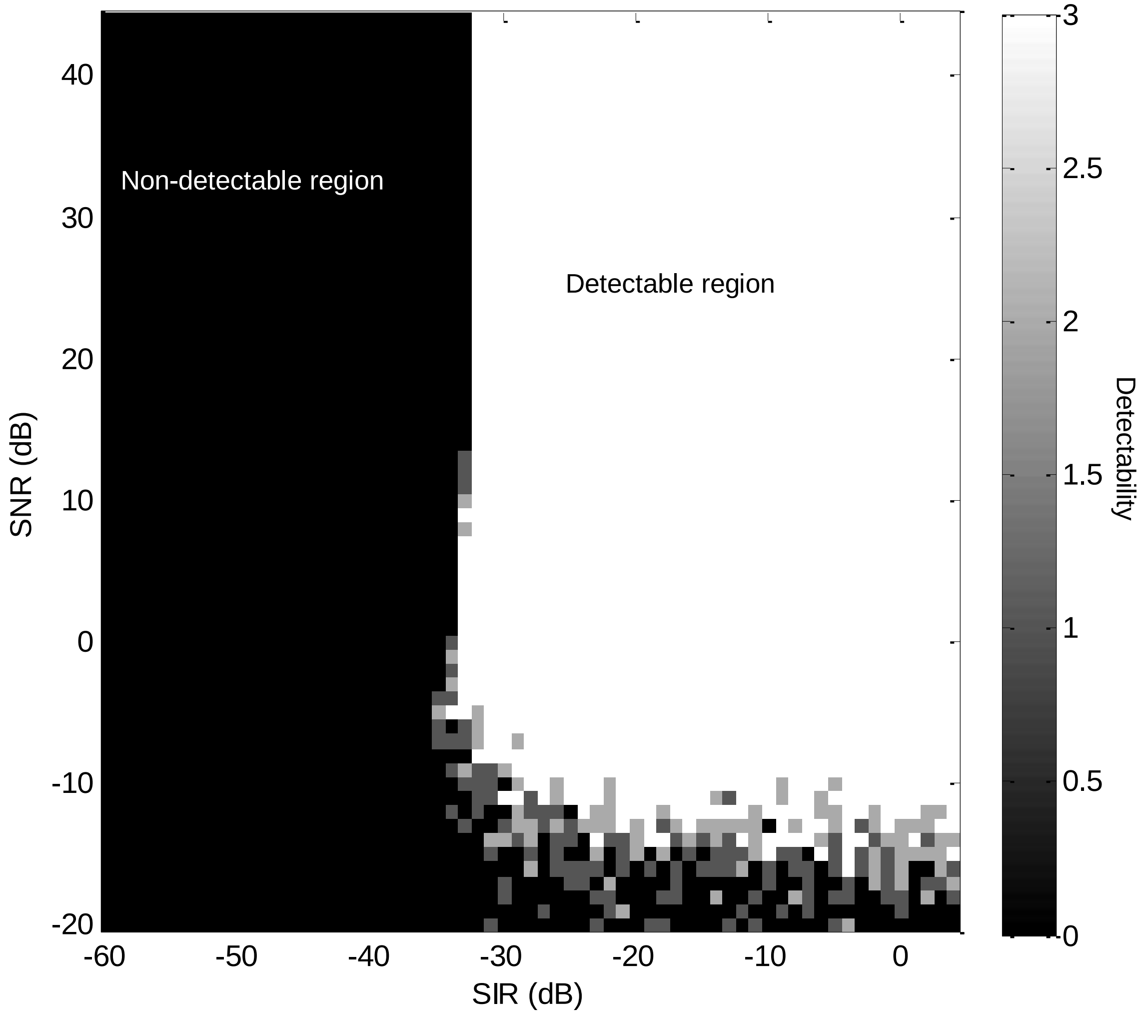

Fig. 7.3. Fault detectability map of the Fourier transform method.

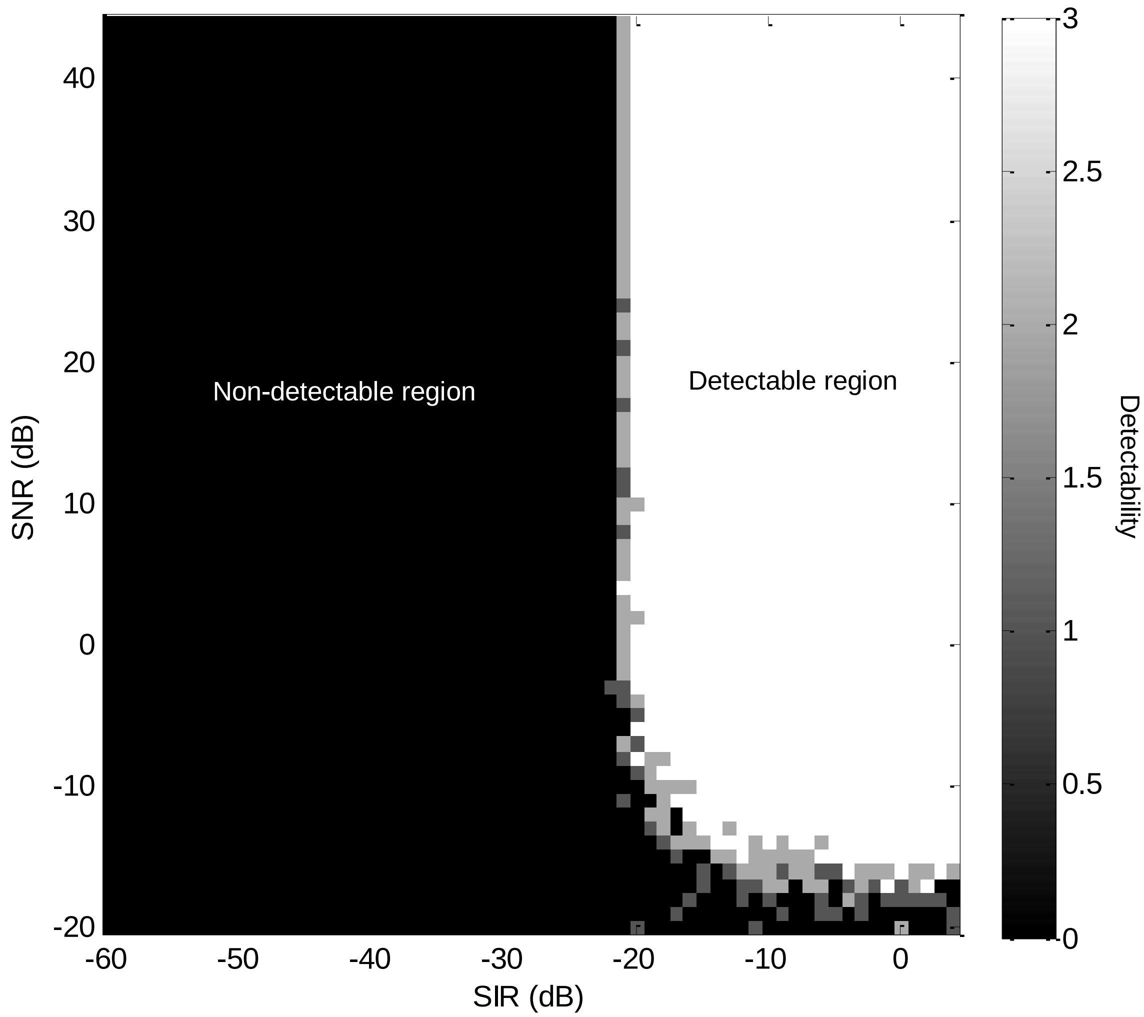

Fig. 7.4. Fault detectability map of the envelope method.

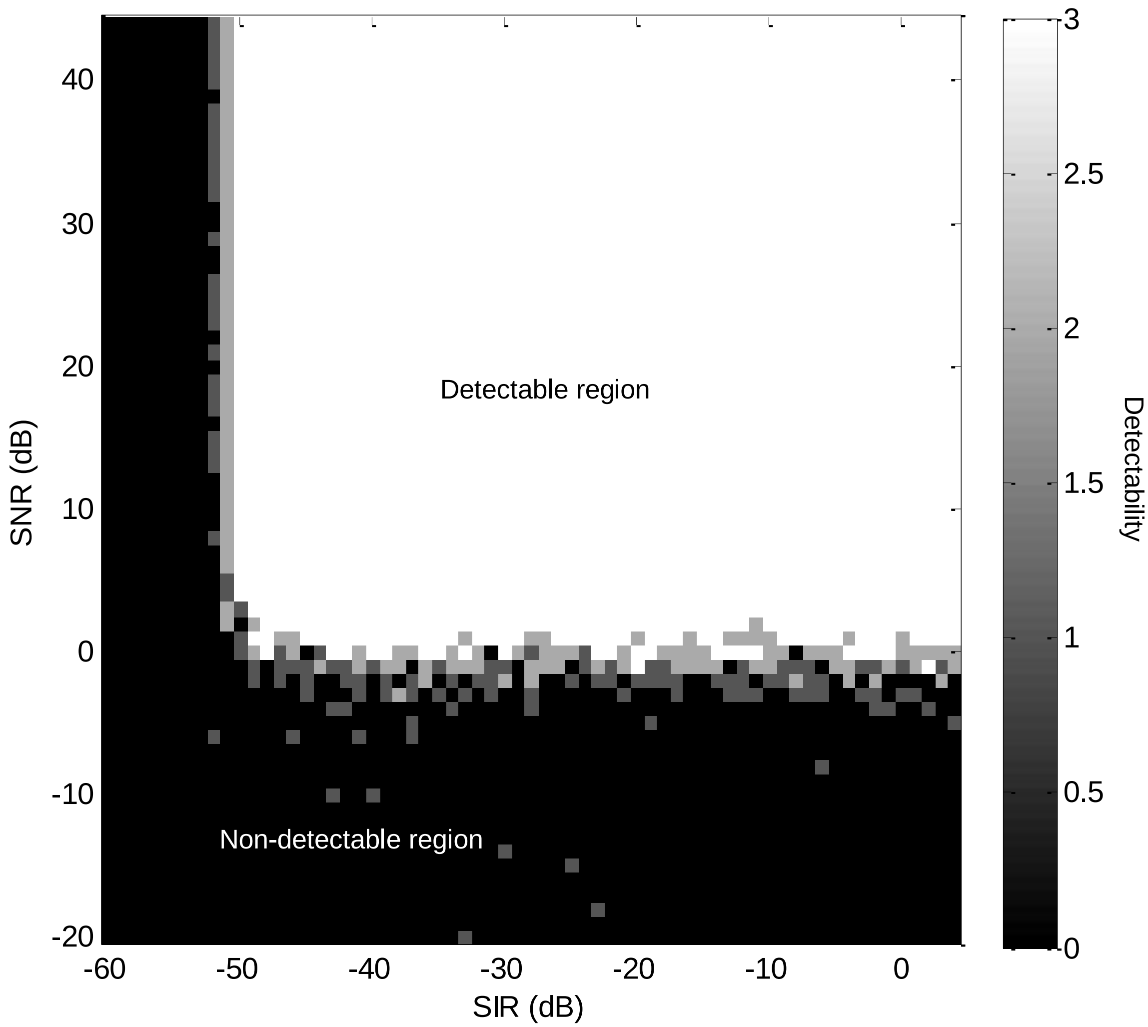

Fig. 7.5. Fault detectability map of the differentiation method (two times of differentiation).

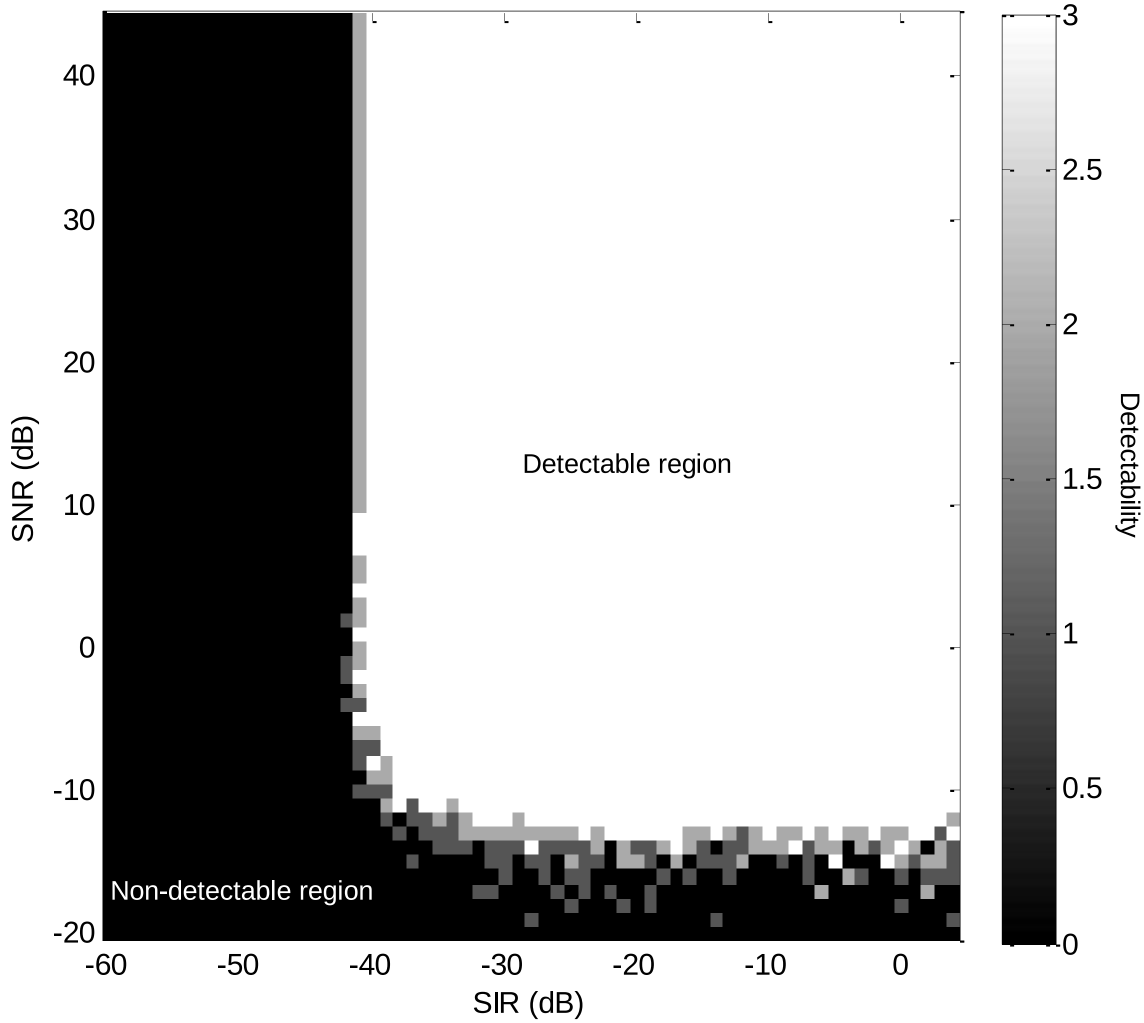

Fig. 7.6. Fault detectability map of the energy operator method.

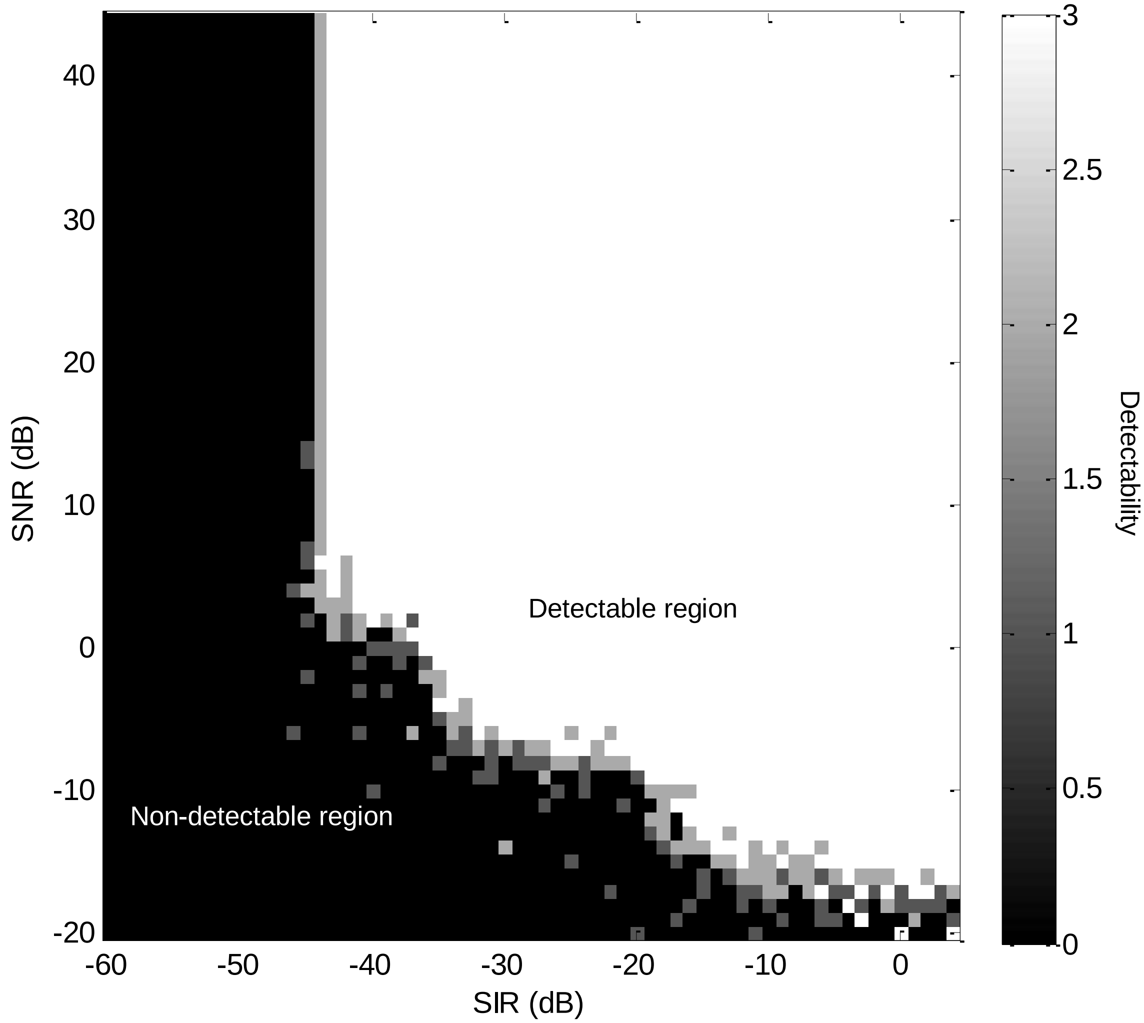

Fig. 7.7. Fault detectability map of the ADD method.

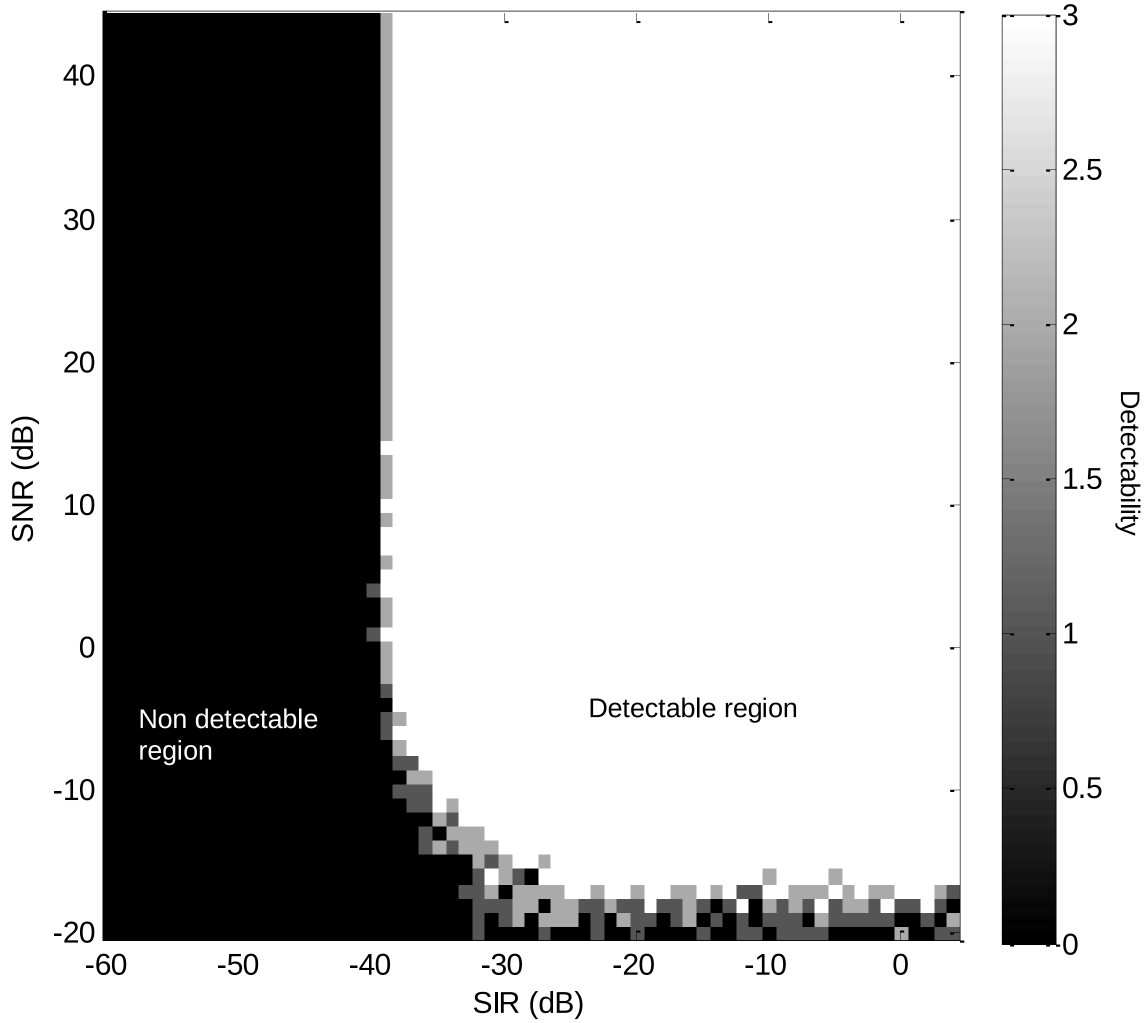

Fig. 7.8. Fault detectability map of the CEEO method.

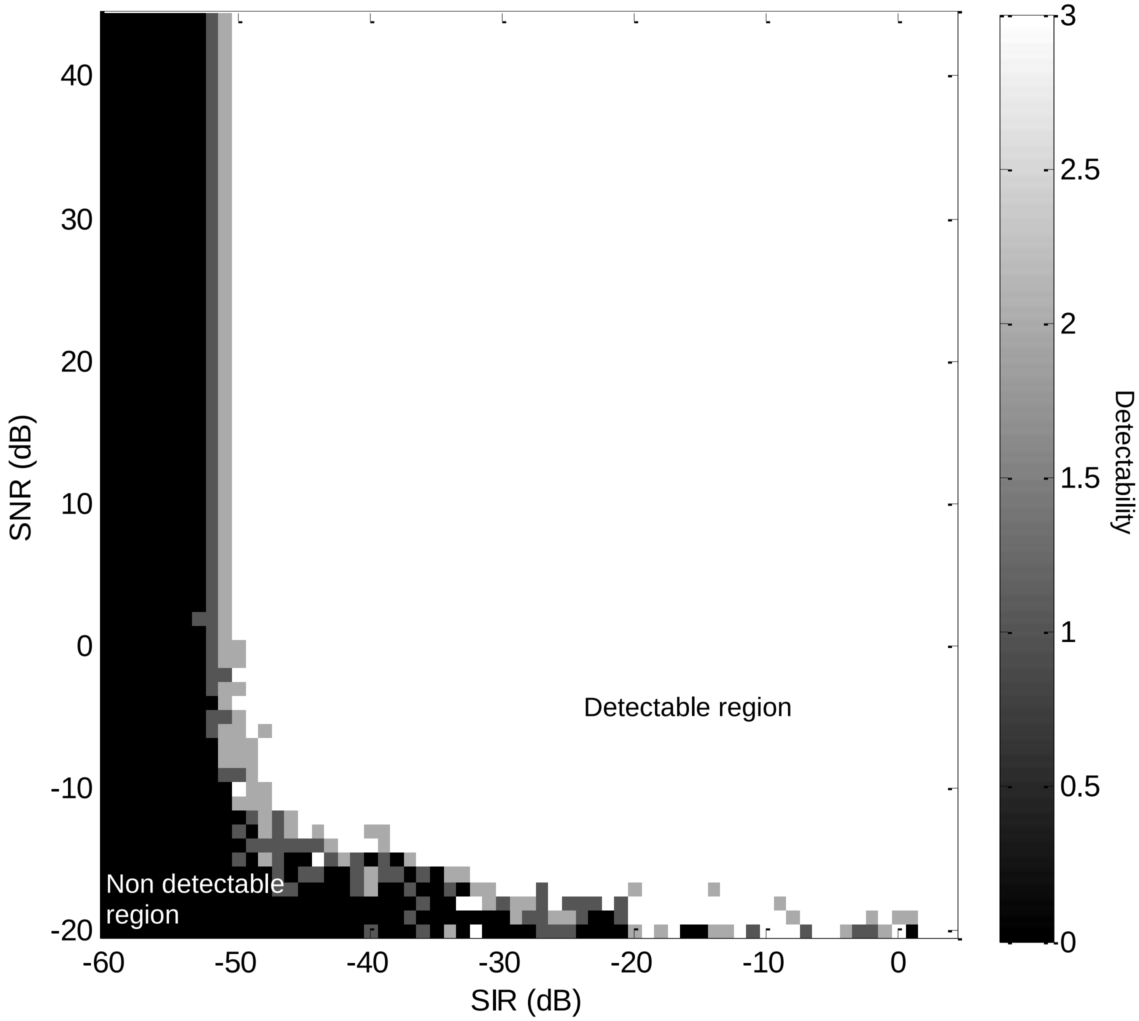

Fig. 7.9. Fault detectability map of the HO_AEO method.

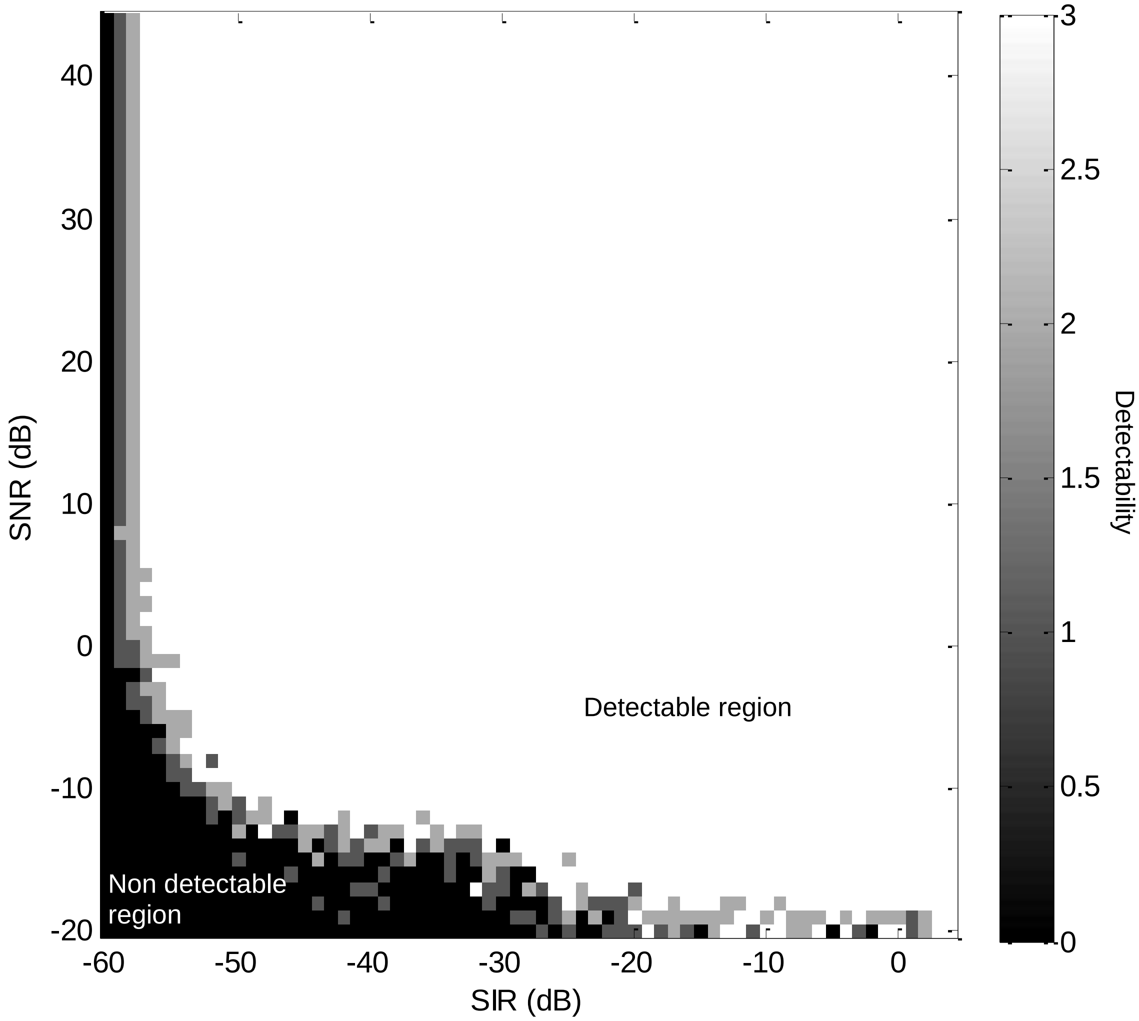

Fig. 7.10. Fault detectability map of the HOEO_F method.

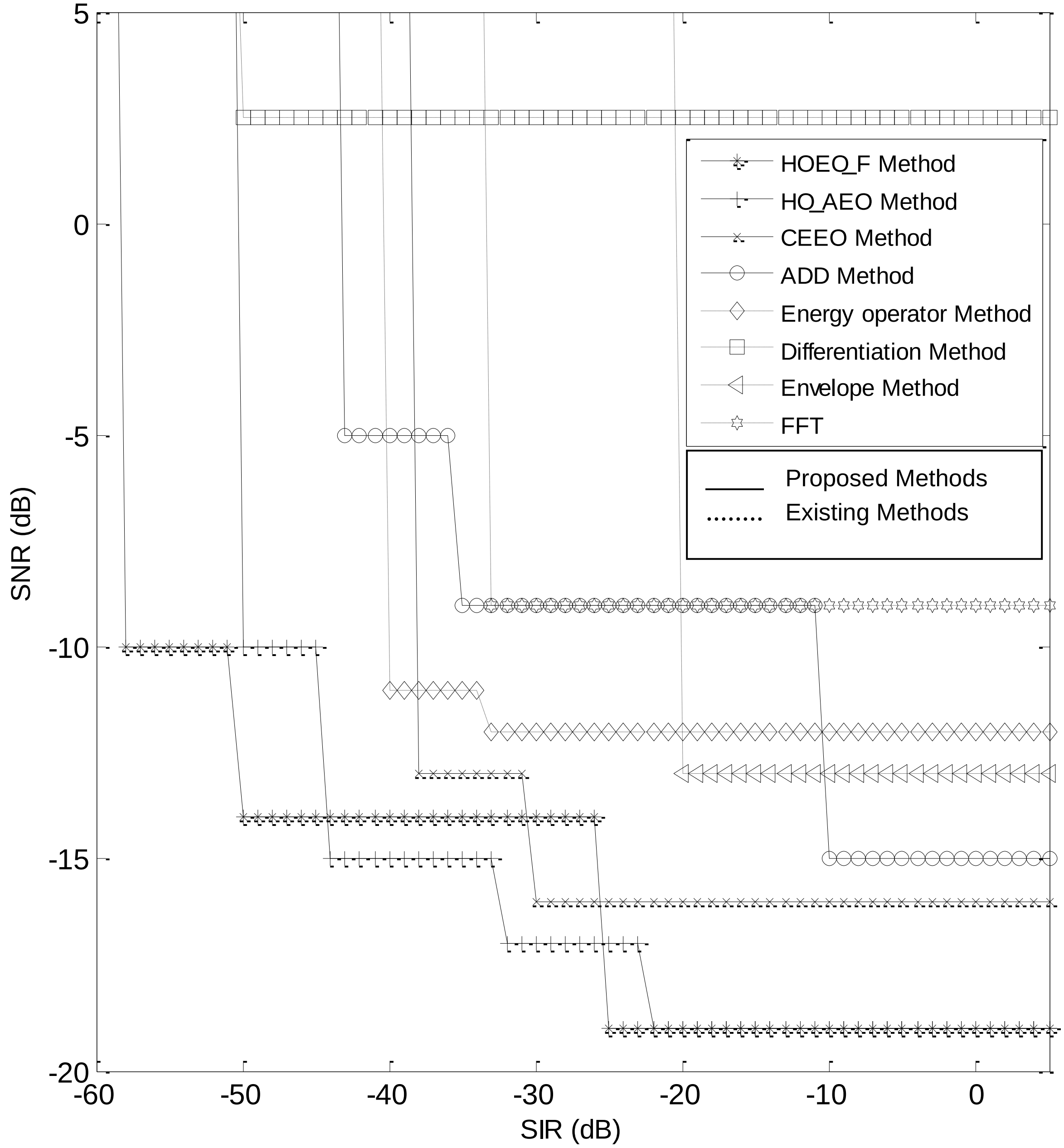

Fig. 7.11. Summary of fault detectability maps of non-parametric methods.

Chapter 8

Conclusions and future work

8.1 Conclusions

Modern industry requires efficient and reliable on-line condition monitoring of bearings to reduce costs, shorten repair time, and prevent catastrophic failures. The bearing working conditions are often very noisy and further complicated by the vibrations of the co-existing machine components. The most widely used methods are the HFR techniques which rely on the availability of a filter designed based on the fault-excited resonant frequency band. However, the search of such a frequency band is a time-consuming and knowledge-demanding process; such techniques may not be well suited to an industrial environment. Furthermore, the frequently changed bearing running conditions also require that the filter be re-designed, i.e., the filter parameters be re-calibrated. This obviously undermined the practical significance of such techniques. As such, this thesis has been directed towards the development of non-parametric, non-filtering and non-resonance methods that are simple and easy to implement. Along this line, four methods have been developed and a methodology for comparing different method is also proposed. The work accomplished in this thesis is summarized in the following.

1. An amplitude demodulation differentiation method (ADD)

An amplitude demodulation differentiation method is proposed to enhance an acquired signal in terms of fault delectability by increasing the signal-to-interference ratio. It has been proved that the SIR could be boosted 2 to 12 times higher than that of the energy operator approach. This new non-parametric, non-filtering method has been evaluated using both simulated and experimental data and compared with the enveloping and energy operator techniques. The results of Chapter 3 show that the ADD method substantially outperforms the enveloping and energy methods in the presence of multiple interferences.

2. A calculus enhanced energy operator (CEEO)

It has been shown that differentiation can improve signal-to-interference ratio and integration can boost signal-to-noise ratio. However, the differentiation alone can intensify noise effect while applying only integration may diminish the impulsiveness of the fault signal. Thus, to take advantage of both differentiation and integration, a calculus enhanced energy operator is developed. Such an operator can improve the SIR and particularly SNR in the presence of strong noise. The CEEO method has been evaluated using both simulated and experimental data and compared favorably with the enveloping, conventional energy operator, and ADD methods.

3. A higher order analytic energy operator (HO_AEO)

This method is based on the joint use of multiple higher order analytical EOs. It is developed to detect bearing fault from vibrations signals that are polluted by strong noise and multiple interferences. The proposed analytic energy operator (AEO) is formed using the raw signal, its Hilbert transform, and their derivatives. In analogy to the conventional energy operator (EO), it represents an alternative energy transformation. However, unlike the conventional EO, the new operator works by exploiting the information from both the real and imaginary parts of the analytic signal. It can also extract both the amplitude and frequency modulations and is thus well suited for the detection of impulsive fault signature. The joint use of multiple higher order AEOs can further offset the noise effect. The built-in amplitude demodulation capability of the proposed HO_AEO eliminates the enveloping step that is required by most high frequency resonance (HFR) methods. Our simulation and experimental results have demonstrated that the proposed method can effectively extract bearing fault signature in the presence of heavy noise and multiple strong vibration interferences. It has also been shown mathematically that the HO_AEO processed signal leads to higher SIR than that done by the conventional EO. The simulation and experimental comparisons also indicate that the proposed method has much better noise and interference handling capabilities than the conventional EO.

4. A higher order energy operator fusion (HOEO_F) method

This method is proposed to detect bearing faults in the presence of harsh noise and strong vibration interferences. In this method, multiple higher order energy operators are fused to form a single simple transform to process the bearing signal obscured by noise and vibration interferences. Unlike the popular high frequency resonance technique, this method does not require the information of resonance excited by the bearing fault. The effects of the HOEO_F method on signal-to-noise ratio (SNR) and signal-to-interference ratio (SIR) are illustrated in this paper. The performance of the proposed method in handling noise and interferences has been examined using both simulated and experimental data. The results indicate that the HOEO_F method outperforms both the envelope method and the original energy operator method.

5. A fault detectability map (FDM)

The literature in the field of machine condition monitoring shows a lack of systematic way to evaluate fault detection method. In this study, a fault detectability map approach has been proposed. With an FDM, the detection methods can be evaluated in terms of SIR and SNR simultaneously. The FDM could serve as a guideline for the selection of detection methods for different applications.

The performance comparison carried out using fault detection map indicates: a) the differentiation and ADD methods are strong in terms of SIR but fall short in dealing with heavy noise, b) the energy operator and CEEO methods seem to be weak in handling strong interferences, c) the overall performances of the proposed ADD and CEEO methods are better than the existing enveloping and EO approaches, d) the HO_AEO method can better handle both strong interferences and heavy noise simultaneously in comparison with the existing approaches as well as the ADD and CEEO methods, e) the HOEO_F technique further broadens detectability zone but it can be less computationally efficient than the HO_AEO method due to the optimization step in the fusion process. It should be noted again that all the proposed methods work without any filter and prior knowledge about the resonance excited by the bearing fault.

8.2 Future work

The following works may be further investigated.

1. Extension of the higher order analytic energy operator (HO_AEO) to non-stationary applications

In Chapter 5, the HO_AEO method can be extended to analyzing the non-stationary signals. Such algorithm should be evaluated under varying shaft speed and load. Therefore, new algorithm can be proposed for time-frequency distribution with better time and frequency resolution.

2. Extension of the higher order energy operator fusion (HOEO_F) to non-stationary applications

Due to incorporation of different orders in HOEO_F method, each order can be used to extract amplitude demodulation and frequency demodulation information. Thus, it may also be potentially promising for fault detection in a non-stationary environment.

3. The extension of the four proposed methods to the detection of gear faults

The gear fault characteristics are much more complex than those of the bearings. It will be interesting to explore the feasibility of using the modified versions of the proposed four methods for gear applications.

References

Antoni, (2007a). Cyclic spectral analysis in practice. Mechanical Systems and Signal Processing *21*, 597–630. [Online]. Available: http://www.sciencedirect.com/science/article/pii/S0888327006001816

Antoni, J. (2007b). Cyclic spectral analysis of rolling-element bearing signals: Facts and fictions. Journal of Sound and Vibration *304*, 497–529. [Online]. Available: http://www.sciencedirect.com/science/article/pii/S0022460X07001551

Antoni, J. (2009). Cyclostationarity by examples. Mechanical Systems and Signal Processing *23*, 987–1036. [Online]. Available: http://www.sciencedirect.com/science/article/pii/S0888327008002690

Antoni, J., and Randall, R.B. (2006). The spectral kurtosis: application to the vibratory surveillance and diagnostics of rotating machines. Mechanical Systems and Signal Processing *20*, 308–331. [Online]. Available: http://www.sciencedirect.com/science/article/pii/S0888327004001529

Antoniadis, I., and Glossiotis, G. (2001). Cyclostationary analysis of rolling-element bearing vibration. Journal of Sound and Vibration *248*, 829–845. [Online]. Available: http://www.sciencedirect.com/science/article/pii/S0022460X01938155

Auger, F., and Flandrin, P. (1995). Improving the readability of time-frequency and time-scale representations by the reassignment method. Signal Processing, IEEE Transactions on *43*, 1068 –1089. [Online]. Available: http://ieeexplore.ieee.org/xpls/abs_all.jsp?arnumber=382394&tag=1

Barszcz, T., and JabŁoński, A. (2011). A novel method for the optimal band selection for vibration signal demodulation and comparison with the Kurtogram. Mechanical Systems and Signal Processing *25*, 431–451. [Online]. Available: http://www.sciencedirect.com/science/article/pii/S0888327010001895

Basseville, M., Abdelghani, M., and Benveniste, A. (2000). Subspace-based fault detection algorithms for vibration monitoring. Automatica *36*, 101–109. [Online]. Available: http://www.sciencedirect.com/science/article/pii/S000510989900093X

Baydar, N., and Ball, A. (2001). A comparative study of acoustic and vibration signals in detection of gear failures using wigner-ville distribution. Mechanical Systems and Signal Processing *15*, 1091–1107. [Online]. Available: http://www.sciencedirect.com/science/article/pii/S0888327000913384

Benitez, D., Gaydecki, P.A., Zaidi, A., and Fitzpatrick, A.P. (2001). The use of the Hilbert transform in ECG signal analysis. Computers in Biology and Medicine *31*, 399–406. [Online]. Available: http://www.sciencedirect.com/science/article/pii/S0010482501000099

Bouillaut, L., and Sidahmed, M. (2000). Comparison of the cyclostationary and the bilinear approaches: theoretical aspects and applications to industrial signals. In Statistical Signal and Array Processing, 2000. Proceedings of the Tenth IEEE Workshop on, pp. 702 –706. [Online]. Available: http://ieeexplore.ieee.org/xpls/abs_all.jsp?arnumber=870217

Bovik, A.C., Maragos, P., and Quatieri, T.F. (1992). Measuring amplitude and frequency modulations in noise using multiband energy operators. In Time-Frequency and Time-Scale Analysis, 1992., Proceedings of the IEEE-SP International Symposium, pp. 3 –6. [Online]. Available: http://ieeexplore.ieee.org/xpls/abs_all.jsp?arnumber=274246

Bozchalooi, I.S., and Liang, M. (2009). Parameter-free bearing fault detection based on maximum likelihood estimation and differentiation. Measurement Science and Technology *20*, 065102. [Online]. Available: http://iopscience.iop.org/0957-0233/20/6/065102

Bozchalooi, I.S., and Liang, M. (2010). Teager energy operator for multi-modulation extraction and its application for gearbox fault detection. Smart Mater. Struct. *19*, 075008. [Online]. Available: http://iopscience.iop.org/0964-1726/19/7/075008

Brie, D., Tomczak, M., Oehlmann, H., and Richard, A. (1997). Gear crack detection by adaptive amplitude and phase. Mechanical Systems and Signal Processing *11*, 149–167. [Online]. Available: http://www.sciencedirect.com/science/article/pii/S0888327096900680

Caviedes, J., and Oberti, F. (2004). A new sharpness metric based on local kurtosis, edge and energy information. Signal Processing: Image Communication *19*, 147–161. [Online]. Available: http://www.sciencedirect.com/science/article/pii/S0923596503000912

Chaturved, G.K., and Thomas, D.W. (1981). Adaptive noise cancelling and condition monitoring. Journal of Sound and Vibration *76*, 391–405. [Online]. Available: http://www.sciencedirect.com/science/article/pii/0022460X81905198

Chen, Z., and Mechefske, C.K. (2002). Diagnosis of Machinery Fault Status Using Transient Vibration Signal Parameters. Journal of Vibration and Control *8*, 321–335. [Online]. Available: http://jvc.sagepub.com/content/8/3/321.short

Cohen, I., and Berdugo, B. (2002). Noise estimation by minima controlled recursive averaging for robust speech enhancement. IEEE Signal Processing Letters *9*, 12–15. [Online]. Available: http://ieeexplore.ieee.org/xpls/abs_all.jsp?arnumber=988717

Cole, M.O.T., Keogh, P.S., Burrows, C.R., and Sahinkaya, M.N. (2006). Adaptive Control of Rotor Vibration Using Compact Wavelets. Journal of Vibration and Acoustics *128*, 653–665. [Online]. Available: http://opus.bath.ac.uk/1905/

Donoho, D.L. (1995). De-noising by soft-thresholding. Information Theory, IEEE Transactions on *41*, 613 –627. [Online]. Available: http://ieeexplore.ieee.org/xpls/abs_all.jsp?arnumber=382009

Dron, J.P., Bolaers, F., and Rasolofondraibe, l. (2004). Improvement of the sensitivity of the scalar indicators (crest factor, kurtosis) using a de-noising method by spectral subtraction: application to the detection of defects in ball bearings. Journal of Sound and Vibration *270*, 61–73. [Online]. Available: http://www.sciencedirect.com/science/article/pii/S0022460X03004838

Dron, J.-P., Rasolofondraibe, L., Chiementin, X., and Bolaers, F. (2010). A comparative experimental study on the use of three denoising methods for bearing defect detection. Meccanica *45*, 265–277. [Online]. Available: http://link.springer.com/article/10.1007/s11012-009-9243-x#page-1

Evangelopoulos, G., and Maragos, P. (2006). Multiband Modulation Energy Tracking for Noisy Speech Detection. IEEE Transactions on Audio, Speech, and Language Processing *14*, 2024 –2038. [Online]. Available: http://ieeexplore.ieee.org/xpls/abs_all.jsp?arnumber=1709892

Fan, X., and Zuo, M.J. (2006). Gearbox fault detection using Hilbert and wavelet packet transform. Mechanical Systems and Signal Processing *20*, 966–982. [Online]. Available: http://www.sciencedirect.com/science/article/pii/S0888327005002037

Feldman, M. (1994a). Non-linear system vibration analysis using Hilbert transform--I. Free vibration analysis method “Freevib.”Mechanical Systems and Signal Processing *8*, 119–127. [Online]. Available: http://www.sciencedirect.com/science/article/pii/S0888327084710119

Feldman, M. (1994b). Non-linear system vibration analysis using Hilbert transform--II. Free vibration analysis method “Forcevib.”Mechanical Systems and Signal Processing *8*, 309-318. [Online]. Available:

http://www.sciencedirect.com/science/article/pii/S0888327084710235

Feldman, M. (2011). Hilbert transform in vibration analysis. Mechanical Systems and Signal Processing *25*, 735–802. [Online]. Available: http://www.sciencedirect.com/science/article/pii/S0888327010002542

Feng, Z., Zuo, M.J., Hao, R., and Chu, F. (2009). Gear crack assessment based on cyclic correlation analysis. In Reliability, Maintainability and Safety, 2009. ICRMS 2009. 8th International Conference on, pp. 1071 –1076. [Online]. Available: http://ieeexplore.ieee.org/xpls/abs_all.jsp?arnumber=5269999

Feng, Z., Zuo, M.J., Hao, R., Chu, F., and El Badaoui, M. (2011). Gear Damage Assessment Based on Cyclic Spectral Analysis. Reliability, IEEE Transactions on *60*, 21 –32. [Online]. Available: http://ieeexplore.ieee.org/xpls/abs_all.jsp?arnumber=5688470

Franaszczuk, P., and Bergey, G. (1999). An autoregressive method for the measurement of synchronization of interictal and ictal EEG signals. Biol. Cybern *81*, 3–9. [Online]. Available: http://link.springer.com/article/10.1007/s004220050540#page-1

Halim, E.B., Shoukat Choudhury, M.A.A., Shah, S.L., and Zuo, M.J. (2008). Time domain averaging across all scales: A novel method for detection of gearbox faults. Mechanical Systems and Signal Processing *22*, 261–278. [Online]. Available: http://www.sciencedirect.com/science/article/pii/S0888327007001537

Hall, D.L., and Llinas, J. (1997). An introduction to multisensor data fusion. Proceedings of the IEEE *85*, 6–23. http://ieeexplore.ieee.org/xpls/abs_all.jsp?arnumber=554205

Hanson, H.M., Maragos, P., and Potamianos, A. (1993). Finding speech formants and modulations via energy separation: with application to a vocoder. In , 1993 IEEE International Conference on Acoustics, Speech, and Signal Processing, 1993. ICASSP-93, pp. 716 –719 vol.2. [Online]. Available: http://ieeexplore.ieee.org/xpls/abs_all.jsp?arnumber=319412

Heng, R.B.W., and Nor, M.J.M. (1998). Statistical analysis of sound and vibration signals for monitoring rolling element bearing condition. Applied Acoustics *53*, 211–226. [Online]. Available: http://www.sciencedirect.com/science/article/pii/S0003682X97000182

Hillis, A.J., Neild, S.A., Drinkwater, B.W., and Wilcox, P.D. (2006). Global Crack Detection Using Bispectral Analysis. Proc. R. Soc. A *462*, 1515–1530. [Online]. Available: http://rspa.royalsocietypublishing.org/content/462/2069/1515.short

Ho, D., and Randall, R.B. (2000). Fault signal optizimation of bearing diagnostic techniques using simulated and actual bearing fault signals. Mechanical Systems and Signal Processing *14*, 763–788.

Hu, Q., He, Z., Zhang, Z., and Zi, Y. (2007). Fault diagnosis of rotating machinery based on improved wavelet package transform and SVMs ensemble. Mechanical Systems and Signal Processing *21*, 688–705. [Online]. Available: http://www.sciencedirect.com/science/article/pii/S0888327006000306

Hyvärinen, A. (1999). Sparse Code Shrinkage: Denoising of Nongaussian Data by Maximum Likelihood Estimation. Neural Computation *11*, 1739–1768. [Online]. Available: http://www.mitpressjournals.org/doi/abs/10.1162/089976699300016214

Iseler, L., and De Maio, J. (2002). An Analysis of US Civil Rotorcraft Accidents by Cost and Injury (1990-1996). http://www3.verticalgateway.com/portals/54/industry_reports/NASA90-96.pdf

Jones, K.J. (2001). Wavelet crack detection algorithm for smart structures. Proceedings of SPIE *4328*, 306–313. [Online]. Available: http://proceedings.spiedigitallibrary.org/proceeding.aspx?articleid=907670

Junsheng, C., Dejie, Y., and Yu, Y. (2006). A fault diagnosis approach for roller bearings based on EMD method and AR model. Mechanical Systems and Signal Processing *20*, 350–362. [Online]. Available: http://www.sciencedirect.com/science/article/pii/S0888327004001736

Junsheng, C., Dejie, Y., and Yu, Y. (2007). Application of an impulse response wavelet to fault diagnosis of rolling bearings. Mechanical Systems and Signal Processing *21*, 920–929. [Online]. Available: http://www.sciencedirect.com/science/article/pii/S0888327005001548

Kaufmann, G.H., and Galizzi, G.E. (1996). Speckle noise reduction in TV holography fringes using wavelet thresholding. Optical Engineering *35*, 9–14. [Online]. Available: http://opticalengineering.spiedigitallibrary.org/article.aspx?articleid=1074033

Kıral, Z., and Karagülle, H. (2006). Vibration analysis of rolling element bearings with various defects under the action of an unbalanced force. Mechanical Systems and Signal Processing *20*, 1967–1991. [Online]. Available: http://www.sciencedirect.com/science/article/pii/S0888327005000841

Lang, M., Guo, H., Odegard, J.E., Burrus, C.S., and Wells, R.O., J. (1996). Noise reduction using an undecimated discrete wavelet transform. Signal Processing Letters, IEEE *3*, 10 –12. [Online]. Available: http://ieeexplore.ieee.org/xpls/abs_all.jsp?arnumber=475823

Lebold, M., McClintic, K, and Campbell, R, G. (2000a). Residual and difference features analysis with transitional gearbox data. In 54th Meeting of the Society, (VA), pp. p. 635–645. [Online]. Available: http://www.personal.psu.edu/users/k/p/kpm128/pubs/ResDifAnalysisFinal.PDF

Lebold, M., McClintic, K, and Campbell, R, G. (2000b). Review of vibration analysis methods for gearbox diagnostics and prognostics. In 54th Meeting of the Society, (VA), pp. p. 623–634. [Online]. Available: http://php.scripts.psu.edu/users/k/p/kpm128/pubs/FeatureTutorialBody18.PDF

Lee, S.U., Robb, D., and Besant, C. (2001). The directional Choi-Williams distribution for the analysis of rotor-vibration signals. Mechanical Systems and Signal Processing *15*, 789–811. [Online]. Available: http://www.sciencedirect.com/science/article/pii/S0888327000913591

Li, C.J., Ma, J., and Hwang, B. (1996). Bearing Condition Monitoring by Pattern Recognition Based on Bicoherence Analysis of Vibrations. Proceedings of the Institution of Mechanical Engineers, Part C: Journal of Mechanical Engineering Science *210*, 277–285. [Online]. Available: http://pic.sagepub.com/content/210/3/277.short

Liang, M., and Soltani Bozchalooi, I. (2010). An energy operator approach to joint application of amplitude and frequency-demodulations for bearing fault detection. Mechanical Systems and Signal Processing *24*, 1473–1494. [Online]. Available: http://www.sciencedirect.com/science/article/pii/S088832701000004X

Lin, J., J, Z.M., and R, F.K. (2004). Mechanical fault detection based on the wavelet de-noising technique. Journal of Vibration and Acoustics *126*, 9–16. [Online]. Available: http://cat.inist.fr/?aModele=afficheN&cpsidt=15517275

Logan, D., and Mathew, J. (1996). Using the correlation dimension for vibration fault diagnosis of rolling element bearing-I.Basic concepts. Mechanical Systems and Signal Processing *10*, 241–250.

Maragos, P., and Potamianos, A. (1995). Higher order differential energy operators. IEEE Signal Processing Letters *2*, 152–154. [Online]. Available: http://ieeexplore.ieee.org/xpls/abs_all.jsp?arnumber=404130

Maragos, P., Kaiser, J.F., and Quatieri, T.F. (1993). On amplitude and frequency demodulation using energy operators. IEEE Transactions on Signal Processing *41*, 1532 – 1550. [Online]. Available:

http://ieeexplore.ieee.org/xpls/abs_all.jsp?arnumber=212729

Martin, H.R., and Honarvar, F. (1995). Application of statistical moments to bearing failure detection. Applied Acoustics *44*, 67–77. [Online]. Available: http://www.sciencedirect.com/science/article/pii/0003682X94P4420B

McFadden, P.D. (1987a). A revised model for the extraction of periodic waveforms by time domain averaging. Mechanical Systems and Signal Processing *1*, 83–95. [Online]. Available: http://www.sciencedirect.com/science/article/pii/0888327087900859

McFadden, P.D. (1987b). Examination of a technique for the early detection of failure in gears by signal processing of the time domain average of the meshing vibration. Mechanical

Systems and Signal Processing *1*, 173–183. [Online]. Available: http://www.sciencedirect.com/science/article/pii/0888327087900690

McFadden, P.D. (1991). A technique for calculating the time domain averages of the vibration of the individual planet gears and the sun gear in an epicyclic gearbox. Journal of Sound and Vibration *144*, 163–172. [Online]. Available: http://www.sciencedirect.com/science/article/pii/0022460X91907397

McFadden, P.D., and Smith, J.D. (1984). Vibration monitoring of rolling element bearings by the high-frequency resonance technique — a review. Tribology International *17*, 3–10. [Online]. Available: http://www.sciencedirect.com/science/article/pii/0301679X84900768

McFadden,P.D., and Smith, J.D. (1985). A Signal Processing Technique for Detecting Local Defects in a Gear from the Signal Average of the Vibration. Proceedings of the Institution of Mechanical Engineers, Part C: Journal of Mechanical Engineering Science *199*, 287–292. [Online]. Available: http://pic.sagepub.com/content/199/4/287.short

McFadden, P.D., and Toozhy, M.M. (2000). Application of synchronous averaging to vibration monitoring of rooling element bearings. Mechanical Systems and Signal Processing *14*, 891–906. [Online]. Available: http://www.sciencedirect.com/science/article/pii/S0888327000912901

McInerny, S.A., and Dai, Y. (2003). Basic vibration signal processing for bearing fault detection. IEEE Transactions on Education *46*, 149– 156. [Online]. Available: http://ieeexplore.ieee.org/xpls/abs_all.jsp?arnumber=1183679

Mevel, L., Hermans, L., and Van Der Auweraer, H. (1999). Application of a subspace-based fault detection method to industrial structures. Mechanical Systems and Signal Processing *13*, 823–838. [Online]. Available: http://www.sciencedirect.com/science/article/pii/S0888327099912475

Moorer, J.A. (1977). Signal processing aspects of computer music: A survey. Proceedings of the IEEE *65*, 1108 – 1137. [Online]. Available: http://ieeexplore.ieee.org/xpls/abs_all.jsp?arnumber=1454929

Nelson, R.. (2006). Time-Normalized Yield: A Natural Unit for Effect Size in Anomalies Experiments. Journal of Scientific Exploration *20*, 177–199. [Online]. Available:

http://leyline.org/papers/pdf/time.norm.yield.pdf

Nikolaou, N.G., and Antoniadis, I.A. (2002). Demodulation of vibration signals generated by defects in rolling element bearings using complex shifted morlet wavelets. Mechanical Systems and Signal Processing *16*, 677–694. [Online]. Available: http://www.sciencedirect.com/science/article/pii/S0888327001914591

Ning, T., and Gao, S.M. (1992). Detection of amplitude modulation using bispectra. In Acoustics, Speech, and Signal Processing, 1992. ICASSP-92., 1992 IEEE International Conference on, pp. 469 –472 vol.5. [Online]. Available: http://ieeexplore.ieee.org/xpls/abs_all.jsp?arnumber=226581

Pachaud, C., Salvetat, R., and Fray, C. (1997). Crest factor and kurtosis contributions to identify defects inducing periodical impulsive forces. Mechanical Systems and Signal Processing *11*, 903–916. [Online]. Available: http://www.sciencedirect.com/science/article/pii/S0888327097901151

Pai, P.F., and Palazotto, A.N. (2008). Detection and identification of nonlinearities by amplitude and frequency modulation analysis. Mechanical Systems and Signal Processing *22*, 1107–1132. [Online]. Available: http://www.sciencedirect.com/science/article/pii/S088832700700235X

Papoulis, A. (1991). Probability, Random Variables and Stochastic Processes (McGraw-Hill Companies).

Peng, Z., Chu, F., and He, Y. (2002). Vibration signal analysis and feature extraction based on reassigned wavelet scalogram. Journal of Sound and Vibration *253*, 1087–1100. [Online]. Available: http://www.sciencedirect.com/science/article/pii/S0022460X01940854

Potamianos, A., and Maragos, P. (1994). A comparison of the energy operator and the Hilbert transform approach to signal and speech demodulation. Signal Processing *37*, 95–120. [Online]. Available: http://www.sciencedirect.com/science/article/pii/0165168494901694

Poulimenos, A.G., and Fassois, S.D. (2006). Parametric time-domain methods for non-stationary random vibration modelling and analysis — A critical survey and comparison. Mechanical Systems and Signal Processing *20*, 763–816. [Online]. Available: http://www.sciencedirect.com/science/article/pii/S0888327005001688

Prashad, H. (1987). The Effect of Cage and Roller Slip on the Measured Defect Frequency Response of Rolling-Element Bearings. A S L E Transactions *30*, 360–367. [Online]. Available: www.tandfonline.com/doi/abs/10.1080/05698198708981768

Quek, S.-T., Wang, Q., Zhang, L., and Ang, K.-K. (2001). Sensitivity analysis of crack detection in beams by wavelet technique. International Journal of Mechanical Sciences *43*, 2899–2910. [Online]. Available: http://www.sciencedirect.com/science/article/pii/S0020740301000649

Raad, A., Antoni, J., and Sidahmed, M. (2008). Indicators of cyclostationarity: Theory and application to gear fault monitoring. Mechanical Systems and Signal Processing *22*, 574–

587. [Online]. Available:
http://www.sciencedirect.com/science/article/pii/S0888327007001847

Rai, V.K., and Mohanty, A.R. (2007). Bearing fault diagnosis using FFT of intrinsic mode functions in Hilbert–Huang transform. Mechanical Systems and Signal Processing *21*, 2607–2615. [Online]. Available:
http://www.sciencedirect.com/science/article/pii/S0888327006002846

Rajagopalan, S., Restrepo, J.A., Aller, J.M., Habetler, T.G., and Harley, R.G. (2005). Wigner-Ville distributions for detection of rotor faults in brushless DC (BLDC) motors operating under non-stationary conditions. In Diagnostics for Electric Machines, Power Electronics and Drives, 2005. SDEMPED 2005. 5th IEEE International Symposium on, pp. 1 –7. [Online]. Available: http://ieeexplore.ieee.org/xpls/abs_all.jsp?arnumber=4662511

Randall, R.B., Antoni, J., and Chobsaard, S. (2001). The relationship between spectral correlation and envelope analysis in the diagnostics of bearing faults and other cyclostationary machine signals. Mechanical Systems and Signal Processing *15*, 945–962. [Online]. Available: http://www.sciencedirect.com/science/article/pii/S0888327001914153

Reed, J. (2005). Introduction to Ultra Wideband Communication Systems, an (Upper Saddle River, NJ, USA: Prentice Hall Press).

Roan, M.J., Erling, J.G., and Sibul, L.H. (2002). A new, non-linear, adaptive, blind source seperation approach to gear tooth failure detection and analysis. Mechanical Systems and Signal Processing *16*, 719–740. [Online]. Available:
http://www.sciencedirect.com/science/article/pii/S0888327002915049

Samanta, B., Al-Balushi, K.R., and Al-Araimi, S.A. (2003). Artificial neural networks and support vector machines with genetic algorithm for bearing fault detection. Engineering Applications of Artificial Intelligence *16*, 657–665. [Online]. Available:
http://www.sciencedirect.com/science/article/pii/S0952197603001143

Satish, L. (1998). Short-time Fourier and wavelet transforms for fault detection in power transformers during impulse tests. Science, Measurement and Technology, IEE Proceedings - *145*, 77 –84. [Online]. Available:
http://ieeexplore.ieee.org/xpls/abs_all.jsp?arnumber=675749

Sawalhi. N., Randall, R.B., and Endo, H. (2007). The enhancement of fault detection and diagnosis in rolling element bearings using minimum entropy deconvolution combined with spectral kurtosis. Mechanical Systems and Signal Processing *21*, 2616–2633. [Online]. Available: http://www.sciencedirect.com/science/article/pii/S0888327006002603

Shao, Y., and Nezu, K. (2005). Design of mixture de-noising for detecting faulty bearing signals. Journal of Sound and Vibration *282*, 899–917. [Online]. Available: http://www.sciencedirect.com/science/article/pii/S0022460X0400330X

Sheen, Y.-T. (2007). An analysis method for the vibration signal with amplitude modulation in a bearing system. Journal of Sound and Vibration *303*, 538–552. [Online]. Available: http://www.sciencedirect.com/science/article/pii/S0022460X0700106X

Stack, J.R., Harley, R.G., and Habetler, T.G. (2004). An amplitude Modulation detector for fault diagnosis in rolling element bearings. Industrial Electronics, IEEE Transactions on *51*, 1097 – 1102. [Online]. Available: http://ieeexplore.ieee.org/xpls/abs_all.jsp?arnumber=1339483

Takalo, R. (2005). Tutorial on univariate autoregressive spectral analysis. Journal of Clinical Monitoring and Computing *19*, 401–410. [Online]. Available: http://link.springer.com/article/10.1007/s10877-005-7089-x#page-1

Tandon, N., and Choudhury, A. (1999). A review of vibration and acoustic measurement methods for the detection of defects in rolling element bearings. Tribology International *32*, 469–480. [Online]. Available: http://www.sciencedirect.com/science/article/pii/S0301679X99000778

Wang, W.J. (2001). Wavelets for detecting mechanical faults with high sensitivity Wavelets. Mechanical Systems and Signal Processing *15*, 685–696. [Online]. Available: http://www.sciencedirect.com/science/article/pii/S0888327000913694

Wang, L., and Liang, M. (2009). Chatter detection based on probability distribution of wavelet modulus maxima. Robotics and Computer-Integrated Manufacturing *25*, 989–998. [Online]. Available: http://www.sciencedirect.com/science/article/pii/S0736584509000453

Wang, W., and Wong, A.K. (2002). Autoregressive Model-Based Gear Fault Diagnosis. Journal of Vibration and Acoustics *124*, 172–179. [Online]. Available: http://cat.inist.fr/?aModele=afficheN&cpsidt=13616769

Wang, W.J., and Lin, R.M. (2003). The application of pseudo-phase portrait in machine condition monitoring. Journal of Sound and Vibration *259*, 1–16. [Online]. Available: http://www.sciencedirect.com/science/article/pii/S0022460X02950765

Wang, W., Golnaraghi, F., and Ismail, F. (2004). Condition monitoring of multistage printing presses. Journal of Sound and Vibration *270*, 755–766. [Online]. Available: http://www.sciencedirect.com/science/article/pii/S0022460X03002098

Williams, T., Ribadeneira, X., Billington, S., and Kurfess, T. (2001). Rolling element bearing diagnostics in run-to-failure lifetime testing. Mechanical Systems and Signal

Processing *15*, 979–993. [Online]. Available: http://www.sciencedirect.com/science/article/pii/S0888327001914189

Yoo, J.-C., Choi, B.D., and Choi, H.-K. (2010). 1-D fast normalized cross-correlation using additions. Digital Signal Processing *20*, 1482–1493. [Online]. Available: www.sciencedirect.com/science/article/pii/S1051200410000047

Zakrajsek, J.J., Dempsey, P.J., Huff, E.M., Augustin, M., Safa-Bakhsh, R., Ephraim, P., Grabil, P., and Decker, H.J. (2006). Rotorcraft Health Management Issues and Challenges. [Online]. Available: http://ntrs.nasa.gov/search.jsp?R=20060008910

Zhao, Y., Atlas, L.E., and Marks, R.J., I. (1990). The use of cone-shaped kernels for generalized time-frequency representations of nonstationary signals. Acoustics, Speech and Signal Processing, IEEE Transactions on *38*, 1084 –1091. [Online]. Available: http://ieeexplore.ieee.org/xpls/abs_all.jsp?arnumber=57537

Zheng, H., Li, Z., and Chen, X. (2002). Transform gear fault diagnosis based on continuous wavelet transform. Mechanical Systems and Signal Processing *16*, 447–457. [Online]. Available: http://www.sciencedirect.com/science/article/pii/S0888327002914822

Zhou, Y., and Leung, H. (1997). Minimum entropy approach for multisensor data fusion. In , Proceedings of the IEEE Signal Processing Workshop on Higher-Order Statistics, 1997, pp. 336–339. [Online]. Available: http://ieeexplore.ieee.org/xpls/abs_all.jsp?arnumber=613542

Zhou, W., Habetler, T.G., and Harley, R.G. (2007). Bearing Condition Monitoring Methods for Electric Machines: A General Review. In IEEE International Symposium on Diagnostics for Electric Machines, Power Electronics and Drives, 2007. SDEMPED 2007, pp. 3–6. [Online]. Available: http://ieeexplore.ieee.org/xpls/abs_all.jsp?arnumber=4393062

Appendices

A Derivations and proofs

The second order of energy operator is calculated for a faulty bearing signal

$$\mathrm{EO}_2\left(r\left(t\right)\right) = A^2\omega_r^2\, e^{-2\beta t} + A Ş\left(t\right)e^{-\beta t} + \sum_{k=1}^{K} L_k^2\omega_{Ik}^2$$

where $q_1(t)$ is given below

$$\begin{aligned} q_1\left(t\right) = {} & \cos\left(\omega_r t+\theta\right) \sum_{k=1}^{K} L_k\left(\left(2\beta\right)\omega_{Ik}\right)\sin\omega_{Ik}t + \sin\left(\omega_r t+\theta\right)\sum_{k=1}^{K} L_k\left(\left(2\omega_r\right)\omega_{Ik}\right)\sin\omega_{Ik}t \\ & + \cos\left(\omega_r t+\theta\right)\sum_{k=1}^{K} L_k\left(\left({\omega_r}^2-\beta^2\right)+\omega_{Ik}^2\right)\cos\omega_{Ik}t + \sin\left(\omega_r t+\theta\right)\sum_{k=1}^{K} L_k\left(-2\beta\omega_r\right)\cos\omega_{Ik}t \end{aligned}$$

The third order is found as follows

$$\begin{aligned} \mathrm{EO}_3\left(r\left(t\right)\right) &= \dot{r}\ddot{r} - r r^{(3)} \\ &= 2A^2\beta{\omega_r}^2 e^{-2\beta t} + A q_2\left(t\right)e^{-\beta t} \end{aligned}$$

where $q_2(t)$ is given by

$$\begin{aligned} q_2\left(t\right) = {} & \cos\left(\omega_r t+\theta\right) \sum_{k=1}^{K} L_k\left(\left(\omega_r^2-\beta^2\right)\omega_{Ik} - \omega_{Ik}^3\right)\sin\omega_{Ik}t \\ & + \sin\left(\omega_r t+\theta\right)\sum_{k=1}^{K} L_k\left(\left(\omega_r\right)\omega_{Ik}^2 - \left(2\beta\omega_r\right)\omega_{Ik}\right)\sin\omega_{Ik}t \\ & + \cos\left(\omega_r t+\theta\right)\sum_{k=1}^{K} L_k\left(\left(L_k\beta\right)\omega_{Ik}^2 + \left(\beta^3 - 3\beta\omega_r^2\right)\right)\cos\omega_{Ik}t \\ & + \sin\left(\omega_r t+\theta\right)\sum_{k=1}^{K} L_k\left(\left(3\beta^2\omega_r\right) - \omega_{Ik}^3\right)\cos\omega_{Ik}t \end{aligned}$$

And the fourth order of energy operator is expanded here,

$$\mathrm{EO}_4\left(r\left(t\right)\right)=\dot{r}r^{(3)}-rr^{(4)}$$
$$=A^2\left(3\beta^2\omega_r{}^2-\omega_r{}^4\right)e^{-2\beta t}+A\check{S}\left(t\right)e^{-\beta t}+\sum_{k=1}^{K}L_k^2\omega_{Ik}^4$$

where $q_3(t)$ is given by

$$q_3\left(t\right)=\cos\left(\omega_r t+\theta\right)\sum_{k=1}^{K}L_k\left(\left(\beta^3-3\beta\omega_r^2\right)\omega_{Ik}-\left(\beta\right)\omega_{Ik}^3\right)\sin\omega_{Ik}t$$
$$+\sin\left(\omega_r t+\theta\right)\sum_{k=1}^{K}L_k\left(\left(3\beta^2\omega_r-\omega_r^3\right)\omega_{Ik}-\left(\omega_r\right)\omega_{Ik}^3\right)\sin\omega_{Ik}t$$
$$+\cos\left(\omega_r t+\theta\right)\sum_{k=1}^{K}L_k\left(\left(\beta^4-6\beta^2\omega_r^2+\omega_r^4\right)-\omega_{Ik}^4\right)\cos\omega_{Ik}t$$
$$+\sin\left(\omega_r t+\theta\right)\sum_{k=1}^{K}L_k\left(4\omega_r\beta^3-4\beta\omega_r^3\right)\cos\omega_{Ik}t$$

Subsequently, the fifth order is calculated

$$\mathrm{EO}_5\left(r\left(t\right)\right)=\dot{r}r^{(4)}-rr^{(5)}$$
$$=A^2\left(4\beta\omega_r{}^4-4\beta^3\omega_r{}^2\right)e^{-2\beta t}+Aq_4\left(t\right)e^{-\beta t}$$

where $q_4(t)$ is given by

$$q_4\left(t\right)=\cos\left(\omega_r t+\theta\right)\sum_{k=1}^{K}L_k\left(-\left(\beta^4-6\beta^2\omega_r^2+\omega_r^4\right)\omega_{Ik}\right)\sin\omega_{Ik}t$$
$$+\sin\left(\omega_r t+\theta\right)\sum_{k=1}^{K}L_k\left(\left(-4\omega_r\beta^3+4\beta\omega_r^3\right)\omega_{Ik}\right)\sin\omega_{Ik}t$$
$$+\cos\left(\omega_r t+\theta\right)\sum_{k=1}^{K}L_k\left(-\beta\omega_{Ik}^4+\omega_{Ik}^5+\left(\beta^5-10\beta^3\omega_r^2+5\beta\omega_r^4\right)\right)\cos\omega_{Ik}t$$
$$+\sin\left(\omega_r t+\theta\right)\sum_{k=1}^{K}L_k\left(\left(\omega_r^5+5\omega_r\beta^4-10\beta^2\omega_r^3\right)-\omega_r\omega_{Ik}^4\right)\cos\omega_{Ik}t$$

Finally, the sixth order is found to obtain the EO method,

$$\mathrm{EO}_6\left(r\left(t\right)\right)=\dot{r}r^{(5)}-rr^{(6)}$$
$$=A^2\left(\omega_r{}^6+5\beta^4\omega_r{}^2-10\beta^2\omega_r{}^4\right)e^{-2\beta t}+Aq_5\left(t\right)e^{-\beta t}+\sum_{k=1}^{K}L_k^2\omega_{Ik}^6$$

where $q_5(t)$ is given by

$$
\begin{aligned}
q_5(t) = {} & \cos(\omega_r t+\theta)\ \sum_{k=1}^{K} L_k\left((\beta)\,\omega_{Ik}^5+\left(\beta^5-10\beta^3\,\omega_r^2+5\beta\omega_r^4\right)\omega_{Ik}\right)\sin\omega_{Ik}t \\
& +\sin(\omega_r t+\theta)\sum_{k=1}^{K} L_k\left((\omega_r)\,\omega_{Ik}^5+\left(\omega_r^5+5\omega_r\beta^4-10\beta^2\omega_r^3\right)\omega_{Ik}\right)\sin\omega_{Ik}t \\
& +\cos(\omega_r t+\theta)\sum_{k=1}^{K} L_k\left(\omega_{Ik}^6-\left(\beta^6-15\beta^4\,\omega_r^2+15\beta^2\,\omega_r^4-\omega_r^6\right)\right)\cos\omega_{Ik}t \\
& +\sin(\omega_r t+\theta)\sum_{k=1}^{K} L_k\left(20\beta^3\omega_r^3-6\omega_r\beta^5-6\beta\omega_r^5\right)\cos\omega_{Ik}t
\end{aligned}
$$

Hence, the result of HOEO_F method is obtained based on fusion of six orders as follows

$$
\text{HOEO\_}F\left(r(t)\right)=\begin{bmatrix}
\alpha_2^* A^2\omega_r^2\,e^{-2\beta t}+2\alpha_3^* A^2\beta{\omega_r}^2 e^{-2\beta t}+\alpha_4^* A^2\left(3\beta^2{\omega_r}^2-{\omega_r}^4\right)e^{-2\beta t} \\
+\alpha_5^* A^2\left(4\beta{\omega_r}^4-4\beta^3{\omega_r}^2\right)e^{-2\beta t}+\alpha_6^* A^2\left({\omega_r}^6+5\beta^4{\omega_r}^2-10\beta^2{\omega_r}^4\right)e^{-2\beta t} \\
+AQ(t)e^{-\beta t}+\alpha_2^*\sum_{k=1}^{K} L_k^2\omega_{Ik}^2+\alpha_4^*\sum_{k=1}^{K} L_k^2\omega_{Ik}^4+\alpha_6^*\sum_{k=1}^{K} L_k^2\omega_{Ik}^6
\end{bmatrix}
$$

$$
Q(t)=\alpha_2^* q_1(t)+\alpha_3^* q_2(t)+\alpha_4^* q_3(t)+\alpha_5^* q_4(t)+\alpha_6^* q_5(t)
$$

B MATLAB programs

B.1 ADD METHOD

```
clear all;
clear;
close all;
% Simulate the fault signal
% Outputs
% outD: faulty bearing vibration (di    splacement)
% outA: faulty bearing vibration (acceleration)
%%
A = 1;          % the amplitude of fault impulse
Tp = 0.02;    % time period corresponding to the fault characteristic
frequency
Fr = 5000;     % the excited resonance frequency
Beta = 1500;  % structural damping characteristic
Fs = 20480;    % sample frequency
Ts = 2;        % Data time span
Ph = pi/8;     % init phase
Fi = 8;        % interference frequency
Aai = [];
Abi = [];
Bi = [];
%% program body

t = [0 : 1/Fs : Ts-(1/Fs)]';         % time
Tps = Tp * [1 : 1 : round(Ts/Tp)]';  % start time point of faulty pulses
production
Sigma = 0.02 * Tp;                   % random slippage
Tps = Tps + (Sigma * rand(length(Tps),1));
Tps = Tps + (Ph/Fr);
%%   outD: faulty bearing vibration (displacement)
outD = zeros(Fs*Ts, 1);
for Np = 1 : length(Tps)
    outDcur = A * robexp(-Beta * (t - Tps(Np))) .* sin(2*pi*Fr * (t -
Tps(Np))) .* stepfun((t - Tps(Np)),0);
    outD = outD + outDcur;
end
outOrg = outD/10;
%%                          Part Az   (INTERFERENCE)
SirAz =  50;       % Sir: signal to interference ratio
SnrAz =  0;          % signal to nose ratio
  DAz = awgn ( outOrg , SnrAz, 'measured');
  xAz = DAz;
%%                          Part Aa   (INTERFERENCE)
SirAa =  50;       % Sir: signal to interference ratio
SnrAa = -5;          % signal to nose ratio
 DAa = awgn ( outOrg    , SnrAa, 'measured');
%%    Add interference
 if isempty(Aai)
   sigPower = sum(abs(outOrg(:)).^2)/length(outOrg(:));
   sigPower = 10*log10(sigPower);
```

```
    intPower = sigPower-SirAa;
    intPower = 10^(intPower/10);
    intPower = intPower/4;
    Aai = sqrt(intPower*2);
  end;
   xAa = DAa  + Aai*sin(2*pi*Fi*t)+ Aai*sin(2*pi*35*t)+
Aai*sin(2*pi*430*t)+Aai*sin(2*pi*650*t);
%%                            Part Ab  (INTERFERENCE)
SirAb =  50;        % Sir: signal to interference ratio
SnrAb = -12;        % signal to nose ratio
 DAb = awgn ( outOrg    , SnrAb, 'measured');
%%    Add interference
 if isempty(Abi)
    sigPower = sum(abs(outOrg(:)).^2)/length(outOrg(:));
    sigPower = 10*log10(sigPower);
    intPower = sigPower-SirAb;
    intPower = 10^(intPower/10);
    intPower = intPower/4;
    Abi = sqrt(intPower*2);
 end;
   xAb = DAb  + Abi*sin(2*pi*Fi*t)+ Abi*sin(2*pi*35*t)+
Abi*sin(2*pi*130*t)+Abi*sin(2*pi*650*t);
%%                             Part B  (NOISE)
SirB = -41;        % Sir: signal to interference ratio
SnrB = -9;        % signal to nose ratio
 DB = awgn ( outOrg    , SnrB, 'measured');
%%    Add interference
 if isempty(Bi)
    sigPower = sum(abs(outOrg(:)).^2)/length(outOrg(:));
    sigPower = 10*log10(sigPower);
    intPower = sigPower-SirB;
    intPower = 10^(intPower/10);
    intPower = intPower/4;
    Bi = sqrt(intPower*2);
 end;
   xB = DB  + Bi*sin(2*pi*Fi*t)+ Bi*sin(2*pi*35*t)+
Bi*sin(2*pi*130*t)+Bi*sin(2*pi*720*t);
%%                          Part A
 bhAa = abs((hilbert( xAa )));
 bhAb = abs((hilbert( xAb )));
 DxAa = diffe(xAa,2);
 EDxAa = abs((hilbert( DxAa )));
 DxAb = diffe(xAb,2);
 EDxAb = abs((hilbert( DxAb )));
 bhAz = abs((hilbert( xAz )));
 DxAz = diffe(xAz,2);
 EDxAz = abs((hilbert( DxAz )));
%%                          Part B
 bhB = abs((hilbert( xB )));
 EB1 = energy ( xB,1);
 EB2 = energy ( xB,2);
[adh1,dh1 ] = dad( xB,1,1/Fs );
[adh2,dh2] = dad( xB,2,1/Fs );
%%                                                                  FFT TRANSFORM
L=length(xB);
NFFT = 2^nextpow2(L);
Y1 = fft( xAa , NFFT)/L;        Y2 = fft( bhAa , NFFT)/L;
```

```
Y3 = fft( xAb , NFFT)/L;        Y4 = fft( bhAb , NFFT)/L;
Y5 = fft(  xB, NFFT)/L;         Y6 = fft( bhB , NFFT)/L;
Y7 = fft(  EB1, NFFT)/L;        Y8 = fft( EB2 , NFFT)/L;
Y9 = fft(  adh1, NFFT)/L;       Y10 = fft( adh2, NFFT)/L;
Y11 = fft( EDxAa, NFFT)/L;      Y12 = fft( EDxAb, NFFT)/L;
Y13 = fft( xAz , NFFT)/L;       Y14 = fft( bhAz , NFFT)/L;
Y15 = fft( EDxAz, NFFT)/L;
f = Fs/2*linspace(0,1,NFFT/2+1);
YY1=2*abs(Y1(1:NFFT/2+1));    YY2=2*abs(Y2(1:NFFT/2+1));
YY3=2*abs(Y3(1:NFFT/2+1));    YY4=2*abs(Y4(1:NFFT/2+1));
YY5=2*abs(Y5(1:NFFT/2+1));    YY6=2*abs(Y6(1:NFFT/2+1));
YY7=2*abs(Y7(1:NFFT/2+1));    YY8=2*abs(Y8(1:NFFT/2+1));
YY9=2*abs(Y9(1:NFFT/2+1));    YY10=2*abs(Y10(1:NFFT/2+1));
YY11=2*abs(Y11(1:NFFT/2+1));  YY12=2*abs(Y12(1:NFFT/2+1));
YY13=2*abs(Y13(1:NFFT/2+1));  YY14=2*abs(Y14(1:NFFT/2+1));
YY15=2*abs(Y15(1:NFFT/2+1));
%%                                                              Figures
fpat='Proposalpart_DAD_Sim';
save ('C:\Hamid,Matlab\MATLAB_PC\Proposalpart_DAD_Sim\frequency-PPart-
DAD','f');
%%                      PART Az [Signal & FFT & Envelope]
figure
hold on;  box on;
donfig('units','centimeters','width',15,'height',5,'font','Helvetica','fon
tsize',10);
plot( xAz );
  xlabel('Sample','FontSize',11);
  ylabel('Amplitude (V)','FontSize',11);
  xlim([1 14000])
  ylim([-0.15 0.15])
   fnam1='PPartAz-signal-
DADsim.emf';saveas(gcf,[fpat,filesep,fnam1],'emf');
   fnam2='PPartAz-signal-
DADsim.fig';saveas(gcf,[fpat,filesep,fnam2],'fig');
   save ('C:\Hamid,Matlab\MATLAB_PC\Proposalpart_DAD_Sim\PPartA-signal-
DADsim','xAz');

figure
hold on; box on;
donfig('units','centimeters','width',7,'height',5,'font','Helvetica','font
size',10);
plot(f(1:end),YY13(1:end));
  xlabel('Frequency (Hz)','FontSize',11);
  ylabel('Magnitude','FontSize',11);
  xlim([1 500])
   fnam1='FFT-PPartAz-signal-
DADsim.emf';saveas(gcf,[fpat,filesep,fnam1],'emf');
   fnam2='FFT-PPartAz-signal-
DADsim.fig';saveas(gcf,[fpat,filesep,fnam2],'fig');
   save ('C:\Hamid,Matlab\MATLAB_PC\Proposalpart_DAD_Sim\FFT-PPartAz-
signal-DADsim','YY13');

   figure
hold on; box on;
donfig('units','centimeters','width',7,'height',5,'font','Helvetica','font
size',10);
```

```
plot(f(1:end),YY14(1:end));
  xlabel('Frequency (Hz)','FontSize',11);
  ylabel('Magnitude','FontSize',11);
  xlim([1 500])
   fnam1='ENV-PPartAz-signal-
DADsim.emf';saveas(gcf,[fpat,filesep,fnam1],'emf');
   fnam2='ENV-PPartAz-signal-
DADsim.fig';saveas(gcf,[fpat,filesep,fnam2],'fig');
   save ('C:\Hamid,Matlab\MATLAB_PC\Proposalpart_DAD_Sim\ENV-PPartAz-
signal-DADsim','YY14');

   figure
hold on; box on;
donfig('units','centimeters','width',7,'height',5,'font','Helvetica','font
size',10);
plot(f(1:end),YY15(1:end));
  xlabel('Frequency (Hz)','FontSize',11);
  ylabel('Magnitude','FontSize',11);
  xlim([1 500])
   fnam1='ENVDif-PPartAz-signal-
DADsim.emf';saveas(gcf,[fpat,filesep,fnam1],'emf');
   fnam2='ENVDif-PPartAz-signal-
DADsim.fig';saveas(gcf,[fpat,filesep,fnam2],'fig');
   save ('C:\Hamid,Matlab\MATLAB_PC\Proposalpart_DAD_Sim\ENVDif-PPartAz-
signal-DADsim','YY15');
%%                      PART Aa [Signal & FFT & Envelope]
figure
hold on;  box on;
donfig('units','centimeters','width',15,'height',5,'font','Helvetica','fon
tsize',10);
plot( xAa );
  xlabel('Sample','FontSize',11);
  ylabel('Amplitude (V)','FontSize',11);
  xlim([1 14000])
   fnam1='PPartAa-signal-
DADsim.emf';saveas(gcf,[fpat,filesep,fnam1],'emf');
   fnam2='PPartAa-signal-
DADsim.fig';saveas(gcf,[fpat,filesep,fnam2],'fig');
   save ('C:\Hamid,Matlab\MATLAB_PC\Proposalpart_DAD_Sim\PPartA-signal-
DADsim','xAa');

figure
hold on; box on;
donfig('units','centimeters','width',7,'height',5,'font','Helvetica','font
size',10);
plot(f(1:end),YY1(1:end));
  xlabel('Frequency (Hz)','FontSize',11);
  ylabel('Magnitude','FontSize',11);
  xlim([1 500])
   fnam1='FFT-PPartAa-signal-
DADsim.emf';saveas(gcf,[fpat,filesep,fnam1],'emf');
   fnam2='FFT-PPartAa-signal-
DADsim.fig';saveas(gcf,[fpat,filesep,fnam2],'fig');
   save ('C:\Hamid,Matlab\MATLAB_PC\Proposalpart_DAD_Sim\FFT-PPartAa-
signal-DADsim','YY1');
```

```
   figure
hold on; box on;
donfig('units','centimeters','width',7,'height',5,'font','Helvetica','font
size',10);
plot(f(1:end),YY2(1:end));
  xlabel('Frequency (Hz)','FontSize',11);
  ylabel('Magnitude','FontSize',11);
  xlim([1 500])
   fnam1='ENV-PPartAa-signal-
DADsim.emf';saveas(gcf,[fpat,filesep,fnam1],'emf');
   fnam2='ENV-PPartAa-signal-
DADsim.fig';saveas(gcf,[fpat,filesep,fnam2],'fig');
   save ('C:\Hamid,Matlab\MATLAB_PC\Proposalpart_DAD_Sim\ENV-PPartAa-
signal-DADsim','YY2');

   figure
hold on; box on;
donfig('units','centimeters','width',7,'height',5,'font','Helvetica','font
size',10);
plot(f(1:end),YY11(1:end));
  xlabel('Frequency (Hz)','FontSize',11);
  ylabel('Magnitude','FontSize',11);
  xlim([1 500])
   fnam1='ENVDif-PPartAa-signal-
DADsim.emf';saveas(gcf,[fpat,filesep,fnam1],'emf');
   fnam2='ENVDif-PPartAa-signal-
DADsim.fig';saveas(gcf,[fpat,filesep,fnam2],'fig');
   save ('C:\Hamid,Matlab\MATLAB_PC\Proposalpart_DAD_Sim\ENVDif-PPartAa-
signal-DADsim','YY11');

   %%                      PART Ab [Signal & FFT & Envelope]
figure
hold on;  box on;
donfig('units','centimeters','width',15,'height',5,'font','Helvetica','fon
tsize',10);
plot( xAb );
  xlabel('Sample','FontSize',11);
  ylabel('Amplitude (V)','FontSize',11);
  xlim([1 14000])
   fnam1='PPartAb-signal-
DADsim.emf';saveas(gcf,[fpat,filesep,fnam1],'emf');
   fnam2='PPartAb-signal-
DADsim.fig';saveas(gcf,[fpat,filesep,fnam2],'fig');
   save ('C:\Hamid,Matlab\MATLAB_PC\Proposalpart_DAD_Sim\PPartA-signal-
DADsim','xAb');

figure
hold on; box on;
donfig('units','centimeters','width',7,'height',5,'font','Helvetica','font
size',10);
plot(f(1:end),YY3(1:end));
  xlabel('Frequency (Hz)','FontSize',11);
  ylabel('Magnitude','FontSize',11);
  xlim([1 500])
   fnam1='FFT-PPartAb-signal-
DADsim.emf';saveas(gcf,[fpat,filesep,fnam1],'emf');
```

```
   fnam2='FFT-PPartAb-signal-
DADsim.fig';saveas(gcf,[fpat,filesep,fnam2],'fig');
   save ('C:\Hamid,Matlab\MATLAB_PC\Proposalpart_DAD_Sim\FFT-PPartAb-
signal-DADsim','YY3');

   figure
hold on; box on;
donfig('units','centimeters','width',7,'height',5,'font','Helvetica','font
size',10);
plot(f(1:end),YY4(1:end));
  xlabel('Frequency (Hz)','FontSize',11);
  ylabel('Magnitude','FontSize',11);
  xlim([1 500])
   fnam1='ENV-PPartAb-signal-
DADsim.emf';saveas(gcf,[fpat,filesep,fnam1],'emf');
   fnam2='ENV-PPartAb-signal-
DADsim.fig';saveas(gcf,[fpat,filesep,fnam2],'fig');
   save ('C:\Hamid,Matlab\MATLAB_PC\Proposalpart_DAD_Sim\ENV-PPartAb-
signal-DADsim','YY4');

   figure
hold on; box on;
donfig('units','centimeters','width',7,'height',5,'font','Helvetica','font
size',10);
plot(f(1:end),YY12(1:end));
  xlabel('Frequency (Hz)','FontSize',11);
  ylabel('Magnitude','FontSize',11);
  xlim([1 500])
   fnam1='ENVDif-PPartAb-signal-
DADsim.emf';saveas(gcf,[fpat,filesep,fnam1],'emf');
   fnam2='ENVDif-PPartAb-signal-
DADsim.fig';saveas(gcf,[fpat,filesep,fnam2],'fig');
   save ('C:\Hamid,Matlab\MATLAB_PC\Proposalpart_DAD_Sim\ENVDif-PPartAb-
signal-DADsim','YY12');
%%                   PART B  [Signal & FFT & Energy operator & DAD]
figure
hold on;  box on;
donfig('units','centimeters','width',10,'height',8,'font','Helvetica','fon
tsize',10);
plot( xB );
  xlabel('Sample','FontSize',11);
  ylabel('Amplitude (V)','FontSize',11);
  xlim([1 14000])
%   ylim([-0.25 0.25])
   fnam1='PPartB-signal-
DADsim.emf';saveas(gcf,[fpat,filesep,fnam1],'emf');
   fnam2='PPartB-signal-
DADsim.fig';saveas(gcf,[fpat,filesep,fnam2],'fig');
   save ('C:\Hamid,Matlab\MATLAB_PC\Proposalpart_DAD_Sim\PPartB-signal-
DADsim','xB');

figure
hold on; box on;
donfig('units','centimeters','width',7,'height',5,'font','Helvetica','font
size',10);
plot(f(1:end),YY5(1:end));
```

```
  xlabel('Frequency (Hz)','FontSize',11);
  ylabel('Magnitude','FontSize',11);
  xlim([1 1000])
   fnam1='FFT-PPartB-signal-
DADsim.emf';saveas(gcf,[fpat,filesep,fnam1],'emf');
   fnam2='FFT-PPartB-signal-
DADsim.fig';saveas(gcf,[fpat,filesep,fnam2],'fig');
   save ('C:\Hamid,Matlab\MATLAB_PC\Proposalpart_DAD_Sim\FFT-PPartB-
signal-DADsim','YY5');

figure
hold on; box on;
donfig('units','centimeters','width',7,'height',5,'font','Helvetica','font
size',10);
plot(f(1:end),YY6(1:end));
  xlabel('Frequency (Hz)','FontSize',11);
  ylabel('Magnitude','FontSize',11);
  xlim([1 1000])
   fnam1='ENV-PPartB-signal-
DADsim.emf';saveas(gcf,[fpat,filesep,fnam1],'emf');
   fnam2='ENV-PPartB-signal-
DADsim.fig';saveas(gcf,[fpat,filesep,fnam2],'fig');
   save ('C:\Hamid,Matlab\MATLAB_PC\Proposalpart_DAD_Sim\ENV-PPartB-
signal-DADsim','YY6');

figure
hold on; box on;
donfig('units','centimeters','width',8,'height',6,'font','Helvetica','font
size',10);
plot(f(1:end),YY7(1:end));
  xlabel('Frequency (Hz)','FontSize',11);
  ylabel('Magnitude','FontSize',11);
  xlim([1 1000])
   fnam1='TEO1-PPartB-signal-
DADsim.emf';saveas(gcf,[fpat,filesep,fnam1],'emf');
   fnam2='TEO1-PPartB-signal-
DADsim.fig';saveas(gcf,[fpat,filesep,fnam2],'fig');
   save ('C:\Hamid,Matlab\MATLAB_PC\Proposalpart_DAD_Sim\TEO1-PPartB-
signal-DADsim','YY7');

figure
hold on; box on;
donfig('units','centimeters','width',7,'height',5,'font','Helvetica','font
size',10);
plot(f(1:end),YY8(1:end));
  xlabel('Frequency (Hz)','FontSize',11);
  ylabel('Magnitude','FontSize',11);
  xlim([1 1000])
   fnam1='TEO2-PPartB-signal-
DADsim.emf';saveas(gcf,[fpat,filesep,fnam1],'emf');
   fnam2='TEO2-PPartB-signal-
DADsim.fig';saveas(gcf,[fpat,filesep,fnam2],'fig');
   save ('C:\Hamid,Matlab\MATLAB_PC\Proposalpart_DAD_Sim\TEO2-PPartB-
signal-DADsim','YY8');

figure
```

```
hold on; box on;
donfig('units','centimeters','width',9,'height',7,'font','Helvetica','font
size',10);
plot(f(1:end),YY9(1:end));
  xlabel('Frequency (Hz)','FontSize',11);
  ylabel('Magnitude','FontSize',11);
  xlim([1 1000])
   fnam1='DAD1-PPartB-signal-
DADsim.emf';saveas(gcf,[fpat,filesep,fnam1],'emf');
   fnam2='DAD1-PPartB-signal-
DADsim.fig';saveas(gcf,[fpat,filesep,fnam2],'fig');
   save ('C:\Hamid,Matlab\MATLAB_PC\Proposalpart_DAD_Sim\DAD1-PPartB-
signal-DADsim','YY9');

figure
hold on; box on;
donfig('units','centimeters','width',9,'height',7,'font','Helvetica','font
size',10);
plot(f(1:end),YY10(1:end));
  xlabel('Frequency (Hz)','FontSize',11);
  ylabel('Magnitude','FontSize',11);
  xlim([1 1000])
   fnam1='DAD2-PPartB-signal-
DADsim.emf';saveas(gcf,[fpat,filesep,fnam1],'emf');
   fnam2='DAD2-PPartB-signal-
DADsim.fig';saveas(gcf,[fpat,filesep,fnam2],'fig');
   save ('C:\Hamid,Matlab\MATLAB_PC\Proposalpart_DAD_Sim\DAD2-PPartB-
signal-DADsim','YY10');
```

B.2 CEEO METHOD

```
clear all;
clear;
close all;
%%                              PART Z
tZ=[0:.1:10]';
xZ1=exp(-10*(tZ-5).^2);
xZ2=exp(-0.25*(tZ-5).^2);
DxZ1=diffe(xZ1,2);
DxZ2=diffe(xZ2,2);
%%
% Simulate the fault signal
% Outputs
% outD: faulty bearing vibration (di    splacement)
% outA: faulty bearing vibration (acceleration)
%%
A = 1;         % the amplitude of fault impulse
Tp = 0.008;    % time period corresponding to the fault characteristic
frequency
Fr = 2048;     % the excited resonance frequency
Beta = 1500;   % structural damping characteristic
Fs = 20480;    % sample frequency
Ts = 2;        % Data time span
Ph = pi/8;     % init phase
Ai = [];
Bi = [];
Ci = [];
%% program body

t = [0 : 1/Fs : Ts-(1/Fs)]';           % time
Tps = Tp * [1 : 1 : round(Ts/Tp)]';  % start time point of faulty pulses
production
Sigma = 0.02 * Tp;                     % random slippage
Tps = Tps + (Sigma * rand(length(Tps),1));
Tps = Tps + (Ph/Fr);
%%  outD: faulty bearing vibration (displacement)
outD = zeros(Fs*Ts, 1);
for Np = 1 : length(Tps)
    outDcur = A * robexp(-Beta * (t - Tps(Np))) .* sin(2*pi*Fr * (t -
Tps(Np))) .* stepfun((t - Tps(Np)),0);
    outD = outD + outDcur;
end
outOrg = outD/10;
%%                         Part A  [DERIVATIVE](INTERFERENCE)
SirA = -20;     % Sir: signal to interference ratio
SnrA = 10;       % signal to nose ratio
 DA = awgn ( outOrg    , SnrA, 'measured');
%%    Add interference
 if isempty(Ai)
   sigPower = sum(abs(outOrg(:)).^2)/length(outOrg(:));
   sigPower = 10*log10(sigPower);
   intPower = sigPower-SirA;
   intPower = 10^(intPower/10);
   intPower = intPower/4;
   Ai = sqrt(intPower*2);
```

```
 end;
  xA = DA  + Ai*sin(2*pi*5*t)+ Ai*sin(2*pi*27*t)+
Ai*sin(2*pi*43*t)+Ai*sin(2*pi*60*t);

%%                          Part B [DERIVATIVE][ACCUMULATION] (NOISE)
SirB = 50;       % Sir: signal to interference ratio
SnrB = 10;       % signal to nose ratio [for dif SnrB=10 and for acu
SnrB=-5]
 DB = awgn ( outOrg    , SnrB, 'measured');
%%    Add interference
 if isempty(Bi)
   sigPower = sum(abs(outOrg(:)).^2)/length(outOrg(:));
   sigPower = 10*log10(sigPower);
   intPower = sigPower-SirB;
   intPower = 10^(intPower/10);
   intPower = intPower/4;
   Bi = sqrt(intPower*2);
 end;
  xB = DB  + Bi*sin(2*pi*5*t)+ Bi*sin(2*pi*35*t)+
Bi*sin(2*pi*13*t)+Bi*sin(2*pi*72*t);
  %%                          Part C  (ENVELOPE&ENERGY)[VTEO]
SirC = -20;     % Sir: signal to interference ratio
SnrC = -15;       % signal to nose ratio
 DC = awgn ( outOrg    , SnrC, 'measured');
%%    Add interference
 if isempty(Ci)
   sigPower = sum(abs(outOrg(:)).^2)/length(outOrg(:));
   sigPower = 10*log10(sigPower);
   intPower = sigPower-SirC;
   intPower = 10^(intPower/10);
   intPower = intPower/4;
   Ci = sqrt(intPower*2);
 end;
  xC = DC  + Ci*sin(2*pi*5*t)+ Ci*sin(2*pi*27*t)+
Ci*sin(2*pi*43*t)+Ci*sin(2*pi*810*t);
%%                         Part A
DxA=diffe(xA,1);
bhDxA = abs((hilbert( DxA )));
bhxA=abs((hilbert( xA )));
%%                         Part B
DxB=diffe(xB,1);
ACxB=accumulal(xB',1);
%%                         Part C
 bhxC = abs((hilbert( xC )));
 ExC = energy ( xC,1);
[ vteo1, vteo2,VTEOxC ] = VTEO( xC,2 );
[adh1,dh1 ] = dad( xC,1,1/Fs );   [adh2,dh2] = dad( xC,2,1/Fs );

%%                                                             FFT TRANSFORM
L=length(xA);
NFFT = 2^nextpow2(L);
Y1 = fft( xA , NFFT)/L;        Y2 = fft( bhDxA, NFFT)/L;
Y3 = fft(  xC, NFFT)/L;        Y4 = fft( bhxC , NFFT)/L;
Y5 = fft(  ExC, NFFT)/L;       Y6 = fft( VTEOxC , NFFT)/L;
Y7 = fft( bhxA , NFFT)/L;
Y8 = fft(  adh1, NFFT)/L;       Y9 = fft( adh2 , NFFT)/L;
```

```
f = Fs/2*linspace(0,1,NFFT/2+1);
YY1=2*abs(Y1(1:NFFT/2+1));    YY2=2*abs(Y2(1:NFFT/2+1));
YY3=2*abs(Y3(1:NFFT/2+1));    YY4=2*abs(Y4(1:NFFT/2+1));
YY5=2*abs(Y5(1:NFFT/2+1));    YY6=2*abs(Y6(1:NFFT/2+1));
YY7=2*abs(Y7(1:NFFT/2+1));
YY8=2*abs(Y8(1:NFFT/2+1));    YY9=2*abs(Y9(1:NFFT/2+1));
%%                                                       Figures
fpat='Proposalpart_VTEO_Sim';
save ('C:\Hamid,Matlab\MATLAB_PC\Proposalpart_VTEO_Sim\frequency-PPart-
VTEO','f');
%%                    PART Z [Signal & 2th Derivation]

figure
hold on;  box on;
donfig('units','centimeters','width',7,'height',5,'font','Helvetica','font
size',10);
plot( xZ1,':b' );
hold on;  box on;
plot( xZ2, '-r');
  xlabel('Sample','FontSize',11);
  ylabel('Amplitude (V)','FontSize',11);
  xlim([1 110])
   fnam1='PPartZ-signal-
VTEOsim.emf';saveas(gcf,[fpat,filesep,fnam1],'emf');
   fnam2='PPartZ-signal-
VTEOsim.fig';saveas(gcf,[fpat,filesep,fnam2],'fig');
   save ('C:\Hamid,Matlab\MATLAB_PC\Proposalpart_VTEO_Sim\PPartZ-signal1-
VTEOsim','xZ1');
   save ('C:\Hamid,Matlab\MATLAB_PC\Proposalpart_VTEO_Sim\PPartZ-signal2-
VTEOsim','xZ2');
figure
hold on;  box on;
donfig('units','centimeters','width',7,'height',5,'font','Helvetica','font
size',10);
plot( DxZ1 ,':b');
hold on;  box on;
plot( DxZ2,'-r' );
  xlabel('Sample','FontSize',11);
  ylabel('Amplitude (V)','FontSize',11);
  xlim([1 110])
   fnam1='PPartZ-Dif-VTEOsim.emf';saveas(gcf,[fpat,filesep,fnam1],'emf');
   fnam2='PPartZ-Dif-VTEOsim.fig';saveas(gcf,[fpat,filesep,fnam2],'fig');
   save ('C:\Hamid,Matlab\MATLAB_PC\Proposalpart_VTEO_Sim\PPartZ1-Dif-
VTEOsim','DxZ1');
   save ('C:\Hamid,Matlab\MATLAB_PC\Proposalpart_VTEO_Sim\PPartZ2-Dif-
VTEOsim','DxZ2');
%%              PART D (SIMULATION SIGNAL FOR SNR ESTIMATION)
figure
hold on;  box on;
donfig('units','centimeters','width',12,'height',5,'font','Helvetica','fon
tsize',10);
plot( outOrg );
  xlabel('Sample','FontSize',11);
  ylabel('Amplitude (V)','FontSize',11);
  xlim([1 10000])
   fnam1='PPartD-signal-
VTEOsim.emf';saveas(gcf,[fpat,filesep,fnam1],'emf');
```

```
   fnam2='PPartD-signal-
VTEOsim.fig';saveas(gcf,[fpat,filesep,fnam2],'fig');
   save ('C:\Hamid,Matlab\MATLAB_PC\Proposalpart_VTEO_Sim\PPartD-signal-
VTEOsim','outOrg');
%%                       PART A [Signal & FFT & EnvelopeDIFF]
figure
hold on;  box on;
donfig('units','centimeters','width',12,'height',5,'font','Helvetica','fon
tsize',10);
plot( outOrg );
  xlabel('Sample','FontSize',11);
  ylabel('Amplitude (V)','FontSize',11);
  xlim([1 5000])
   fnam1='PPartA-signal0-
VTEOsim.emf';saveas(gcf,[fpat,filesep,fnam1],'emf');
   fnam2='PPartA-signal0-
VTEOsim.fig';saveas(gcf,[fpat,filesep,fnam2],'fig');
   save ('C:\Hamid,Matlab\MATLAB_PC\Proposalpart_VTEO_Sim\PPartA-signal0-
VTEOsim','outOrg');

figure
hold on;  box on;
donfig('units','centimeters','width',7,'height',5,'font','Helvetica','font
size',10);
plot( xA );
  xlabel('Sample','FontSize',11);
  ylabel('Amplitude (V)','FontSize',11);
  xlim([1 5000])
   fnam1='PPartA-signal-
VTEOsim.emf';saveas(gcf,[fpat,filesep,fnam1],'emf');
   fnam2='PPartA-signal-
VTEOsim.fig';saveas(gcf,[fpat,filesep,fnam2],'fig');
   save ('C:\Hamid,Matlab\MATLAB_PC\Proposalpart_VTEO_Sim\PPartA-signal-
VTEOsim','xA');

figure
hold on; box on;
donfig('units','centimeters','width',7,'height',5,'font','Helvetica','font
size',10);
plot(f(1:end),YY1(1:end));
  xlabel('Frequency (Hz)','FontSize',11);
  ylabel('Magnitude','FontSize',11);
  xlim([1 500])
   fnam1='FFT-PPartA-signal-
VTEOsim.emf';saveas(gcf,[fpat,filesep,fnam1],'emf');
   fnam2='FFT-PPartA-signal-
VTEOsim.fig';saveas(gcf,[fpat,filesep,fnam2],'fig');
   save ('C:\Hamid,Matlab\MATLAB_PC\Proposalpart_VTEO_Sim\FFT-PPartA-
signal-VTEOsim','YY1');

figure
hold on; box on;
donfig('units','centimeters','width',7,'height',5,'font','Helvetica','font
size',10);
plot(f(1:end),YY2(1:end));
  xlabel('Frequency (Hz)','FontSize',11);
```

```
  ylabel('Magnitude','FontSize',11);
  xlim([1 800])
   fnam1='ENVDIFF-PPartA-signal-
VTEOsim.emf';saveas(gcf,[fpat,filesep,fnam1],'emf');
   fnam2='ENVDIFF-PPartA-signal-
VTEOsim.fig';saveas(gcf,[fpat,filesep,fnam2],'fig');
   save ('C:\Hamid,Matlab\MATLAB_PC\Proposalpart_DAD_Sim\ENVDIFF-PPartA-
signal-VTEOsim','YY2');

figure %(NEW CONFIG)
hold on; box on;
donfig('units','centimeters','width',7,'height',5,'font','Helvetica','font
size',10);
plot(f(1:end),YY7(1:end));
  xlabel('Frequency (Hz)','FontSize',11);
  ylabel('Magnitude','FontSize',11);
  xlim([1 500])
   fnam1='ENV-PPartA-signal-
VTEOsim.emf';saveas(gcf,[fpat,filesep,fnam1],'emf');
   fnam2='ENV-PPartA-signal-
VTEOsim.fig';saveas(gcf,[fpat,filesep,fnam2],'fig');
   save ('C:\Hamid,Matlab\MATLAB_PC\Proposalpart_DAD_Sim\ENV-PPartA-
signal-VTEOsim','YY7');
%%                    PART B  [Signal & DIFF & ACCUMILATION](NOISE)
figure
hold on;  box on;
donfig('units','centimeters','width',7,'height',5,'font','Helvetica','font
size',10);
plot( xB );
  xlabel('Sample','FontSize',11);
  ylabel('Amplitude (V)','FontSize',11);
  xlim([1 8000])
   fnam1='PPartB-signal-
VTEOsim.emf';saveas(gcf,[fpat,filesep,fnam1],'emf');
   fnam2='PPartB-signal-
VTEOsim.fig';saveas(gcf,[fpat,filesep,fnam2],'fig');
   save ('C:\Hamid,Matlab\MATLAB_PC\Proposalpart_VTEO_Sim\PPartB-signal-
VTEOsim','xB');

figure
hold on;  box on;
donfig('units','centimeters','width',7,'height',5,'font','Helvetica','font
size',10);
plot( DxB );
  xlabel('Sample','FontSize',11);
  ylabel('Amplitude (V)','FontSize',11);
  xlim([1 8000])
   fnam1='PPartB-DIFFsignal-
VTEOsim.emf';saveas(gcf,[fpat,filesep,fnam1],'emf');
   fnam2='PPartB-DIFFsignal-
VTEOsim.fig';saveas(gcf,[fpat,filesep,fnam2],'fig');
   save ('C:\Hamid,Matlab\MATLAB_PC\Proposalpart_VTEO_Sim\PPartB-
DIFFsignal-VTEOsim','DxB');

figure
hold on;  box on;
```

```
donfig('units','centimeters','width',7,'height',5,'font','Helvetica','font
size',10);
plot( ACxB );
  xlabel('Sample','FontSize',11);
  ylabel('Amplitude (V)','FontSize',11);
  xlim([1 8000])
   fnam1='PPartB-ACsignal-
VTEOsim.emf';saveas(gcf,[fpat,filesep,fnam1],'emf');
   fnam2='PPartB-ACsignal-
VTEOsim.fig';saveas(gcf,[fpat,filesep,fnam2],'fig');
   save ('C:\Hamid,Matlab\MATLAB_PC\Proposalpart_VTEO_Sim\PPartB-ACsignal-
VTEOsim','ACxB');
   %%             PART C [MAIN PART OF SIMULATION](VTEO)
figure
hold on;  box on;
donfig('units','centimeters','width',7,'height',5,'font','Helvetica','font
size',10);
plot( xC );
  xlabel('Sample','FontSize',11);
  ylabel('Amplitude (V)','FontSize',11);
  xlim([1 10000])
   fnam1='PPartC-signal-
VTEOsim.emf';saveas(gcf,[fpat,filesep,fnam1],'emf');
   fnam2='PPartC-signal-
VTEOsim.fig';saveas(gcf,[fpat,filesep,fnam2],'fig');
   save ('C:\Hamid,Matlab\MATLAB_PC\Proposalpart_VTEO_Sim\PPartC-signal-
VTEOsim','xC');

figure
hold on;  box on;
donfig('units','centimeters','width',7,'height',5,'font','Helvetica','font
size',10);
plot(f(1:end),YY3(1:end));
  xlabel('Frequency (Hz)','FontSize',11);
  ylabel('Magnitude','FontSize',11);
  xlim([1 1000])
   fnam1='FFT-PPartC-signal-
VTEOsim.emf';saveas(gcf,[fpat,filesep,fnam1],'emf');
   fnam2='FFT-PPartC-signal-
VTEOsim.fig';saveas(gcf,[fpat,filesep,fnam2],'fig');
   save ('C:\Hamid,Matlab\MATLAB_PC\Proposalpart_VTEO_Sim\FFT-PPartC-
signal-VTEOsim','YY3');

figure
hold on;  box on;
donfig('units','centimeters','width',7,'height',5,'font','Helvetica','font
size',10);
plot(f((1:end),YY4(1:end));
  xlabel('Frequency (Hz)','FontSize',11);
  ylabel('Magnitude','FontSize',11);
  xlim([1 1000])
   fnam1='ENV-PPartC-signal-
VTEOsim.emf';saveas(gcf,[fpat,filesep,fnam1],'emf');
   fnam2='ENV-PPartC-signal-
VTEOsim.fig';saveas(gcf,[fpat,filesep,fnam2],'fig');
```

```
   save ('C:\Hamid,Matlab\MATLAB_PC\Proposalpart_VTEO_Sim\ENV-PPartC-
signal-VTEOsim','YY4');

figure
hold on;  box on;
donfig('units','centimeters','width',7,'height',5,'font','Helvetica','font
size',10);
plot(f(1:end),YY5(1:end));
  xlabel('Frequency (Hz)','FontSize',11);
  ylabel('Magnitude','FontSize',11);
  xlim([1 1000])
   fnam1='TEO-PPartC-signal-
VTEOsim.emf';saveas(gcf,[fpat,filesep,fnam1],'emf');
   fnam2='TEO-PPartC-signal-
VTEOsim.fig';saveas(gcf,[fpat,filesep,fnam2],'fig');
   save ('C:\Hamid,Matlab\MATLAB_PC\Proposalpart_VTEO_Sim\TEO-PPartC-
signal-VTEOsim','YY5');

figure
hold on;  box on;
donfig('units','centimeters','width',10,'height',8,'font','Helvetica','fon
tsize',10);
plot(f(1:end),YY6(1:end));
  xlabel('Frequency (Hz)','FontSize',11);
  ylabel('Magnitude','FontSize',11);
  xlim([1 1000])
   fnam1='VTEO-PPartC-signal-
VTEOsim.emf';saveas(gcf,[fpat,filesep,fnam1],'emf');
   fnam2='VTEO-PPartC-signal-
VTEOsim.fig';saveas(gcf,[fpat,filesep,fnam2],'fig');
   save ('C:\Hamid,Matlab\MATLAB_PC\Proposalpart_VTEO_Sim\VTEO-PPartC-
signal-VTEOsim','YY6');
   %% new config to add ADD part
figure
hold on;  box on;
donfig('units','centimeters','width',7,'height',5,'font','Helvetica','font
size',10);
plot(f(1:end),YY8(1:end));
  xlabel('Frequency (Hz)','FontSize',11);
  ylabel('Magnitude','FontSize',11);
  xlim([1 1000])
   fnam1='ADD1-PPartC-signal-
VTEOsim.emf';saveas(gcf,[fpat,filesep,fnam1],'emf');
   fnam2='ADD1-PPartC-signal-
VTEOsim.fig';saveas(gcf,[fpat,filesep,fnam2],'fig');
   save ('C:\Hamid,Matlab\MATLAB_PC\Proposalpart_VTEO_Sim\ADD1-PPartC-
signal-VTEOsim','YY8');

figure
hold on;  box on;
donfig('units','centimeters','width',7,'height',5,'font','Helvetica','font
size',10);
plot(f(1:end),YY9(1:end));
  xlabel('Frequency (Hz)','FontSize',11);
  ylabel('Magnitude','FontSize',11);
  xlim([1 1000])
```

```
   fnam1='ADD2-PPartC-signal-
VTEOsim.emf';saveas(gcf,[fpat,filesep,fnam1],'emf');
   fnam2='ADD2-PPartC-signal-
VTEOsim.fig';saveas(gcf,[fpat,filesep,fnam2],'fig');
   save ('C:\Hamid,Matlab\MATLAB_PC\Proposalpart_VTEO_Sim\ADD2-PPartC-
signal-VTEOsim','YY9');
```

B.3 HO_AEO METHOD

```
clear all;
clear;
close all;
% Simulate the fault signal
% Outputs
% outD: faulty bearing vibration (di    splacement)
% outA: faulty bearing vibration (acceleration)
%%
A = 1;          % the amplitude of fault impulse
Tp = 0.008;     % time period corresponding to the fault characteristic
frequency
Fr = 2048;      % the excited resonance frequency
Beta = 1500;    % structural damping characteristic
Fs = 20480;     % sample frequency
Ts = 2;         % Data time span
Ph = pi/8;      % init phase
Fi = 5;         % interference frequency
Ai = [];
Bi = [];
Ci = [];
%% program body

t = [0 : 1/Fs : Ts-(1/Fs)]';          % time
Tps = Tp * [1 : 1 : round(Ts/Tp)]';   % start time point of faulty pulses
production
Sigma = 0.02 * Tp;                    % random slippage
Tps = Tps + (Sigma * rand(length(Tps),1));
Tps = Tps + (Ph/Fr);
%%   outD: faulty bearing vibration (displacement)
outD = zeros(Fs*Ts, 1);
for Np = 1 : length(Tps)
    outDcur = A * robexp(-Beta * (t - Tps(Np))) .* sin(2*pi*Fr * (t -
Tps(Np))) .* stepfun((t - Tps(Np)),0);
    outD = outD + outDcur;
end
outOrg = outD/10;
%%                           Part A   (INTERFERENCE)
SirA =  -35;      % Sir: signal to interference ratio
SnrA = -10;        % signal to nose ratio
 DA = awgn ( outOrg    , SnrA, 'measured');
%%    Add interference
 if isempty(Ai)
   sigPower = sum(abs(outOrg(:)).^2)/length(outOrg(:));
   sigPower = 10*log10(sigPower);
   intPower = sigPower-SirA;
   intPower = 10^(intPower/10);
   intPower = intPower/4;
   Ai = sqrt(intPower*2);
 end;
  xA = DA   + Ai*sin(2*pi*Fi*t)+ Ai*sin(2*pi*27*t)+
Ai*sin(2*pi*43*t)+Ai*sin(2*pi*650*t);

%%                            Part B   (NOISE)
SirB =  5;       % Sir: signal to interference ratio
```

```
SnrB = -17;        % signal to nose ratio
 DB = awgn ( outOrg    , SnrB, 'measured');
%%    Add interference
 if isempty(Bi)
   sigPower = sum(abs(outOrg(:)).^2)/length(outOrg(:));
   sigPower = 10*log10(sigPower);
   intPower = sigPower-SirB;
   intPower = 10^(intPower/10);
   intPower = intPower/4;
   Bi = sqrt(intPower*2);
 end;
  xB = DB  + Bi*sin(2*pi*Fi*t)+ Bi*sin(2*pi*27*t)+
Bi*sin(2*pi*43*t)+Bi*sin(2*pi*650*t);
  %%                           Part C  (NOISE)
SirC = -15;        % Sir: signal to interference ratio
SnrC = -15;        % signal to nose ratio
 DC = awgn ( outOrg    , SnrC, 'measured');
%%    Add interference
 if isempty(Ci)
   sigPower = sum(abs(outOrg(:)).^2)/length(outOrg(:));
   sigPower = 10*log10(sigPower);
   intPower = sigPower-SirC;
   intPower = 10^(intPower/10);
   intPower = intPower/4;
   Ci = sqrt(intPower*2);
 end;
  xC = DC  + Ci*sin(2*pi*Fi*t)+ Ci*sin(2*pi*27*t)+
Ci*sin(2*pi*43*t)+Ci*sin(2*pi*650*t);
%%                         Part A
 bhA = abs((hilbert( xA )));
 EA = energy ( xA,1);
[HSC1A,HSC2A,HSC3A] = HSCO( xA,4 );
bh2A= bhA.^2;
x2A=xA.^2;
%%                         Part B
 bhB = abs((hilbert( xB )));
 EB = energy ( xB,1);
[HSC1B,HSC2B,HSC3B] = HSCO( xB,4 );
bh2B= bhB.^2;
x2B=xB.^2;
%%                         Part C
 bhC = abs((hilbert( xC )));
 EC = energy ( xC,1);
[HSC1C,HSC2C,HSC3C] = HSCO( xC,4 );
bh2C= bhC.^2;
x2C=xC.^2;
%%                                                                   FFT TRANSFORM
L=length(xA);
NFFT = 2^nextpow2(L);
Y1 = fft( xA , NFFT)/L;        Y2 = fft( xB , NFFT)/L;    Y3 = fft( xC ,
NFFT)/L;
Y4 = fft(  x2A, NFFT)/L;       Y5 = fft( x2B , NFFT)/L;   Y6 = fft( x2C ,
NFFT)/L;
Y7 = fft(  bhA, NFFT)/L;       Y8 = fft( EA , NFFT)/L;
Y9 = fft(  bhB, NFFT)/L;       Y10 = fft( EB, NFFT)/L;
Y11 = fft(  bhC, NFFT)/L;      Y12 = fft( EC, NFFT)/L;
```

```
Y13 = fft(  bh2A, NFFT)/L;      Y14 = fft( bh2B, NFFT)/L;   Y15 = fft(
bh2C, NFFT)/L;
Y16 = fft(  HSC1A, NFFT)/L;     Y17 = fft( HSC1B, NFFT)/L;  Y18 = fft(
HSC1C, NFFT)/L;
Y19 = fft( HSC2A , NFFT)/L;     Y20 = fft( HSC2B , NFFT)/L; Y21 = fft(
HSC2C , NFFT)/L;
Y22 = fft( HSC3A, NFFT)/L;      Y23 = fft( HSC3B , NFFT)/L; Y24 = fft(
HSC3C , NFFT)/L;
f = Fs/2*linspace(0,1,NFFT/2+1);
YY1=2*abs(Y1(1:NFFT/2+1));    YY2=2*abs(Y2(1:NFFT/2+1));
YY3=2*abs(Y3(1:NFFT/2+1));
YY4=2*abs(Y4(1:NFFT/2+1));    YY5=2*abs(Y5(1:NFFT/2+1));
YY6=2*abs(Y6(1:NFFT/2+1));
YY7=2*abs(Y7(1:NFFT/2+1));    YY8=2*abs(Y8(1:NFFT/2+1));
YY9=2*abs(Y9(1:NFFT/2+1));    YY10=2*abs(Y10(1:NFFT/2+1));
YY11=2*abs(Y11(1:NFFT/2+1));  YY12=2*abs(Y12(1:NFFT/2+1));
YY13=2*abs(Y13(1:NFFT/2+1));  YY14=2*abs(Y14(1:NFFT/2+1));
YY15=2*abs(Y15(1:NFFT/2+1));
YY16=2*abs(Y16(1:NFFT/2+1));  YY17=2*abs(Y17(1:NFFT/2+1));
YY18=2*abs(Y18(1:NFFT/2+1));
YY19=2*abs(Y19(1:NFFT/2+1));  YY20=2*abs(Y20(1:NFFT/2+1));
YY21=2*abs(Y21(1:NFFT/2+1));
YY22=2*abs(Y22(1:NFFT/2+1));  YY23=2*abs(Y23(1:NFFT/2+1));
YY24=2*abs(Y24(1:NFFT/2+1));
%%                                                              Figures
fpat='PAPER_HO_AEO_Sim';
save ('C:\Hamid,Matlab\MATLAB_PC\PAPER_HO_AEO_Sim\frequency','f');
%%                PART 000
figure
hold on;  box on;
donfig('units','centimeters','width',14,'height',7,'font','Helvetica','fon
tsize',10);
plot( outOrg );
  xlabel('Sample','FontSize',11);
  ylabel('Amplitude','FontSize',11);
  xlim([1 10000])
   fnam1='Part000-signal-
simHO_AEO.emf';saveas(gcf,[fpat,filesep,fnam1],'emf');
   fnam2='Part000-signal-
simHO_AEO.fig';saveas(gcf,[fpat,filesep,fnam2],'fig');
   save ('C:\Hamid,Matlab\MATLAB_PC\PAPER_HO_AEO_Sim\Part000-signal-
simHO_AEO','outOrg');
%%                      PART A [Signal & FFT]
figure
hold on;  box on;
donfig('units','centimeters','width',7,'height',5,'font','Helvetica','font
size',10);
plot( xA );
  xlabel('Sample','FontSize',11);
  ylabel('Amplitude','FontSize',11);
  xlim([1 10000])
   fnam1='PartA-signal-
simHO_AEO.emf';saveas(gcf,[fpat,filesep,fnam1],'emf');
   fnam2='PartA-signal-
simHO_AEO.fig';saveas(gcf,[fpat,filesep,fnam2],'fig');
   save ('C:\Hamid,Matlab\MATLAB_PC\PAPER_HO_AEO_Sim\PartA-signal-
simHO_AEO','xA');
```

```
figure
hold on; box on;
donfig('units','centimeters','width',7,'height',5,'font','Helvetica','font
size',10);
plot(f(1:end),YY1(1:end));
  xlabel('Frequency (Hz)','FontSize',11);
  ylabel('Magnitude','FontSize',11);
  xlim([1 1000])
   fnam1='FFT-PartA-signal-
simHO_AEO.emf';saveas(gcf,[fpat,filesep,fnam1],'emf');
   fnam2='FFT-PartA-signal-
simHO_AEO.fig';saveas(gcf,[fpat,filesep,fnam2],'fig');
   save ('C:\Hamid,Matlab\MATLAB_PC\PAPER_HO_AEO_Sim\FFT-PartA-signal-
simHO_AEO','YY1');
%%                   PART B  [Signal & FFT]
figure
hold on;  box on;
donfig('units','centimeters','width',7,'height',5,'font','Helvetica','font
size',10);
plot( xB );
  xlabel('Sample','FontSize',11);
  ylabel('Amplitude','FontSize',11);
  xlim([1 10000])
  ylim([-0.6 0.6])
   fnam1='PartB-signal-
simHO_AEO.emf';saveas(gcf,[fpat,filesep,fnam1],'emf');
   fnam2='PartB-signal-
simHO_AEO.fig';saveas(gcf,[fpat,filesep,fnam2],'fig');
   save ('C:\Hamid,Matlab\MATLAB_PC\PAPER_HO_AEO_Sim\PartB-signal-
simHO_AEO','xB');

figure
hold on; box on;
donfig('units','centimeters','width',7,'height',5,'font','Helvetica','font
size',10);
plot(f(1:end),YY2(1:end));
  xlabel('Frequency (Hz)','FontSize',11);
  ylabel('Magnitude','FontSize',11);
  xlim([1 1000])
   fnam1='FFT-PartB-signal-
simHO_AEO.emf';saveas(gcf,[fpat,filesep,fnam1],'emf');
   fnam2='FFT-PartB-signal-
simHO_AEO.fig';saveas(gcf,[fpat,filesep,fnam2],'fig');
   save ('C:\Hamid,Matlab\MATLAB_PC\PAPER_HO_AEO_Sim\FFT-PartB-signal-
simHO_AEO','YY2');
   %%                   PART C  [Signal & FFT]
figure
hold on;  box on;
donfig('units','centimeters','width',7,'height',5,'font','Helvetica','font
size',10);
plot( xC );
  xlabel('Sample','FontSize',11);
  ylabel('Amplitude','FontSize',11);
  xlim([1 10000])
  ylim([-0.6 0.6])
```

```
   fnam1='PartC-signal-
simHO_AEO.emf';saveas(gcf,[fpat,filesep,fnam1],'emf');
   fnam2='PartC-signal-
simHO_AEO.fig';saveas(gcf,[fpat,filesep,fnam2],'fig');
   save ('C:\Hamid,Matlab\MATLAB_PC\PAPER_HO_AEO_Sim\PartC-signal-
simHO_AEO','xC');

figure
hold on; box on;
donfig('units','centimeters','width',7,'height',5,'font','Helvetica','font
size',10);
plot(f(1:end),YY3(1:end));
  xlabel('Frequency (Hz)','FontSize',11);
  ylabel('Magnitude','FontSize',11);
  xlim([1 1000])
   fnam1='FFT-PartC-signal-
simHO_AEO.emf';saveas(gcf,[fpat,filesep,fnam1],'emf');
   fnam2='FFT-PartC-signal-
simHO_AEO.fig';saveas(gcf,[fpat,filesep,fnam2],'fig');
   save ('C:\Hamid,Matlab\MATLAB_PC\PAPER_HO_AEO_Sim\FFT-PartC-signal-
simHO_AEO','YY3');
 %%                      PART A Power2 [FFT]

% figure
% hold on; box on;
%
donfig('units','centimeters','width',7,'height',5,'font','Helvetica','font
size',10);
% plot(f(5:4000),YY4(5:4000));
%   xlabel('Frequency (Hz)','FontSize',11);
%   ylabel('Magnitude','FontSize',11);
%   xlim([1 1000])
%    fnam1='FFT-PartAP2-signal-
simHO_AEO.emf';saveas(gcf,[fpat,filesep,fnam1],'emf');
%    fnam2='FFT-PartAP2-signal-
simHO_AEO.fig';saveas(gcf,[fpat,filesep,fnam2],'fig');
%    save ('C:\Hamid,Matlab\MATLAB_PC\PAPER_HO_AEO_Sim\FFT-PartAP2-signal-
simHO_AEO','YY4');
%%                   PART B Power2  [FFT]

% figure
% hold on; box on;
%
donfig('units','centimeters','width',7,'height',5,'font','Helvetica','font
size',10);
% plot(f(5:4000),YY5(5:4000));
%   xlabel('Frequency (Hz)','FontSize',11);
%   ylabel('Magnitude','FontSize',11);
%   xlim([1 1000])
%    fnam1='FFT-PartBP2-signal-
simHO_AEO.emf';saveas(gcf,[fpat,filesep,fnam1],'emf');
%    fnam2='FFT-PartBP2-signal-
simHO_AEO.fig';saveas(gcf,[fpat,filesep,fnam2],'fig');
%    save ('C:\Hamid,Matlab\MATLAB_PC\PAPER_HO_AEO_Sim\FFT-PartBP2-signal-
simHO_AEO','YY5');
  %%                   PART C Power2  [FFT]
```

```
%  figure
% hold on; box on;
%
donfig('units','centimeters','width',7,'height',5,'font','Helvetica','font
size',10);
% plot(f(5:4000),YY6(5:4000));
%   xlabel('Frequency (Hz)','FontSize',11);
%   ylabel('Magnitude','FontSize',11);
%   xlim([1 1000])
%    fnam1='FFT-PartCP2-signal-
simHO_AEO.emf';saveas(gcf,[fpat,filesep,fnam1],'emf');
%    fnam2='FFT-PartCP2-signal-
simHO_AEO.fig';saveas(gcf,[fpat,filesep,fnam2],'fig');
%    save ('C:\Hamid,Matlab\MATLAB_PC\PAPER_HO_AEO_Sim\FFT-PartCP2-signal-
simHO_AEO','YY6');
   %%             PART A [Envelope & Energy evaluation]
figure
hold on; box on;
donfig('units','centimeters','width',7,'height',5,'font','Helvetica','font
size',10);
plot(f(1:end),YY7(1:end));
  xlabel('Frequency (Hz)','FontSize',11);
  ylabel('Magnitude','FontSize',11);
  xlim([1 1000])
   fnam1='ENV-PartA-simHO_AEO.emf';saveas(gcf,[fpat,filesep,fnam1],'emf');
   fnam2='ENV-PartA-simHO_AEO.fig';saveas(gcf,[fpat,filesep,fnam2],'fig');
   save ('C:\Hamid,Matlab\MATLAB_PC\PAPER_HO_AEO_Sim\ENV-PartA-
simHO_AEO','YY7');

figure
hold on; box on;
donfig('units','centimeters','width',7,'height',5,'font','Helvetica','font
size',10);
plot(f(1:end),YY8(1:end));
  xlabel('Frequency (Hz)','FontSize',11);
  ylabel('Magnitude','FontSize',11);
  xlim([1 1000])
   fnam1='TEO-PartA-simHO_AEO.emf';saveas(gcf,[fpat,filesep,fnam1],'emf');
   fnam2='TEO-PartA-simHO_AEO.fig';saveas(gcf,[fpat,filesep,fnam2],'fig');
   save ('C:\Hamid,Matlab\MATLAB_PC\PAPER_HO_AEO_Sim\TEO-PartA-
simHO_AEO','YY8');


%%             PART B [Envelope & Energy evaluation]
figure
hold on; box on;
donfig('units','centimeters','width',7,'height',5,'font','Helvetica','font
size',10);
plot(f(1:end),YY9(1:end));
  xlabel('Frequency (Hz)','FontSize',11);
  ylabel('Magnitude','FontSize',11);
  xlim([1 1000])
   fnam1='ENV-PartB-simHO_AEO.emf';saveas(gcf,[fpat,filesep,fnam1],'emf');
   fnam2='ENV-PartB-simHO_AEO.fig';saveas(gcf,[fpat,filesep,fnam2],'fig');
   save ('C:\Hamid,Matlab\MATLAB_PC\PAPER_HO_AEO_Sim\ENV-PartB-
simHO_AEO','YY9');
```

```
figure
hold on; box on;
donfig('units','centimeters','width',7,'height',5,'font','Helvetica','font
size',10);
plot(f(1:end),YY10(1:end));
  xlabel('Frequency (Hz)','FontSize',11);
  ylabel('Magnitude','FontSize',11);
  xlim([1 1000])
   fnam1='TEO-PartB-simHO_AEO.emf';saveas(gcf,[fpat,filesep,fnam1],'emf');
   fnam2='TEO-PartB-simHO_AEO.fig';saveas(gcf,[fpat,filesep,fnam2],'fig');
   save ('C:\Hamid,Matlab\MATLAB_PC\PAPER_HO_AEO_Sim\TEO-PartB-
simHO_AEO','YY10');

   %%              PART C [Envelope & Energy evaluation]
figure
hold on; box on;
donfig('units','centimeters','width',7,'height',5,'font','Helvetica','font
size',10);
plot(f(1:end),YY11(1:end));
  xlabel('Frequency (Hz)','FontSize',11);
  ylabel('Magnitude','FontSize',11);
  xlim([1 1000])
   fnam1='ENV-PartC-simHO_AEO.emf';saveas(gcf,[fpat,filesep,fnam1],'emf');
   fnam2='ENV-PartC-simHO_AEO.fig';saveas(gcf,[fpat,filesep,fnam2],'fig');
   save ('C:\Hamid,Matlab\MATLAB_PC\PAPER_HO_AEO_Sim\ENV-PartC-
simHO_AEO','YY11');

figure
hold on; box on;
donfig('units','centimeters','width',7,'height',5,'font','Helvetica','font
size',10);
plot(f(1:end),YY12(1:end));
  xlabel('Frequency (Hz)','FontSize',11);
  ylabel('Magnitude','FontSize',11);
  xlim([1 1000])
   fnam1='TEO-PartC-simHO_AEO.emf';saveas(gcf,[fpat,filesep,fnam1],'emf');
   fnam2='TEO-PartC-simHO_AEO.fig';saveas(gcf,[fpat,filesep,fnam2],'fig');
   save ('C:\Hamid,Matlab\MATLAB_PC\PAPER_HO_AEO_Sim\TEO-PartC-
simHO_AEO','YY12');
 %%              PART A/B/C [Envelope Powe 2]
% figure
% hold on; box on;
%
donfig('units','centimeters','width',7,'height',5,'font','Helvetica','font
size',10);
% plot(f(5:4000),YY13(5:4000));
%   xlabel('Frequency (Hz)','FontSize',11);
%   ylabel('Magnitude','FontSize',11);
%   xlim([1 1000])
%    fnam1='ENVP2-PartA-
simHO_AEO.emf';saveas(gcf,[fpat,filesep,fnam1],'emf');
%    fnam2='ENVP2-PartA-
simHO_AEO.fig';saveas(gcf,[fpat,filesep,fnam2],'fig');
%    save ('C:\Hamid,Matlab\MATLAB_PC\PAPER_HO_AEO_Sim\ENVP2-PartA-
simHO_AEO','YY13');
```

```
%
% figure
% hold on; box on;
%
donfig('units','centimeters','width',7,'height',5,'font','Helvetica','font
size',10);
% plot(f(5:4000),YY14(5:4000));
%   xlabel('Frequency (Hz)','FontSize',11);
%   ylabel('Magnitude','FontSize',11);
%   xlim([1 1000])
%    fnam1='ENVP2-PartB-
simHO_AEO.emf';saveas(gcf,[fpat,filesep,fnam1],'emf');
%    fnam2='ENVP2-PartB-
simHO_AEO.fig';saveas(gcf,[fpat,filesep,fnam2],'fig');
%    save ('C:\Hamid,Matlab\MATLAB_PC\PAPER_HO_AEO_Sim\ENVP2-PartB-
simHO_AEO','YY14');
%
%    figure
% hold on; box on;
%
donfig('units','centimeters','width',7,'height',5,'font','Helvetica','font
size',10);
% plot(f(5:4000),YY15(5:4000));
%   xlabel('Frequency (Hz)','FontSize',11);
%   ylabel('Magnitude','FontSize',11);
%   xlim([1 1000])
%    fnam1='ENVP2-PartC-
simHO_AEO.emf';saveas(gcf,[fpat,filesep,fnam1],'emf');
%    fnam2='ENVP2-PartC-
simHO_AEO.fig';saveas(gcf,[fpat,filesep,fnam2],'fig');
%    save ('C:\Hamid,Matlab\MATLAB_PC\PAPER_HO_AEO_Sim\ENVP2-PartC-
simHO_AEO','YY15');
%%                       PART A // B // C [Mew method]{1}
figure
hold on; box on;
donfig('units','centimeters','width',9,'height',7,'font','Helvetica','font
size',10);
plot(f(1:end),YY16(1:end));
  xlabel('Frequency (Hz)','FontSize',11);
  ylabel('Magnitude','FontSize',11);
  xlim([1 1000])
   fnam1='HSC1-PartA-
simHO_AEO.emf';saveas(gcf,[fpat,filesep,fnam1],'emf');
   fnam2='HSC1-PartA-
simHO_AEO.fig';saveas(gcf,[fpat,filesep,fnam2],'fig');
    save ('C:\Hamid,Matlab\MATLAB_PC\PAPER_HO_AEO_Sim\HSC1-PartA-
simHO_AEO','YY16');

figure
hold on; box on;
donfig('units','centimeters','width',9,'height',7,'font','Helvetica','font
size',10);
plot(f(1:end),YY17(1:end));
  xlabel('Frequency (Hz)','FontSize',11);
  ylabel('Magnitude','FontSize',11);
  xlim([1 1000])
```

```
   fnam1='HSC1-PartB-
simHO_AEO.emf';saveas(gcf,[fpat,filesep,fnam1],'emf');
   fnam2='HSC1-PartB-
simHO_AEO.fig';saveas(gcf,[fpat,filesep,fnam2],'fig');
    save ('C:\Hamid,Matlab\MATLAB_PC\PAPER_HO_AEO_Sim\HSC1-PartB-
simHO_AEO','YY17');

figure
hold on; box on;
donfig('units','centimeters','width',9,'height',7,'font','Helvetica','font
size',10);
plot(f(1:end),YY18(1:end));
  xlabel('Frequency (Hz)','FontSize',11);
  ylabel('Magnitude','FontSize',11);
  xlim([1 1000])
   fnam1='HSC1-PartC-
simHO_AEO.emf';saveas(gcf,[fpat,filesep,fnam1],'emf');
   fnam2='HSC1-PartC-
simHO_AEO.fig';saveas(gcf,[fpat,filesep,fnam2],'fig');
    save ('C:\Hamid,Matlab\MATLAB_PC\PAPER_HO_AEO_Sim\HSC1-PartC-
simHO_AEO','YY18');

%%                   PART A // B // C [Mew method]{2}
figure
hold on; box on;
donfig('units','centimeters','width',9,'height',7,'font','Helvetica','font
size',10);
plot(f(1:end),YY19(1:end));
  xlabel('Frequency (Hz)','FontSize',11);
  ylabel('Magnitude','FontSize',11);
  xlim([1 1000])
   fnam1='HSC2-PartA-
simHO_AEO.emf';saveas(gcf,[fpat,filesep,fnam1],'emf');
   fnam2='HSC2-PartA-
simHO_AEO.fig';saveas(gcf,[fpat,filesep,fnam2],'fig');
    save ('C:\Hamid,Matlab\MATLAB_PC\PAPER_HO_AEO_Sim\HSC2-PartA-
simHO_AEO','YY19');

figure
hold on; box on;
donfig('units','centimeters','width',9,'height',7,'font','Helvetica','font
size',10);
plot(f(1:end),YY20(1:end));
  xlabel('Frequency (Hz)','FontSize',11);
  ylabel('Magnitude','FontSize',11);
  xlim([1 1000])
   fnam1='HSC2-PartB-
simHO_AEO.emf';saveas(gcf,[fpat,filesep,fnam1],'emf');
   fnam2='HSC2-PartB-
simHO_AEO.fig';saveas(gcf,[fpat,filesep,fnam2],'fig');
    save ('C:\Hamid,Matlab\MATLAB_PC\PAPER_HO_AEO_Sim\HSC2-PartB-
simHO_AEO','YY20');

figure
hold on; box on;
```

```
donfig('units','centimeters','width',9,'height',7,'font','Helvetica','font
size',10);
plot(f(1:end),YY21(1:end));
  xlabel('Frequency (Hz)','FontSize',11);
  ylabel('Magnitude','FontSize',11);
  xlim([1 1000])
   fnam1='HSC2-PartC-
simHO_AEO.emf';saveas(gcf,[fpat,filesep,fnam1],'emf');
   fnam2='HSC2-PartC-
simHO_AEO.fig';saveas(gcf,[fpat,filesep,fnam2],'fig');
    save ('C:\Hamid,Matlab\MATLAB_PC\PAPER_HO_AEO_Sim\HSC2-PartC-
simHO_AEO','YY21');
%%                 PART A // B // C    [Mew method]{3}
figure
hold on; box on;
donfig('units','centimeters','width',9,'height',7,'font','Helvetica','font
size',10);
plot(f(1:end),YY22(1:end));
  xlabel('Frequency (Hz)','FontSize',11);
  ylabel('Magnitude','FontSize',11);
  xlim([1 1000])
   fnam1='HSC3-PartA-
simHO_AEO.emf';saveas(gcf,[fpat,filesep,fnam1],'emf');
   fnam2='HSC3-PartA-
simHO_AEO.fig';saveas(gcf,[fpat,filesep,fnam2],'fig');
    save ('C:\Hamid,Matlab\MATLAB_PC\PAPER_HO_AEO_Sim\HSC3-PartA-
simHO_AEO','YY22');

figure
hold on; box on;
donfig('units','centimeters','width',9,'height',7,'font','Helvetica','font
size',10);
plot(f(1:end),YY23(1:end));
  xlabel('Frequency (Hz)','FontSize',11);
  ylabel('Magnitude','FontSize',11);
  xlim([1 1000])
   fnam1='HSC3-PartB-
simHO_AEO.emf';saveas(gcf,[fpat,filesep,fnam1],'emf');
   fnam2='HSC3-PartB-
simHO_AEO.fig';saveas(gcf,[fpat,filesep,fnam2],'fig');
    save ('C:\Hamid,Matlab\MATLAB_PC\PAPER_HO_AEO_Sim\HSC3-PartB-
simHO_AEO','YY23');

figure
hold on; box on;
donfig('units','centimeters','width',9,'height',7,'font','Helvetica','font
size',10);
plot(f(1:end),YY24(1:end));
  xlabel('Frequency (Hz)','FontSize',11);
  ylabel('Magnitude','FontSize',11);
  xlim([1 1000])
   fnam1='HSC3-PartC-
simHO_AEO.emf';saveas(gcf,[fpat,filesep,fnam1],'emf');
   fnam2='HSC3-PartC-
simHO_AEO.fig';saveas(gcf,[fpat,filesep,fnam2],'fig');
```

```
    save ('C:\Hamid,Matlab\MATLAB_PC\PAPER_HO_AEO_Sim\HSC3-PartC-
simHO_AEO','YY24');
```

B.4 HOEO_F METHOD

```
clear all;
clear;
close all;
%%
A = 1;          % the amplitude of fault impulse
Tp = 0.0125;     % time period corresponding to the fault characteristic
frequency
Fr = 2048;      % the excited resonance frequency
Beta = 1500;    % structural damping characteristic
Fs = 20480;     % sample frequency
Ts = 3;         % Data time span
Ph = pi/8;      % init phase
Fi = 33;         % interference frequency
Ai = [];
Bi = [];
Ci = [];
Zi = [];
%% program body

t = [0 : 1/Fs : Ts-(1/Fs)]';          % time
Tps = Tp * [1 : 1 : round(Ts/Tp)]';  % start time point of faulty pulses
production
Sigma = 0.02 * Tp;                    % random slippage
Tps = Tps + (Sigma * rand(length(Tps),1));
Tps = Tps + (Ph/Fr);
%%   outD: faulty bearing vibration (displacement)
outD = zeros(Fs*Ts, 1);
for Np = 1 : length(Tps)
    outDcur = A * robexp(-Beta * (t - Tps(Np))) .* sin(2*pi*Fr * (t -
Tps(Np))) .* stepfun((t - Tps(Np)),0);
    outD = outD + outDcur;
end
outOrg = outD/10;
%%                           Part A  (LOW SIR, AVERAGE SNR)
SirA =  -45;      % Sir: signal to interference ratio
SnrA = 5;        % signal to nose ratio
 DA = awgn ( outOrg    , SnrA, 'measured');
%%    Add interference
 if isempty(Ai)
   sigPower = sum(abs(outOrg(:)).^2)/length(outOrg(:));
   sigPower = 10*log10(sigPower);
   intPower = sigPower-SirA;
   intPower = 10^(intPower/10);
   intPower = intPower/4;
   Ai = sqrt(intPower*2);
 end;
  xA = DA  + Ai*sin(2*pi*Fi*t)+ Ai*sin(2*pi*43*t)+
Ai*sin(2*pi*50*t)+Ai*sin(2*pi*310*t);

%%                            Part B (LOW SNR, AVERAGE SIR)
SirB =  5;        % Sir: signal to interference ratio
SnrB = -19;        % signal to nose ratio
 DB = awgn ( outOrg    , SnrB, 'measured',2);
%%    Add interference
```

```
 if isempty(Bi)
   sigPower = sum(abs(outOrg(:)).^2)/length(outOrg(:));
   sigPower = 10*log10(sigPower);
   intPower = sigPower-SirB;
   intPower = 10^(intPower/10);
   intPower = intPower/4;
   Bi = sqrt(intPower*2);
 end;
  xB = DB   + Bi*sin(2*pi*Fi*t)+ Bi*sin(2*pi*43*t)+
Bi*sin(2*pi*50*t)+Bi*sin(2*pi*310*t);
  %%                             Part C    (LOW SNR, LOW SIR)
SirC = -20;        % Sir: signal to interference ratio
SnrC = -18;        % signal to nose ratio
 DC = awgn ( outOrg    , SnrC, 'measured',1);
%%    Add interference
 if isempty(Ci)
   sigPower = sum(abs(outOrg(:)).^2)/length(outOrg(:));
   sigPower = 10*log10(sigPower);
   intPower = sigPower-SirC;
   intPower = 10^(intPower/10);
   intPower = intPower/4;
   Ci = sqrt(intPower*2);
 end;
  xC = DC   + Ci*sin(2*pi*Fi*t)+ Ci*sin(2*pi*43*t)+
Ci*sin(2*pi*50*t)+Ci*sin(2*pi*310*t);
%%                          PART Z
SirZ = -28;        % Sir: signal to interference ratio
SnrZ = -10;        % signal to nose ratio
 DZ = awgn ( outOrg    , SnrZ, 'measured',1);
 %%    Add interference
 if isempty(Zi)
   sigPower = sum(abs(outOrg(:)).^2)/length(outOrg(:));
   sigPower = 10*log10(sigPower);
   intPower = sigPower-SirZ;
   intPower = 10^(intPower/10);
   intPower = intPower/4;
   Zi = sqrt(intPower*2);
 end;
  xZ = DZ   + Zi*sin(2*pi*Fi*t)+ Zi*sin(2*pi*43*t)+
Zi*sin(2*pi*50*t)+Zi*sin(2*pi*310*t);
  %%                          Part Z
 EZ = energy ( xZ,1);

%%                          Part A
 bhA = abs((hilbert( xA )));
 EA = energy ( xA,1);
[HOE1A,HOE2A] = HOEO( xA,4);

%%                          Part B
 bhB = abs((hilbert( xB )));
 EB = energy ( xB,1);
[HOE1B,HOE2B] = HOEO( xB,4);



%%                          Part C
 bhC = abs((hilbert( xC )));
```

```
 EC = energy ( xC,1);
[HOE1C,HOE2C] = HOEO( xC,4);

%%                                                              FFT TRANSFORM
L=length(xA);
NFFT = 2^nextpow2(L);
Y1 = fft(  xA , NFFT)/L;       Y2 = fft( xB , NFFT)/L;   Y3 = fft( xC ,
NFFT)/L;
Y4 = fft(  bhA, NFFT)/L;       Y5 = fft( EA , NFFT)/L;
Y6 = fft(  bhB, NFFT)/L;       Y7 = fft( EB, NFFT)/L;
Y8 = fft(  bhC, NFFT)/L;       Y9 = fft( EC, NFFT)/L;
Y10 = fft( HOE1A, NFFT)/L;     Y11 = fft( HOE2A, NFFT)/L;
Y12 = fft( HOE1B, NFFT)/L;     Y13 = fft( HOE2B , NFFT)/L;
Y14 = fft( HOE1C , NFFT)/L;    Y15 = fft( HOE2C , NFFT)/L;
Y16 = fft( xZ , NFFT)/L;       Y17 = fft( EZ , NFFT)/L;

f = Fs/2*linspace(0,1,NFFT/2+1);
YY1=2*abs(Y1(1:NFFT/2+1));    YY2=2*abs(Y2(1:NFFT/2+1));
YY3=2*abs(Y3(1:NFFT/2+1));
YY4=2*abs(Y4(1:NFFT/2+1));    YY5=2*abs(Y5(1:NFFT/2+1));
YY6=2*abs(Y6(1:NFFT/2+1));    YY7=2*abs(Y7(1:NFFT/2+1));
YY8=2*abs(Y8(1:NFFT/2+1));    YY9=2*abs(Y9(1:NFFT/2+1));
YY10=2*abs(Y10(1:NFFT/2+1));  YY11=2*abs(Y11(1:NFFT/2+1));
YY12=2*abs(Y12(1:NFFT/2+1));  YY13=2*abs(Y13(1:NFFT/2+1));
YY14=2*abs(Y14(1:NFFT/2+1));  YY15=2*abs(Y15(1:NFFT/2+1));
YY16=2*abs(Y16(1:NFFT/2+1));  YY17=2*abs(Y17(1:NFFT/2+1));
%%                                                                 Figures
fpat='PAPER_HOEO_Sim';
save ('C:\Hamid,Matlab\MATLAB_PC\PAPER_HOEO_Sim\frequency','f');
%%                  PART IMPLUSIVE FAULTY SIGNAL (PART Z)
figure
hold on;  box on;
donfig('units','centimeters','width',14,'height',5,'font','Helvetica','fon
tsize',10);
plot( outOrg );
  xlabel('Sample','FontSize',11);
  ylabel('Amplitude','FontSize',11);
  xlim([1 5000])
   fnam1='PartZ-signal-
simHOEO.emf';saveas(gcf,[fpat,filesep,fnam1],'emf');
   fnam2='PartZ-signal-
simHOEO.fig';saveas(gcf,[fpat,filesep,fnam2],'fig');
   save ('C:\Hamid,Matlab\MATLAB_PC\PAPER_HOEO_Sim\PartZ-signal-
simHOEO','outOrg');

figure;
hold on;  box on;
donfig('units','centimeters','width',15.5,'height',7,'font','Helvetica','f
ontsize',10);

subplot(4,1,1);plot( Zi*sin(2*pi*33*t),'r') ;  xlim([1 5000])
subplot(4,1,2);plot( Zi*sin(2*pi*43*t),'r' );  xlim([1 5000])
subplot(4,1,3);plot(Zi*sin(2*pi*50*t),'r' );  xlim([1 5000])
subplot(4,1,4);plot(Zi*sin(2*pi*310*t),'r' ); xlim([1 5000])

xlabel('Sample','FontSize',11);
```

```
YL=ylabel('Amplitude','FontSize',11);
set(YL,'position',get(YL,'position')-[0.5,-3,0])
   fnam1='PartZ-Intersignal-
simHOEO.emf';saveas(gcf,[fpat,filesep,fnam1],'emf');
   fnam2='PartZ-Intersignal-
simHOEO.fig';saveas(gcf,[fpat,filesep,fnam2],'fig');

   figure
hold on;  box on;
donfig('units','centimeters','width',14,'height',5,'font','Helvetica','fon
tsize',10);
plot( xZ );
  xlabel('Sample','FontSize',11);
  ylabel('Amplitude','FontSize',11);
  xlim([1 5000])
   fnam1='PartZ-mixsignal-
simHOEO.emf';saveas(gcf,[fpat,filesep,fnam1],'emf');
   fnam2='PartZ-mixsignal-
simHOEO.fig';saveas(gcf,[fpat,filesep,fnam2],'fig');
   save ('C:\Hamid,Matlab\MATLAB_PC\PAPER_HOEO_Sim\PartZ-mixsignal-
simHOEO','xZ');

   figure
hold on; box on;
donfig('units','centimeters','width',10,'height',6,'font','Helvetica','fon
tsize',10);
plot(f(1:end),YY16(1:end));
  xlabel('Frequency (Hz)','FontSize',11);
  ylabel('Magnitude','FontSize',11);
  xlim([1 500])
   fnam1='FFT-PartZ-signal-
simHOEO.emf';saveas(gcf,[fpat,filesep,fnam1],'emf');
   fnam2='FFT-PartZ-signal-
simHOEO.fig';saveas(gcf,[fpat,filesep,fnam2],'fig');
   save ('C:\Hamid,Matlab\MATLAB_PC\PAPER_HOEO_Sim\FFT-PartZ-signal-
simHOEO','YY16');

figure
hold on; box on;
donfig('units','centimeters','width',10,'height',6,'font','Helvetica','fon
tsize',10);
plot(f(1:end),YY17(1:end));
  xlabel('Frequency (Hz)','FontSize',11);
  ylabel('Magnitude','FontSize',11);
  xlim([1 500])
   fnam1='TEO-PartZ-simHOEO.emf';saveas(gcf,[fpat,filesep,fnam1],'emf');
   fnam2='TEO-PartZ-simHOEO.fig';saveas(gcf,[fpat,filesep,fnam2],'fig');
   save ('C:\Hamid,Matlab\MATLAB_PC\PAPER_HOEO_Sim\TEO-PartZ-
simHOEO','YY17');
%%                      PART A [Signal & FFT]
figure
hold on;  box on;
donfig('units','centimeters','width',7,'height',5,'font','Helvetica','font
size',10);
plot( xA );
  xlabel('Sample','FontSize',11);
```

```
  ylabel('Amplitude','FontSize',11);
  xlim([1 10000])
   fnam1='PartA-signal-
simHOEO.emf';saveas(gcf,[fpat,filesep,fnam1],'emf');
   fnam2='PartA-signal-
simHOEO.fig';saveas(gcf,[fpat,filesep,fnam2],'fig');
   save ('C:\Hamid,Matlab\MATLAB_PC\PAPER_HOEO_Sim\PartA-signal-
simHOEO','xA');

figure
hold on; box on;
donfig('units','centimeters','width',7,'height',5,'font','Helvetica','font
size',10);
plot(f(1:end),YY1(1:end));
  xlabel('Frequency (Hz)','FontSize',11);
  ylabel('Magnitude','FontSize',11);
  xlim([1 1000])
   fnam1='FFT-PartA-signal-
simHOEO.emf';saveas(gcf,[fpat,filesep,fnam1],'emf');
   fnam2='FFT-PartA-signal-
simHOEO.fig';saveas(gcf,[fpat,filesep,fnam2],'fig');
   save ('C:\Hamid,Matlab\MATLAB_PC\PAPER_HOEO_Sim\FFT-PartA-signal-
simHOEO','YY1');
%%                   PART B  [Signal & FFT]
figure
hold on;  box on;
donfig('units','centimeters','width',7,'height',5,'font','Helvetica','font
size',10);
plot( xB );
  xlabel('Sample','FontSize',11);
  ylabel('Amplitude','FontSize',11);
  xlim([1 10000])
  ylim([-0.6 0.6])
   fnam1='PartB-signal-
simHOEO.emf';saveas(gcf,[fpat,filesep,fnam1],'emf');
   fnam2='PartB-signal-
simHOEO.fig';saveas(gcf,[fpat,filesep,fnam2],'fig');
   save ('C:\Hamid,Matlab\MATLAB_PC\PAPER_HOEO_Sim\PartB-signal-
simHOEO','xB');

figure
hold on; box on;
donfig('units','centimeters','width',7,'height',5,'font','Helvetica','font
size',10);
plot(f(1:end),YY2(1:end));
  xlabel('Frequency (Hz)','FontSize',11);
  ylabel('Magnitude','FontSize',11);
  xlim([1 1000])
   fnam1='FFT-PartB-signal-
simHOEO.emf';saveas(gcf,[fpat,filesep,fnam1],'emf');
   fnam2='FFT-PartB-signal-
simHOEO.fig';saveas(gcf,[fpat,filesep,fnam2],'fig');
   save ('C:\Hamid,Matlab\MATLAB_PC\PAPER_HOEO_Sim\FFT-PartB-signal-
simHOEO','YY2');
   %%                   PART C  [Signal & FFT]
figure
```

```
hold on;  box on;
donfig('units','centimeters','width',7,'height',5,'font','Helvetica','font
size',10);
plot( xC );
  xlabel('Sample','FontSize',11);
  ylabel('Amplitude','FontSize',11);
  xlim([1 10000])
  ylim([-0.6 0.6])
   fnam1='PartC-signal-
simHOEO.emf';saveas(gcf,[fpat,filesep,fnam1],'emf');
   fnam2='PartC-signal-
simHOEO.fig';saveas(gcf,[fpat,filesep,fnam2],'fig');
   save ('C:\Hamid,Matlab\MATLAB_PC\PAPER_HOEO_Sim\PartC-signal-
simHOEO','xC');

figure
hold on; box on;
donfig('units','centimeters','width',7,'height',5,'font','Helvetica','font
size',10);
plot(f(1:end),YY3(1:end));
  xlabel('Frequency (Hz)','FontSize',11);
  ylabel('Magnitude','FontSize',11);
  xlim([1 1000])
   fnam1='FFT-PartC-signal-
simHOEO.emf';saveas(gcf,[fpat,filesep,fnam1],'emf');
   fnam2='FFT-PartC-signal-
simHOEO.fig';saveas(gcf,[fpat,filesep,fnam2],'fig');
   save ('C:\Hamid,Matlab\MATLAB_PC\PAPER_HOEO_Sim\FFT-PartC-signal-
simHOEO','YY3');

   %%              PART A [Envelope & Energy evaluation]
figure
hold on; box on;
donfig('units','centimeters','width',7,'height',5,'font','Helvetica','font
size',10);
plot(f(1:end),YY4(1:end));
  xlabel('Frequency (Hz)','FontSize',11);
  ylabel('Magnitude','FontSize',11);
  xlim([1 500])
   fnam1='ENV-PartA-simHOEO.emf';saveas(gcf,[fpat,filesep,fnam1],'emf');
   fnam2='ENV-PartA-simHOEO.fig';saveas(gcf,[fpat,filesep,fnam2],'fig');
   save ('C:\Hamid,Matlab\MATLAB_PC\PAPER_HOEO_Sim\ENV-PartA-
simHOEO','YY4');

figure
hold on; box on;
donfig('units','centimeters','width',7,'height',5,'font','Helvetica','font
size',10);
plot(f(1:end),YY5(1:end));
  xlabel('Frequency (Hz)','FontSize',11);
  ylabel('Magnitude','FontSize',11);
  xlim([1 500])
   fnam1='TEO-PartA-simHOEO.emf';saveas(gcf,[fpat,filesep,fnam1],'emf');
   fnam2='TEO-PartA-simHOEO.fig';saveas(gcf,[fpat,filesep,fnam2],'fig');
   save ('C:\Hamid,Matlab\MATLAB_PC\PAPER_HOEO_Sim\TEO-PartA-
simHOEO','YY5');
```

```
%%              PART B [Envelope & Energy evaluation]
figure
hold on; box on;
donfig('units','centimeters','width',7,'height',5,'font','Helvetica','font
size',10);
plot(f(1:end),YY6(1:end));
  xlabel('Frequency (Hz)','FontSize',11);
  ylabel('Magnitude','FontSize',11);
  xlim([1 500])
   fnam1='ENV-PartB-simHOEO.emf';saveas(gcf,[fpat,filesep,fnam1],'emf');
   fnam2='ENV-PartB-simHOEO.fig';saveas(gcf,[fpat,filesep,fnam2],'fig');
   save ('C:\Hamid,Matlab\MATLAB_PC\PAPER_HOEO_Sim\ENV-PartB-
simHOEO','YY6');

figure
hold on; box on;
donfig('units','centimeters','width',7,'height',5,'font','Helvetica','font
size',10);
plot(f(1:end),YY7(1:end));
  xlabel('Frequency (Hz)','FontSize',11);
  ylabel('Magnitude','FontSize',11);
  xlim([1 500])
   fnam1='TEO-PartB-simHOEO.emf';saveas(gcf,[fpat,filesep,fnam1],'emf');
   fnam2='TEO-PartB-simHOEO.fig';saveas(gcf,[fpat,filesep,fnam2],'fig');
   save ('C:\Hamid,Matlab\MATLAB_PC\PAPER_HOEO_Sim\TEO-PartB-
simHOEO','YY7');

   %%              PART C [Envelope & Energy evaluation]
figure
hold on; box on;
donfig('units','centimeters','width',7,'height',5,'font','Helvetica','font
size',10);
plot(f(1:end),YY8(1:end));
  xlabel('Frequency (Hz)','FontSize',11);
  ylabel('Magnitude','FontSize',11);
  xlim([1 500])
   fnam1='ENV-PartC-simHOEO.emf';saveas(gcf,[fpat,filesep,fnam1],'emf');
   fnam2='ENV-PartC-simHOEO.fig';saveas(gcf,[fpat,filesep,fnam2],'fig');
   save ('C:\Hamid,Matlab\MATLAB_PC\PAPER_HOEO_Sim\ENV-PartC-
simHOEO','YY8');

figure
hold on; box on;
donfig('units','centimeters','width',7,'height',5,'font','Helvetica','font
size',10);
plot(f(1:end),YY9(1:end));
  xlabel('Frequency (Hz)','FontSize',11);
  ylabel('Magnitude','FontSize',11);
  xlim([1 500])
   fnam1='TEO-PartC-simHOEO.emf';saveas(gcf,[fpat,filesep,fnam1],'emf');
   fnam2='TEO-PartC-simHOEO.fig';saveas(gcf,[fpat,filesep,fnam2],'fig');
   save ('C:\Hamid,Matlab\MATLAB_PC\PAPER_HOEO_Sim\TEO-PartC-
simHOEO','YY9');
```

```
%%                        PART A // B // C [Mew method]{1}
figure
hold on; box on;
donfig('units','centimeters','width',9,'height',7,'font','Helvetica','font
size',10);
plot(f(1:end),YY10(1:end));
  xlabel('Frequency (Hz)','FontSize',11);
  ylabel('Magnitude','FontSize',11);
  xlim([1 500])
   fnam1='HOE1-PartA-
simHO_AEO.emf';saveas(gcf,[fpat,filesep,fnam1],'emf');
   fnam2='HOE1-PartA-
simHO_AEO.fig';saveas(gcf,[fpat,filesep,fnam2],'fig');
    save ('C:\Hamid,Matlab\MATLAB_PC\PAPER_HOEO_Sim\HOE1-PartA-
simHOEO','YY10');

figure
hold on; box on;
donfig('units','centimeters','width',9,'height',7,'font','Helvetica','font
size',10);
plot(f(1:end),YY12(1:end));
  xlabel('Frequency (Hz)','FontSize',11);
  ylabel('Magnitude','FontSize',11);
  xlim([1 500])
   fnam1='HOE1-PartB-simHOEO.emf';saveas(gcf,[fpat,filesep,fnam1],'emf');
   fnam2='HOE1-PartB-simHOEO.fig';saveas(gcf,[fpat,filesep,fnam2],'fig');
    save ('C:\Hamid,Matlab\MATLAB_PC\PAPER_HOEO_Sim\HOE1-PartB-
simHOEO','YY12');

figure
hold on; box on;
donfig('units','centimeters','width',9,'height',7,'font','Helvetica','font
size',10);
plot(f(1:end),YY14(1:end));
  xlabel('Frequency (Hz)','FontSize',11);
  ylabel('Magnitude','FontSize',11);
  xlim([1 500])
   fnam1='HOE1-PartC-simHOEO.emf';saveas(gcf,[fpat,filesep,fnam1],'emf');
   fnam2='HOE1-PartC-simHOEO.fig';saveas(gcf,[fpat,filesep,fnam2],'fig');
    save ('C:\Hamid,Matlab\MATLAB_PC\PAPER_HOEO_Sim\HOE1-PartC-
simHOEO','YY14');

%%                   PART A // B // C [Mew method]{2}
figure
hold on; box on;
donfig('units','centimeters','width',9,'height',7,'font','Helvetica','font
size',10);
plot(f(1:end),YY11(1:end));
  xlabel('Frequency (Hz)','FontSize',11);
  ylabel('Magnitude','FontSize',11);
  xlim([1 500])
   fnam1='HOE2-PartA-simHOEO.emf';saveas(gcf,[fpat,filesep,fnam1],'emf');
   fnam2='HOE2-PartA-simHOEO.fig';saveas(gcf,[fpat,filesep,fnam2],'fig');
    save ('C:\Hamid,Matlab\MATLAB_PC\PAPER_HOEO_Sim\HOE2-PartA-
simHOEO','YY11');
```

```
figure
hold on; box on;
donfig('units','centimeters','width',9,'height',7,'font','Helvetica','font
size',10);
plot(f(1:end),YY13(1:end));
  xlabel('Frequency (Hz)','FontSize',11);
  ylabel('Magnitude','FontSize',11);
  xlim([1 500])
   fnam1='HOE2-PartB-simHOEO.emf';saveas(gcf,[fpat,filesep,fnam1],'emf');
   fnam2='HOE2-PartB-simHOEO.fig';saveas(gcf,[fpat,filesep,fnam2],'fig');
    save ('C:\Hamid,Matlab\MATLAB_PC\PAPER_HOEO_Sim\HOE2-PartB-
simHOEO','YY13');

figure
hold on; box on;
donfig('units','centimeters','width',9,'height',7,'font','Helvetica','font
size',10);
plot(f(1:end),YY15(1:end));
  xlabel('Frequency (Hz)','FontSize',11);
  ylabel('Magnitude','FontSize',11);
  xlim([1 500])
   fnam1='HOE2-PartC-simHOEO.emf';saveas(gcf,[fpat,filesep,fnam1],'emf');
   fnam2='HOE2-PartC-simHOEO.fig';saveas(gcf,[fpat,filesep,fnam2],'fig');
    save ('C:\Hamid,Matlab\MATLAB_PC\PAPER_HOEO_Sim\HOE2-PartC-
simHOEO','YY15');
```

B.5 FAULT DETECTION MAP

```
clear all;
clear;
close all;clock
% Simulate the fault signal

% Inputs
% A : the amplitude of fault impulse
% Tp: time period corresponding to the fault characteristic frequency
% Fr: the excited resonance frequency
% Beta£°structural damping characteristic
% Fs: sample frequency
% Ts: Data time span - (large value may produces NaN, e.g 1)
% snr: signal to noise ratio
% Ph: init phase
% Fi: interference frequency
% Ai: interference amplitude
% Sir: signal to interference ratio

% Outputs
% outD: faulty bearing vibration (displacement)
% outA: faulty bearing vibration (acceleration)
%%
A = 1;          % the amplitude of fault impulse
Tp = 0.008;     % time period corresponding to the fault characteristic
frequency
Fr = 2048;      % the excited resonance frequency
Beta = 1500;    %structural damping characteristic
Fs = 20480;     % sample frequency
Ts = 2;         % Data time span
Ph = pi/8;      % init phase
Fi = 5;         % interference frequency
Ai = [];        % interference amplitude
% Sir =  -30;      % Sir: signal to interference ratio
% Snr = -5;     %signal to nose ratio
%% program body

t = [0 : 1/Fs : Ts-(1/Fs)]';          % time
Tps = Tp * [1 : 1 : round(Ts/Tp)]';   % start time point of faulty pulses
production
Sigma = 0.02 * Tp;                    % random slippage
Tps = Tps + (Sigma * rand(length(Tps),1));
Tps = Tps + (Ph/Fr);

%%   outD: faulty bearing vibration (displacement)
outD = zeros(Fs*Ts, 1);
for Np = 1 : length(Tps)
    outDcur = A * robexp(-Beta * (t - Tps(Np))) .* sin(2*pi*Fr * (t -
Tps(Np))) .* stepfun((t - Tps(Np)),0);
    outD = outD + outDcur;
 end

outOrg = outD;
```

```
N=60;M=60;   pbh=zeros(N,N);pE=zeros(N,N);
for j=1:1:N
 for i=1:1:M
    z=i+(j-1)*M;
    SIR(i,j)= 5-j;  Sir = SIR(i,j);
    SNR(i,j)= 40-i;   Snr = SNR(i,j);
 %% Add noise
% [outD,IS,measuredSIR]= genSignalForSIR(outOrg',Sir,Fs);

 outD = awgn ( outOrg    , Snr, 'measured');
 %%    Add interference
 if isempty(Ai)
   sigPower = sum(abs(outOrg(:)).^2)/length(outOrg(:));
   sigPower = 10*log10(sigPower);
   intPower = sigPower-Sir;
   intPower = 10^(intPower/10);
   intPower = intPower/4;
   Ai = sqrt(intPower*2);
 end;
 outD =outD  + Ai*sin(2*pi*Fi*t)+ Ai*sin(2*pi*27*t)+
Ai*sin(2*pi*43*t)+Ai*sin(2*pi*600*t);
 %%    Proposal MFD  [FFT:outD; Envelope:bh; Energy method:E1; ADD: bh-
adh1-adh2{PFDDMS}; CEEO:vteo3; HOSC:HSC1 ;;; size[14*14 cm]//[17*15]with
bar ]
 bh = abs((hilbert( outD )));
 E1 = energy ( outD,1);
 [adh1,dh1] = dad( outD,1,1/Fs );[adh2,dh2] = dad( outD,2,1/Fs );
%  [HSC1,HSC2,HSC3] = HSCO( outD,1);
%  [ vteo1, vteo2, vteo3 ] = VTEO( outD,2 );
 DX2=diffe(outD,2);EDX2=abs((hilbert( DX2 )));
%%  Test several new methods
%  E2 = energy ( outD,2);
%  NE = dh1.^2-bh.*dh2;
%  [ HSC1,HSC2,HSC3 ] = HSCO_new1( outD,1 );
 [HOE1,HOE2,HOE3,HOE4] = HOEO( outD,5);
%  [ADMO1,ADMO2]=ADMO(outD);
%  [GE1,GE2] = GEO(outD,2);
%  DX1=diffe(outD,1);EDX1=abs((hilbert( DX1 )));
%  HSC=HSC1./max(abs(HSC1))+HSC2./max(abs(HSC2))+HSC3./max(abs(HSC3));
 %%
 L=length(outD);
 NFFT = 2^nextpow2(L);
 Y1 = fft(  outD , NFFT)/L;         Y2 = fft( bh, NFFT)/L;
 Y3 = fft(  EDX2 , NFFT)/L;         Y4 = fft( E1 , NFFT)/L;
 Y5 = fft(  HOE1', NFFT)/L;         Y6 = fft( HOE2', NFFT)/L;
 Y7 = fft(  HOE3, NFFT)/L;          Y8 = fft( HOE4, NFFT)/L;
 f = Fs/2*linspace(0,1,NFFT/2+1);
 YY1=2*abs(Y1(1:NFFT/2+1));  YY2=2*abs(Y2(1:NFFT/2+1));
 YY3=2*abs(Y3(1:NFFT/2+1));  YY4=2*abs(Y4(1:NFFT/2+1));
 YY5=2*abs(Y5(1:NFFT/2+1));  YY6=2*abs(Y6(1:NFFT/2+1));
 YY7=2*abs(Y7(1:NFFT/2+1));  YY8=2*abs(Y8(1:NFFT/2+1));
 %%
  [ PY1(i,j)]  = PFDD( f,YY1,1,1/Tp);
  [ PY2(i,j)]  = PFDD( f,YY2,1,1/Tp);
  [ PY3(i,j)]  = PFDD( f,YY3,1,1/Tp);
  [ PY4(i,j)]  = PFDD( f,YY4,1,1/Tp);
  [ PY5(i,j)]  = PFDD( f,YY5,1,1/Tp);
```

```
  [ PY6(i,j)]  = PFDD( f,YY6,1,1/Tp);
  [ PY7(i,j)]  = PFDD( f,YY7,1,1/Tp);
  [ PY8(i,j)]  = PFDD( f,YY8,1,1/Tp);
  [ PYADD(i,j)]  = PFDDMS( f,YY2,YY5,YY6,1,1/Tp);
   Ai = [];
 end
end

%% Figure {contourf; imagesc; pcolor; [figure palette-variable-right
click-plot catalog] }
% figure
% hold on;  box on;
% plot( outOrg(1:10000) )

% figure
% hold on;  box on;
% plot(f(10:2500),YY1(10:2500))
% xlabel('Frequency')
% ylabel('Magnitude')
 %%
figure
imagesc(reshape(SIR,1,[]),reshape(SNR,1,[]),PY1);
  xlabel('SIR (dB)')
  ylabel('SNR (dB)')
%   colormap(gray)
   colormap(jet)
figure
imagesc(reshape(SIR,1,[]),reshape(SNR,1,[]),PY2);
 xlabel('SIR (dB)')
  ylabel('SNR (dB)')
%   colormap(gray)
  colormap(jet)
figure
imagesc(reshape(SIR,1,[]),reshape(SNR,1,[]),PY3);
  xlabel('SIR (dB)')
  ylabel('SNR (dB)')
%   colormap(gray)
   colormap(jet)
figure
imagesc(reshape(SIR,1,[]),reshape(SNR,1,[]),PY4);
  xlabel('SIR (dB)')
  ylabel('SNR (dB)')
%   colormap(gray)
   colormap(jet)
figure
imagesc(reshape(SIR,1,[]),reshape(SNR,1,[]),PY5);
  xlabel('SIR (dB)')
  ylabel('SNR (dB)')
%   colormap(gray)
  colormap(jet)
figure
imagesc(reshape(SIR,1,[]),reshape(SNR,1,[]),PY6);
  xlabel('SIR (dB)')
  ylabel('SNR (dB)')
%   colormap(gray)
  colormap(jet)
```

```
figure
imagesc(reshape(SIR,1,[]),reshape(SNR,1,[]),PY7);
  xlabel('SIR (dB)')
  ylabel('SNR (dB)')
%   colormap(gray)
  colormap(jet)

figure
imagesc(reshape(SIR,1,[]),reshape(SNR,1,[]),PY8);
  xlabel('SIR (dB)')
  ylabel('SNR (dB)')
  set(gca,'yDir','reverse')
%    ylim([max(SNR(:)) min(SNR(:))])
%   colormap(gray)
  colormap(jet)

figure
imagesc(reshape(SIR,1,[]),reshape(SNR,1,[]),PYADD);
  xlabel('SIR (dB)')
  ylabel('SNR (dB)')
%    set(gca,'YDir','reverse')
%   colormap(gray)
  colormap(jet)
  clock
   %%
```